Properties of Artificially Created Spin Structures Studied by Scanning Probe Methods

Von der Fakultät für Mathematik, Informatik und Naturwissenschaften der RWTH Aachen University zur Erlangung des akademischen Grades eines Doktors der Naturwissenschaften genehmigte Dissertation

vorgelegt von

Soroush Arabi

aus Teheran, Iran

Berichter:

Prof. Dr. Markus Ternes
Prof. Dr. Klaus Kern

Tag der mündlichen Prüfung: August 31, 2022

Contents

Declaration of authorship

I, Soroush Arabi
declare that this thesis and the work presented in it are my own and has been generated by me as the result of my own original research. I do solemnely swear that:

1. This work was done wholly or mainly while in candidature for the doctoral degree at this faculty and university;

2. Where any part of this thesis has previously been submitted for a degree or any other qualification at this university or any other institution, this has been clearly stated;

3. Where I have consulted the published work of others or myself, this is always clearly attributed;

4. Where I have quoted from the work of others or myself, the source is always given. This thesis is entirely my own work, with the exception of such quotations;

5. I have acknowledged all major sources of assistance;

6. Where the thesis is based on work done by myself jointly with others, I have made clear exactly what was done by others and what I have contributed myself;

7. Parts of this work have been published before as:
Wang, Y., Arabi, S., Kern, K., Ternes, M. Commun Phys 4, 103 (2021)

Signature: Soroush Arabi

Date and place: 19.07.2022, Stuttgart, Germany

Abstract

In the last three decades, two-dimensional artificial lattices have served as a promising testbed for studying quantum states of matter [1–4]. They have the advantage of controlling the microscopic degrees of freedom and tailoring interactions between their constituents. Such lattices have been experimentally realized in various setups, including optical lattices [5], self-assembled atomic/molecular lattices [6–8], quantum dots [9–11], trapped ions [12], and very recently in superconducting circuits [13], and patterned devices [14]. Among these platforms, the self-assembled atomic/molecular lattices and surface-supported structures are natural choices to characterize new quantum states, owing to their tunability and simple *in situ* preparation routines. On this account, low-temperature scanning probe methods (SPM) are versatile tools for their imaging and spectroscopic capabilities and their atomic-scale manipulation to create and characterize such structures. These capabilities have placed the SPM as the major experimental technique that combines unprecedented spatial and energy resolutions to reveal the detail of the state of matter that emerges under harsh physical conditions, namely the strongly correlated electron systems, that have been far beyond the reach of other techniques.

The strongly correlated electron systems, especially those confined in two dimensions, are an integral part of modern condensed matter physics. Their ground states are predominantly governed by the repulsive electron-electron interaction, in contrast to many simple materials such as gold, silver, and silicon, whose properties are roughly intact by the interaction. These materials generally possess exceptional properties, and transitions between distinct, competing states with remarkably different electronic and magnetic orders [15]. In this regard, this thesis is devoted to studying the strongly correlated electron systems manifested in two-dimensional artificial lattices and also in the van der Waals layered materials. We are mainly concerned with understanding the role of a single spin and also its ensemble in the ground state of a system.

The Kondo effect is an archetype for the strong interaction that, even after more than half a century since its realization, condensed matter physicists use its observation as a gateway, or a starting point, to understand the underlying physics of a very complicated system. Ubiquitous in this research, the Kondo effect appears in both single-ion and lattice form. In our first project, we study NTCDA molecule, which is a π-conjugated spin$-1/2$ system [16, 17]. It forms a 2D Kondo lattice, developed by the self-assembly of molecules on the surface of Ag(111) metal. In this work, we aim to understand the elementary excitations of the lattice and their real-space manifestation, particularly the quasiparticle excitations, and follow their fate upon quantum phase transition. In our second project, we revisit the Kondo effect afresh: this time in a superconducting tunnel junction and disguised in partially spin screened Yu-Shiba-Rusinov bound states. In this work, we study CoPc molecule, a spin$-1/2$ system, adsorbed on the surface of the 2D superconductor 2H-$NbSe_2$. As we will show, this system captures a subtle angle-dependent interplay between the Kondo effect, superconductivity, and Dzyaloshinskii Moriya interaction.

Keywords: artificial lattice, self-assembled molecular/atomic lattices, spin structures, van

der Waals layered materials, scanning probe methods, strongly correlated electron system, electron-electron interaction, Kondo effect, Kondo lattice, NTCDA molecule, quantum phase transition, CoPc molecule, 2D superconductor, 2H-$NbSe_2$, Dzyaloshinskii Moriya interaction

Structure of the thesis

- In chapter 1, we provide the detail of the experimental setup in **The Max Planck Institute for Solid State Research**, Precision Laboratory, Nanoscale Science Department, where the author of this thesis takes the measurements and also present an introduction to the scanning tunneling microscopy with a theory toolbox to read and analyze measurements in a tunneling junction.
- In chapter 2, we provide an introduction to the self-assembled NTCDA/Ag(111) system, where we attempt to review past works on this topic performed by our collaborators in The Jülich Research Center, RWTH Aachen University, and others, plus presenting some of our new results.
- In chapter 3, we review some of the primary models in the strongly correlated electron physics and discuss the historical example of the quantum phase transition in the Kondo lattice, which we later realize in our measurements. Subsequently, we present some of our high-resolution spectroscopic images at low and high energies of the NTCDA Kondo lattice and compare them with our modeling.
- In chapter 4, we provide a collection of real-space portrays of the quasiparticle interference patterns of the Kondo lattice, which we imaged under different conditions. One of them is presented as an instance in chapter 3.
- In chapter 5, we develop a tight-binding model in great detail to simulate the general properties of the interference patterns presented in chapter 4 and further supplement it with a scripted python code.
- In chapter 6, we provide a comprehensive review of our published work on the interplay of molecular magnetism and superconductivity in 2D materials (CoPc/$NbSe_2$).

Chapter 1

Scanning tunneling microscopy

Scanning tunneling microscopy (STM) is a non-optical imaging technique with ultra-high resolution images at the atomic scale invented based on the quantum tunneling phenomenon. Historically, STM was developed by Binnig, Rohrer, and Gerber in 1982 for which the first two were awarded the Nobel prize in physics [18]. Instrumentally, STM is a tunneling junction comprised of a sharp conducting tip which is scanned over a flat conducting sample, while a bias voltage is applied between them to allow electrons to tunnel across the insulating vacuum barrier in close proximity (< 1 nm gap). The measurement of this minuscule tunneling current is at the heart of the STM technique. In this chapter, I discuss the basic principles of STM from both experiment and theory standpoints. The experiment section outlines the setup under which the measurements are taken, and the theory section reviews the standard derivation of the formulas used to interpret the STM results. The derivations are presented in great detail, and therefore, an advanced reader can skip this section as only the final well-known formulas will be referred to later in the thesis.

1.1 Experimental setup

The experimental setup, Fig.(1.1), incorporates a combined scanning tunneling and atomic force microscope (STM/AFM) with an *in-situ* sample preparation in an ultra-high vacuum (UHV) chamber. The measurements are taken in the STM head, installed at the bottom of a helium cryostat with 100 hours holding time and 4.2 K temperature, which can be further reduced to 1.2 K in a Joule-Thompson cycle. The head is encircled by a superconducting magnet, creating vertical magnetic fields up to 14 T.

1.1.1 Ultra high-vacuum system

The UHV chamber is divided into two parts separated by a UHV-gate-valve. One part is used for the preparation of the sample (left side of Fig.(1.1a), while the other one, the STM chamber, contains the sample stage and cryostat. A horizontal manipulator is used to transfer the sample between the two chambers. The STM chamber is also connected to the loadlock (backside of Fig.(1.1a), which allows transferring the sample to outside without venting the chamber. To keep the base pressure in the lower 10^{-10} mbar range, a combination of scroll pump, turbo molecular pumps, ion getter pumps, and titanium sublimation pump are used.

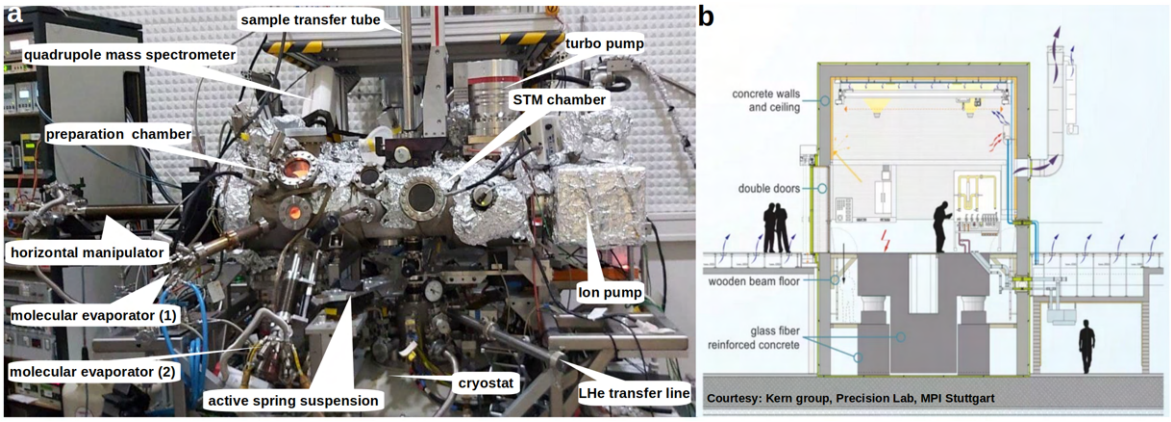

Figure 1.1: Scanning probe microscope setup. a, Image of the custom-built ultra high-vacuum sub-Kelvin scanning probe microscope in MPI, Stuttgart. **b,** Schematic view of the acoustic box hosting the STM setup, fixed on 100 tons of concrete and air springs.

1.1.2 Noise isolation and instabilities

In order to reach sub-angstrom precision in STM measurements, the setup must be isolated from low- and high-frequency environmental and instrumental noises. The sub-Kelvin STM machine is located inside an acoustic box (floating room) which is set on 100 tons of concrete block and active air spring suspensions, Fig.(1.1b), providing an exceptional shielding[1] from

[1] 60 dB attenuation

the environment. Moreover, all mechanical pumps are placed in a separate room, and the pumping lines are fixed in the heavy concrete wall to isolate the box from vibrations of the pumps. Despite these efforts, the 50 Hz noise and the noise due to liquid helium boiling are always present in the current channel of the junction. The latter is the major drawback arising from the large cryostat. Besides, having a tuning fork induces further instability to the current channel.

1.1.3 STM head

A significant advantage of the STM junction over other designs is the sub-angstrom control over distances in all directions (x, y, z), promoting it from an imaging technique to a local probe for transport measurements. The junction is housed inside the STM head, Fig.(1.2a), constituting a sample and tip, which is stationed above a piezo tube for lateral scanning, and six piezo stacks for the coarse approach [19]. The tip is mounted on the free prong of a tuning fork with an extra contact to simultaneously read the current and force signal [20]. Practically, the very sharp STM tip moves laterally and vertically by applying voltages to a calibrated xyz–piezo tube and recording the tunneling current signal. The tunneling current, which is exponentially dependent on the vacuum gap width, requires an amplification circuit that converts the current into a voltage signal and subsequently feeds it into a closed feedback loop and records the z–height, Fig.(1.2c).

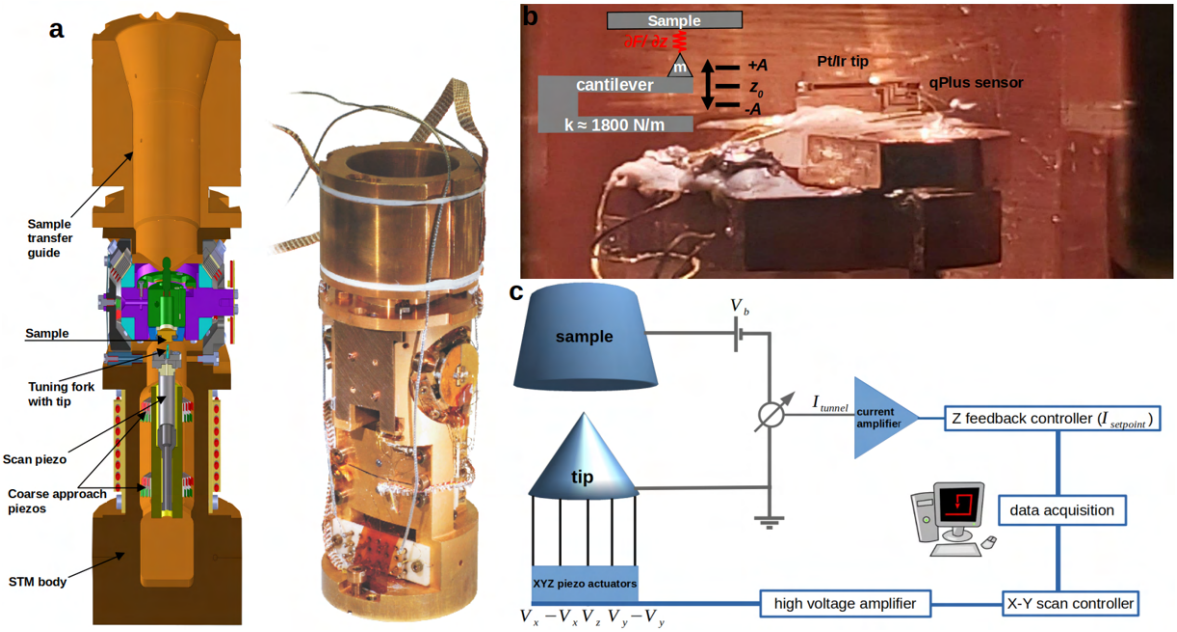

Figure 1.2: Scanning probe microscope head. **a,** Image of the home-built STM/AFM head of the subK machine in MPI, Stuttgart (image by courtesy of Tobias Herden & Markus Ternes). **b,** Pt/Ir STM tip of 25 micron diameter mounted on the free prong of a qPlus sensor. **c,** Schematic diagram of STM circuit including the junction, feedback loop, and data acquisition.

1.1.4 Operational modes

STM has two standard modes of operation: The constant-current mode and the constant-height mode. In the constant-current mode, the feedback loop is controlled such that the tunnelling current is constant over time, whilst the height signal is recorded as the topography of the sample. The STM scan control unit actuates the $xy-$piezos and raster the tip laterally over the sample at constant bias. The resulting image is topographic map of the sample surface. It is worth mentioning that the recorded height profile does not necessarily equal to the true topography of the sample. Since the tunneling current is used to control the $z-$height, the height signal is in fact a surface of constant conductivity. Alternatively, in the constant-height mode, the feedback loop is open, and therefore, the scanner moves the tip only in-plane at constant-height and bias. For this mode to be used it is crucial to have a flat surface to avoid tip-sample crash.

1.2 Quantum theory of STM

Intuitively, the single-particle properties of a many-body system are encoded in how a particle propagates in the system. In quantum mechanics, the particle propagation is the process of annihilation of the particle in a state ($|\psi_\nu\rangle$) and creation in another one ($|\psi_\mu\rangle$), i.e., terms like $t_{\nu\mu}c^\dagger_\nu c_\mu$, where $t_{\nu\mu}$ gives the amplitude of the process. Conceptually, such a process can be realized as the insertion and ejection of particles into a state. Experimentally, there are two generic methods to probe the single-particle properties; by subjecting the system to a flow of either photons or electrons. The former is realized in optical and photoemission spectroscopy measurements, where an electron is ejected from an occupied state by absorbing a photon and subsequently refilling it by another electron, and the latter in tunneling junctions. **The formalism of this section closely follows the approach developed in reference [21], and occasionally uses reference [22, 23]**. Historically, it is based on Bardeen's approach where he applied time-dependent perturbation theory to two weakly coupled electrodes [24]; and here, it is re-derived in second-quantization using linear response theory.

1.2.1 Tunneling spectroscopy

The simplest tunneling junction consists of two metallic leads and an insulating gap (vacuum) in between, wherein close proximity, an electron can tunnel from one lead to the other. The two conducting leads are described by Hamiltonian $\mathcal{H}_1$ and $\mathcal{H}_2$,

$$\mathcal{H}_1 = \sum_\nu \xi_{1,\nu} c^\dagger_{1,\nu} c_{1,\nu} \qquad , \qquad \mathcal{H}_2 = \sum_\mu \xi_{2,\mu} c^\dagger_{2,\mu} c_{2,\mu} \, ,$$

with $(c^\dagger_{1\nu},\, c_{1\nu})$ and $(c^\dagger_{1\mu},\, c_{1\mu})$ being the creation/annihilation operators of the electrons in lead 1 and 2 with ν and μ denoting the complete set of their quantum numbers, e.g.,

$\nu = (\mathbf{k}, \sigma)$. The dispersion relations of the leads are given as

$$\begin{cases} \xi_{1,\nu} = \epsilon_{1,\nu} - eV_1 \\ \\ \xi_{2,\mu} = \epsilon_{1,\mu} - eV_2 \end{cases} , \tag{1.1}$$

which are subject to voltages V_1 and V_2.
The tunneling between the two electrodes across the junction is realized by a finite overlap of the wave functions of each system, resulting in the following hybridization Hamiltonian

$$\mathcal{H}_T = \sum_{\nu\mu} \left(T_{\nu\mu} c^\dagger_{1,\nu} c_{2,\mu} + T^*_{\nu\mu} c^\dagger_{2,\mu} c_{1,\nu} \right) . \tag{1.2}$$

Therefore, the full Hamiltonian of the junction reads

$$\mathcal{H} = \mathcal{H}_1 + \mathcal{H}_2 + \mathcal{H}_T.$$

The tunnelling matrix element is defined as

$$T_{\nu\mu} = \langle \psi_\nu | \mathcal{H} | \psi_\mu \rangle = \langle \psi_\nu | \mathcal{H} \, \mathbb{1} | \psi_\mu \rangle = \langle \psi_\nu | \mathcal{H} \left(\int d\mathbf{r} \, |\mathbf{r}\rangle \langle \mathbf{r}| \right) |\psi_\mu\rangle = \int d\mathbf{r} \, \psi^*_\nu(\mathbf{r}) \mathcal{H}(\mathbf{r}) \psi_\mu(\mathbf{r})$$

where $\mathcal{H}(\mathbf{r})$ is the real-space representation of the full single-particle Hamiltonian. Here, it is assumed that the full Hamiltonian H is diagonal in the real-space.
Now, we define current through the junction as the rate of change of particles,

$$I_e = -e \langle I \rangle ,$$

where $I = \dot{N}_1 = i[\mathcal{H}, N_1]$, and hence

$$I = i[\mathcal{H}_1 + \mathcal{H}_2 + \mathcal{H}_T, N_1] = i[\mathcal{H}_1, N_1] + i[\mathcal{H}_2, N_1] + i[\mathcal{H}_T, N_1].$$

The problem reduced to evaluating three commutators

$$\begin{aligned} I = i \sum_{\nu,\nu'} \xi_{1,\nu} \underbrace{\left[c^\dagger_{1,\nu} c_{1,\nu} \, , \, c^\dagger_{1,\nu'} c_{1,\nu'} \right]}_{(1) \qquad = 0} + i \sum_{\mu,\nu'} \xi_{2,\mu} \underbrace{\left[c^\dagger_{2,\mu} c_{2,\mu} \, , \, c^\dagger_{1,\nu'} c_{1,\nu'} \right]}_{(2) \qquad = 0} \\ + i \sum_{\nu,\mu} \sum_{\nu'} \left[\left(T_{\nu\mu} c^\dagger_{1,\nu} c_{2,\mu} + T^*_{\nu\mu} c^\dagger_{2,\mu} c_{1,\nu} \right) , c^\dagger_{1,\nu'} c_{1,\nu'} \right] \\ = i \sum_{\nu,\mu} \sum_{\nu'} T_{\nu\mu} \underbrace{\left[c^\dagger_{1,\nu} c_{2,\mu} , c^\dagger_{1,\nu'} c_{1,\nu'} \right]}_{(3)} + i \sum_{\nu,\mu} \sum_{\nu'} T^*_{\nu\mu} \underbrace{\left[c^\dagger_{2,\mu} c_{1,\nu} , c^\dagger_{1,\nu'} c_{1,\nu'} \right]}_{(4)} . \end{aligned} \tag{1.3}$$

where we used the definition of the total particle number operator $N_1 = \sum_{\nu'} c^\dagger_{1,\nu'} c_{1,\nu'}$ for lead 1. In Eq.(1.3), the commutators (1) and (2) are nullified using

$$\left[c^\dagger_{1,\alpha} c_{1,\alpha} \, , \, c^\dagger_{1,\alpha'} c_{1,\alpha'} \right] = [n_\alpha, n_{\alpha'}] = 0,$$

and for the commutators (3) and (4) we use the following identity between commutators and anti-commutators

$$\begin{cases} [AB, CD] = [AB, C]D \, + \, C[AB, D] \\ \\ [AB, C] = A\{B, \, C\} - \{A, \, C\}B \end{cases} .$$

In this way, the two commutators in Eq.(1.3) give

$$
\begin{aligned}
(3): \quad \left[c^\dagger_{1,\nu}c_{2,\mu}, c^\dagger_{1,\nu'}c_{1,\nu'}\right] &= c^\dagger_{1,\nu'}\left[c^\dagger_{1,\nu}c_{2,\mu}, c_{1,\nu'}\right] + \left[c^\dagger_{1,\nu}c_{2,\mu}, c^\dagger_{1,\nu'}\right]c_{1,\nu'} \\
&= c^\dagger_{1,\nu'}c^\dagger_{1,\nu}\{c_{2,\mu}, c_{1,\nu'}\} - c^\dagger_{1,\nu'}\{c^\dagger_{1,\nu}, c_{1,\nu'}\}c_{2,\mu} \\
&\quad + c^\dagger_{1,\nu}\{c_{2,\mu}, c^\dagger_{1,\nu'}\}c_{1,\nu'} - \{c^\dagger_{1,\nu}, c^\dagger_{1,\nu'}\}c_{2,\mu}c_{1,\nu'} \\
&= 0 - \delta_{\nu,\nu'}c^\dagger_{1,\nu'}c_{2,\mu} + 0 - 0 \\
&= -\delta_{\nu,\nu'}c^\dagger_{1,\nu'}c_{2,\mu}
\end{aligned}
$$

and

$$
\begin{aligned}
(4): \quad \left[c^\dagger_{2,\mu}c_{1,\nu}, c^\dagger_{1,\nu'}c_{1,\nu'}\right] &= c^\dagger_{1,\nu'}\left[c^\dagger_{2,\mu}c_{1,\nu}, c_{1,\nu'}\right] + \left[c^\dagger_{2,\mu}c_{1,\nu}, c^\dagger_{1,\nu'}\right]c_{1,\nu'} \\
&= c^\dagger_{1,\nu'}c^\dagger_{2,\mu}\{c_{1,\nu}, c_{1,\nu'}\} - c^\dagger_{1,\nu'}\{c^\dagger_{2,\mu}, c_{1,\nu'}\}c_{1,\nu} \\
&\quad + c^\dagger_{2,\mu}\{c_{1,\nu}, c^\dagger_{1,\nu'}\}c_{1,\nu'} - \{c^\dagger_{2,\mu}, c^\dagger_{1,\nu'}\}c_{1,\nu}c_{1,\nu'} \\
&= 0 - 0 + \delta_{\nu,\nu'}c^\dagger_{2,\mu}c_{1,\nu'} - 0 \\
&= \delta_{\nu,\nu'}c^\dagger_{2,\mu}c_{1,\nu'}\,,
\end{aligned}
$$

which then by substituting (3) and (4) into Eq.(1.3), it simplifies to

$$
\begin{aligned}
I &= i\sum_{\nu,\mu}\sum_{\nu'}T_{\nu\mu}\left(-\delta_{\nu,\nu'}c^\dagger_{1,\nu'}c_{2,\mu}\right) + i\sum_{\nu,\mu}\sum_{\nu'}T^*_{\nu\mu}\left(\delta_{\nu,\nu'}c^\dagger_{2,\mu}c_{1,\nu'}\right) \\
&= -i\sum_{\nu,\mu}\left(T_{\nu\mu}c^\dagger_{1,\nu}c_{2,\mu} - T^*_{\nu\mu}c^\dagger_{2,\mu}c_{1,\nu}\right) \\
&\equiv -i\left(L - L^\dagger\right).
\end{aligned}
$$

Therefore, the current in the tunneling junction reads

$$
I \equiv -i\left(L - L^\dagger\right), \tag{1.4}
$$

where we have defined

$$
L = \sum_{\nu,\mu}T_{\nu\mu}c^\dagger_{1,\nu}c_{2,\mu} \iff L^\dagger = \sum_{\nu,\mu}T^*_{\nu\mu}c^\dagger_{2,\mu}c_{1,\nu}\,, \tag{1.5}
$$

to be the current operator tunneling from lead 1 to 2 and the operator for the opposite direction. Taking into account that each electrode is a different thermodynamic system, we can assign a separate chemical potential to each of them. In this way, the tunneling current between the two systems can be induced only by an imbalance in the chemical potentials $(\mu_1 \neq \mu_2)$.

Considering that the tunneling matrix element $T_{\nu\mu}$ is an exponentially decaying function of the gap between the two leads [24, 25], and the tunneling current operator is linear in $T_{\nu\mu}$, we can calculate the tunneling current $\langle I\rangle$ to the lowest order in tunneling matrix using linear response theory [21, 23]. According to the general Kubo formula, the particle current to first order in tunneling Hamiltonian $\mathcal{H}_T$ is given by

$$
\langle I\rangle(t) = \int_{-\infty}^{+\infty} dt' C^{\mathrm{R}}_{I_p\mathcal{H}_T}(t,t'), \tag{1.6}
$$

with $C^{\mathrm{R}}_{I_pH_T}(t-t')$ being the retarded correlation function defined as

$$C^{\mathrm{R}}_{I_pH_T}(t-t') = -i\theta(t-t')\left\langle[I_p(t), \mathcal{H}_{\mathrm{T}}(t')]\right\rangle_0 . \tag{1.7}$$

Here, the 0 subscript in the equilibrium thermal average $\langle\cdots\rangle_0$ denotes that the time evolution is governed by the bare Hamiltonian, $\mathcal{H}_0 = \mathcal{H}_1 + \mathcal{H}_2$. By substituting Eq.(1.2) and Eq.(1.4) into Eq.(1.7), we obtain

$$\begin{aligned} C^{\mathrm{R}}_{I_p\mathcal{H}_T}(t-t') &= -\theta(t-t')\left\langle\left[L(t) - L^\dagger(t)\,,\, L(t') + L^\dagger(t')\right]\right\rangle_0 \\ &= -\theta(t-t')\left[\left\langle[L(t)\,,\, L(t')]\right\rangle_0 - \left\langle\left[L^\dagger(t)\,,\, L(t')\right]\right\rangle_0 + c.c.\right] . \end{aligned} \tag{1.8}$$

The commutators $\langle[L(t)\,,\, L(t')]\rangle_0$ and $\langle[L^\dagger(t)\,,\, L^\dagger(t')]\rangle_0$ contain quartic operators of the form

$$\left\langle\left(c^\dagger_{1,\nu}c_{2,\mu}\right)(t)\,,\, \left(c^\dagger_{1,\nu}c_{2,\mu}\right)(t')\right\rangle_0 , \left\langle\left(c^\dagger_{2,\mu}c_{1,\nu}\right)(t)\,,\, \left(c^\dagger_{2,\mu}c_{1,\nu}\right)(t')\right\rangle_0$$

where two electrons are created in one system and two electrons annihilated in the other at different times; meaning that particle number is not conserved in each system[2]. Since the particle number is a strictly conserved quantity, the matrix elements $(T_{\nu\mu})$ related to these terms must vanish. Therefore, Eq.(1.8) simplifies to

$$C^{\mathrm{R}}_{I_p\mathcal{H}_{\mathrm{T}}}(t-t') = -\theta(t-t')\left[\left\langle\left[L(t)\,,\, L^\dagger(t')\right]\right\rangle_0 - \left\langle\left[L^\dagger(t)\,,\, L(t')\right]\right\rangle_0\right],$$

whereby using the following identity: $\langle[L(t)\,,\, L^\dagger(t')]\rangle_0 = -\langle[L^\dagger(t)\,,\, L(t')]\rangle^*_0$, which has a straightforward proof considering the complex conjugation of inner product, we arrive at

$$C^{\mathrm{R}}_{I_p\mathcal{H}_{\mathrm{T}}}(t-t') = -\theta(t-t')\left[-\left\langle\left[L^\dagger(t)\,,\, L(t')\right]\right\rangle^*_0 - \left\langle\left[L^\dagger(t)\,,\, L(t')\right]\right\rangle_0\right].$$

Now by using the complex numbers identity $z + z^* = 2\mathcal{R}e(z)$, and expand the current operators in terms of creation/annihilation operators, Eq.(1.5), we obtain

$$\begin{aligned} C^{\mathrm{R}}_{I_p\mathcal{H}_{\mathrm{T}}}(t-t') &= 2\,\mathcal{R}e\,\theta(t-t')\left\langle\left[L^\dagger(t)\,,\, L(t')\right]\right\rangle_0 \\ &= 2\,\mathcal{R}e\,\theta(t-t')\sum_{\nu\mu}\sum_{\nu'\mu'}T^*_{\nu\mu}T_{\nu'\mu'}\left\langle\left[c^\dagger_{2,\mu}(t)c_{1,\nu}(t)\,,\, c^\dagger_{1,\nu'}(t)c_{2,\mu'}(t)\right]\right\rangle_0 . \end{aligned} \tag{1.9}$$

By substituting Eq.(1.9) into Eq.(1.6), the particle current becomes

$$\langle I\rangle(t) = 2\,\mathcal{R}e\int_{-\infty}^{+\infty} dt'\theta(t-t')\sum_{\nu\mu}\sum_{\nu'\mu'}T^*_{\nu\mu}T_{\nu'\mu'}\underbrace{\left\langle\left[c^\dagger_{2,\mu}(t)c_{1,\nu}(t)\,,\, c^\dagger_{1,\nu'}(t)c_{2,\mu'}(t)\right]\right\rangle_0}_{(*)} . \tag{1.10}$$

To further simplify the current, we have to calculate the thermal average of time-dependent quartic operators in $(*)$, for which we use the Wick's theorem. But in advance, we need to decompose the quartic operators into quadratic ones.
In general, operators of two decoupled systems, described by $\mathcal{H}_A$ and $\mathcal{H}_B$ satisfy

$$[\mathcal{H}_A, B] = [\mathcal{H}_B, A] = 0, \tag{1.11}$$

[2] The total particle number is still conserved.

and therefore, the thermal average of the product of A and B is decomposable, since

$$\begin{aligned}\langle AB\rangle_0(t,t') &= \frac{1}{Z_0^{AB}}\sum_{n_A,n_B}\langle n_A,n_B|\,e^{-\beta\mathcal{H}}A(t)B(t')\,|n_A,n_B\rangle_0\\ &= \frac{1}{Z_0^{A}Z_0^{B}}\sum_{n_A,n_B}\langle n_A|\,\langle n_B|\,e^{-\beta(\mathcal{H}_A+\mathcal{H}_B)}A(t)B(t')\,|n_A\rangle_0\,|n_B\rangle_0\\ &= \frac{1}{Z_0^{A}}\sum_{n_A}\langle n_A|\,e^{-\beta\mathcal{H}_A}A(t)\,|n_A\rangle_0\;\;\frac{1}{Z_0^{B}}\sum_{n_B}\langle n_B|\,e^{-\beta\mathcal{H}_B}B(t')\,|n_B\rangle_0\\ &= \langle A(t)\rangle_0\,\langle B(t')\rangle_0\,, \end{aligned}\tag{1.12}$$

where we expanded A and B using grand canonical density matrix in occupation representation $|n_A,n_B\rangle_0$, and also used Eq.(1.11) to commute the operators.
The four-point correlation function $(*)$ can be expanded as

$$\begin{aligned}\left\langle\left[c^\dagger_{2,\mu}(t)c_{1,\nu}(t)\,,\,c^\dagger_{1,\nu'}(t')c_{2,\mu'}(t')\right]\right\rangle_0 &= \left\langle c^\dagger_{2,\mu}(t)c_{1,\nu}(t)c^\dagger_{1,\nu'}(t')c_{2,\mu'}(t') - c^\dagger_{1,\nu'}(t')c_{2,\mu'}(t')c^\dagger_{2,\mu}(t)c_{1,\nu}(t)\right\rangle_0\\ &= \left\langle c^\dagger_{2,\mu}(t)c_{1,\nu}(t)c^\dagger_{1,\nu'}(t')c_{2,\mu'}(t')\right\rangle_0\\ &\quad-\left\langle c^\dagger_{1,\nu'}(t')c_{2,\mu'}(t')c^\dagger_{2,\mu}(t)c_{1,\nu}(t)\right\rangle_0,\end{aligned}$$

in which by two commutators and using Eq.(1.12), we can pair operators of the same kind and decompose them as

$$\begin{aligned}\left\langle\left[c^\dagger_{2,\mu}(t)c_{1,\nu}(t)\,,\,c^\dagger_{1,\nu'}(t')c_{2,\mu'}(t')\right]\right\rangle_0 &= (-1)^2\left\langle c_{1,\nu}(t)c^\dagger_{1,\nu'}(t')c^\dagger_{2,\mu}(t)c_{2,\mu'}(t')\right\rangle_0\\ &\quad-(-1)^2\left\langle c^\dagger_{1,\nu'}(t')c_{1,\nu}(t)c_{2,\mu'}(t')c^\dagger_{2,\mu}(t)\right\rangle_0\\ &= \left\langle c_{1,\nu}(t)c^\dagger_{1,\nu'}(t')\right\rangle_0\left\langle c^\dagger_{2,\mu}(t)c_{2,\mu'}(t')\right\rangle_0\\ &\quad-\left\langle c^\dagger_{1,\nu'}(t')c_{1,\nu}(t)\right\rangle_0\left\langle c_{2,\mu'}(t')c^\dagger_{2,\mu}(t)\right\rangle_0.\end{aligned}\tag{1.13}$$

By plugging Eq.(1.13) in Eq.(1.10) we obtain the the current as

$$\begin{aligned}I_p(t) = \langle I\rangle(t) = 2\mathcal{R}e\int_{-\infty}^{+\infty}dt'\theta(t-t')\sum_{\nu,\mu}\sum_{\nu',\mu'}T^*_{\nu\mu}T_{\nu'\mu'}\Big(&\left\langle c_{1,\nu}(t)c^\dagger_{1,\nu'}(t')\right\rangle_0\left\langle c^\dagger_{2,\mu}(t)c_{2,\mu'}(t')\right\rangle_0\\ &-\left\langle c^\dagger_{1,\nu'}(t')c_{1,\nu}(t)\right\rangle_0\left\langle c_{2,\mu'}(t')c^\dagger_{2,\mu}(t)\right\rangle_0\Big).\end{aligned}\tag{1.14}$$

Let's now explicitly extract the time dependence of the fermionic operators $\left(c_{1,\nu}(t),\,c_{2,\mu}(t)\right)$ due voltages V_1 and V_2, Eq.(1.1), and define a new set of operators $\left(\tilde{c}_{1,\nu},\,\tilde{c}_{2,\mu}\right)$ with respect to a common chemical potential

$$\begin{cases}c_{1,\nu}(t) = \tilde{c}_{1,\nu}(t)e^{-i(-e)V_1t} = \tilde{c}_{1,\nu}(t)\,e^{ieV_1t}\\[2ex] c_{2,\mu}(t) = \tilde{c}_{2,\mu}(t)e^{-i(-e)V_2t} = \tilde{c}_{2,\mu}(t)\,e^{ieV_2t}\end{cases},\tag{1.15}$$

and substitute them into Eq.(1.14)

$$\begin{aligned}I_p(t) = 2\mathcal{R}e\int_{-\infty}^{+\infty}dt'\theta(t-t')\sum_{\nu\mu}\sum_{\nu'\mu'}T^*_{\nu\mu}T_{\nu'\mu'}\Big(&\left\langle\tilde{c}_{1,\nu}(t)e^{ieV_1t}\,\tilde{c}^\dagger_{1,\nu'}(t')e^{-ieV_1t'}\right\rangle_0\left\langle\tilde{c}^\dagger_{2,\mu}(t)e^{-ieV_2t}\,\tilde{c}_{2,\mu'}(t')e^{ieV_2t'}\right\rangle_0\\ &-\left\langle\tilde{c}^\dagger_{1,\nu'}(t')e^{-ieV_1t'}\,\tilde{c}_{1,\nu}(t)\,e^{ieV_1t}\right\rangle_0\left\langle\tilde{c}_{2,\mu'}(t')e^{ieV_2t'}\,\tilde{c}^\dagger_{2,\mu}(t)\,e^{-ieV_2t}\right\rangle_0\Big).\end{aligned}$$

This equation can be simplified to

$$
\begin{aligned}
I_p(t) = 2\mathcal{R}e \int_{-\infty}^{+\infty} dt' \theta(t-t') \sum_{\nu\mu} \sum_{\nu'\mu'} T^*_{\nu\mu} T_{\nu'\mu'} \Big(\Big\langle \tilde{c}_{1,\nu}(t) \tilde{c}^\dagger_{1,\nu'}(t') \Big\rangle_0 e^{ieV_1(t-t')} \Big\langle \tilde{c}^\dagger_{2,\mu}(t) \tilde{c}_{2,\mu'}(t') \Big\rangle_0 e^{-ieV_2(t-t')} \\
- \Big\langle \tilde{c}^\dagger_{1,\nu'}(t') \, \tilde{c}_{1,\nu}(t) \Big\rangle_0 e^{ieV_1(t-t')} \Big\langle \tilde{c}_{2,\mu'}(t') \, \tilde{c}^\dagger_{2,\mu}(t) \Big\rangle_0 e^{-ieV_2(t-t')} \Big) \\
= 2\mathcal{R}e \int_{-\infty}^{+\infty} dt' \theta(t-t') \sum_{\nu\mu} \sum_{\nu'\mu'} T^*_{\nu\mu} T_{\nu'\mu'} \Big(\Big\langle \tilde{c}_{1,\nu}(t) \, \tilde{c}^\dagger_{1,\nu'}(t') \Big\rangle_0 \Big\langle \tilde{c}^\dagger_{2,\mu}(t) \, \tilde{c}_{2,\mu'}(t') \Big\rangle_0 \\
- \Big\langle \tilde{c}^\dagger_{1,\nu'}(t') \, \tilde{c}_{1,\nu}(t) \Big\rangle_0 \Big\langle \tilde{c}_{2,\mu'}(t') \, \tilde{c}^\dagger_{2,\mu}(t) \Big\rangle_0 \Big) e^{ie(V_1-V_2)(t-t')} .
\end{aligned}
$$

By defining the common chemical potential in terms of voltage difference in the junction, i.e., bias voltage $\mu = V_b = V_1 - V_2$,

$$
\begin{aligned}
I_p(t) = 2\mathcal{R}e \int_{-\infty}^{+\infty} dt' \theta(t-t') \sum_{\nu\mu} \sum_{\nu'\mu'} T^*_{\nu\mu} T_{\nu'\mu'} \Big(\Big\langle \tilde{c}_{1,\nu}(t) \, \tilde{c}^\dagger_{1,\nu'}(t') \Big\rangle_0 \Big\langle \tilde{c}^\dagger_{2,\mu}(t) \, \tilde{c}_{2,\mu'}(t') \Big\rangle_0 \\
- \Big\langle \tilde{c}^\dagger_{1,\nu'}(t') \, \tilde{c}_{1,\nu}(t) \Big\rangle_0 \Big\langle \tilde{c}_{2,\mu'}(t') \, \tilde{c}^\dagger_{2,\mu}(t) \Big\rangle_0 \Big) e^{ieV_b(t-t')},
\end{aligned}
$$

and shifting time variable $t' \to t' + t$, we arrive at

$$
\begin{aligned}
I_p(t) = 2\,\mathcal{R}e \int_{-\infty}^{+\infty} dt' \theta(-t') \sum_{\nu\mu} \sum_{\nu'\mu'} T^*_{\nu\mu} T_{\nu'\mu'} \Big(\Big\langle \tilde{c}_{1,\nu}(t) \, \tilde{c}^\dagger_{1,\nu'}(t'+t) \Big\rangle_0 \Big\langle \tilde{c}^\dagger_{2,\mu}(t) \, \tilde{c}_{2,\mu'}(t'+t) \Big\rangle_0 \\
- \Big\langle \tilde{c}^\dagger_{1,\nu'}(t'+t) \, \tilde{c}_{1,\nu}(t) \Big\rangle_0 \Big\langle \tilde{c}_{2,\mu'}(t'+t) \, \tilde{c}^\dagger_{2,\mu}(t) \Big\rangle_0 \Big) e^{ieV_b(-t')} .
\end{aligned}
$$

The Heaviside function modifies the integration limits, $\int_{-\infty}^{+\infty} dt' \theta(-t') \langle \cdots \rangle = \int_{-\infty}^{0} dt' \langle \cdots \rangle$, to

$$
\begin{aligned}
I_p(t) = 2\,\mathcal{R}e \int_{-\infty}^{0} dt' \sum_{\nu\mu} \sum_{\nu'\mu'} T^*_{\nu\mu} T_{\nu'\mu'} \Big(\Big\langle \tilde{c}_{1,\nu}(t) \, \tilde{c}^\dagger_{1,\nu'}(t'+t) \Big\rangle_0 \Big\langle \tilde{c}^\dagger_{2,\mu}(t) \, \tilde{c}_{2,\mu'}(t'+t) \Big\rangle_0 \\
- \Big\langle \tilde{c}^\dagger_{1,\nu'}(t'+t) \, \tilde{c}_{1,\nu}(t) \Big\rangle_0 \Big\langle \tilde{c}_{2,\mu'}(t'+t) \, \tilde{c}^\dagger_{2,\mu}(t) \Big\rangle_0 \Big) e^{-ieV_b t'} .
\end{aligned}
$$

Without loss of generality, one can set $t = 0$ (time translation symmetry)

$$
\begin{aligned}
I_p(t=0) = I_p = 2\,\mathcal{R}e \int_{-\infty}^{0} dt' \sum_{\nu\mu} \sum_{\nu'\mu'} T^*_{\nu\mu} T_{\nu'\mu'} \Big(\Big\langle \tilde{c}_{1,\nu}(0) \, \tilde{c}^\dagger_{1,\nu'}(t') \Big\rangle_0 \Big\langle \tilde{c}^\dagger_{2,\mu}(0) \, \tilde{c}_{2,\mu'}(t') \Big\rangle_0 \\
- \Big\langle \tilde{c}^\dagger_{1,\nu'}(t') \, \tilde{c}_{1,\nu}(0) \Big\rangle_0 \Big\langle \tilde{c}_{2,\mu'}(t') \, \tilde{c}^\dagger_{2,\mu}(0) \Big\rangle_0 \Big) e^{-ieV_b t'} .
\end{aligned} \tag{1.16}
$$

We can more elegantly express the two-point correlation functions in Eq.(1.16) in terms of greater and lesser Green's functions, in which we have to be cautious about the time order of the operators

$$
\begin{cases} \mathcal{G}^>_1(\nu,\nu';t') &= -i\langle \tilde{c}_{1,\nu}(0) \tilde{c}^\dagger_{1,\nu'}(t') \rangle \\ \mathcal{G}^<_1(\nu,\nu';t') &= i\langle \tilde{c}^\dagger_{1,\nu'}(t') \tilde{c}_{1,\nu}(0) \rangle \end{cases} \xrightarrow{0 \leftrightarrow t'} \begin{cases} \mathcal{G}^>_1(\nu,\nu';-t') &= -i\langle \tilde{c}_{1,\nu}(t') \tilde{c}^\dagger_{1,\nu'}(0) \rangle \\ \mathcal{G}^<_1(\nu,\nu';-t') &= i\langle \tilde{c}^\dagger_{1,\nu'}(0) \tilde{c}_{1,\nu}(t') \rangle \end{cases} . \tag{1.17}
$$

By plugging Eq.(1.17) into Eq.(1.16), we obtain

$$
I_p = 2\mathcal{R}e \int_{-\infty}^{0} dt' \sum_{\nu,\mu} \sum_{\nu'\mu'} T^*_{\nu\mu} T_{\nu'\mu'} e^{-ieV_b t'} \left[\mathcal{G}^>_1(\nu,\nu';t') \mathcal{G}^<_2(\mu,\mu';-t') - \mathcal{G}^<_1(\nu,\nu';t') \mathcal{G}^>_2(\mu,\mu';-t') \right] . \tag{1.18}
$$

The expression under bracket in Eq.(1.18) contains the Green's functions of the decoupled systems, which are diagonal since H_1 and H_2 are non-interacting Hamiltonians,

$$\mathcal{G}_1^{</>}(\nu,\nu';t') = \delta_{\nu\nu'}\mathcal{G}_1^{</>}(\nu;t')\,,\ \mathcal{G}_2^{</>}(\mu,\mu';t') = \delta_{\mu\mu'}\mathcal{G}_{2\mu}^{</>}(\mu;t'). \tag{1.19}$$

Using Eq.(1.19), the particle current then becomes

$$I_p = 2\,\mathcal{R}e\int_{-\infty}^{0} dt' \sum_{\nu,\mu} |T_{\nu\mu}|^2 e^{i(-e)V_b t'}\left[\mathcal{G}_1^{>}(\nu;t')\mathcal{G}_2^{<}(\mu;-t') - \mathcal{G}_1^{<}(\nu;t')\mathcal{G}_2^{>}(\mu;-t')\right]. \tag{1.20}$$

Now by change of variable $t' \to -t'$:

$$I_p = 2\,\mathcal{R}e\int_{0}^{+\infty} dt' \sum_{\nu,\mu} |T_{\nu\mu}|^2 e^{ieV_b t'}\left[\mathcal{G}_1^{>}(\nu;-t')\mathcal{G}_2^{<}(\mu;t') - \mathcal{G}_1^{<}(\nu;-t')\mathcal{G}_2^{>}(\mu;t')\right]$$

and Fourier transforming the Green's functions to frequency-space, Eq.(1.25) simplifies to

$$\begin{aligned} I_p = 2\,\mathcal{R}e\int_{0}^{+\infty} dt' \sum_{\nu,\mu} |T_{\nu\mu}|^2 e^{ieV_b t'}\Bigg[&\int_{-\infty}^{+\infty}\frac{d\omega}{2\pi}\mathcal{G}_1^{>}(\nu;\omega)e^{-i\omega t'}\int_{-\infty}^{+\infty}\frac{d\omega'}{2\pi}\mathcal{G}_2^{<}(\mu;\omega')e^{i\omega' t'} \\ &- \int_{-\infty}^{+\infty}\frac{d\omega}{2\pi}\mathcal{G}_1^{<}(\nu;\omega)e^{-i\omega t'}\int_{-\infty}^{+\infty}\frac{d\omega'}{2\pi}\mathcal{G}_2^{>}(\mu;\omega')e^{i\omega' t'}\Bigg]. \end{aligned}$$

By recasting all exponentials into and extending the time integration limits, we obtain a Dirac delta function,

$$\int_{0}^{+\infty} dt' e^{ieV_b t'} e^{-i\omega t'} e^{i\omega' t'} = \frac{1}{2}\int_{-\infty}^{+\infty} e^{i(\omega'-\omega+eV_b)t'} = \pi\delta(\omega'-\omega+eV_b),$$

with which we can directly take one the frequency integrals, $\int_{-\infty}^{+\infty} d\omega'\,\delta(\omega'-\omega+eV_b)[\cdots]$, to obtain

$$I_p = \mathcal{R}e\int_{-\infty}^{+\infty}\frac{d\omega}{2\pi}\sum_{\nu,\mu}|T_{\nu\mu}|^2\left[\mathcal{G}_1^{>}(\nu;\omega)\mathcal{G}_2^{<}(\mu;\omega-eV_b) - \mathcal{G}_1^{<}(\nu;\omega)\mathcal{G}_2^{>}(\mu;\omega-eV_b)\right].$$

We use the fluctuation dissipation theorem

$$\begin{cases} i\,\mathcal{G}_1^{<}(\nu;\omega) = \mathcal{A}_1(\nu;\omega)\big[1-n_{\mathrm{F}}(\omega)\big] \\ \\ -i\,\mathcal{G}_1^{>}(\nu;\omega) = \mathcal{A}_1(\nu;\omega)\,n_{\mathrm{F}}(\omega) \end{cases}, \tag{1.21}$$

to rewrite the lesser and greater Green's functions in terms of spectral functions,

$$\begin{aligned} I_p = &\int_{-\infty}^{+\infty}\frac{d\omega}{2\pi}\sum_{\nu,\mu}|T_{\nu\mu}|^2(-i)^2\Big[\mathcal{A}_1(\nu;\omega)n_{\mathrm{F}}(\omega)\mathcal{A}_2(\mu;\omega-eV_b)\big[1-n_{\mathrm{F}}(\omega-eV_b)\big] \\ &\qquad - \mathcal{A}_1(\nu;\omega)\big[1-n_{\mathrm{F}}(\omega)\big]\mathcal{A}_2(\mu;\omega-eV_b)n_{\mathrm{F}}(\omega-eV_b)\Big] \\ = &\int_{-\infty}^{+\infty}\frac{d\omega}{2\pi}\sum_{\nu,\mu}|T_{\nu\mu}|^2\mathcal{A}_1(\nu;\omega)\mathcal{A}_2(\mu;\omega-eV_b)\Big[n_{\mathrm{F}}(\omega)\big[1-n_{\mathrm{F}}(\omega-eV_b)\big] - \big[1-n_{\mathrm{F}}(\omega)\big]n_{\mathrm{F}}(\omega-eV)\Big] \\ = &\int_{-\infty}^{+\infty}\frac{d\omega}{2\pi}\sum_{\nu,\mu}|T_{\nu\mu}|^2\mathcal{A}_1(\nu;\omega)\mathcal{A}_2(\mu;\omega-eV_b)\big[n_{\mathrm{F}}(\omega)-n_{\mathrm{F}}(\omega-eV_b)\big]. \end{aligned}$$

Here, we dropped the $\mathcal{R}e(\cdots)$ operator because the integrand is a real number. Thus, we finally derived the particle current as

$$\boxed{I_p = \int_{-\infty}^{+\infty} \frac{d\omega}{2\pi} \sum_{\nu,\mu} |T_{\nu\mu}|^2 \mathcal{A}_1(\nu;\omega)\mathcal{A}_2(\mu;\omega - eV_b)\big[n_{\mathrm{F}}(\omega) - n_{\mathrm{F}}(\omega - eV_b)\big]}\,. \tag{1.22}$$

Let's now discuss different terms in Eq.(1.22). As we can see, the current depends on the product of the spectral functions and the difference of Fermi-Dirac distributions. Since the fermionic spectral functions are positive-definite, their product, $\mathcal{A}_1(\nu;\omega)\mathcal{A}_2(\mu;\omega - eV_b)$, is finite only if both are non-zero, which means there are available density of states at the Fermi level. Furthermore, the difference in the Fermi-Dirac distributions $\big[n_{\mathrm{F}}(\omega) - n_{\mathrm{F}}(\omega - eV_b)\big]$, is nonvanishing only if bias (V_b) is finite, i.e., the tunneling is merely between an occupied and unoccupied state. Thus, in summary, in the tunneling spectroscopy, one measures the tunneling current by variation of the bias voltage, which controls the Fermi level and direction of the current across the junction.

1.2.2 Tersoff-Hamann approximation

The fact that one has limited knowledge about the STM tip spectral function $A_2(\mu;\omega - eV_b)$ and the corresponding matrix elements $T_{\nu\mu}$ makes calculation of the current from Eq.(1.22) often impossible without further simplification. A simplification scheme was suggested by Tersoff and Hamann and is probably the approach most widely used in the interpretation of STM images [26]. It is based on the assumption that the STM tip is a simple conductor where one can assume that the product of the tunneling matrix $T_{\nu\mu}$ with its spectral function is roughly constant ($s-$wave tip),

$$\sum_{\mu} |T_{\nu\mu}|^2 \mathcal{A}_2(\mu;\omega - eV) \approx \text{constant}. \tag{1.23}$$

Now by Taylor expanding the Fermi-Dirac distributions for small eV up to the second-order

$$n_{\mathrm{F}}(\omega - eV) \approx n_{\mathrm{F}}(\omega) + (-eV)\frac{\partial n(\omega - eV)}{\partial \omega} + \mathcal{O}(\delta\omega^2) \tag{1.24}$$

and substituting Eq.(1.23) and Eq.(1.24) into Eq.(1.22)

$$I_p \propto \int_{-\infty}^{+\infty} \frac{d\omega}{2\pi} \sum_{\nu} \mathcal{A}_1(\nu;\omega)\left[n_{\mathrm{F}}(\omega) - n_{\mathrm{F}}(\omega) - (-eV)\frac{\partial n(\omega - eV)}{\partial \omega}\right],$$

we obtain the current as

$$I_p \propto eV \int_{-\infty}^{+\infty} \frac{d\omega}{2\pi} \sum_{\nu} \mathcal{A}_1(\nu;\omega)\frac{\partial n(\omega - eV)}{\partial \omega}\,. \tag{1.25}$$

At low temperatures the Fermi-Dirac distribution can be approximated by Heaviside function

$$n_{\mathrm{F}}(\omega - eV) \approx \theta(\omega - eV)$$

and its first derivative by Delta function

$$\frac{\partial n_{\mathrm{F}}(\omega - eV)}{\partial \omega} = \frac{\partial \theta(\omega - eV)}{\partial \omega} = \delta(\omega - eV).$$

It simplifies Eq.(1.25) to

$$I_p \propto eV \int_{-\infty}^{+\infty} \frac{d\omega}{2\pi} \sum_{\nu} \mathcal{A}_1(\nu;\omega)\delta(\omega - eV)\,. \tag{1.26}$$

If we take a derivative from current with respect to V,

$$\frac{dI}{dV} \propto \int_{-\infty}^{+\infty} \frac{d\omega}{2\pi} \sum_{\nu} \mathcal{A}_1(\nu;\omega)\delta(\omega - eV)$$

and take the frequency integration, we finally obtain the differential conductance as

$$\boxed{\frac{dI}{dV} \propto \sum_{\nu} \mathcal{A}_1(\nu; eV)}\,. \tag{1.27}$$

1.2.3 Tunneling Hamiltonian of an interacting electron region

So far, we have studied only the tunneling between two simple metals in close proximity. We can now extend the formalism to the calculation of conductance of the Anderson-type models for tunneling junctions, which allows us to have a sample system inside the junction. The Hamiltonian is given by

$$\mathcal{H} = \mathcal{H}_{\mathrm{L}} + \mathcal{H}_{\mathrm{R}} + \mathcal{H}_{\mathrm{d}} + \mathcal{H}_{\mathrm{T}}$$

where $\mathcal{H}_{\mathrm{L}}$ and $\mathcal{H}_{\mathrm{R}}$ are the Hamiltonian for the left and right lead, $\mathcal{H}_{\mathrm{d}}$ is a generic Hamiltonian describing the sample in between the leads (tip and substrate), and $\mathcal{H}_{\mathrm{T}}$ is the tunneling Hamiltonian for the two junctions: tip-sample and sample-substrate. The electronic states are created in the decoupled sample by $d^{\dagger}_{\mathbf{k},\sigma}$, in the left lead by $c^{\dagger}_{\nu_{\mathrm{L}},\sigma}$, and in the right lead by $c^{\dagger}_{\nu_{\mathrm{R}},\sigma}$. The tunneling Hamiltonian $\mathcal{H}_{\mathrm{T}}$ coupling these three subsystems (tip, sample, and substrate) is given by

$$\mathcal{H}_{\mathrm{T}} = \mathcal{H}_{\mathrm{TL}} + \mathcal{H}_{\mathrm{TR}}$$

where $\mathcal{H}_{\mathrm{TL}}$ is

$$\mathcal{H}_{\mathrm{TL}} = \sum_{\nu_{\mathrm{L}},\mathbf{k},\sigma} \left(t_{\mathrm{L}}\, c^{\dagger}_{\nu_{\mathrm{L}},\sigma} d_{\mathbf{k},\sigma} + t^{*}_{\mathrm{L}}\, d^{\dagger}_{\mathbf{k},\sigma} c_{\nu_{\mathrm{L}},\sigma} \right) \tag{1.28}$$

and $\mathcal{H}_{\mathrm{TR}}$ is

$$\mathcal{H}_{\mathrm{TR}} = \sum_{\nu_{\mathrm{R}},\mathbf{k},\sigma} \left(t_{\mathrm{R}}\, c^{\dagger}_{\nu_{\mathrm{R}},\sigma} d_{\mathbf{k},\sigma} + t^{*}_{\mathrm{R}}\, d^{\dagger}_{\mathbf{k},\sigma} c_{\nu_{\mathrm{R}},\sigma} \right)\,. \tag{1.29}$$

As we assumed in the last section, we describe electrons in the left and right leads by non-interacting Hamiltonians

$$\begin{cases} \mathcal{H}_{\mathrm{L}} = \sum_{\nu_{\mathrm{L}}} \xi_{\nu_{\mathrm{L}}} c^{\dagger}_{\nu_{\mathrm{L}},\sigma} c_{\nu_{\mathrm{L}},\sigma} \\ \\ \mathcal{H}_{\mathrm{R}} = \sum_{\nu_{\mathrm{R}}} \xi_{\nu_{\mathrm{R}}} c^{\dagger}_{\nu_{\mathrm{R}},\sigma} c_{\nu_{\mathrm{R}},\sigma} \end{cases}\,. \tag{1.30}$$

The Hamiltonian of the tip and substrate in Eq.(1.30) can be elegantly combined by performing a unitary transformation, i.e., rotation of basis, in the space of L- and R-electron operators. The convenience of this change of basis becomes clear as we go further in the derivations. Hence, we define the even (e) and odd (o) operators as a linear combination of the left and right operators

$$\begin{cases} c_{\nu_e,\sigma} = \frac{1}{\sqrt{|t_{\rm L}|^2+|t_{\rm R}|^2}} \left(t_{\rm L}^* c_{\nu_{\rm L},\sigma} + t_R^* c_{\nu_{\rm R},\sigma}\right) \\ \\ c_{\nu_o,\sigma} = \frac{1}{\sqrt{|t_{\rm L}|^2+|t_{\rm R}|^2}} \left(-t_{\rm R} c_{\nu_{\rm L},\sigma} + t_{\rm L} c_{\nu_{\rm R},\sigma}\right) \end{cases}, \tag{1.31}$$

or arranged in spinor representation as

$$\Psi_{\nu_e,\nu_o,\sigma} = \begin{pmatrix} c_{\nu_e,\sigma} \\ c_{\nu_o,\sigma} \end{pmatrix} = \frac{1}{\sqrt{|t_{\rm L}|^2+|t_{\rm R}|^2}} \begin{pmatrix} t_{\rm L}^* & t_{\rm R}^* \\ -t_{\rm R} & t_{\rm L} \end{pmatrix} \begin{pmatrix} c_{\nu_{\rm L},\sigma} \\ c_{\nu_{\rm R},\sigma} \end{pmatrix}. \tag{1.32}$$

The inverse transformation of Eq.(1.32) follows

$$\Psi_{\nu_{\rm L},\nu_{\rm R},\sigma} = \begin{pmatrix} c_{\nu_{\rm L},\sigma} \\ c_{\nu_{\rm R},\sigma} \end{pmatrix} = \sqrt{|t_{\rm L}|^2+|t_{\rm R}|^2} \begin{pmatrix} t_{\rm L}^* & t_{\rm R}^* \\ -t_{\rm R} & t_{\rm L} \end{pmatrix}^{-1} \begin{pmatrix} c_{\nu_e,\sigma} \\ c_{\nu_o,\sigma} \end{pmatrix} = \frac{\sqrt{|t_{\rm L}|^2+|t_{\rm R}|^2}}{|t_{\rm L}|^2+|t_{\rm R}|^2} \begin{pmatrix} t_{\rm L} & -t_{\rm R}^* \\ t_{\rm R} & t_{\rm L}^* \end{pmatrix} \begin{pmatrix} c_{\nu_e,\sigma} \\ c_{\nu_o,\sigma} \end{pmatrix}.$$

This gives the left-right annihilation spinor in terms of even and odd operators as

$$\Psi_{\nu_{\rm L},\nu_{\rm R},\sigma} = \begin{pmatrix} c_{\nu_{\rm L},\sigma} \\ c_{\nu_{\rm R},\sigma} \end{pmatrix} = \frac{1}{\sqrt{|t_L|^2+|t_R|^2}} \begin{pmatrix} t_{\rm L} & -t_{\rm R}^* \\ t_{\rm R} & t_{\rm L}^* \end{pmatrix} \begin{pmatrix} c_{\nu_e,\sigma} \\ c_{\nu_o,\sigma} \end{pmatrix}. \tag{1.33}$$

and by complex transpose we obtain the creation spinor as

$$\Psi^\dagger_{\nu_{\rm L},\nu_{\rm R},\sigma} = \begin{pmatrix} c^\dagger_{\nu_{\rm L},\sigma} & c^\dagger_{\nu_{\rm R},\sigma} \end{pmatrix} = \frac{1}{\sqrt{|t_{\rm L}|^2+|t_{\rm R}|^2}} \begin{pmatrix} c^\dagger_{\nu_e,\sigma} & c^\dagger_{\nu_o,\sigma} \end{pmatrix} \begin{pmatrix} t_{\rm L}^* & t_{\rm R}^* \\ -t_{\rm R} & t_{\rm L} \end{pmatrix}. \tag{1.34}$$

It is straightforward to check $|\Psi_{\nu_e,\nu_o,\sigma}|^2 = |\Psi_{\nu_{\rm L},\nu_{\rm R},\sigma}|^2$

$$\Psi^\dagger_{\nu_e,\nu_o,\sigma}\Psi_{\nu_e,\nu_o,\sigma} = \frac{1}{|t_L|^2+|t_R|^2} \begin{pmatrix} c^\dagger_{\nu_L,\sigma} & c^\dagger_{\nu_R,\sigma} \end{pmatrix} \begin{pmatrix} t_L & -t_R^* \\ t_R & t_L^* \end{pmatrix} \begin{pmatrix} t_L^* & t_R^* \\ -t_R & t_L \end{pmatrix} \begin{pmatrix} c_{\nu_L,\sigma} \\ c_{\nu_R,\sigma} \end{pmatrix},$$

which gives

$$\begin{aligned} \Psi^\dagger_{\nu_e,\nu_o,\sigma}\Psi_{\nu_e,\nu_o,\sigma} &= \frac{1}{|t_L|^2+|t_R|^2} \begin{pmatrix} c^\dagger_{\nu_L,\sigma} & c^\dagger_{\nu_R,\sigma} \end{pmatrix} \begin{pmatrix} |t_L|^2+|t_R|^2 & 0 \\ 0 & |t_L|^2+|t_R|^2 \end{pmatrix} \begin{pmatrix} c_{\nu_L,\sigma} \\ c_{\nu_R,\sigma} \end{pmatrix} \\ &= \begin{pmatrix} c_{\nu_L,\sigma} & c_{\nu_R,\sigma} \end{pmatrix} \begin{pmatrix} 1 & 0 \\ 0 & 1 \end{pmatrix} \begin{pmatrix} c_{\nu_L,\sigma} \\ c_{\nu_R,\sigma} \end{pmatrix} = \begin{pmatrix} c_{\nu_L,\sigma} & c_{\nu_R,\sigma} \end{pmatrix} \begin{pmatrix} c_{\nu_L,\sigma} \\ c_{\nu_R,\sigma} \end{pmatrix} = |\Psi_{\nu_L,\nu_R,\sigma}|^2 \end{aligned}$$

Thus, as expected, under such unitary transformation Eq.(1.31), norm of the states are preserved. Using this transformation, we rewrite the left and right Hamiltonian in terms of even and odd operators. First, we combine Eq.(1.30)

$$\mathcal{H}_{\rm LR} = \sum_{\nu_{\rm L},\nu_{\rm R},\sigma} \begin{pmatrix} c^\dagger_{\nu_{\rm L},\sigma} & c^\dagger_{\nu_{\rm R},\sigma} \end{pmatrix} \begin{pmatrix} \xi_{\nu_{\rm L}} & 0 \\ 0 & \xi_{\nu_{\rm R}} \end{pmatrix} \begin{pmatrix} c_{\nu_{\rm L},\sigma} \\ c_{\nu_{\rm R},\sigma} \end{pmatrix}$$

and then substitute Eq.(1.33) and Eq.(1.34) into Eq.(1.2.3) to obtain

$$\mathcal{H}_{\mathrm{LR}} = \sum_{\nu_e,\nu_o,\sigma} \begin{pmatrix} c^\dagger_{\nu_e,\sigma} & c^\dagger_{\nu_o,\sigma} \end{pmatrix} \frac{1}{\sqrt{|t_{\mathrm{L}}|^2+|t_{\mathrm{R}}|^2}} \begin{pmatrix} t^*_{\mathrm{L}} & t^*_{\mathrm{R}} \\ -t_{\mathrm{R}} & t_{\mathrm{L}} \end{pmatrix} \begin{pmatrix} \xi_{\nu_e} & 0 \\ 0 & \xi_{\nu_o} \end{pmatrix} \times \frac{1}{\sqrt{|t_{\mathrm{L}}|^2+|t_{\mathrm{R}}|^2}} \begin{pmatrix} t_{\mathrm{L}} & -t^*_{\mathrm{R}} \\ t_{\mathrm{R}} & t^*_{\mathrm{L}} \end{pmatrix} \begin{pmatrix} c_{\nu_e,\sigma} \\ c_{\nu_o,\sigma} \end{pmatrix}.$$

By taking the matrix product from the left side

$$\mathcal{H}_{\mathrm{LR}} = \sum_{\nu_e,\nu_o,\sigma} \frac{1}{|t_{\mathrm{L}}|^2+|t_{\mathrm{R}}|^2} \begin{pmatrix} c^\dagger_{\nu_e,\sigma} & c^\dagger_{\nu_o,\sigma} \end{pmatrix} \begin{pmatrix} \xi_{\nu_e} t^*_{\mathrm{L}} & \xi_{\nu_o} t^*_{\mathrm{R}} \\ -\xi_{\nu_e} t_{\mathrm{R}} & \xi_{\nu_o} t_{\mathrm{L}} \end{pmatrix} \begin{pmatrix} t_{\mathrm{L}} & -t^*_{\mathrm{R}} \\ t_{\mathrm{R}} & t^*_{\mathrm{L}} \end{pmatrix} \begin{pmatrix} c_{\nu_e,\sigma} \\ c_{\nu_o,\sigma} \end{pmatrix},$$

and rearranging the terms, we obtain

$$\mathcal{H}_{\mathrm{LR}} = \sum_{\nu_e,\nu_o,\sigma} \frac{1}{|t_{\mathrm{L}}|^2+|t_{\mathrm{R}}|^2} \begin{pmatrix} c^\dagger_{\nu_e,\sigma} & c^\dagger_{\nu_o,\sigma} \end{pmatrix} \begin{pmatrix} \xi_{\nu_e}|t_{\mathrm{L}}|^2+\xi_{\nu_o}|t_{\mathrm{R}}|^2 & -\xi_{\nu_e} t^*_{\mathrm{L}} t^*_{\mathrm{R}} + \xi_{\nu_o} t^*_{\mathrm{L}} t^*_{R} \\ -\xi_{\nu_e} t_{\mathrm{R}} t_{\mathrm{L}} + \xi_{\nu_o} t_{\mathrm{L}} t_{\mathrm{R}} & \xi_{\nu_e}|t_{\mathrm{R}}|^2+\xi_{\nu_o}|t_{\mathrm{L}}|^2 \end{pmatrix} \begin{pmatrix} c_{\nu_e,\sigma} \\ c_{\nu_o,\sigma} \end{pmatrix}. \tag{1.35}$$

Now we make a simplifying assumption and let the two leads to have an identical dispersion relation ($\xi_{\nu_e} = \xi_{\nu_o} = \xi_\nu$), we arrive at

$$\boxed{\mathcal{H}_{\mathrm{LR}} = \sum_{\nu=(\nu_e,\nu_o)} \sum_{\sigma} \begin{pmatrix} c^\dagger_{\nu_e,\sigma} & c^\dagger_{\nu_o,\sigma} \end{pmatrix} \begin{pmatrix} \xi_\nu & 0 \\ 0 & \xi_\nu \end{pmatrix} \begin{pmatrix} c_{\nu_e,\sigma} \\ c_{\nu_o,\sigma} \end{pmatrix}}. \tag{1.36}$$

In this way, we can rewrite the tunneling Hamiltonian between the left lead and the sample, Eq.(1.28), in terms of even and odd operators using Eq.(1.31)

$$\begin{aligned}
\mathcal{H}_{\mathrm{TL}} &= \sum_{\nu_{\mathrm{L}},\mathbf{k},\sigma} \left(t_{\mathrm{L}} c^\dagger_{\nu_{\mathrm{L}},\sigma} d_{\mathbf{k},\sigma} + t^*_{\mathrm{L}} d^\dagger_{\mathbf{k},\sigma} c_{\nu_{\mathrm{L}},\sigma} \right) \\
&= \frac{1}{\sqrt{|t_{\mathrm{L}}|^2+|t_{\mathrm{R}}|^2}} \sum_{\nu_e,\nu_o,\mathbf{k},\sigma} \left(t_{\mathrm{L}} \left(t^*_{\mathrm{L}} c^\dagger_{\nu_e,\sigma} - t_{\mathrm{R}} c^\dagger_{\nu_o,\sigma} \right) d_{\mathbf{k},\sigma} + t^*_{\mathrm{L}} d^\dagger_{\mathbf{k},\sigma} \left(t_{\mathrm{L}} c_{\nu_e,\sigma} - t^*_{\mathrm{R}} c_{\nu_o,\sigma} \right) \right) \\
&= \frac{1}{\sqrt{|t_{\mathrm{L}}|^2+|t_{\mathrm{R}}|^2}} \sum_{\nu_e,\mathbf{k},\sigma} |t_{\mathrm{L}}|^2 \left(c^\dagger_{\nu_e,\sigma} d_{\mathbf{k},\sigma} + d^\dagger_{\mathbf{k},\sigma} c_{\nu_e,\sigma} \right) - \frac{1}{\sqrt{|t_{\mathrm{L}}|^2+|t_R|^2}} \sum_{\nu_o,\mathbf{k},\sigma} \left(t_L t_{\mathrm{R}} c^\dagger_{\nu_o,\sigma} d_{\mathbf{k},\sigma} + t^*_{\mathrm{L}} t^*_{\mathrm{R}} d^\dagger_{\mathbf{k},\sigma} c_{\nu_o,\sigma} \right)
\end{aligned}$$

and similarly, for the tunneling Hamiltonian between the right lead and the sample, Eq.(1.29), we have

$$\begin{aligned}
\mathcal{H}_{\mathrm{TR}} &= \sum_{\nu_{\mathrm{R}},\mathbf{k},\sigma} \left(t_{\mathrm{R}}\, c^\dagger_{\nu_{\mathrm{R}},\sigma} d_{\mathbf{k},\sigma} + t^*_{\mathrm{R}}\, d^\dagger_{\mathbf{k},\sigma} c_{\nu_{\mathrm{R}},\sigma} \right) \\
&= \frac{1}{\sqrt{|t_{\mathrm{L}}|^2+|t_{\mathrm{R}}|^2}} \sum_{\nu_e,\nu_o,\mathbf{k},\sigma} \left(t_{\mathrm{R}} \left(t^*_{\mathrm{R}} c^\dagger_{\nu_e,\sigma} + t_{\mathrm{L}} c^\dagger_{\nu_o,\sigma} \right) d_{\mathbf{k},\sigma} + t^*_{\mathrm{R}} d^\dagger_{\mathbf{k},\sigma} \left(t_{\mathrm{R}} c_{\nu_e,\sigma} + t^*_{\mathrm{L}} c_{\nu_o,\sigma} \right) \right) \\
&= \frac{1}{\sqrt{|t_{\mathrm{L}}|^2+|t_{\mathrm{R}}|^2}} \sum_{\nu_e,\mathbf{k},\sigma} |t_{\mathrm{R}}|^2 \left(c^\dagger_{\nu_e,\sigma} d_{\mathbf{k},\sigma} + d^\dagger_{\mathbf{k},\sigma} c_{\nu_e,\sigma} \right) + \frac{1}{\sqrt{|t_{\mathrm{L}}|^2+|t_{\mathrm{R}}|^2}} \sum_{\nu_o,\mathbf{k},\sigma} \left(t_{\mathrm{L}} t_{\mathrm{R}} c^\dagger_{\nu_o,\sigma} d_{\mathbf{k},\sigma} + t^*_{\mathrm{R}} t^*_{\mathrm{L}} d^\dagger_{\mathbf{k},\sigma} c_{\nu_o,\sigma} \right).
\end{aligned}$$

Now by recollecting the two terms, we obtain the total tunneling Hamiltonian as

$$\begin{aligned}
\mathcal{H}_{\mathrm{T}} &= \mathcal{H}_{\mathrm{TR}} + \mathcal{H}_{\mathrm{TL}} \\
&= \frac{1}{\sqrt{|t_{\mathrm{L}}|^2+|t_{\mathrm{R}}|^2}} \sum_{\nu_e,\mathbf{k},\sigma} |t_{\mathrm{L}}|^2 \left(c^\dagger_{\nu_e,\sigma} d_{\mathbf{k},\sigma} + d^\dagger_{\mathbf{k},\sigma} c_{\nu_e,\sigma} \right) + \frac{1}{\sqrt{|t_{\mathrm{L}}|^2+|t_{\mathrm{R}}|^2}} \sum_{\nu_e,\mathbf{k},\sigma} |t_{\mathrm{R}}|^2 \left(c^\dagger_{\nu_e,\sigma} d_{\mathbf{k},\sigma} + d^\dagger_{\mathbf{k},\sigma} c_{\nu_e,\sigma} \right) \\
&= \frac{1}{\sqrt{|t_{\mathrm{L}}|^2+|t_{\mathrm{R}}|^2}} \sum_{\nu_e,\mathbf{k},\sigma} \left(|t_{\mathrm{L}}|^2+|t_{\mathrm{R}}|^2 \right) \left(c^\dagger_{\nu_e,\sigma} d_{\mathbf{k},\sigma} + d^\dagger_{\mathbf{k},\sigma} c_{\nu_e,\sigma} \right) \\
&= \sum_{\nu_e,\mathbf{k},\sigma} \sqrt{|t_{\mathrm{L}}|^2+|t_{\mathrm{R}}|^2} \left(c^\dagger_{\nu_e,\sigma} d_{\mathbf{k},\sigma} + d^\dagger_{\mathbf{k},\sigma} c_{\nu_e,\sigma} \right).
\end{aligned}$$

Therefore, the tunneling Hamiltonian can be written merely in terms of the *even* sector of the lead's electrons,

$$\boxed{\mathcal{H}_{\mathrm{T}} = \sum_{\nu_e,\mathbf{k},\sigma} \sqrt{|t_{\mathrm{L}}|^2 + |t_{\mathrm{R}}|^2}\left(c^{\dagger}_{\nu_e,\sigma} d_{\mathbf{k},\sigma} + d^{\dagger}_{\mathbf{k},\sigma} c_{\nu_e,\sigma}\right)}. \tag{1.37}$$

This is a huge simplification since we absorbed two of the particle operators $(c^{\dagger}_{\nu_{\mathrm{L}},\sigma}, c^{\dagger}_{\nu_{\mathrm{R}},\sigma})$ into one $(c^{\dagger}_{\nu_e,\sigma})$.

1.2.4 Conductance of an interacting tunnel junction

We have shown before the conductance of tunnel junction can be directly computed by the retarded current-current correlation function $C^{\mathrm{R}}_{II}(\omega)$, which needs the current operator of each lead. For this, we first define the particle-current operator for the left and right leads

$$\begin{cases} I_{\mathrm{L}} = \dot{N}_{\mathrm{L}} \\ \\ I_{\mathrm{R}} = \dot{N}_{\mathrm{R}} \end{cases},$$

where they obey Eq.(1.4) as

$$\begin{cases} I_{\mathrm{L}} = i \sum_{\nu_{\mathrm{L}},\mathbf{k},\sigma} \left(t_{\mathrm{L}}\, c^{\dagger}_{\nu_{\mathrm{L}},\sigma} d_{\mathbf{k},\sigma} - t^{*}_{\mathrm{L}}\, d^{\dagger}_{\mathbf{k},\sigma} c_{\nu_{\mathrm{L}},\sigma}\right) \\ \\ I_{\mathrm{R}} = i \sum_{\nu_{\mathrm{R}},\mathbf{k},\sigma} \left(t_{\mathrm{R}}\, c^{\dagger}_{\nu_{\mathrm{R}},\sigma} d_{\mathbf{k},\sigma} - t^{*}_{\mathrm{R}}\, d^{\dagger}_{\mathbf{k},\sigma} c_{\nu_{\mathrm{R}},\sigma}\right) \end{cases}. \tag{1.38}$$

Now by substituting left and right creation/annihilation operators with even and odd electron operators

$$\begin{cases} c^{\dagger}_{\nu_{\mathrm{L}}} = \frac{1}{\sqrt{|t_{\mathrm{L}}|^2+|t_{\mathrm{R}}|^2}} \left(t^{*}_{\mathrm{L}} c^{\dagger}_{\nu_e,\sigma} - t_{\mathrm{R}}\, c^{\dagger}_{\nu_o,\sigma}\right) \\ \\ c^{\dagger}_{\nu_{\mathrm{R}}} = \frac{1}{\sqrt{|t_{\mathrm{L}}|^2+|t_{\mathrm{R}}|^2}} \left(t^{*}_{\mathrm{R}}\, c^{\dagger}_{\nu_e,\sigma} + t_{\mathrm{L}}\, c^{\dagger}_{\nu_o,\sigma}\right) \end{cases}, \quad \begin{cases} c_{\nu_{\mathrm{L}}} = \frac{1}{\sqrt{|t_{\mathrm{L}}|^2+|t_{\mathrm{R}}|^2}} \left(t_{\mathrm{L}} c_{\nu_e,\sigma} - t^{*}_{\mathrm{R}}\, c_{\nu_o,\sigma}\right) \\ \\ c_{\nu_{\mathrm{R}}} = \frac{1}{\sqrt{|t_{\mathrm{L}}|^2+|t_{\mathrm{R}}|^2}} \left(t_R\, c_{\nu_e,\sigma} + t^{*}_{\mathrm{L}}\, c_{\nu_o,\sigma}\right) \end{cases}$$

into the particle-current operator Eq.(1.38), we obtain I_{L} as

$$\begin{aligned} I_{\mathrm{L}} &= i \sum_{\nu_e,\nu_o,\mathbf{k},\sigma} \left(\frac{t_{\mathrm{L}}}{\sqrt{|t_{\mathrm{L}}|^2 + |t_R|^2}} \left(t^{*}_{\mathrm{L}} c^{\dagger}_{\nu_e,\sigma} - t_R\, c^{\dagger}_{\nu_o,\sigma}\right) d_{\mathbf{k},\sigma} - d^{\dagger}_{\mathbf{k},\sigma} \frac{t^{*}_{L}}{\sqrt{|t_L|^2 + |t_R|^2}} \left(t_L c_{\nu_e,\sigma} - t^{*}_{R}\, c_{\nu_o,\sigma}\right) \right) \\ &= \frac{i}{\sqrt{|t_{\mathrm{L}}|^2 + |t_{\mathrm{R}}|^2}} \sum_{\nu_e,\nu_o,\mathbf{k},\sigma} \left(\left(|t_{\mathrm{L}}|^2 c^{\dagger}_{\nu_e,\sigma} - t_{\mathrm{L}} t_{\mathrm{R}}\, c^{\dagger}_{\nu_o,\sigma}\right) d_{\mathbf{k},\sigma} - d^{\dagger}_{\mathbf{k},\sigma} \left(|t_{\mathrm{L}}|^2 c_{\nu_e,\sigma} - t^{*}_{\mathrm{L}} t^{*}_{\mathrm{R}}\, c_{\nu_o,\sigma}\right) \right) \\ &= \frac{i}{\sqrt{|t_{\mathrm{L}}|^2 + |t_{\mathrm{R}}|^2}} \sum_{\nu_e,\nu_o,\mathbf{k},\sigma} \left(|t_{\mathrm{L}}|^2 \left(c^{\dagger}_{\nu_e,\sigma} d_{\mathbf{k},\sigma} - d^{\dagger}_{\mathbf{k},\sigma} c_{\nu_e,\sigma}\right) - \left(t_{\mathrm{L}} t_{\mathrm{R}}\, c^{\dagger}_{\nu_o,\sigma} d_{\mathbf{k},\sigma} - t^{*}_{\mathrm{L}} t^{*}_{\mathrm{R}}\, d^{\dagger}_{\mathbf{k},\sigma} c_{\nu_o,\sigma}\right) \right) \end{aligned}$$

and similarly, I_{R} as

$$
\begin{aligned}
I_{\mathrm{R}} &= i \sum_{\nu_e,\nu_o,\mathbf{k},\sigma} \left(\frac{t_{\mathrm{R}}}{\sqrt{|t_{\mathrm{L}}|^2+|t_{\mathrm{R}}|^2}} \left(t_{\mathrm{R}}^* c_{\nu_e,\sigma}^\dagger + t_{\mathrm{L}}\, c_{\nu_o,\sigma}^\dagger \right) d_{\mathbf{k},\sigma} - d_{\mathbf{k},\sigma}^\dagger \frac{t_{\mathrm{R}}^*}{\sqrt{|t_{\mathrm{L}}|^2+|t_{\mathrm{R}}|^2}} \left(t_{\mathrm{R}} c_{\nu_e,\sigma} + t_{\mathrm{L}}^*\, c_{\nu_o,\sigma} \right) \right) \\
&= \frac{i}{\sqrt{|t_{\mathrm{L}}|^2+|t_{\mathrm{R}}|^2}} \sum_{\nu_e,\nu_o,\mathbf{k},\sigma} \Big(\left(|t_{\mathrm{R}}|^2 c_{\nu_e,\sigma}^\dagger + t_{\mathrm{L}} t_{\mathrm{R}}\, c_{\nu_o,\sigma}^\dagger \right) d_{\mathbf{k},\sigma} - d_{\mathbf{k},\sigma}^\dagger \left(|t_{\mathrm{R}}|^2 c_{\nu_e,\sigma} + t_{\mathrm{R}}^* t_L^*\, c_{\nu_o,\sigma} \right) \Big) \\
&= \frac{i}{\sqrt{|t_{\mathrm{L}}|^2+|t_{\mathrm{R}}|^2}} \sum_{\nu_e,\nu_o,\mathbf{k},\sigma} \left(|t_{\mathrm{R}}|^2 \left(c_{\nu_e,\sigma}^\dagger d_{\mathbf{k},\sigma} - d_{\mathbf{k},\sigma}^\dagger c_{\nu_e,\sigma} \right) + \left(t_L t_{\mathrm{R}}\, c_{\nu_o,\sigma}^\dagger d_{\mathbf{k},\sigma} - t_{\mathrm{L}}^* t_{\mathrm{R}}^*\, d_{\mathbf{k},\sigma}^\dagger c_{\nu_o,\sigma} \right) \right) .
\end{aligned}
$$

Thus, we arrive at

$$
\begin{cases}
I_{\mathrm{L}} = \frac{i}{\sqrt{|t_{\mathrm{L}}|^2+|t_{\mathrm{R}}|^2}} \sum_{\nu_e,\nu_o,\mathbf{k},\sigma} \left(|t_{\mathrm{L}}|^2 \left(c_{\nu_e,\sigma}^\dagger d_{\mathbf{k},\sigma} - d_{\mathbf{k},\sigma}^\dagger c_{\nu_e,\sigma} \right) - \left(t_{\mathrm{L}} t_{\mathrm{R}}\, c_{\nu_o,\sigma}^\dagger d_{\mathbf{k},\sigma} - t_{\mathrm{L}}^* t_{\mathrm{R}}^*\, d_{\mathbf{k},\sigma}^\dagger c_{\nu_o,\sigma} \right) \right) \\
I_{\mathrm{R}} = \frac{i}{\sqrt{|t_{\mathrm{L}}|^2+|t_{\mathrm{R}}|^2}} \sum_{\nu_e,\nu_o,\mathbf{k},\sigma} \left(|t_{\mathrm{R}}|^2 \left(c_{\nu_e,\sigma}^\dagger d_{\mathbf{k},\sigma} - d_{\mathbf{k},\sigma}^\dagger c_{\nu_e,\sigma} \right) + \left(t_{\mathrm{L}} t_{\mathrm{R}}\, c_{\nu_o,\sigma}^\dagger d_{\mathbf{k},\sigma} - t_{\mathrm{L}}^* t_{\mathrm{R}}^*\, d_{\mathbf{k},\sigma}^\dagger c_{\nu_o,\sigma} \right) \right)
\end{cases} .
\tag{1.39}
$$

In the case of time-independent tunneling current (DC), we can calculate the expectation value of the current operator in each lead separately using Eq.(1.39), or alternatively, we can use the linear combination of the two, i.e.,

$$
I \equiv \alpha I_{\mathrm{L}} - (1-\alpha) I_{\mathrm{R}} \,, \tag{1.40}
$$

where α is defined as,

$$
\alpha = \frac{|t_{\mathrm{R}}|^2}{|t_{\mathrm{L}}|^2+|t_{\mathrm{R}}|^2} \quad \rightarrow \quad 1-\alpha = \frac{|t_{\mathrm{L}}|^2}{|t_{\mathrm{L}}|^2+|t_{\mathrm{R}}|^2} \,. \tag{1.41}
$$

With this definition of α, the particle-current operator becomes merely a function of odd electrons. This can be simply shown by plugging Eq.(1.41) and Eq.(1.39) into Eq.(1.40)

$$
\begin{aligned}
I &= \frac{1}{|t_{\mathrm{L}}|^2+|t_{\mathrm{R}}|^2} \frac{i}{\sqrt{|t_{\mathrm{L}}|^2+|t_{\mathrm{R}}|^2}} \sum_{\nu_e,\nu_o,\mathbf{k},\sigma} \left(|t_{\mathrm{R}}|^2 |t_{\mathrm{L}}|^2 \left(c_{\nu_e,\sigma}^\dagger d_{\mathbf{k},\sigma} - d_{\mathbf{k},\sigma}^\dagger c_{\nu_e,\sigma} \right) - |t_R|^2 \left(t_L t_{\mathrm{R}}\, c_{\nu_o,\sigma}^\dagger d_{\mathbf{k},\sigma} - t_{\mathrm{L}}^* t_{\mathrm{R}}^*\, d_{\mathbf{k},\sigma}^\dagger c_{\nu_o,\sigma} \right) \right) \\
&\quad - \frac{1}{|t_{\mathrm{L}}|^2+|t_{\mathrm{R}}|^2} \frac{i}{\sqrt{|t_{\mathrm{L}}|^2+|t_{\mathrm{R}}|^2}} \sum_{\nu_e,\nu_o,\mathbf{k},\sigma} \left(|t_{\mathrm{L}}|^2 |t_{\mathrm{R}}|^2 \left(c_{\nu_e,\sigma}^\dagger d_{\mathbf{k},\sigma} - d_{\mathbf{k},\sigma}^\dagger c_{\nu_e,\sigma} \right) + |t_{\mathrm{L}}|^2 \left(t_{\mathrm{L}} t_{\mathrm{R}}\, c_{\nu_o,\sigma}^\dagger d_{\mathbf{k},\sigma} - t_{\mathrm{L}}^* t_R^*\, d_{\mathbf{k},\sigma}^\dagger c_{\nu_o,\sigma} \right) \right) \\
&= -\frac{1}{|t_{\mathrm{L}}|^2+|t_{\mathrm{R}}|^2} \frac{i}{\sqrt{|t_{\mathrm{L}}|^2+|t_{\mathrm{R}}|^2}} \sum_{\nu_o,\mathbf{k},\sigma} \left(|t_{\mathrm{L}}|^2+|t_{\mathrm{R}}|^2 \right) \left(t_{\mathrm{L}} t_{\mathrm{R}}\, c_{\nu_o,\sigma}^\dagger d_{\mathbf{k},\sigma} - t_{\mathrm{L}}^* t_{\mathrm{R}}^*\, d_{\mathbf{k},\sigma}^\dagger c_{\nu_o,\sigma} \right) ,
\end{aligned}
$$

resulting in

$$
\boxed{ I = \frac{-i}{\sqrt{|t_{\mathrm{L}}|^2+|t_{\mathrm{R}}|^2}} \sum_{\nu_o,\mathbf{k},\sigma} \left(t_{\mathrm{L}} t_{\mathrm{R}}\, c_{\nu_o,\sigma}^\dagger d_{\mathbf{k},\sigma} - t_{\mathrm{R}}^* t_L^*\, d_{\mathbf{k},\sigma}^\dagger c_{\nu_o,\sigma} \right) } .
$$

With this result, the computation of the current-current correlation function immensely simplifies since the odd electron operator c_{ν_o} and the sample operator $d_{\mathbf{k},\sigma}$ belong to separate sector of the Hamiltonian, and therefore, commutable. We derive it by starting from the definition of the particle-current operator

$$
I = -i(L - L^\dagger) \,,
$$

with L and $L^\dagger$ operator being defined as

$$
L = \frac{t_{\mathrm{L}} t_{\mathrm{R}}}{\sqrt{|t_{\mathrm{L}}|^2+|t_{\mathrm{R}}|^2}} \sum_{\nu_o,\mathbf{k},\sigma} c_{\nu_o,\sigma}^\dagger d_{\mathbf{k},\sigma} \quad \leftrightarrow \quad L^\dagger = \frac{t_R^* t_{\mathrm{L}}^*}{\sqrt{|t_{\mathrm{L}}|^2+|t_{\mathrm{R}}|^2}} \sum_{\nu_o,\mathbf{k},\sigma} d_{\mathbf{k},\sigma}^\dagger c_{\nu_o,\sigma} . \tag{1.42}
$$

By substituting Eq.(1.42) into current-current correlation function

$$C_{II}^{\mathrm{R}}(t) = -i\theta(t)\left\langle\left[I(t), I(0)\right]\right\rangle = -i\theta(t)\left\langle\left[L(t) - L^{\dagger}(t)\,,\, L(0) - L^{\dagger}(0)\right]\right\rangle . \tag{1.43}$$

and ignoring $\langle[L(t), L(0)]\rangle = \langle[L^{\dagger}(t), L^{\dagger}(0)]\rangle = 0$ terms, as they do not conserve the number of particles, we arrive at

$$C_{II}^{\mathrm{R}}(t) = -i\theta(t)\Bigg(\underbrace{\left\langle\left[L(t), L^{\dagger}(0)\right]\right\rangle}_{(1)} + \underbrace{\left\langle\left[L^{\dagger}(t), L(0)\right]\right\rangle}_{(2)}\Bigg). \tag{1.44}$$

The expectation value (1) in Eq.(1.44) simplifies to

$$\begin{aligned}
\left\langle\left[L(t), L^{\dagger}(0)\right]\right\rangle &= \sum_{\nu_o,\nu_o'}\sum_{\mathbf{k},\mathbf{k}'}\sum_{\sigma,\sigma'}\left\langle\left[c_{\nu_o,\sigma}^{\dagger}(t)d_{\mathbf{k},\sigma}(t), d_{\mathbf{k}',\sigma'}^{\dagger}c_{\nu_o',\sigma'}\right]\right\rangle \\
&= \sum_{\nu_o,\nu_o'}\sum_{\mathbf{k},\mathbf{k}'}\sum_{\sigma,\sigma'}\frac{|t_{\mathrm{L}}|^2|t_{\mathrm{R}}|^2}{\sqrt{|t_{\mathrm{L}}|^2+|t_{\mathrm{R}}|^2}}\left[\left\langle c_{\nu_o,\sigma}^{\dagger}(t)d_{\mathbf{k},\sigma}(t)d_{\mathbf{k}',\sigma'}^{\dagger}c_{\nu_o',\sigma'}\right\rangle - \left\langle d_{\mathbf{k}',\sigma'}^{\dagger}c_{\nu_o',\sigma'}c_{\nu_o,\sigma}^{\dagger}(t)d_{\mathbf{k},\sigma}(t)\right\rangle\right] \\
&= \sum_{\nu_o,\nu_o'}\sum_{\mathbf{k},\mathbf{k}'}\sum_{\sigma,\sigma'}\frac{|t_{\mathrm{L}}|^2|t_{\mathrm{R}}|^2}{\sqrt{|t_{\mathrm{L}}|^2+|t_{\mathrm{R}}|^2}}\Big[(-1)^2\left\langle c_{\nu_o,\sigma}^{\dagger}(t)c_{\nu_o',\sigma'}\right\rangle\left\langle d_{\mathbf{k},\sigma}(t)d_{\mathbf{k}',\sigma'}^{\dagger}\right\rangle \\
&\qquad -(-1)^2\left\langle d_{\mathbf{k}',\sigma'}^{\dagger}d_{\mathbf{k},\sigma}(t)\right\rangle\left\langle c_{\nu_o',\sigma'}c_{\nu_o,\sigma}^{\dagger}(t)\right\rangle\Big]
\end{aligned}$$

where we commuted the c and d operators twice in the last step to bring us to

$$\left\langle\left[L(t), L^{\dagger}(0)\right]\right\rangle = \sum_{\nu_o,\nu_o'}\sum_{\mathbf{k},\mathbf{k}'}\sum_{\sigma,\sigma'}\frac{|t_{\mathrm{L}}|^2|t_{\mathrm{R}}|^2}{\sqrt{|t_{\mathrm{L}}|^2+|t_{\mathrm{R}}|^2}}\left[\left\langle c_{\nu_o,\sigma}^{\dagger}(t)c_{\nu_o',\sigma'}\right\rangle\left\langle d_{\mathbf{k},\sigma}(t)d_{\mathbf{k}',\sigma'}^{\dagger}\right\rangle - \left\langle c_{\nu_o',\sigma'}c_{\nu_o,\sigma}^{\dagger}(t)\right\rangle\left\langle d_{\mathbf{k}',\sigma'}^{\dagger}d_{\mathbf{k},\sigma}(t)\right\rangle\right]. \tag{1.45}$$

Now by recalling the definition of greater Green's function $\mathcal{G}^{>}(\nu,t;\nu',t') = -i\left\langle c_{\nu}(t)c_{\nu'}^{\dagger}(t')\right\rangle$ and setting $t' = 0$, we find the odd- and d-electron Green's functions as

$$\begin{cases}\mathcal{G}^{>}(\nu_o\sigma,t;\nu_o'\sigma',0) = -i\left\langle c_{\nu_o,\sigma}(t)c_{\nu_o',\sigma'}^{\dagger}(0)\right\rangle \\ \mathcal{G}^{>}(d\mathbf{k}\sigma,t;\mathbf{k}'\sigma',0) = -i\left\langle d_{\mathbf{k},\sigma}(t)d_{\mathbf{k}',\sigma'}^{\dagger}(0)\right\rangle\end{cases} \xrightarrow{(t\to -t)} \begin{cases}\mathcal{G}^{>}(\nu_o\sigma,-t;\nu_o',\sigma',0) = -i\left\langle c_{\nu_o,\sigma}(0)c_{\nu_o',\sigma'}^{\dagger}(t)\right\rangle \\ \mathcal{G}^{>}(d\mathbf{k}\sigma,-t;\mathbf{k}'\sigma',0) = -i\left\langle d_{\mathbf{k},\sigma}(0)d_{\mathbf{k}',\sigma'}^{\dagger}(t)\right\rangle\end{cases} \tag{1.46}$$

and also for the lesser Green's function $\mathcal{G}^{<}(\nu,t;\nu',t') = i\left\langle c_{\nu'}^{\dagger}(t')c_{\nu}(t)\right\rangle$, we have

$$\begin{cases}\mathcal{G}^{<}(\nu_o\sigma,t;\nu_o'\sigma',0) = i\left\langle c_{\nu_o',\sigma'}^{\dagger}(0)c_{\nu_o,\sigma}(t)\right\rangle \\ \mathcal{G}^{<}(d\mathbf{k}\sigma,t;\mathbf{k}'\sigma',0) = i\left\langle d_{\mathbf{k}',\sigma'}^{\dagger}(0)d_{\mathbf{k},\sigma}(t)\right\rangle\end{cases} \xrightarrow{(t\to -t)} \begin{cases}\mathcal{G}^{<}(\nu_o\sigma,-t;\nu_o'\sigma',0) = i\left\langle c_{\nu_o',\sigma'}^{\dagger}(t)c_{\nu_o,\sigma}(0)\right\rangle \\ \mathcal{G}^{<}(d\mathbf{k}\sigma,-t;\mathbf{k}'\sigma',0) = i\left\langle d_{\mathbf{k}',\sigma'}^{\dagger}(t)d_{\mathbf{k},\sigma}(0)\right\rangle\end{cases}. \tag{1.47}$$

By substituting the thermal averages in Eq.(1.45) with greater and lesser Green's function from Eq.(1.47) and Eq.(1.47), we obtain

$$\begin{aligned}
\left\langle\left[L(t), L^{\dagger}(0)\right]\right\rangle = \sum_{\nu_o,\nu_o'}\sum_{\mathbf{k},\mathbf{k}'}\sum_{\sigma,\sigma'}\frac{|t_L|^2|t_R|^2}{\sqrt{|t_L|^2+|t_R|^2}}\big[&\,\mathcal{G}^{<}(\nu_o'\sigma',-t;\nu_o\sigma,0)\,\mathcal{G}^{>}(d\mathbf{k}\sigma,t;\mathbf{k}'\sigma',0) \\
&-\mathcal{G}^{>}(\nu_o'\sigma',-t;\nu_o\sigma,0)\,\mathcal{G}^{<}(d\mathbf{k}\sigma,t;\mathbf{k}'\sigma',0)\big].
\end{aligned} \tag{1.48}$$

Considering the symmetries of the Hamiltonian for the left and right lead, and also the tunneling Hamiltonian will allow us to simplify the Green's functions in Eq.(1.48). Since the

Hamiltonian of the left and right lead is diagonal in terms of even and odd electron operators, Eq.(1.36), and the tunneling Hamiltonian, Eq.(1.37), is in terms of only even electrons; the Green's function of odd electrons must be diagonal

$$\mathcal{G}^{</>}(\nu_o'\sigma', -t; \nu_o\sigma, 0) = \delta_{\sigma,\sigma'}\delta_{\nu,\nu_o'}\mathcal{G}^{</>}(\nu_o\sigma, -t).$$

and by considering translational invariance in the sample, the Green's function of the d-electrons become diagonal

$$\mathcal{G}^{</>}(d\mathbf{k}\sigma, t; \mathbf{k}'\sigma', 0) = \delta_{\sigma,\sigma'}\delta_{\mathbf{k},\mathbf{k}'}\mathcal{G}^{</>}(d\mathbf{k}\sigma, t).$$

Here, we have also assumed that the tunneling ($\mathcal{H}_{\mathrm{T}}$) and sample's Hamiltonian ($\mathcal{H}_{\mathrm{d}}$) are diagonal in spin space. With these simplifications, Eq.(1.48) reduces to

$$\left\langle\left[L(t), L^\dagger(0)\right]\right\rangle = \sum_{\nu_o,\mathbf{k},\sigma} \frac{|t_{\mathrm{L}}|^2|t_{\mathrm{R}}|^2}{\sqrt{|t_{\mathrm{L}}|^2 + |t_{\mathrm{R}}|^2}} \left[\mathcal{G}^{<}(\nu_o\sigma, -t)\mathcal{G}^{>}(d\mathbf{k}\sigma, t) - \mathcal{G}^{>}(\nu_o\sigma, -t;)\mathcal{G}^{<}(d\mathbf{k}\sigma, t)\right]. \tag{1.49}$$

The commutator (2) in Eq.(1.44) exactly follows from Eq.(1.49) by a change of sign (-1) in the commutator by exchanging terms

$$\left[L(t), L^\dagger(0)\right] = -\left[L^\dagger(0), L(t)\right],$$

and reversal of time $(t \to -t)$

$$-\left[L^\dagger(0), L(t)\right] \xrightarrow{(t\to -t)} -\left[L^\dagger(t), L(0)\right].$$

Therefore, under these operations the commutator (2) in Eq.(1.44) can be easily computed based on the expression we found for the commutator (1), Eq.(1.45), as

$$\left\langle\left[L^\dagger(t), L(0)\right]\right\rangle = -\sum_{\nu_o,\mathbf{k},\sigma} \frac{|t_{\mathrm{L}}|^2|t_{\mathrm{R}}|^2}{\sqrt{|t_{\mathrm{L}}|^2 + |t_{\mathrm{R}}|^2}} \left[\,\mathcal{G}^{<}(\nu_o\sigma, t)\,\mathcal{G}^{>}(d\mathbf{k}\sigma, -t) \;-\; \mathcal{G}^{>}(\nu_o\sigma, t;)\,\mathcal{G}^{<}(d\mathbf{k}\sigma, -t)\right]. \tag{1.50}$$

Thus, we obtain the retarded current-current correlation function in time domain by substituting Eq.(1.49) and Eq.(1.50) into Eq.(1.44) as

$$\begin{aligned} C_{II}^{\mathrm{R}}(t) = -i\theta(t)\Bigg(&\frac{|t_{\mathrm{L}}|^2|t_{\mathrm{R}}|^2}{\sqrt{|t_{\mathrm{L}}|^2 + |t_{\mathrm{R}}|^2}}\Big[\mathcal{G}^{<}(\nu_o\sigma, -t)\,\mathcal{G}^{>}(d\mathbf{k}\sigma, t) \;-\; \mathcal{G}^{>}(\nu_o\sigma, -t;)\,\mathcal{G}^{<}(d\mathbf{k}\sigma, t) \\ &- \mathcal{G}^{<}(\nu_o\sigma, t)\,\mathcal{G}^{>}(d\mathbf{k}\sigma, -t) \;+\; \mathcal{G}^{>}(\nu_o\sigma, t;)\,\mathcal{G}^{<}(d\mathbf{k}\sigma, -t)\Big]\Bigg). \end{aligned} \tag{1.51}$$

Now we want to calculate the imaginary part of Eq(1.51). In order to do that, we notice the following properties of complex number

$$\begin{cases} \text{real number:} & z^* = z \\ \text{pure imaginary number:} & z^* = -z \end{cases}.$$

Applying this identity to the greater and lesser Green's functions leads to

$$\begin{cases} (\mathcal{G}^{>}(\nu,t))^{*} = \left(-i\left\langle c_\nu(t)c_\nu^{\dagger}\right\rangle\right)^{*} = i\left\langle c_\nu c_\nu^{\dagger}(t)\right\rangle = -\mathcal{G}^{>}(\nu,-t) \\ (\mathcal{G}^{<}(\nu,t))^{*} = \left(i\left\langle c_\nu^{\dagger}c_\nu(t)\right\rangle\right)^{*} = -i\left\langle c_\nu^{\dagger}(t)c_\nu\right\rangle = -\mathcal{G}^{<}(\nu,-t) \end{cases},$$

which means that they are pure imaginary. The multiplication of two purely imaginary functions is real, and therefore, the expression under the square bracket in Eq.(1.51) is real. Thus, if we take the imaginary part of Eq.(1.51) ,

$$\mathcal{I}mC_{II}^{\mathrm{R}}(t) = -\theta(t)\Bigg(\frac{|t_{\mathrm{L}}|^2|t_{\mathrm{R}}|^2}{\sqrt{|t_{\mathrm{L}}|^2+|t_{\mathrm{R}}|^2}}\Big[\mathcal{G}^{<}(\nu_o,\sigma,-t)\,\mathcal{G}^{>}(d\mathbf{k},\sigma,t) - \mathcal{G}^{>}(\nu_o,\sigma,-t;)\,\mathcal{G}^{<}(d\mathbf{k},\sigma,t) - \mathcal{G}^{<}(\nu_o,\sigma,t)\,\mathcal{G}^{>}(d\mathbf{k},\sigma,-t) + \mathcal{G}^{>}(\nu_o,\sigma,t;)\,\mathcal{G}^{<}(d\mathbf{k},\sigma,-t)\Big]\Bigg), \tag{1.52}$$

only the (i) prefactor drops out.

In order to calculate the conductance, we need to Fourier transform Eq.(1.52) to frequency domain

$$\begin{aligned} \mathcal{I}mC_{II}^{\mathrm{R}}(\omega) &= \int_{-\infty}^{+\infty} dt\, e^{i\omega t}\,\mathcal{I}mC_{II}^{\mathrm{R}}(t) \\ &= -\int_{-\infty}^{+\infty} dt\, e^{i\omega t}\theta(t)\Bigg(\sum_{\nu_o,\mathbf{k},\sigma}\frac{|t_{\mathrm{L}}|^2|t_{\mathrm{R}}|^2}{\sqrt{|t_{\mathrm{L}}|^2+|t_{\mathrm{R}}|^2}}\Big[\mathcal{G}^{<}(\nu_o\sigma,-t)\,\mathcal{G}^{>}(d\mathbf{k}\sigma,t) - \mathcal{G}^{>}(\nu_o\sigma,-t;)\,\mathcal{G}^{<}(d\mathbf{k}\sigma,t) \\ &\qquad - \mathcal{G}^{<}(\nu_o\sigma,t)\,\mathcal{G}^{>}(d\mathbf{k}\sigma,-t) + \mathcal{G}^{>}(\nu_o\sigma,t)\,\mathcal{G}^{<}(d\mathbf{k}\sigma,-t)\Big]\Bigg) \\ &= -\int_{0}^{+\infty} dt\, e^{i\omega t}\sum_{\nu_o,\mathbf{k},\sigma}\frac{|t_{\mathrm{L}}|^2|t_{\mathrm{R}}|^2}{|t_{\mathrm{L}}|^2+|t_{\mathrm{R}}|^2}\Big[\mathcal{G}^{<}(\nu_o\sigma,-t)\mathcal{G}^{>}(d\mathbf{k}\sigma,t) - \mathcal{G}^{>}(\nu_o\sigma,-t)\mathcal{G}^{<}(d\mathbf{k}\sigma,t) \\ &\qquad - \mathcal{G}^{<}(\nu_o\sigma,t)\mathcal{G}^{>}(d\mathbf{k}\sigma,-t) + \mathcal{G}^{>}(\nu_o\sigma,t)\mathcal{G}^{<}(d\mathbf{k}\sigma,-t)\Big], \end{aligned} \tag{1.53}$$

where we used the fact that $\int_{-\infty}^{+\infty} dt\,\theta(t)[\cdots] = \int_{0}^{+\infty} dt[\cdots]$. We can see that the expression within the square bracket in Eq.(1.53) is an odd function of time

$$\begin{aligned} &\left[\left(\mathcal{G}^{<}(\nu_o\sigma,-t)\mathcal{G}^{>}(d\mathbf{k}\sigma,t) - \mathcal{G}^{>}(\nu_o\sigma,-t)\mathcal{G}^{<}(d\mathbf{k}\sigma,t)\right) - \left(\mathcal{G}^{<}(\nu_o\sigma,t)\mathcal{G}^{>}(d\mathbf{k}\sigma,-t) - \mathcal{G}^{>}(\nu_o\sigma,t)\mathcal{G}^{<}(d\mathbf{k}\sigma,-t)\right)\right] \xrightarrow{t\to -t} \\ &\to \left[\left(\mathcal{G}^{<}(\nu_o\sigma,t)\mathcal{G}^{>}(d\mathbf{k}\sigma,-t) - \mathcal{G}^{>}(\nu_o\sigma,t)\mathcal{G}^{<}(d\mathbf{k}\sigma,-t)\right) - \left(\mathcal{G}^{<}(\nu_o\sigma,-t)\mathcal{G}^{>}(d\mathbf{k}\sigma,t) - \mathcal{G}^{>}(\nu_o\sigma,-t)\mathcal{G}^{<}(d\mathbf{k}\sigma,t)\right)\right] \\ &= -\left[\left(\mathcal{G}^{<}(\nu_o\sigma,-t)\mathcal{G}^{>}(d\mathbf{k}\sigma,t) - \mathcal{G}^{>}(\nu_o\sigma,-t)\mathcal{G}^{<}(d\mathbf{k}\sigma,t)\right) - \left(\mathcal{G}^{<}(\nu_o\sigma,t)\mathcal{G}^{>}(d\mathbf{k}\sigma,-t) - \mathcal{G}^{>}(\nu_o\sigma,t)\mathcal{G}^{<}(d\mathbf{k}\sigma,-t)\right)\right]. \end{aligned}$$

This means that we can absorb the (-1) prefactor in Eq.(1.53) by switching the time argument of the expression under the square bracket. Furthermore, by using the following property of Fourier transform of odd functions

$$\int_{0}^{+\infty} dt\, e^{i\omega t}\,O(t) = \frac{1}{2}\int_{-\infty}^{+\infty} dt\, e^{i\omega t}\,O(t)\,,$$

we can rewrite Eq.(1.53) as

$$\mathcal{I}mC_{II}^{\mathrm{R}}(\omega) = \frac{1}{2}\int_{-\infty}^{+\infty} dt\, e^{i\omega t}\sum_{\nu_o,\mathbf{k},\sigma}\frac{|t_{\mathrm{L}}|^2|t_{\mathrm{R}}|^2}{|t_{\mathrm{L}}|^2+|t_{\mathrm{R}}|^2}\left[\mathcal{G}^{<}(\nu_o\sigma,t)\mathcal{G}^{>}(d\mathbf{k}\sigma,-t) - \mathcal{G}^{>}(\nu_o\sigma,t)\mathcal{G}^{<}(d\mathbf{k}\sigma,-t) - \mathcal{G}^{<}(\nu_o\sigma,-t)\mathcal{G}^{>}(d\mathbf{k}\sigma,t) + \mathcal{G}^{>}(\nu_o\sigma,-t)\mathcal{G}^{<}(d\mathbf{k}\sigma,t)\right]. \tag{1.54}$$

The expression under the square bracket in Eq.(1.54) is comprised of pair products of greater and lesser Green's functions which can be significantly simplified using the following property of the Fourier transformation for product functions

$$\begin{aligned}\int dt e^{i\omega t} f(t)g(-t) &= \int dt e^{i\omega t} \int \frac{d\omega'}{2\pi} e^{-i\omega' t} f(\omega') \int \frac{d\omega''}{2\pi} e^{-i\omega''(-t)} g(\omega'') \\ &= \int \frac{d\omega'}{2\pi} f(\omega') \int \frac{d\omega''}{2\pi} g(\omega'') \int dt e^{i(\omega''+\omega-\omega')t} \\ &= \int \frac{d\omega'}{2\pi} f(\omega') \int \frac{d\omega''}{2\pi} g(\omega'') 2\pi\delta(\omega''+\omega-\omega') \\ &= \int \frac{d\omega'}{2\pi} f(\omega') g(\omega'-\omega)\end{aligned}$$

and with a change of variable $(\omega' \to \omega' + \omega)$, it gives

$$\int dt e^{i\omega t} f(t)g(-t) = \int \frac{d\omega'}{2\pi} f(\omega'+\omega) g(\omega') \,. \tag{1.55}$$

Hence, by using Eq.(1.55) for the product of Green's functions in Eq.(1.54) we obtain

$$\begin{aligned}\mathcal{I}mC^{\mathrm{R}}_{II}(\omega) = \frac{1}{2}\int_{-\infty}^{+\infty} \frac{d\omega'}{2\pi} \sum_{\nu_o,\mathbf{k},\sigma} \frac{|t_{\mathrm{L}}|^2|t_{\mathrm{R}}|^2}{|t_{\mathrm{L}}|^2+|t_{\mathrm{R}}|^2} \big[&\mathcal{G}^<(\nu_o\sigma,\omega'+\omega)\mathcal{G}^>(d\mathbf{k}\sigma,\omega') - \mathcal{G}^>(\nu_o\sigma,\omega'+\omega)\mathcal{G}^<(d\mathbf{k}\sigma,\omega') \\ &-\mathcal{G}^<(\nu_o\sigma,\omega')\mathcal{G}^>(d\mathbf{k}\sigma,\omega'+\omega) + \mathcal{G}^>(\nu_o\sigma,\omega')\mathcal{G}^<(d\mathbf{k}\sigma,\omega'+\omega)\big] \,.\end{aligned}$$

By a shift of variable for the third and fourth product in the square bracket $(\omega' \to \omega' - \omega)$,

$$\begin{aligned}\mathcal{I}mC^{\mathrm{R}}_{II}(\omega) = \frac{1}{2}\int_{-\infty}^{+\infty} \frac{d\omega'}{2\pi} \sum_{\nu_o,\mathbf{k},\sigma} \frac{|t_{\mathrm{L}}|^2|t_{\mathrm{R}}|^2}{|t_{\mathrm{L}}|^2+|t_{\mathrm{R}}|^2} \big[&\mathcal{G}^<(\nu_o\sigma,\omega'+\omega)\mathcal{G}^>(d\mathbf{k}\sigma,\omega') - \mathcal{G}^>(\nu_o\sigma,\omega'+\omega)\mathcal{G}^<(d\mathbf{k}\sigma,\omega') \\ &-\mathcal{G}^<(\nu_o\sigma,\omega'-\omega)\mathcal{G}^>(d\mathbf{k}\sigma,\omega') + \mathcal{G}^>(\nu_o\sigma,\omega'-\omega)\mathcal{G}^<(d\mathbf{k}\sigma,\omega')\big] \,,\end{aligned}$$

we can factorize d-electron Green's function as

$$\begin{aligned}\mathcal{I}mC^{\mathrm{R}}_{II}(\omega) = \frac{1}{2}\int_{-\infty}^{+\infty} \frac{d\omega'}{2\pi} \sum_{\nu_o,\mathbf{k},\sigma} \frac{|t_{\mathrm{L}}|^2|t_{\mathrm{R}}|^2}{|t_{\mathrm{L}}|^2+|t_{\mathrm{R}}|^2} \Big[&\mathcal{G}^>(d\mathbf{k}\sigma,\omega')\Big\{\mathcal{G}^<(\nu_o\sigma,\omega'+\omega) - \mathcal{G}^<(\nu_o\sigma,\omega'-\omega)\Big\} \\ &-\mathcal{G}^<(d\mathbf{k}\sigma,\omega')\Big\{\mathcal{G}^>(\nu_o\sigma,\omega'+\omega) - \mathcal{G}^>(\nu_o\sigma,\omega'-\omega)\Big\}\Big] \,.\end{aligned}$$

Now by rewriting the greater and lesser Green's functions in terms of spectral function and Fermi-Dirac distribution,

$$\begin{cases} i\,\mathcal{G}^<(\nu;\omega) = \mathcal{A}(\nu,\omega)[1-n_{\mathrm{F}}(\omega)] \\ -i\,\mathcal{G}^>(\nu;\omega) = \mathcal{A}(\nu,\omega)\,n_{\mathrm{F}}(\omega) \end{cases},$$

we obtain

$$\begin{aligned}\mathcal{I}mC^{\mathrm{R}}_{II}(\omega) = \frac{1}{2}\int_{-\infty}^{+\infty} \frac{d\omega'}{2\pi} \sum_{\nu_o,\mathbf{k},\sigma} \frac{|t_{\mathrm{L}}|^2|t_{\mathrm{R}}|^2}{|t_{\mathrm{L}}|^2+|t_{\mathrm{R}}|^2} \Big[&\mathcal{A}(d\mathbf{k}\sigma,\omega')\,n_{\mathrm{F}}(\omega')\Big\{\mathcal{A}(\nu_o\sigma,\omega'+\omega)[1-n_{\mathrm{F}}(\omega'+\omega)] \\ &-\mathcal{A}(\nu_o\sigma,\omega'-\omega)[1-n_{\mathrm{F}}(\omega'-\omega)]\Big\} - \mathcal{A}(d\mathbf{k}\sigma,\omega')[1-n_{\mathrm{F}}(\omega')]\Big\{\mathcal{A}(\nu_o\sigma,\omega'+\omega)\,n_{\mathrm{F}}(\omega'+\omega) \\ &-\mathcal{A}(\nu_o\sigma,\omega'-\omega)\,n_{\mathrm{F}}(\omega'-\omega)\Big\}\Big] \,.\end{aligned}$$

The expression under square bracket can be simplified by rearranging terms as

$$
\begin{aligned}
[\cdots] &= \mathcal{A}(d\mathbf{k}\sigma,\omega')\, n_{\mathrm{F}}(\omega')\Big\{\mathcal{A}(\nu_o\sigma,\omega'+\omega)[1-n_{\mathrm{F}}(\omega'+\omega)]-\mathcal{A}(\nu_o\sigma,\omega'-\omega)[1-n_{\mathrm{F}}(\omega'-\omega)]\Big\}\\
&\quad-\mathcal{A}(d\mathbf{k}\sigma,\omega')[1-n_{\mathrm{F}}(\omega')]\Big\{\mathcal{A}(\nu_o\sigma,\omega'+\omega)\, n_{\mathrm{F}}(\omega'+\omega)-\mathcal{A}(\nu_o\sigma,\omega'-\omega)\, n_{\mathrm{F}}(\omega'-\omega)\Big\}\\
&= \mathcal{A}(d\mathbf{k}\sigma,\omega')\Big\{\mathcal{A}(\nu_o\sigma,\omega'+\omega)n_{\mathrm{F}}(\omega')[1-n_{\mathrm{F}}(\omega'+\omega)]-\mathcal{A}(\nu_o\sigma,\omega'-\omega)n_{\mathrm{F}}(\omega')[1-n_{\mathrm{F}}(\omega'-\omega)]\\
&\quad-\mathcal{A}(\nu_o\sigma,\omega'+\omega)\, n_{\mathrm{F}}(\omega'+\omega)[1-n_{\mathrm{F}}(\omega')]+\mathcal{A}(\nu_o\sigma,\omega'-\omega)\, n_{\mathrm{F}}(\omega'-\omega)[1-n_{\mathrm{F}}(\omega')]\Big\}\\
&= \mathcal{A}(d\mathbf{k}\sigma,\omega')\Big\{\mathcal{A}(\nu_o\sigma,\omega'+\omega)\big[n_{\mathrm{F}}(\omega')-n_{\mathrm{F}}(\omega'+\omega)\big]-\mathcal{A}(\nu_o\sigma,\omega'-\omega)\big[n_{\mathrm{F}}(\omega')-n_{\mathrm{F}}(\omega'-\omega)\big]\Big\}\\
&= \mathcal{A}(d\mathbf{k}\sigma,\omega')\mathcal{A}(\nu_o\sigma,\omega'+\omega)\big[n_{\mathrm{F}}(\omega')-n_{\mathrm{F}}(\omega'+\omega)\big]-\mathcal{A}(\nu_o\sigma,\omega'-\omega)n_{\mathrm{F}}(\omega')\big[n_{\mathrm{F}}(\omega')-n_{\mathrm{F}}(\omega'-\omega)\big].
\end{aligned}
$$

Therefore, we arrive at

$$
\begin{aligned}
\mathcal{I}mC^{\mathrm{R}}_{II}(\omega) = \frac{1}{2}\int_{-\infty}^{+\infty}\frac{d\omega'}{2\pi}\sum_{\nu_o,\mathbf{k},\sigma}\frac{|t_{\mathrm{L}}|^2|t_{\mathrm{R}}|^2}{|t_{\mathrm{L}}|^2+|t_{\mathrm{R}}|^2}\Big[&\mathcal{A}(d\mathbf{k}\sigma,\omega')\mathcal{A}(\nu_o\sigma,\omega'+\omega)\Big\{n_{\mathrm{F}}(\omega')-n_{\mathrm{F}}(\omega'+\omega)\Big\}\\
&-\mathcal{A}(d\mathbf{k}\sigma,\omega')\mathcal{A}(\nu_o\sigma,\omega'-\omega)\Big\{n_{\mathrm{F}}(\omega')-n_{\mathrm{F}}(\omega'-\omega)\Big\}\Big].
\end{aligned}
\tag{1.56}
$$

Since we should insert $\mathcal{I}mC^{\mathrm{R}}_{II}(\omega)$ into the Kubo formula for the conductance

$$
G = \lim_{\omega\to 0}\mathcal{R}e\left(\frac{ie^2}{\omega}C^{\mathrm{R}}_{II}(\omega)\right) \tag{1.57}
$$

and take the limit $\omega\to 0$, we are allowed to Taylor expand the Fermi-Dirac distributions in Eq.(1.56) to the first order in ω as they are exponentially decaying functions of frequency,

$$
\begin{cases}
n_{\mathrm{F}}(\omega'+\omega)\approx n_{\mathrm{F}}(\omega')+\omega\,\frac{\partial n_{\mathrm{F}}(\omega')}{\partial\omega'}+\mathcal{O}(\omega^2)\\[2ex]
n_{\mathrm{F}}(\omega'-\omega)\approx n_{\mathrm{F}}(\omega')-\omega\,\frac{\partial n_{\mathrm{F}}(\omega')}{\partial\omega'}+\mathcal{O}(\omega^2)
\end{cases}.
$$

It gives

$$
\begin{aligned}
\mathcal{I}mC^{\mathrm{R}}_{II}(\omega) = \frac{1}{2}\int_{-\infty}^{+\infty}\frac{d\omega'}{2\pi}\sum_{\nu_o,\mathbf{k},\sigma}\frac{|t_{\mathrm{L}}|^2|t_{\mathrm{R}}|^2}{|t_{\mathrm{L}}|^2+|t_{\mathrm{R}}|^2}\Big[&\mathcal{A}(d\mathbf{k}\sigma,\omega')\mathcal{A}(\nu_o\sigma,\omega'+\omega)\Big\{n_{\mathrm{F}}(\omega')-n_{\mathrm{F}}(\omega')-\omega\,\frac{\partial n_{\mathrm{F}}(\omega')}{\partial\omega'}\Big\}\\
&-\mathcal{A}(d\mathbf{k}\sigma,\omega')\mathcal{A}(\nu_o\sigma,\omega'-\omega)\Big\{n_{\mathrm{F}}(\omega')-n_{\mathrm{F}}(\omega')+\omega\,\frac{\partial n_{\mathrm{F}}(\omega')}{\partial\omega'}\Big\}\Big],
\end{aligned}
$$

which simplifies to

$$
\begin{aligned}
\mathcal{I}mC^{\mathrm{R}}_{II}(\omega) = -\frac{1}{2}\int_{-\infty}^{+\infty}\frac{d\omega'}{2\pi}\sum_{\nu_o,\mathbf{k},\sigma}\frac{|t_{\mathrm{L}}|^2|t_{\mathrm{R}}|^2}{|t_{\mathrm{L}}|^2+|t_{\mathrm{R}}|^2}\Big[&\mathcal{A}(d\mathbf{k}\sigma,\omega')\mathcal{A}(\nu_o\sigma,\omega'+\omega)\,\omega\,\frac{\partial n_{\mathrm{F}}(\omega')}{\partial\omega'}\\
&+\mathcal{A}(d\mathbf{k}\sigma,\omega')\mathcal{A}(\nu_o\sigma,\omega'-\omega)\,\omega\,\frac{\partial n_{\mathrm{F}}(\omega')}{\partial\omega'}\Big].
\end{aligned}
\tag{1.58}
$$

Furthermore, we use the fact that decoupled lead electrons are described by a non-interacting Hamiltonian, which have Dirac delta spectral functions,

$$\mathcal{A}(\nu_o\sigma,\omega) = 2\pi\delta(\omega-\xi_{\nu_o})\,.$$

This allows us to simply take the frequency integration in Eq.(1.58) as

$$\begin{aligned}\mathcal{I}mC^{\mathrm{R}}_{II}(\omega) &= -\frac{\omega}{2}\int_{-\infty}^{+\infty}\frac{d\omega'}{2\pi}\sum_{\nu_o,\mathbf{k},\sigma}\frac{|t_{\mathrm{L}}|^2|t_{\mathrm{R}}|^2}{|t_{\mathrm{L}}|^2+|t_{\mathrm{R}}|^2}\Bigg[\mathcal{A}(d\mathbf{k}\sigma,\omega')2\pi\delta(\omega'+\omega-\xi_{\nu_o})\frac{\partial n_{\mathrm{F}}(\omega')}{\partial\omega'}\\ &\qquad +\mathcal{A}(d\mathbf{k}\sigma,\omega')2\pi\delta(\omega'-\omega-\xi_{\nu_o})\frac{\partial n_{\mathrm{F}}(\omega')}{\partial\omega'}\Bigg]\\ &= -\frac{\omega}{2}\sum_{\nu_o,\mathbf{k},\sigma}\frac{|t_L|^2|t_R|^2}{|t_L|^2+|t_R|^2}\left[\mathcal{A}(d\mathbf{k}\sigma,-\omega+\xi_{\nu_o})\frac{\partial n_{\mathrm{F}}(-\omega+\xi_{\nu_o})}{\partial\xi_{\nu_o}}+\mathcal{A}(d\mathbf{k}\sigma,\omega+\xi_{\nu_o})\frac{\partial n_{\mathrm{F}}(\omega+\xi_{\nu_o})}{\partial\xi_{\nu_o}}\right].\end{aligned} \tag{1.59}$$

The conductance of the junction can be found by recalling the Kubo formula for conductance [21], and decomposing $C^{\mathrm{R}}_{II}(\omega)$ into its real and imaginary part

$$G = \lim_{\omega\to0}\mathcal{R}e\left(\frac{ie^2}{\omega}C^{\mathrm{R}}_{II}(\omega)\right) = \lim_{\omega\to0}\mathrm{R}e\left(\frac{ie^2}{\omega}\left[\mathcal{R}eC^{\mathrm{R}}_{II}(\omega)+i\,\mathcal{I}mC^{\mathrm{R}}_{II}(\omega)\right]\right). \tag{1.60}$$

As proved above, $C^{\mathrm{R}}_{II}(\omega)$ is a pure imaginary function of frequency $\left(\mathcal{R}e\,C^{\mathrm{R}}_{II}(\omega)=0\right)$, and therefore, the conductance has the following limit

$$G = -\lim_{\omega\to0}\frac{e^2}{\omega}\mathcal{I}mC^{\mathrm{R}}_{II}(\omega). \tag{1.61}$$

Now by substituting Eq.(1.59) into Eq.(1.61), we arrive at

$$\begin{aligned}G &= -\lim_{\omega\to0}\frac{e^2}{\omega}\left\{-\frac{\omega}{2}\sum_{\nu_o,\mathbf{k},\sigma}\frac{|t_{\mathrm{L}}|^2|t_{\mathrm{R}}|^2}{|t_{\mathrm{L}}|^2+|t_{\mathrm{R}}|^2}\left[\mathcal{A}(d\mathbf{k}\sigma,-\omega+\xi_{\nu_o})\frac{\partial n_{\mathrm{F}}(-\omega+\xi_{\nu_o})}{\partial\xi_{\nu_o}}+\mathcal{A}(d\mathbf{k}\sigma,\omega+\xi_{\nu_o})\frac{\partial n_{\mathrm{F}}(\omega+\xi_{\nu_o})}{\partial\xi_{\nu_o}}\right]\right\}\\ &= \frac{e^2}{2}\sum_{\nu_o,\mathbf{k},\sigma}\frac{|t_{\mathrm{L}}|^2|t_{\mathrm{R}}|^2}{|t_{\mathrm{L}}|^2+|t_{\mathrm{R}}|^2}\left[\mathcal{A}(d\mathbf{k}\sigma,\xi_{\nu_o})\frac{\partial n_{\mathrm{F}}(\xi_{\nu_o})}{\partial\xi_{\nu_o}}+\mathcal{A}(d\mathbf{k}\sigma,\xi_{\nu_o})\frac{\partial n_{\mathrm{F}}(\xi_{\nu_o})}{\partial\xi_{\nu_o}}\right].\end{aligned}$$

Thus, we finally obtain the conductance formula as

$$G = e^2\sum_{\nu_o,\mathbf{k},\sigma}\frac{|t_{\mathrm{L}}|^2|t_{\mathrm{R}}|^2}{|t_{\mathrm{L}}|^2+|t_{\mathrm{R}}|^2}\mathcal{A}(d\mathbf{k},\sigma,\xi_{\nu_o})\left(-\frac{\partial n_{\mathrm{F}}(\xi_{\nu_o})}{\partial\xi_{\nu_o}}\right).$$

Now by converting the discrete sum over lead states to an integral, $\sum_{\nu_o}\to\int d\xi\rho(\xi)$, we find

$$\begin{aligned}G &= e^2\sum_{\mathbf{k},\sigma}\int d\xi\,\rho(\xi)\frac{|t_{\mathrm{L}}|^2|t_{\mathrm{R}}|^2}{|t_{\mathrm{L}}|^2+|t_{\mathrm{R}}|^2}\mathcal{A}(d\mathbf{k},\sigma,\xi)\left(-\frac{\partial n_{\mathrm{F}}(\xi)}{\partial\xi}\right) \quad \xrightarrow{\times\frac{\rho(\xi)}{\rho(\xi)}}\\ \rightarrow\quad &= e^2\sum_{\mathbf{k},\sigma}\int d\xi\frac{\rho(\xi)\,|t_{\mathrm{L}}|^2|\,\rho(\xi)\,t_{\mathrm{R}}|^2}{\rho(\xi)\,|t_{\mathrm{L}}|^2+\rho(\xi)\,|t_{\mathrm{R}}|^2}\mathcal{A}(d\mathbf{k},\sigma,\xi)\left(-\frac{\partial n_{\mathrm{F}}(\xi)}{\partial\xi}\right).\end{aligned} \tag{1.62}$$

One can define the tunneling (hybridization) strength for the left and right leads as

$$\Gamma^{\mathrm{L/R}}(\xi) = 2\pi|t_{\mathrm{L/R}}|^2\rho(\xi).$$

With this definition, we can rewrite Eq.(1.62) as

$$G = e^2 \sum_{\mathbf{k},\sigma} \int \frac{d\xi}{2\pi} \frac{\Gamma^{\mathrm{L}}(\xi)\Gamma^{\mathrm{R}}(\xi)}{\Gamma^{\mathrm{L}}(\xi) + \Gamma^{\mathrm{R}}(\xi)} \mathcal{A}(d\mathbf{k}, \sigma, \xi) \left(-\frac{\partial n_{\mathrm{F}}(\xi)}{\partial \xi} \right). \tag{1.63}$$

Without loss of generality, we consider that the tunneling strength is energy independent: $\Gamma^{\mathrm{R}}(\xi) \equiv \Gamma^{\mathrm{R}}$ and $\Gamma^{\mathrm{L}}(\xi) \equiv \Gamma^{\mathrm{L}}$. This assumption is valid as long as the left and right leads have a featureless density of states at the Fermi level. This brings us to the final form of the conductance

$$\boxed{G = e^2 \sum_{\mathbf{k},\sigma} \int \frac{d\xi}{2\pi} \frac{\Gamma^{\mathrm{L}}\Gamma^{\mathrm{R}}}{\Gamma^{\mathrm{L}} + \Gamma^{\mathrm{R}}} \mathcal{A}(d\mathbf{k}, \sigma, \xi) \left(-\frac{\partial n_{\mathrm{F}}(\xi)}{\partial \xi} \right)}. \tag{1.64}$$

This is a fascinating result because all the complexities of the left and right leads (tip and substrate) are absorbed into two coupling constants (Γ^{R}, Γ^{L}) and the conductance of the tunneling junction solely depends on the spectral functions of the sample system. To achieve this result, we have made no approximation other than those in the linear response theory (Kubo formula for conductance) and the assumption that left and right leads have identical dispersion relations with constant tunneling strengths.

1.3 Conclusion

In summary, we have seen that the scanning tunneling spectroscopy describes how a single electron with definite energy propagates between the surface and the tip of the STM. In other words, it takes a direct measurement of the single-particle spectral function. In the simplest description of the STM junction, we have shown that the measured differential conductance is proportional to the product of the tip and substrate spectral functions at the position of the tip. For a generic STM junction with a sample in between (interacting or non-interacting), we have shown that the differential conductance is proportional to the sample's spectral function $A(d\mathbf{k}, \sigma, \xi)$ for small bias voltages, while all details of the tip and substrate are absorbed in a few constant prefactors. In fact, one can generalize it to a finite bias voltage using Meir and Wingreen formula [21, 23, 27],

$$I = e \sum_{\mathbf{k},\sigma} \int \frac{d\xi}{2\pi} \frac{\Gamma^{\mathrm{L}}\Gamma^{\mathrm{R}}}{\Gamma^{\mathrm{L}} + \Gamma^{\mathrm{R}}} \mathcal{A}(d\mathbf{k}\sigma, \xi) \left[n_{\mathrm{F}}(\xi - \mu_L) - n_{\mathrm{F}}(\xi - \mu_R) \right]. \tag{1.65}$$

where μ_L and μ_R are the chemical potentials of the left and right leads, which can be alternatively defined in terms of the bias voltage ($\mu_L = \mu_R - V_b$). In this way, by sweeping the bias voltage (V_b) and simulaneously recording the tunneling current, one can extract the spectral function of the sample.

Chapter 2

Introduction to the NTCDA Kondo Lattice system

Control over microscopic and quantum degrees of freedom is the focal point of interest for different technological purposes portrayed [28–30], for instance, in the newly surging competition to manufacture quantum computers [31, 32], and has been one of the chief driving forces in the experimental condensed matter physics to search for novel phases of matter [33–35]. Charge and spin degrees of freedom have been for long the main and supporting character in this quantum play. To this aim, an enormous enthusiasm is shown to 2D materials such as graphene and transition metal dichalcogenides (TMDs)—for they have a sufficiently decoupled 2D layer and offer a wide range of physics bracketing from strongly correlated electron systems to the topological and exotic states of matter[36–38]. In order to skip the arduous process of the top-down fabrication and preparation of atomically-precise 2D material, the alternative avenues to achieve these functionalities have also been paved in bottom-up approaches [1, 39–41]. Metal mediated atomic and molecular self-assembly implemented inside scanning tunneling microscope (STM) provides us with a tour de force platform to synthesize and locally probe and manipulate the nanoscale quantum degree of freedom [42–44].

A self-assembled monolayer of 1,4,5,6-naphthalene tetracarboxylic acid dianhydride (NTCDA) on Ag(111) substrate can create an artificial lattice of π-conjugated organic molecules [16, 17, 45–47]. It inheres in the perks of the two ingredients: delocalized electronic states from the metallic substrate, which facilitate the formation of a genuine 2D lattice [48], and localized molecular orbitals that manifest both Kondo and discharging resonance on the same orbital. This is particularly a contentious situation since, typically, these two resonances demand opposite settings. The Kondo resonance occurs when the spin of the local electron strongly interacts with the substrate; on the other hand, the discharging resonance occurs when there is sufficient decoupling from the substrate—making NTCDA/Ag(111) an ideal system to study the interplay of spin and charge.

This chapter serves three purposes. First, it provides a motivation for the study of the NTCDA/Ag(111) project. Second, it summons significant reported findings in the literature to make a general understanding and lubricate the flow of arguments for the following chapters. Finally, it recapitulates some representative results and preliminary notions that we will discuss in more detail throughout this thesis.

2.1 NTCDA molecule

1,4,5,6-naphthalene tetracarboxylic acid dianhydride (NTCDA) is a planar molecule with gas-phase D_{2h} symmetry. Geometry and location of different functional groups/atoms of the molecule are sketched in Fig.(2.1). Upon adsorption on the substrate and forming self-assembled nanostructures [16], the molecule interacts with the surface and other molecules at two locations. At the center of the molecule, the aromatic naphthalene core interacts via the spatially extended π-orbital electrons with the substrate and at the two ends via the carboxyl and anhydride groups with the substrate and neighboring molecules as well [49]. The interactions of these two electronic systems at the metal-organic interface push the character of adsorption towards weak chemisorption [17].

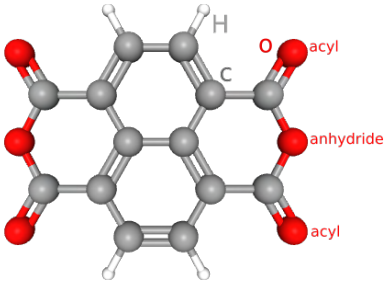

Figure 2.1: Graphical representation of gas phase NTCDA molecule ($C_{14}H_4O_6$).

Consequent to adsorption on the silver substrate, the NTCDA lowest unoccupied molecular orbital (LUMO) becomes partially occupied with a net charge transfer from silver $4s$-band, and possibly the Shockley surface state [50, 51]. As a result, it spectrally broadens and aligns slightly below the silver's Fermi level (E_F). Correspondingly, HOMO and HOMO-1 orbitals get fully occupied and bury deep below E_F.

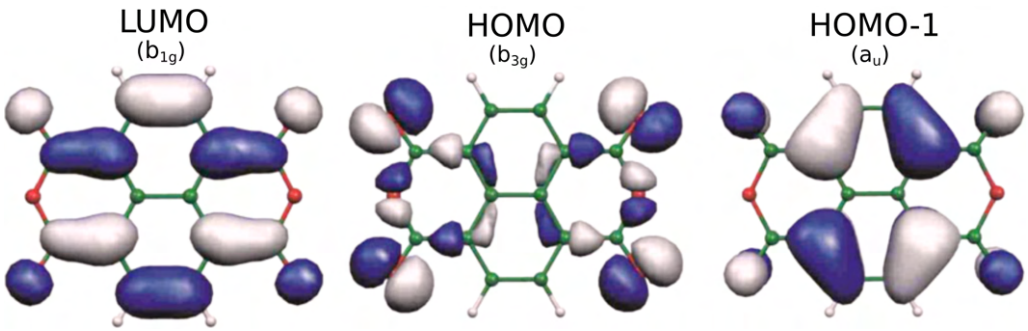

Figure 2.2: The gas-phase LUMO, HOMO, and HOMO-1 orbitals of NTCDA overlaid on the molecule structure (taken from [52]).

Therefore, the behavior of molecule electronic and vibronic states takes a LUMO character around the Fermi level predominantly [49, 50]. The summary of NTCDA frontier orbitals properties is presented in Tab.(2.1).

Orbital	Symmetry	Binding energy (eV)	Occupation	Net charge (e)	Method	Ref.
HOMO-1	a_u	3.4, 3.5	2	neutral	DFT, UPS	[50, 53]
HOMO	b_{3g}	2.2, 2.5, 2.4	2	neutral	DFT, UPS	[50, 51, 53]
LUMO	b_{1g}	0.4, 0.48	0.94, 1.42	-0.35	DFT, UPS	[49–51, 54]

Table 2.1: Molecular orbital energy levels of an NTCDA molecule adsorbed on Ag(111) substrate.

2.2 Conformational phases of NTCDA/Ag(111) lattice

Depending on the imposed preparation conditions, various conformational phases of a monolayer (ML) of NTCDA on Ag(111) substrate can develop. Historically, first, the two stable long-range ordered phases: Relaxed monolayer (r-ML) and compressed monolayer (c-ML), were reported to exist at the (sub-)monolayer regime, where the former transforms to the latter through post-deposition of molecules in the sample preparation process [16, 45]. Later, a plethora of intermediate phases at the coexistence regime was discovered by various groups [17, 46, 47]. The hitherto reported phases and their characteristics are classified at Tab.(2.2). This thesis is concerned with the electronic properties of r-ML in the great majority and to lower extents with the rippled phase in the coexistence regime. Therefore, the discussions are restricted only to these two specific phases.

Phase	Lattice	Unit cell	superstructure matrix	Coverage (ML)	Ref.
r-ML (commensurate)	Brick-wall	Rectangular	$\begin{pmatrix} 4.0 & 0.0 \\ 3.0 & 6.0 \end{pmatrix}$	< 0.9	[16, 45]
c-ML (incommensurate)[a]	Herringbone	Hexagonal	$\begin{pmatrix} 6.52 & 3.97 \\ 0.58 & 2.98 \end{pmatrix}$	~ 1	[16, 45, 46]
Coexistence regime	Stripy brick-wall	Rectangular	–[b]	0.9 – 1	[16]
	Rippled brick-wall	Rectangular	–[b]	0.9 – 1	[17]
	Uniaxially compressed brick-wall[c]	Rectangular	$\begin{pmatrix} 3.8 & 0.0 \\ 3.0 & 6.0 \end{pmatrix}$	0.9 – 1	[46]
	Vertical standing brick-wall[d]	Rectangular	$\begin{pmatrix} 3.0 & 0.2 \\ 1.1 & 4.7 \end{pmatrix}$	1<	[47]

[a] Unit cell assignment changed in the posterior publication of the same group and here is adapted accordingly [46] .
[b] Not reported.
[c] 4% compression along the short axis.
[d] Termed 'NTCDA-vert' and created via post-adsorption of NTCDA on r-ML phase with slight annealing.

Table 2.2: Properties of conformational phases of NTCDA/Ag(111) lattice.

As illustrated in Fig.(2.3), the r-ML phase contains two molecules per unit cell, forming a brick-wall lattice with a rectangular unit cell. The lattice is commensurate, and hence both molecules are aligned with their long axis along the $[01\bar{1}]$ direction of the substrate [46]. Though chemically the same, the two molecules exhibit in rows of dark and bright contrast in STM images and have different spectroscopic features. The apparent contrast is explained in terms of the difference in the LDOS of the two molecules at the Fermi level, which has yet been tentatively hypothesized to pertain to different adsorption geometry (top- and bridge-site) [47]. General properties of r-ML lattice are summarized in Tab.(2.3).

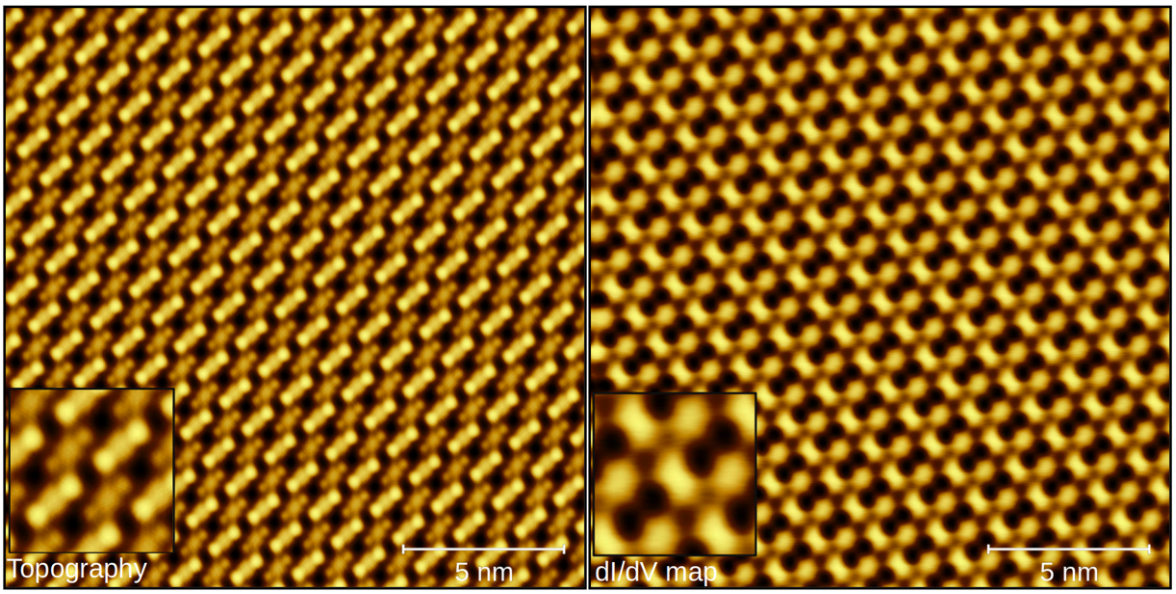

Figure 2.3: Imaging the NTCDA/Ag(111) r-ML phase. Left panel: Constant-current STM image (V_b = 48 mV, I_t = 1 nA, V_{mod} = 5 mV), and right panel: simultaneously recorded dI/dV-map.

Ag(111) unit vector $\lvert\mathbf{g_1}\rvert$	2.89 Å	[16]
NTCDA unit vector $\lvert\mathbf{a_1}\rvert$	11.57 Å	[16]
NTCDA unit vector $\lvert\mathbf{a_2}\rvert$	15.04 Å	[16]
$\angle(\mathbf{a_1}, \mathbf{a_2})$	90^o	[16]
$\angle(\mathbf{a_1}, \mathbf{g_1})$	0^o	[16]
Area per unit cell	174 $Å^2$	[46]
Molecule per unit cell	2	[16]
Ag(111) point group symmetry	$C_{3\nu}$	[55]
NTCDA point group symmetry (free)	D_{2h}	[49]
NTCDA point group symmetry (adsorbed)	$C_{2\nu}$	[49]

Table 2.3: Geometry and symmetries of the NTCDA/Ag(111) in the r-ML phase.

A counter-argument for this hypothesis is the existence of the long-range ordered rippled phase where rows of bright and dark molecules periodically change character along their long and short axis, i.e., the bright molecule smoothly transforms to a dark molecule, and vice versa [17]. Typically, rippled phase occurs in islands with triangular or deformed rims that emphasize the role of lattice boundaries over the local adsorption geometry in its formation. In Fig.(2.4), the created rippled phase has a fast and slow axis. Along the long molecular axis, alteration takes roughly between 9 to 12 unit cells, while it takes 3 to 7 unit cells along the short axis.

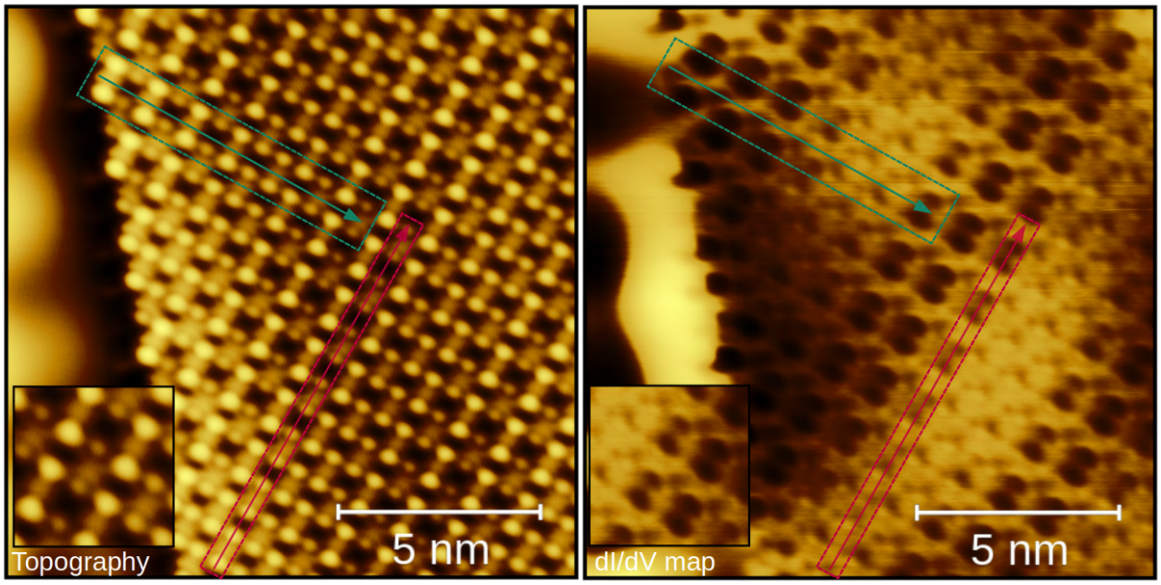

Figure 2.4: Imaging the NTCDA/Ag(111) rippled phase. Left panel: Constant-current STM image (V_b = 10 mV, I_t = 800 pA, V_{mod} = 5 mV), and right panel: simultaneously recorded dI/dV map. The Green and red arrows indicate the line along the molecule's short and long axis respectively where molecule smoothly changes character from bright to dark and vice versa.

Unlike having complicated-looking frontier orbitals, interestingly enough, the dI/dV map in Fig.(2.3) shows that the wave function of NTCDA/Ag(111) r-ML has a dumbbell-shape-orbital around the Fermi level. A similar wave function structure can be traced in the rippled phase with a periodic pattern. The dumbbell's center-of-mass is located at the bridge between two molecules, i.e., each lobe is situated in the hydrogen atoms of a different molecule.

2.3 A perspective to the electronic and vibrational properties of NTCDA/Ag(111) r-ML

The STM dI/dV curve of the highly ordered NTCDA/Ag(111) monolayer manifests the presence of a rich physics, ranging from single- to many-body and strongly correlated electron systems. It encompasses phenomena such as Kondo effect, electron-vibron interaction, molecular orbital hybridization, formation of a dispersive 2D band, and discharging resonance. The synopsis of these effects are featured in Fig.(2.5). Starting from the negative end of the spectrum, initially, the HOMO of the molecule appears superimposed on the tail of the silver substrate's bulk $4d$-band with binding energy around 2.4 eV [50, 51]. Subsequently, the singly-occupied LUMO of the molecule comes out as a very broad and elusive satellite, centered around -0.4 eV [50, 51]. So long as the LUMO's tail crosses the Fermi level, it renders a metallic ground state to the lattice. Around the Fermi level, as displayed in the inset of Fig.(2.5), and the positive side of the spectrum comprise more intricate features

that we briefly outline in the following.

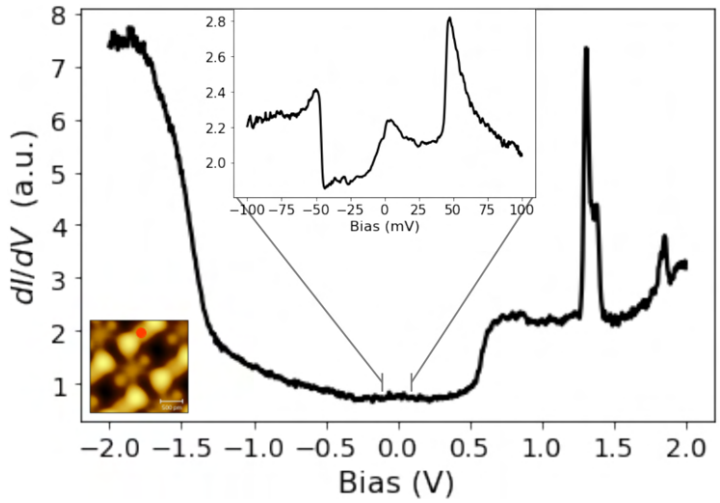

Figure 2.5: Multitude of spectroscopic features appearing on STM dI/dV point-spectrum acquired on the bright molecule center of NTCDA/Ag(111) lattice. The spectra were acquired at the bright molecule center with parameters V_b = 2.0 V, I_t = 4.0 nA, V_{mod} = 8 mV, T = 1.39 K, and the zoom-in inset at V_b = 100 mV, I_t = 2.0 nA, V_{mod} = 1 mV.

2.3.1 The vibrational modes and zero bias Kondo resonance

The low bias differential conductance acquired on various sites of the r-ML lattice, Fig.(2.6), shows two common features around the Fermi level: (i) a zero-bias-peak (ZBP) with a tiny gap precisely at zero energy, and (ii) a series of symmetric side peaks, with width, intensity, and energy varying across different sites. Most notably, the side-peaks appear on the center of the bright and dark molecule at $\approx \pm 47$ mV and are attributed to the predominantly out-of-plane vibrational modes of the LUMO [17]. Conceivably, the other symmetric side-peaks with energies $\approx \pm 75$ and ± 30 mV [1] might also be vibrational [17]. The nature of the ZBP, however, is spin-related [50]. It is associated with *Kondo effect* [51]: a many-body elastic spin-flip scattering between the spin of the local electron occupying the LUMO and the itinerant electrons in the substrate. The outcome is the quench of the singly-occupied LUMO's spin via forming a transient many-body singlet state.
The presence of the strong vibrational mode around the Fermi level is encoded into the interactions involved with the LUMO and its symmetry reduction [49]. The metal-organic interactions and charge transfer from the substrate to the NTCDA molecule modify the symmetry of its LUMO. In general, charge transfer to LUMO leads to an increase in electron density at certain bonds, increasing the strength of those bonds and resulting in their compression. Conversely, all bonds involved in nodes of the orbital stretch with respect to a free LUMO. Besides these in-plane distortions, the planarity of the molecule is also subject to vertical distortions. Due to the covalent bonding at the acyl oxygen atoms, the molecule

[1] The ± 75 mV peaks have not yet been reported as a vibrational state. However, the existence of many vibrational modes predicted by *ab initio* calculations in this energy range also justifies the assignment [49].

bends downwards at its four corners, and due to the push-back effect, which originates from Pauli repulsion at the naphthalene carbon core, the molecule bulge out in the center [49, 56–58]. Such configuration makes the out-of-plane vibrational modes, "rocking-modes," of the molecule susceptible to vertical perturbations [17, 59]. Conceivably, the strong vibrational states appearing on the STM differential conductance measurements belong to the out-of-plane modes—since the tunneling electron probing those states has negligible in-plane momentum to excite them. As a result of these distortions, the local molecular symmetry reduces from D_{2h} to $C_{2\nu}$, which, however, can be further reduced to C_s by considering the marginal effect of the inequivalent threefold hollow sites of the underlying Ag(111) below the two carbon rings [49, 56].

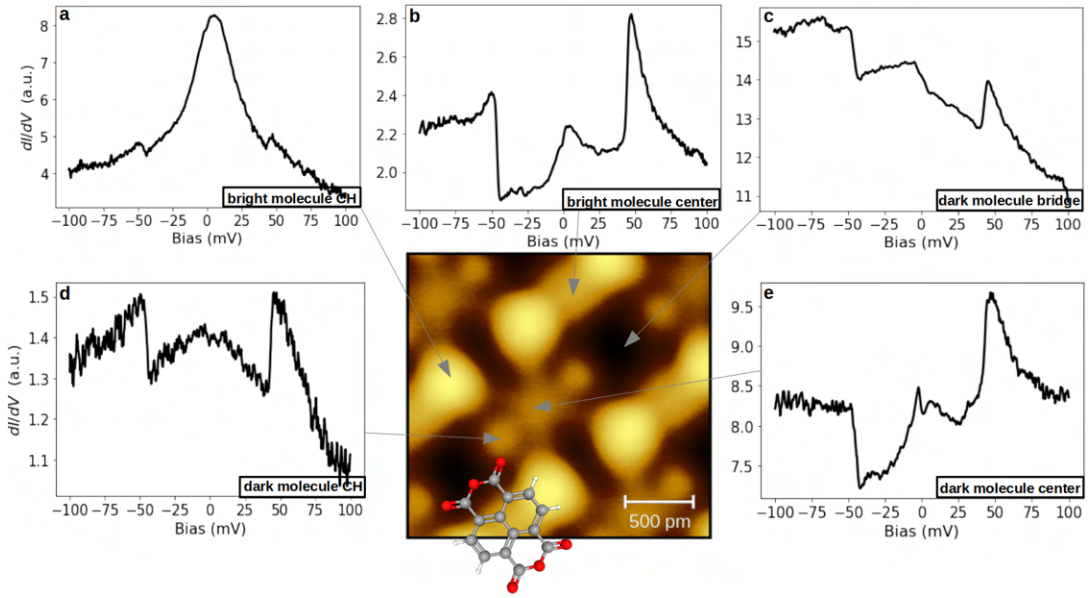

Figure 2.6: STM dI/dV point spectra of different sites of the NTCDA/Ag(111) r-ML lattice around the Fermi level. a, Bright molecule CH. **b,** Bright molecule center. **c,** Dark molecule bridge. **d,** Dark molecule CH. **e,** Dark molecule center. The constant-current STM image (central panel) acquired at V_b = 10 mV, I_t = 0.5 nA, with the graphical representation of NTCDA molecule is overlaid on a bright molecule. The dI/dV point spectra are highly oversampled and averaged over 3 sweeps with parameters: V_b = 100 mV, I_t = 2 nA, V_{mod} = 1 mV, T = 1.27 K, B = 0 T.

As remarked above, it is posited that the ubiquitous ZBP and its continuous modulation extending all across the r-ML originates from the Kondo effect [17], which, if so, connotes the creation of a Kondo lattice. The Kondo peak takes its maximum intensity at the bright molecule CH, centered around 2.5 mV with a tiny drop towards the bright molecule bridge-site and an appreciable drop approaching its central naphthalene core. The width (FWHM) of this Kondo peak is approximated to 28.5 mV at T = 4.3 K [17][2]. On the dark molecule, however, the ZBP humps down on the CH-site with a width approximated to 52.1 mV and even a further drop towards its bridge-site [17].

[2] We report a width of 24.4 mV and 57.4 mV for the bright and dark molecules at T = 1.27 K.

The difference in the line shape of the ZBP at different sites has been attributed to the role of quantum interference of possible tunneling paths between tip, substrate and the LUMO's wave function [17]. Unlike the center of the molecule where the wave function has a nodal plane and encourages only indirect tunneling path, i.e., tip's electron tunnels first to the substrate and then hop to the molecule; on the CH-site, the wave function takes a finite value and allows direct tunneling. In this scheme, the quantum interference of all possible indirect and direct paths with the corresponding scattering amplitudes at a given point transforms the Kondo resonance to the so-called Fano resonance [60], which varies spatially.

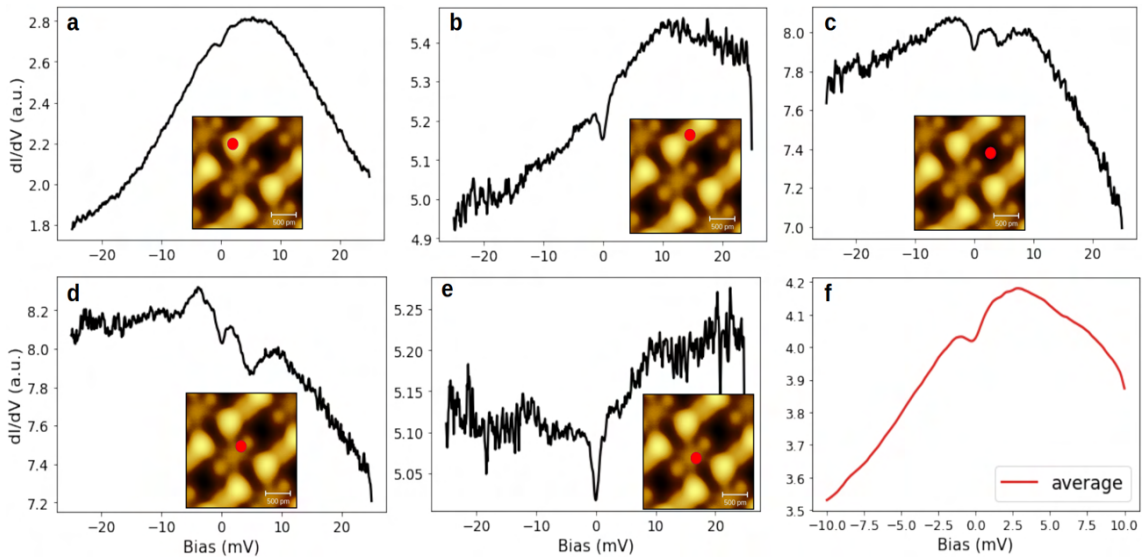

Figure 2.7: Zoom-in dI/dV point spectra around Fermi level at different sites of the NTCDA/Ag(111) r-ML lattice reveal two small gaps. **a,** Bright molecule CH. **b,** Bright molecule center. **c,** Dark molecule bridge. **d,** Dark molecule CH. **e,** Dark molecule center. **f,** Spatial average spectrum of 900 spectra over a 3×3 nm^2 area. To reveal the two small gaps, the dI/dV point spectra (**a-e**), were set to be highly oversampled and temporally slow, with lock-in time-constant (τ_c) of 100 ms and each was averaged over 5 sweeps with parameters: V_b = 20 mV, I_t = 4 nA, V_{mod} = 500 μV, T = 1.27 K, B = 0 T. The spatial average spectrum (**f**) was measured at V_b = 10 mV, T = 1.30 K, B = 0 T. The inset STM images with red dot marker illustrates the respective location where the spectrum was acquired.

The zoom-in spectra, Fig(2.7), reveal the existence of hitherto unreported fine structures at ZBP. *Precisely* at zero bias, a pervasive gap appears at every point on the lattice with different relative intensity. More accurately, the absolute intensity of the gap remains almost constant all over the lattice. The nature of this gap is not fully known. Even though it could be assigned to the Coulomb blockade (CB) phenomenon, its irregular size and persistence in temperature change from 1.2 to 4.4 K and magnetic field change from −10 to 10 T attributes ambiguity to such CB gap. There is also *a second gap* which appear asymmetrically at ≈ 5 mV, exclusively pronounced at dark molecule CH and bridge site. The nature of this gap is even more elusive. Together with other possibilities, such as the presence of very

low energy vibrational modes, it can also be assigned to a spin-related gap.

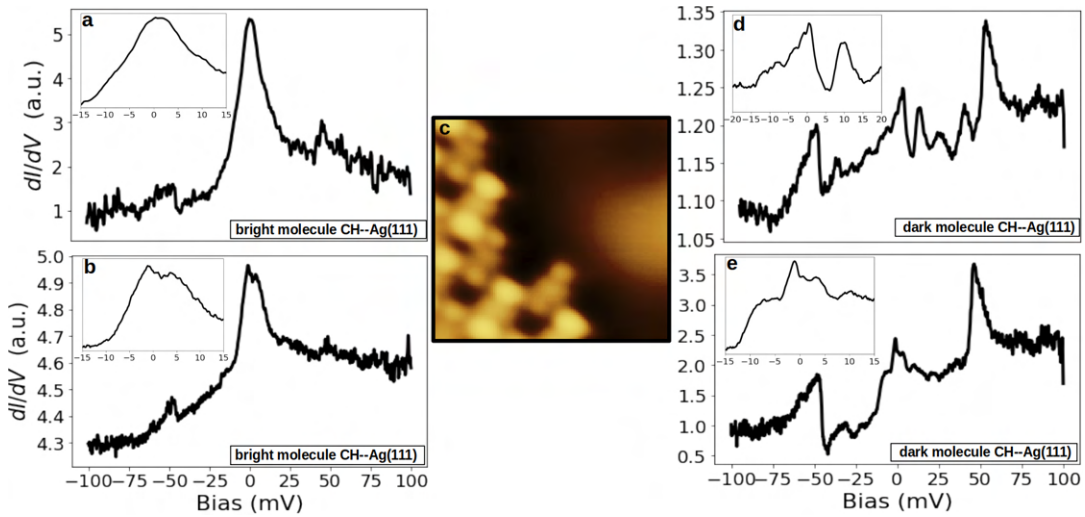

Figure 2.8: STM dI/dV point spectra of CH-sites at the lattice border of the NTCDA/Ag(111) r-ML around the Fermi level. **a, b,** Spectra acquired from the bright molecule CH at the lattice border with different coordination number. **c,** STM image of NTCDA/Ag(111) r-ML rim (V_b = 10 mV, I_t = 400 pA). **d, e,** Spectra acquired from the dark molecule CH at the lattice border with different coordination number. The dI/dV measurements were taken with parameters V_b = 100 mV, I_t = 14 nA, T = 1.51 K, V_{mod} = 200 μV, B = 10 T. To resolve the ZBP splitting and fine structure, the dI/dV spectra were set to be highly oversampled and temporally slow, with lock-in time-constant of 300 ms and each was averaged over 3 sweeps. The large current setpoint (I_t = 14 nA) was used to enhance the signal-to-noise ratio at small AC modulation voltage, which was chosen to avoid the spectral broadening inherent to the lock-in detection scheme.

Resolving the Fermi level at the lattice border further discloses the nature of ZBPs, Fig.(2.8). Depending on the coordination number, two typical spectra on the CH-site of each molecule have been observed at 10 T magnetic field. On the bright molecule, Fig.(2.8 a,b), the Kondo resonance peak is either slightly sharpened or tiny split into two unequal peaks flanked around 2.7 meV. On the dark molecule, however, the ZBP has been dramatically changed, Fig.(2.8 d,e). There, it is either noticeably split around 5 meV or appears with a fine structure at its summit. Naively speaking, the fine structure looks like a split Kondo peak with a minimal width superimposed on a broad Fano resonance. It's worth mentioning that at 0 T, there is no perceptible variation among the spectra in the middle and border of the lattice. Therefore, the changes arise from the magnetic nature of the ZBPs, which is masked by the (intra)inter-molecular and molecule-substrate hybridization[3] in the middle, and unveiled in the border of the lattice due to lower coordination number and deformed configuration.

[3] The strong inter/intra-molecular hybridization is encoded into the highly organized arrangement of alternating bright and dark molecules in the r-ML lattice, which would be otherwise impossible to form, and the strong molecule-substrate hybridization is reflected on the very broad Kondo resonance.

Additionally, it is noted that the symmetric pair of vibronic states at ±47 mV appears on all spectra, though with suppressed size compared to the middle of the lattice. On the other hand, the broad humps around ±30 mV, formerly identified as vibronic states, proliferate into more peaks and becomes further pronounced. This observation undermines the validity of such an assignment. Lastly, it must be pointed out that a common feature among all curves is an overall positive spectral tilt, which is the opposite trend to its counterpart in the middle of the lattice.

2.3.2 Interface state

The step-like spectroscopic feature in the positive bias side of Fig.(2.5) is associated with the formerly Shockley surface state of the metallic substrate Ag(111) located at ≈ −63 mV that is shifted above the Fermi level upon adsorption of the π-conjugated organic monolayer, to form the so-called interface state [61]. It has a 2D band structure with an anisotropic free-electron-like parabolic dispersion which has coverage-dependent onset energy of ≈ 560 meV [48]. The anisotropic dispersion is staggered along the $x-$ and $y-$axis, with an smaller renormalized electron mass along the long-axis of the molecule $(m_y^* < m_x^*)$ [48].

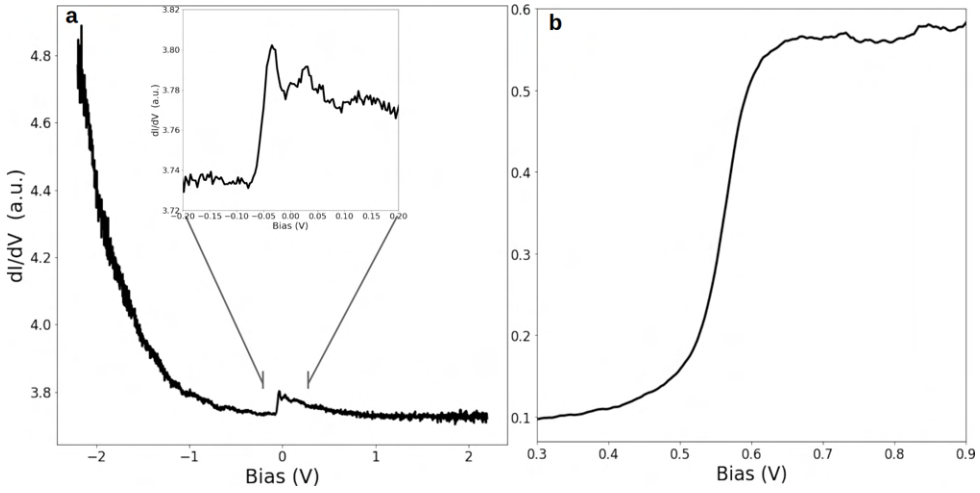

Figure 2.9: Formation of the 2D interface state in the NTCDA/Ag(111) lattice. a, Shockley surface state of bare Ag(111) measured at V_b = −2.2 V, I_t = 0.5 nA, T = 4.2 K, B = 0 T. **b,** Interface state spectrum measured at V_b = 0.9 V, I_t = 1 nA, T = 1.29 K, B = 0 T.

2.3.3 Discharging resonance

The monumental sharp peak pedestalized on the ensuing baseline of the interface state, aroused at $V_b \approx 1.4$ V in Fig.(2.5), is the spectroscopic resonance of a charging event originated from the center of the bright molecule[4] [62]. Typically, it is accompanied by a shoulder and followed by several subsequent discharging peaks that develop at larger bias, stemming from the neighboring molecules located several nanometers away, which also sense

[4] The peak was reported by Sabitova, A. *et al.*

the electric potential of the tip. Thus, adhere to its discharging nature, the peak lineshape (width and height) and energy is directly related to the applied bias voltage in the STM junction and the distance between the molecule's charging center and the tip [63–75]. Moreover, the geometrical shape of the tip also determines the applied electric field to the molecule, i.e., the sharper, the larger, which in turn allows the discharging peak to appear at lower bias [76, 77].

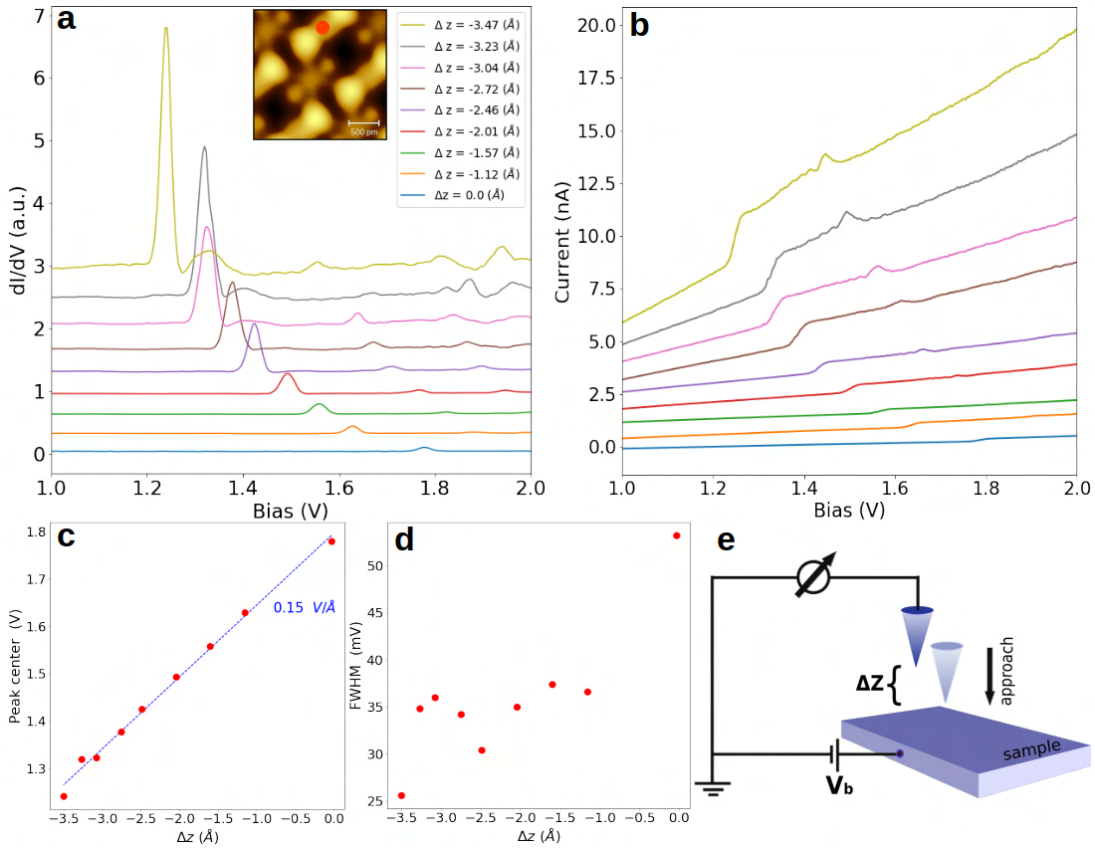

Figure 2.10: Distance-dependent dI/dV point spectra showing a linear approach of the discharging peak towards the Fermi level concomitant of sharpening of the resonance. **a,** dI/dV spectra of consecutive measurements. **b,** The corresponding $I - V$ curves. All spectra are shifted by a constant for clarity. **c,** Compilation of the main discharging peak center with a linear fit (slope $\alpha = 0.15$ V/Å). **d,** Compilation of the main discharging peak FWHM. The measurements were performed with parameters: $V_b = 2$ V, $I_t = 0.1 - 20$ nA, $V_{mod} = 5$ mV, $T = 1.29$ K, $B = 0$ T. **e,** The sketch shows the procedure of distance-dependent differential conductance measurement. Tip is stabilized for a fixed bias $V_b = 2$ V and a given tunneling current setpoint (I_t) to perform spectroscopy and approaches $(\Delta z < 0)$ by increasing I_t to perform the consecutive measurement. The inset STM image of panel **(a)** shows the parking position of the tip on top of the bright molecule center where measurements were executed.

The generic dependencies mentioned above about the discharging resonance can be directly measured by distance-dependent and bias-dependent differential conductance mea-

surements. In Fig.(2.10), dI/dV point spectra are acquired while successively reducing the tip-sample distance on top of the bright molecule center. As it is depicted in Fig.(2.10a), the discharging peak, its shoulder, and all other higher energetic peaks linearly shift to lower energies as the tip-sample distance reduces. Meaning that the required energy to elevate an electron located on the molecule and discharge has been reduced. Associated to each discharging peak, there is a jump in the $I-V$ curve, Fig.(2.10b), in which respectively steepens and shifts to lower energies upon approaching the tip. Another general trend in $I-V$ curves is the increase of the overall slope, diverging out by shrinking the tip-sample distance, which results in constant upshifts of the dI/dV spectra.

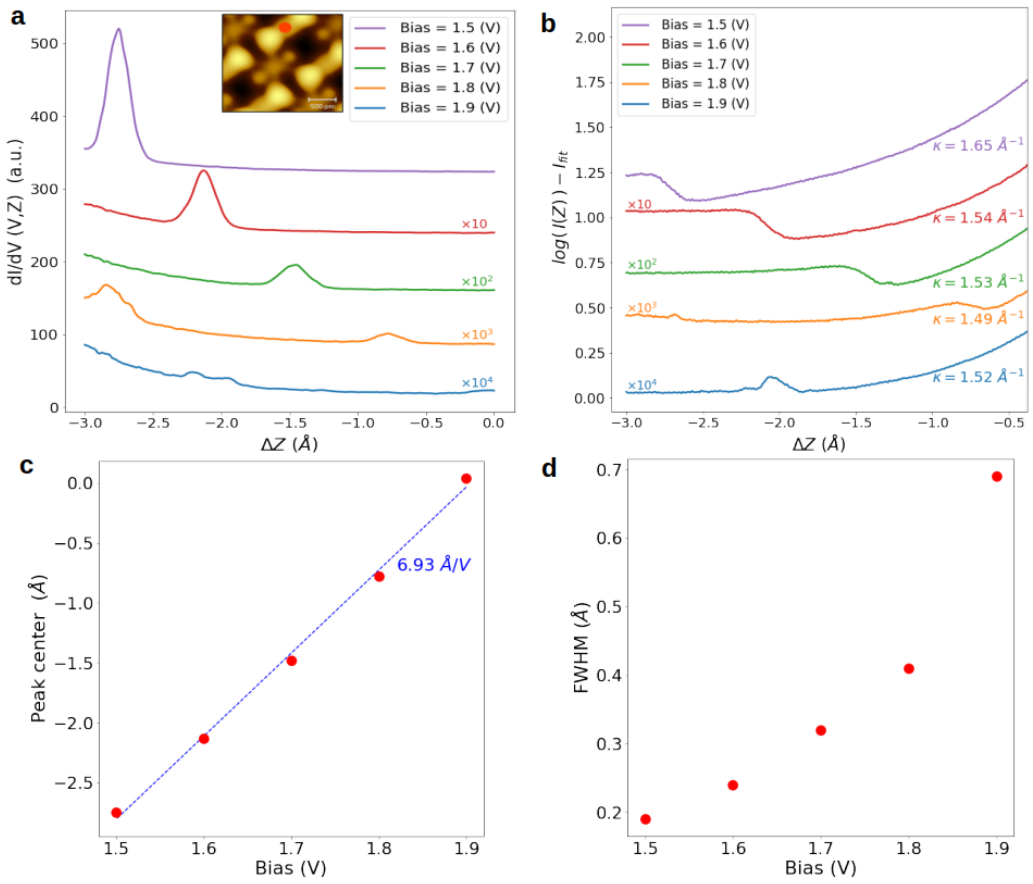

Figure 2.11: Bias-dependent dI/dV point spectra showing a linear approach of the discharging peak towards the Fermi level concomitant of sharpening of the resonance. a, $dI/dV(Z)$ spectra of consecutive measurements. **b,** Semilogarithmic plot of the corresponding $I-Z$ curves, $log(I-\delta I) = log(I_0) - \kappa z$, subtracted from a linear fit. The curved-up offset in the $I-Z$ curves is not physical and has an artificial instrumental cause created by Nanonis control system. All spectra are shifted by a constant for clarity. **c,** Compilation of the main discharging peak center with a linear fit (slope $1/\alpha = 6.93$ Å$/V$). **d,** Compilation of the main discharging peak FWHM with a quadratic fit. The measurements were performed with parameters: $V_b = 1.5 - 1.9$ V, $I_t = 2$ nA, $V_{mod} = 5$ mV, $T = 1.29$ K, $B = 0$ T. The inset STM image of panel **(a)** shows the parking position of the tip on top of the bright molecule center where measurements were executed.

With a similar method, the voltage dependence of the resonance can be studied via sweeping the tip-sample distance while keeping the bias constant. Evidently, in Fig.(2.11 a), the discharging peak shifts linearly towards the Fermi level as we successively reduce the bias. Furthermore, the FWHM of the peak drops from 0.7 to just below 0.2 Å, featuring position-localization of the resonance, and the corresponding $I - Z$ curves, Fig.(2.11 b), show deviation from a linear fit on a semilogarithmic plot by a broad step. Comparing the two methods mentioned above, the distance-dependent and bias-dependent STS, shows a perfect self-consistency among curves and their fit parameters.

2.4 Experimental procedure

The STM measurements of the NTCDA/Ag(111) systems were taken using a home-built combined scanning tunneling and atomic force microscope operating in ultrahigh vacuum ($p \leq 10^{-10}$ mbar), at fields perpendicular to the sample surface of up to 14 T, and at a base temperature of 1.2 K. The dI/dV spectra were acquired by modulating the bias voltage with a sinusoidal of $0.05-0.2$ mV amplitude and 617 Hz frequency employing a lock-in amplifier.

The tip conditioning was performed $in\text{-}situ$ using field emission with bias voltage between $100-150$ V and emission current between $3-6$ μA, and indentation of the bare Pt/Ir tip into a clean Ag(111) surface. The Ag(111) crystal was prepared by repeated cycles of Ar^+ sputtering and annealing to $250-300$ C° for 25 minutes.[5] Afterwards, NTCDA molecules were deposited onto the clean Ag(111) surface held at room temperature and a base pressure of $p \leq 10^{-9}$ mbar from a Knudsen cell molecule evaporator held at 215 C°.

2.5 Conclusion

I close this chapter by mentioning two remarks regarding the role of tip in the breakdown of local charge neutrality in the NTCDA/Ag(111) system; and roughly estimating a microscopic quantity, namely Pauli repulsion force, by extracting information from the previously discussed results. At positive bias, where discharging resonance occurs, the tip is negatively charged and, as a result, creates a positive image charge, i.e., a hole, on the sample. An ideally point-like tip creates a point-like hole, and a realistic tip with a nanometer size apex creates a nanoscale quantum dot. This hole can also be viewed as the migration of electrons in the sample from the area underneath the tip in response to its repulsive potential. Such imbalance of positive and negative charges around the molecule breaks the local charge neutrality. The created hole encourages an electron to tunnel from the tip and discharge it, i.e., electron doping of the sample by the tip, which results in a jump in the tunneling current, as displayed in Fig.(2.10b).

We stated earlier in this chapter that there is a contention in the fact that Kondo and discharging resonance happen on the same molecular orbital, as the former requires a strong coupling to the substrate and the latter decoupling. Considering the configuration of an

[5] Surface temperature measurement was performed by an infrared pyrometer.

adsorbed molecule may help us to reconcile the two effects and to extract a constant from measurements to estimate a microscopic quantity responsible for such concomitance. Based on Fig.(2.11d), the FWHM of the discharging peak drops from ≈ 0.7 to 0.2 Å along the z-axis, which, as I mentioned above, may be interpreted as a signal for reordering of charges at the Fermi level extending over many molecules at the largest bias (1.9 V) to being localized to a single molecule at the lowest bias (1.5 V).

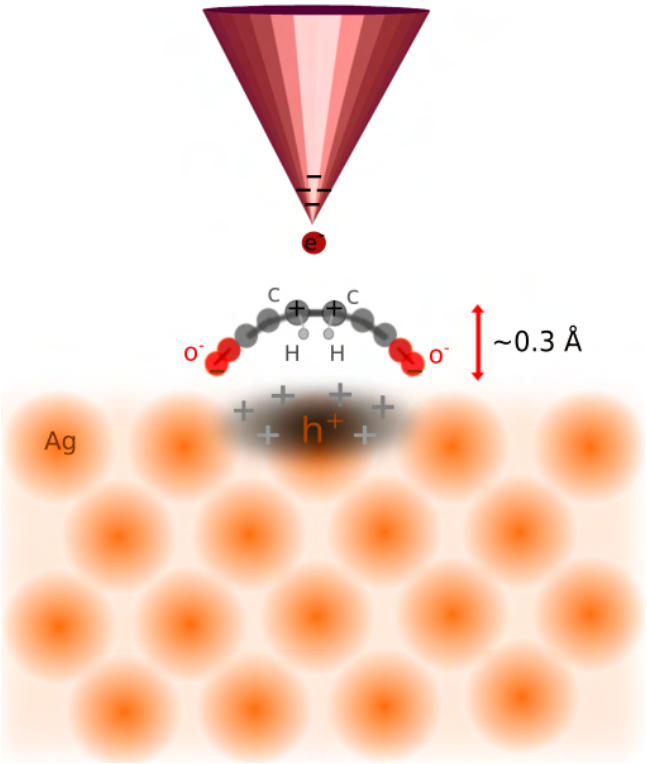

Figure 2.12: Cartoon illustrating the creation of an image charge (hole) and symmetry breaking in vicinity of a negatively charged STM tip.

The molecule does not adsorb entirely flat on the substrate. It is arched at the carbon rings [49, 56]. The Tab.(2.4) shows the DFT calculation and experimental result for the vertical adsorption distances of different elements of an individual NTCDA molecule on Ag(111) substrate. The shortest distance belongs to the acyl oxygen group (d_O^{acyl}) where the molecule forms a covalent bond with the substrate, and the longest belongs to the carbon rings (d_C) where discharging resonance occurs, the charge center of the molecule. Depending on the adopted method and adsorption geometry, the subtraction of these two vertical distances changes between $0.25 - 0.39$ Å. This vertical distance is the deviation of the molecule from a flat-lying configuration due to the Pauli repulsion [57, 58]. Principally, this should be the force providing the molecule with sufficient decoupling from the substrate to undergo a discharging resonance.

Config.	$\overline{d}_{all}$ (Å)[a]	d_C (Å)	d_O^{acyl} (Å)	d_O^{anhyd} (Å)	d_H (Å)	Method	Ref.
Isolated	2.86	2.94	2.66	2.88	2.82	DFT (Siesta)	[48]
Top_1	2.89, –	2.96, 3.01, 2.89	2.70, 2.69, 2.622	2.91, 2.85, 2.798	2.88, 2.91, –	DFT (Siesta, PBE-$D3_{PBC}$)	[48, 49, 56]
$Bridge_1$	2.86, –	2.94, 3.03, 2.905	2.65, 2.61, 2.577	2.90, 2.85, 2.806	2.84, 2.93, –	DFT (Siesta, PBE-$D3_{PBC}$)	[48, 49, 56]
Exp.	–	2.997	2.747	3.004	–	NIXSW	[78]

[a] Averaged over all elements.

Table 2.4: Compilation of vertical adsorption distances of NTCDA's elements in the r-ML phase.

With a series of cursory arguments, we can naively define the discharging force as the electrostatic force needed to bring a charge from below to the Fermi level. In principle, such force should overcome a threshold value to change the concentration of charge at the Fermi level $\left(|F_{\text{thresh}}| \leq |F_{\text{discharge}}|\right)$. Thus, the *minimum* required discharging force must satisfy the following condition

$$\vec{F}_{\text{discharge}} + \vec{F}_{\text{thresh}} = 0 \quad \rightarrow \quad \vec{F}_{\text{thresh}} = -\vec{F}_{\text{discharge}} \,.$$

In fact, we have access to the vertical component of the discharging force,

$$F^z_{\text{discharge}} = -\nabla_z U = -\frac{dU}{dz} \approx -\frac{\Delta U}{\Delta z} \,,$$

it is nothing but the slope (α) in the distance-dependent STS, or equivalently, $(1/\alpha)$ in the bias-dependent STS fitting curve:

$$\alpha = \frac{\Delta V}{\Delta z} = 0.15 \ \frac{\text{V}}{\text{Å}}$$

which we found in Fig.(2.10) and Fig.(2.11). Therefore, we can roughly estimate the microscopic threshold force along the z-axis as

$$F^z_{\text{thresh}} = -(-0.15 \ \frac{\text{eV}}{\text{Å}}) \,.$$

Now by considering the conversion factor $1\frac{\text{eV}}{\text{Å}} = 1.602$ nN, we obtain

$$\boxed{F^z_{\text{thresh}} \approx 240 \text{ pN}} \,.$$

As it will be clarified later, the *gating efficiency* renormalizes this force by more than an order of magnitude.

Chapter 3

Electric field driven quantum phase transition in a molecular Kondo lattice

The concept of quasiparticle (QP) is archetypal and ubiquitous to condensed matter physics, enabling the understanding of essential properties of the ground and lowest-lying excited states in otherwise inaccessible in many-body and strongly correlated electron systems. Its triumph encompasses a simple and accurate description of many solid-state materials such as normal metals, semiconductors, topological insulators, etc., and even with its failure in cases like the Kondo effect[15] and high-temperature superconductivity[79], the concept has remained as a guideline for the physicist. In this work, we drive the quasiparticle excitations (QPE) of a molecular Kondo lattice to the Fermi level by employing the local electric field of a scanning probe microscope (SPM) tip and simultaneously imaging them in real space. The tuning of such QPEs across the Fermi level with a non-thermal parameter leads to the change of the ground state, and hence, a quantum phase transition (QPT). Furthermore, our spectroscopic imaging of the Kondo lattice with sub-angstrom resolution reveals the creation of a real-space quasiparticle interference (QPI) pattern, in which we resolve hybridization gaps and superposition of the QPEs. To capture the underlying physics, we employ a tight-binding

model (TBM) to simulate the experimental results. Our study illuminates the understanding of fundamental excitations in low dimensional strongly correlated and topological materials.

To put into perspective the findings presented in this chapter, before discussing them, we first briefly review the basic concepts and models in strongly correlated physics. Moreover, to enhance the fluency of the reading, some of the experimental results and calculations that demands deeper analysis are further expanded in later chapters without harming the discussions here.

3.1 Single impurity Kondo effect

The Kondo effect is fundamentally a collective spin-screening process resulting in a strongly correlated many-body ground state generated by the quantum entanglement between a localized magnetic impurity (local moment) embedded on an itinerant non-magnetic (paramagnetic) fermionic bath. At high temperatures, the magnetic moment of the impurity remains uncorrelated in a paramagnetic phase. However, as the temperature is decreased below a characteristic scale, the so-called Kondo temperature (T_{K}), the local moment is quenched cooperatively by the spins of the itinerant electrons in the bath and eventually creates a many-body singlet, the so-called Kondo singlet [80]. Such a Kondo singlet enhances the scattering of the itinerant electrons and leads to an increase in their resistivity [81, 82].

The microscopic minimal model Hamiltonian was proposed in the seminal work of the Jun Kondo [83].

$$\mathcal{H}_{\mathrm{K}} = \sum_{\mathbf{k},\sigma} \varepsilon_{\mathbf{k}}\, c^{\dagger}_{\mathbf{k},\sigma} c_{\mathbf{k},\sigma} + J_{\mathrm{K}}\, \mathbf{S_d} \cdot \mathbf{s_c} \tag{3.1}$$

where $c^{\dagger}_{\mathbf{k},\sigma}$ and $c_{\mathbf{k},\sigma}$ creates and annihilates electrons in the non-interacting bath and the second term describes the antiferromagnetic exchange interaction ($J_{\mathrm{K}} > 0$) of the impurity spin ($\mathbf{S}$) with the spin of the itinerant electrons ($\mathbf{s_c}$). The single-site eigenstates and energies are

$$\begin{array}{lll}
\text{triplet} & \begin{cases} |\Uparrow\rangle_d\,|\uparrow\rangle_c \\ |\Downarrow\rangle_d\,|\downarrow\rangle_c \\ \frac{1}{\sqrt{2}}\left(|\Uparrow\rangle_d\,|\downarrow\rangle_c + |\Downarrow\rangle_d\,|\uparrow\rangle_c\right) \end{cases} & E = \frac{1}{4}J_{\mathrm{K}} \\
\text{doublet} & |\Uparrow\rangle_d\,|\uparrow\downarrow\rangle_c \text{ and } |\Downarrow\rangle_d\,|\uparrow\downarrow\rangle_c & E = 0 \\
\text{doublet} & |\Uparrow\rangle_d\,|0\rangle_c \text{ and } |\Downarrow\rangle_d\,|0\rangle_c & E = 0 \\
\text{singlet} & \frac{1}{\sqrt{2}}\left(|\Uparrow\rangle_d\,|\downarrow\rangle_c - |\Downarrow\rangle_d\,|\uparrow\rangle_c\right) & E = -\frac{3}{4}J_{\mathrm{K}}.
\end{array}$$

The lowest spin excitation from the ground state is obtained by breaking a singlet to form a triplet. The gap for this excitation is $\Delta_s = \frac{1}{4}J_{\mathrm{K}} - \left(-\frac{3}{4}J_{\mathrm{K}}\right) = J_{\mathrm{K}}$. The quasiparticle gap, which is the energy required to create a quasiparticle (electron-like or hole-like) via adding or removing an electron at the Fermi level by breaking the Kondo singlet is $\Delta_{qp} = 0 - \left(-\frac{3}{4}J_{\mathrm{K}}\right) = \frac{3}{4}J_{\mathrm{K}}$.

Developing a perturbative expansion in small J_{K} (up to the third order) for the electrical resistivity, Kondo reproduced the experimentally observed resistivity minimum and the

ensuing logarithmic divergence in dilute magnetic alloys [84].

$$\rho_{\text{imp}} = \frac{3\pi m J_{\text{K}}^2 S(S+1)}{2e^2\hbar\varepsilon_F}\left[1 - J_{\text{K}}\,\rho_c(\varepsilon_F)\ln\left(\frac{k_B T}{D}\right) + \mathcal{O}(J_{\text{K}}^3)\right] \tag{3.2}$$

where e is the electron charge, $\hbar$ is the reduced Planck constant, ε_F is the Fermi energy, m is the electron mass, S is the impurity's total spin, $\rho_c(\varepsilon_F)$ is the density of states of the itinerant electrons at the Fermi energy, and D is the bandwidth of the itinerant electrons.

At high temperatures, the coupling $J_{\text{K}}\,\rho_c(\varepsilon_F)$ is very small, and therefore, the expansion remains regular. However, when the temperature is decreased, the logarithmic corrections cause an increase in the resistivity and eventually diverge for $T \to 0$. The breaks down of the perturbation theory happen when the first and second term of the expansion becomes equal, which effectively defines a small fundamental scale for the single impurity problem, the so-called Kondo temperature [84].

$$T_{\text{K}} \sim D\, e^{-1/J_{\text{K}}\,\rho(\varepsilon_F)}\,, \tag{3.3}$$

which only relates to few material-dependent parameters. The essence of the problem roots in the spin-flip scattering of the itinerant electrons from the degenerate local quantum level, which becomes the dominant scattering channel below the Kondo temperature scale. Interestingly, even though the perturbative expansion diverges at the Kondo temperature, it does not produce a phase transition but rather a cross-over, indicating a smooth change from the paramagnetic local moment regime to the Kondo singlet phase. This behavior is encoded into the spin susceptibility of the impurity, which shows a $\chi \sim 1/T$ Curie-law behavior at high temperature and smoothly connects to a constant paramagnetic Pauli susceptibility $\chi \sim 1/T_{\text{K}}$ at low-temperature [84].

3.2 Anderson impurity model: interacting limits

The Kondo model Eq.(3.1) suffices to explain the Kondo effect by a priory assuming the spin-spin interaction at the E_{F} to be the cause, but it remains silent about why and how the spin of a local level which should be originally residing far below E_{F} shifts to it and elastically scatter off the electrons of the metallic host [80, 85]. It was only made clear after Friedel (1951&1956) showed that scattering of an impurity, modeled as a static potential with a finite depth below E_{F}, with itinerant electrons can create a virtual bound state with finite width near E_{F} [80, 86, 87]. The idea was employed to explain the d-electron resonance in transition metals. Building upon this, later Anderson (1961) proposed a model for the formation of a magnetic impurity in metal [85],

$$\mathcal{H} = \sum_{\mathbf{k},\sigma} \varepsilon_{\mathbf{k}}\, c^\dagger_{\mathbf{k},\sigma} c_{\mathbf{k},\sigma} + \sum_{\sigma} \varepsilon_d\, d^\dagger_\sigma d_\sigma + \sum_{\mathbf{k},\sigma} V\left(c^\dagger_{\mathbf{k},\sigma} d_\sigma + d^\dagger_\sigma c_{\mathbf{k},\sigma}\right) + U_d\, n_{d\uparrow} n_{d\downarrow} \tag{3.4}$$

which assumes that the localized d-electrons of the magnetic impurity located at ε_d below E_{F} have a sizeable on-site Coulomb repulsion (U_d) as a result of the confinement of their wave function. The local Hamiltonian

$$H_{\text{imp}} = \sum_{\sigma} \varepsilon_d\, d^\dagger_\sigma d_\sigma + U_d\, n_{d\uparrow} n_{d\downarrow}$$

with four local states $|0\rangle$, $|\Uparrow\rangle$, $|\Downarrow\rangle$, and $|2\rangle$, with bare energy levels 0, ε_d (doublet) and $2\varepsilon_d+U$, and also the hybridization (V) of these d-electrons with the itinerant Bloch electrons ($c_{\mathbf{k},\sigma}$), which shifts their bare energy level to the E_{F} and forms a renormalized band.

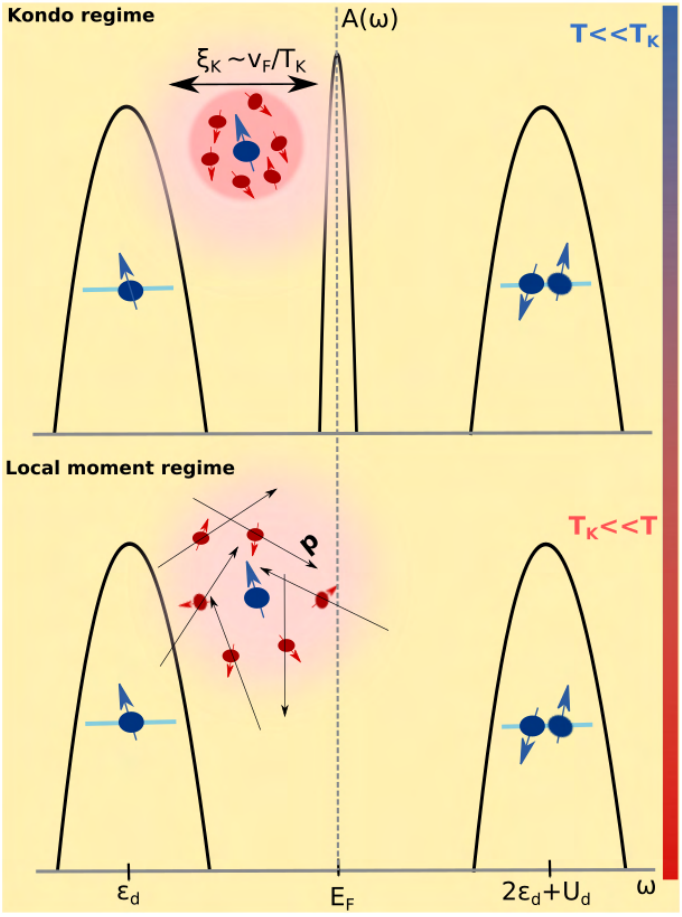

Figure 3.1: Cartoon illustrating the interaction limits of the Anderson impurity model. At high temperature and large Coulomb repulsion, the ground state is an unscreened local moment decoupled from fast-moving itinerant electrons. At temperatures below the characteristic Kondo temperature (T_{K}), the degenerate local moment hybridize with the itinerant electrons and forms coherent, long-lived quasiparticles, amounting to a resonance near the Fermi level with a spatial extension determined by the Kondo screening cloud given by $\xi_{\mathrm{K}} \equiv \hbar v_{\mathrm{F}}/k_B T_{\mathrm{K}}$ [88, 89], where v_{F} is the Fermi velocity.

Even in its infancy age, the model could successfully describe different regimes of the impurity problem. Initially, Anderson performed a Hartree-Fock mean-field theory on the model [85], and showed that a doubly-degenerate local moment ($|\Uparrow\rangle$, $|\Downarrow\rangle$) is the ground state of the high energy sector of the Hamiltonian, and can be self-consistently generated in the limit that bare energy level $|\varepsilon_d|$ and the Coulomb interaction ($\pi\rho_c(\varepsilon_F)V^2 \leq U_d$) are the dominant scales of the problem [90]. This is the limit where spin excitations are generally neglected. Later, it was shown that the original Kondo model Eq.(3.1) lives in the low energy sector of the Anderson impurity model, where charge excitations are completely gaped, and its Kondo singlet ground state can be accessed by the Schrieffer-Wolff transformation [80,

91], which accounts the Kondo exchange coupling to

$$J_{\mathrm{K}} = V^2 \left(-\frac{1}{\varepsilon_d} + \frac{1}{\varepsilon_d + U_d} \right). \tag{3.5}$$

At this low energy scale, the Coulomb interaction is relatively small. The impurity level is partially occupied with spin-up and spin-down electrons, and the ground-state is a paramagnetic Fermi liquid. In this limit, coherent spin fluctuations dominate the physics of the system and lead to a formation of a new bound-state near E_{F}. This amounts to a peak in the density of states of the itinerant electron, which is called the Abrikosov-Suhl (Kondo) resonance [92, 93]. The width of this resonance determines the Kondo temperature scale in the particle-hole symmetric Anderson impurity model as

$$T_{\mathrm{K}} = \sqrt{\frac{2U_d\Gamma}{\pi^2}}\, e^{-\frac{\pi U_d}{8\Gamma}} \tag{3.6}$$

where $\Gamma = \pi\rho_c(\varepsilon_F)V^2$ is the hybridization strength [80, 94, 95].

3.3 Resonant level model

The non-interacting limit ($U_d = 0$) of the Anderson impurity model Eq.(3.4) has a simple and interesting physics. Historically it is called the resonant level model [80, 96]

$$\mathcal{H}_{\mathrm{RLM}} = \sum_{\mathbf{k},\sigma} \varepsilon_{\mathbf{k}}\, c^\dagger_{\mathbf{k},\sigma} c_{\mathbf{k},\sigma} + \sum_{\sigma} \varepsilon_d\, d^\dagger_\sigma d_\sigma + \sum_{\mathbf{k},\sigma} \left(V\, c^\dagger_{\mathbf{k},\sigma} d_\sigma + V^*\, d^\dagger_\sigma c_{\mathbf{k},\sigma} \right). \tag{3.7}$$

It describes scattering between a non-interacting local level (d) and a lattice of itinerant electrons (c) by a hybridization (tunneling) amplitude (V).

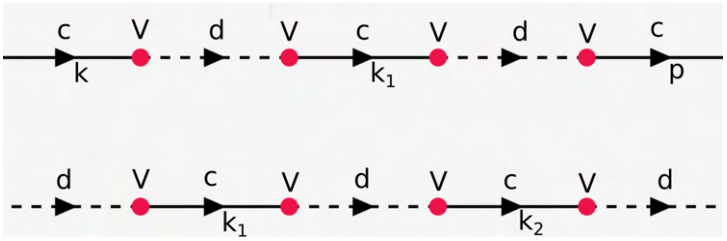

Figure 3.2: Feynman diagram for the local (d) and itinerant electrons (c) in the resonant level model. (adapted from [80])

Despite the fact that the translational invariance of the lattice is lost due to the presence of the local level, the model can be exactly solved. This can be done by summing all Feynman diagrams in powers of hybridization, Fig.(3.2), to obtain the single-particle Matsubara Green's function of the local level

$$G_d^{-1}(i\omega_n) = i\omega_n - \varepsilon_d - \Sigma_c(i\omega_n) = i\omega_n - \varepsilon_d - \frac{1}{V_{\mathrm{BZ}}} \sum_{\mathbf{k}} \frac{|V|^2}{i\omega_n - \varepsilon_{\mathbf{k}}} \tag{3.8}$$

where we used the c-electron self-energy $\Sigma_c(i\omega_n) = \frac{1}{V_{\mathrm{BZ}}}\sum_{\mathbf{k}} \frac{|V|^2}{i\omega_n - \varepsilon_{\mathbf{k}}}$.
Now by converting the discrete momentum sum to integration using the c-electron density of states, we obtain

$$G_d^{-1}(i\omega_n) = i\omega_n - \varepsilon_d - \int d\varepsilon \, \frac{\rho_c(\varepsilon)|V|^2}{i\omega_n - \varepsilon}.$$

This integral contains a branch cut along the real axis. It can be simply taken out if we approximate the density of the states of the itinerant electrons by its value at the Fermi level, $\rho_c(\varepsilon_F)$, and performing an analytic continuation $(i\omega_n \to \omega + i\eta)$. It gives the retarded Green's function as

$$G_d^{\mathrm{R}}(\omega) = \frac{\Gamma}{\omega - \tilde{\varepsilon_d} + i\Gamma \mathrm{sgn}(\omega)}$$

where we have restricted the integral to the bandwidth (D) of c-electrons, and also used the fact that the real part of the c-electron self-energy has a negligible frequency dependence, which merely renormalizes the bare local level $(\tilde{\varepsilon_d} = \varepsilon_d + \mathrm{Re}\Sigma_c(\omega))$. In this way, the density of states on the local level is a Lorentzian peak of width Γ

$$\rho_d(\omega) = -\frac{1}{\pi}\mathrm{Im}G_{d,\sigma}^{\mathrm{R}}(\omega) = \frac{1}{\pi}\frac{\Gamma}{(\omega - \tilde{\varepsilon_d})^2 + \Gamma^2}$$

which describes the d-electron on the local level with the renormalized energy $\tilde{\varepsilon_d}$ and lifetime of $1/\Gamma$, as it tunnels coherently into the itinerant electrons band (continuum).

3.4 Kondo lattice system: Doniach's phase diagram

The extension of the single-impurity Kondo problem to a lattice of impurities brings us to the concept of the Kondo lattice model (KLM). In its simplest form, the KLM describes a lattice of spin-$1/2$ magnetic moments coupled antiferromagnetically via the Kondo exchange coupling J_{K} to a single band of itinerant electrons at each lattice site.

$$\mathcal{H}_{\mathrm{KLM}} = \sum_{i,j}\sum_{\sigma} t_c \, c_{i,\sigma}^{\dagger} c_{j,\sigma} + J_{\mathrm{K}} \sum_i \mathbf{S_d}(\mathbf{x_i}) \cdot \mathbf{s_c}(\mathbf{x_i}), \tag{3.9}$$

where the spin operators are represented in terms of fermionic operators and Pauli matrices as

$$\mathbf{S_d}(\mathbf{x_i}) = \frac{1}{2}\sum_{\alpha,\alpha'} d_{\alpha}^{\dagger}(\mathbf{x_i})\sigma_{\alpha,\alpha'}d_{\alpha'}(\mathbf{x_i}) \quad \text{and} \quad \mathbf{s_c}(\mathbf{x_j}) = \frac{1}{2}\sum_{\alpha,\alpha'} c_{\alpha}^{\dagger}(\mathbf{x_j})\sigma_{\alpha,\alpha'}c_{\alpha'}(\mathbf{x_j}).$$

Like the single impurity version, the KLM also forbids charge fluctuations of the d-electrons and strictly enforces single-occupancy at each lattice site. Even though the physics of the single impurity Kondo problem is well established, the KLM still poses a challenge, theoretically and experimentally, even after more than half a century since its original conception [97–101]. As Doniach depicted the KLM's physics [102], the core of the problem underlies the presence of two competing energy scales: The Kondo temperature, which, as mentioned before, is associated with the screening of impurity spins and the formation of a Kondo singlet at each lattice site, and additionally, a new energy scale, under which the local moments tend to order and destroy the singlets.
In the lattice problem, the magnetic polarisation of the c-electron around a local moment

can couple to the neighboring local moments leading to an effective long-range interaction between them. This interaction is called Ruderman-Kittel-Kasuya-Yosida (RKKY) interaction [103–105],

$$\mathcal{H}_{\mathrm{RKKY}} = \sum_{i,j} I_{\mathrm{RKKY}}(\mathbf{x_i} - \mathbf{x_j})\, \mathbf{S_d}(\mathbf{x_i}) \cdot \mathbf{S_d}(\mathbf{x_j}) \tag{3.10}$$

and is associated with the ordering energy scale. Generally, the RKKY scale dominates at the weak Kondo exchange coupling and is the driving force for the observed continuous quantum phase transitions between an antiferromagnetic phase and a Kondo screened state in Doniach's picture. More specifically, in this picture, Fig.(3.4), for a small Kondo coupling, the RKKY interaction dominates, and an antiferromagnetic ground state is favored below a critical temperature. With increasing the Kondo coupling, the spin screening enhances, ultimately prevails the RKKY coupling, and the ground state transforms to a paramagnetic Fermi liquid phase comprised of the Kondo singlets. Interestingly, for temperatures higher than the lattice Kondo temperature (T_{K}^{*}), there is another regime where the singlets dissolve into free spins (paramagnet). In between these phases, particularly when the energy scales of the Kondo and RKKY couplings are proportionate, there is a quantum critical point (QCP), with non-Fermi liquid behavior [106–112].

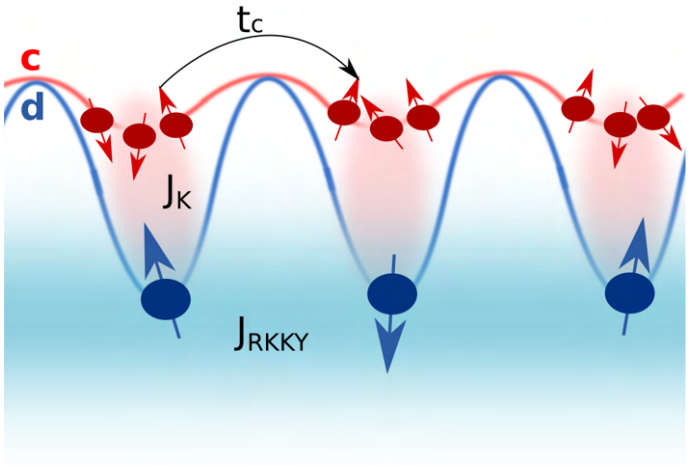

Figure 3.3: Cartoon illustrating the coupling scheme of a Kondo lattice. The lattice Kondo effect is produced by the quantum fluctuations between c-electrons and degenerate spin states (d-electrons) near the Fermi surface that constantly hybridize to form a Kondo singlet, which develops coherence with other singlets in the lattice. The coherence can be suppressed by the presence of a magnetic instability, e.g., RKKY interaction, that favors ordering the spins and destroying the Kondo singlets.

Such a magnetic quantum phase transition has been observed in various heavy fermion materials, with even more complicated phase diagrams, such as the celebrated $YbRh_2Si_2$ [113], and also in $YbRh_2(Si_{1-x}Ge_x)_2$ [114], $CeRh_{1-x}Co_xIn_5$ [115], $CePd_2Si_2$ [116], $Ce_{1-x}La_xRu_2Si_2$ [117], $CeIn_3$ [116], $CeCu_{6-x}Au_x$ [118], etc. Experimentally, the QPT is tuned by changing the Kondo coupling via non-thermal control parameters such as by applying pressure, chemical doping, an external magnetic field, or as we will show later in this thesis, an applied electric field which can effectively dope the lattice an drive the transition.

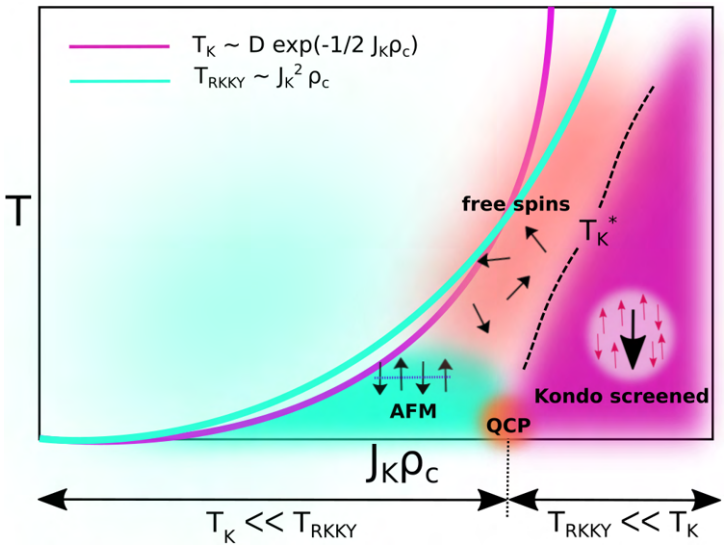

Figure 3.4: Doniach's phase diagram for the quantum phase transition between an antiferromagnetic phase and a Kondo screened phase (Fermi liquid), with free spins regime (paramagnet) and quantum critical point $(T = 0)$ in between. (Figure adapted from [106])

3.5 Periodic Anderson model: the slave-boson mean-field theory

An alternative way to study heavy fermion systems and Kondo lattice is provided by the periodic Anderson model (PAM), which captures both charge and spin degrees of freedom of the f-electrons, unlike KLM that regards only the spin dynamics[1]. Similar to its single impurity version, Sec.(3.2), PAM describes how local moments form in a lattice as a result of a strong Coulomb repulsion which blocks charge fluctuation and electron transport at the local level. It also describes how a Kondo resonance occurs as a virtual bound state resonance at the Fermi level due to the tunneling process between the itinerant and local band. The PAM Hamiltonian is

$$\mathcal{H}_{\text{PAM}} = \mathcal{H}_c + \mathcal{H}_{hyb} + \mathcal{H}_d \tag{3.11}$$

where the conduction electrons have a nearest-neighbor hopping

$$\mathcal{H}_c = -\sum_{<i,j>}\sum_{\sigma} t_c \left(c^{\dagger}_{i,\sigma} c_{j,\sigma} + h.c.\right) - \sum_{i,\sigma} \mu\, c^{\dagger}_{i,\sigma} c_{i,\sigma}$$

and an on-site hybridization with the local levels

$$\mathcal{H}_{hyb} = \sum_{i,\sigma} \left(V\, c^{\dagger}_{i,\sigma} d_{i,\sigma} + V^*\, d^{\dagger}_{i,\sigma} c_{i,\sigma}\right).$$

[1] Similar to the single impurity Kondo problem, the ground state of the KLM can be derived from the PAM via a Schrieffer-Wolff transformation. In this way, the KLM coupling parameter is related to the PAM parameters as $J \sim \frac{V^2}{U}$ [119]. We recognize that the large U limit of the PAM is equivalent to the small J limit of the KLM.

The local levels have a nearest-neighbor hopping and also Coulomb interaction,

$$\mathcal{H}_d = \sum_{i,\sigma} \varepsilon_d \, d^\dagger_{i,\sigma} d_{i,\sigma} - \sum_{<i,j>} \sum_{\sigma} t_d \left(d^\dagger_{i,\sigma} d_{j,\sigma} + h.c. \right) + \sum_i U_d \, n_{d,i,\uparrow} n_{d,i,\downarrow}$$

where $d^\dagger_{i,\sigma}$ and $d_{i,\sigma}$ are the creation/annihilation operators for the 'physical' $4f$-fermions, and $c^\dagger_{i,\sigma}$ and $c_{i,\sigma}$ for the itinerant band.

To qualitatively layout the low energy physics of PAM, let's restrict the discussion to the infinite-U regime[2] of a $4f$ system, where double-occupancy at the local levels is forbidden, and the coherent charge fluctuations occur between the following valence configurations [80]

$$f^0 + e^- \rightleftharpoons f^1.$$

Here, we can regard the intermediate state as an exchange boson, and use the auxiliary particle method (slave-boson representation) to decompose the physical operator $(d^\dagger_{i,\sigma})$ into the product of a pseudofermion $(|f^1, \sigma\rangle = f^\dagger_\sigma |0\rangle)$ and a slave-boson $(|f^0\rangle = b^\dagger |0\rangle)$ as $d^\dagger_{i,\sigma} = f^\dagger_{i,\sigma} b_i$. Subsequently, we define the conserved charge at each site $\mathcal{Q}_i = n_{f,i} + n_{b,i} = \sum_{\sigma=\uparrow,\downarrow} f^\dagger_{i,\sigma} f_{i,\sigma} + b^\dagger_i b_i$, and let the slave-bosons b_i measure the deviations of the valence state from its maximum charge. At this step, a simplification can be made by considering a (spurious) slave-boson condensation and applying a mean-field treatment (slave-boson mean-field theory [120]), which demands that the average value of the slave-boson operator is static over the unit cell $\langle b_i \rangle \to b_i$. The consequence is the following renormalizations: the Kondo resonance width, which scales by the hybridization, narrows around the Fermi energy $V \to \tilde{V} = bV$ and the dispersion of the f-electrons flattens $\varepsilon^f_{\mathbf{k}} \to \tilde{\varepsilon}^f_{\mathbf{k}} = b^2 \varepsilon^f_{\mathbf{k}}$ for $b < 1$. Furthermore, by imposing a non-holonomic constraint on the average charge per lattice site $(\langle \mathcal{Q}_i \rangle \leq 1)$ with a Lagrange multiplier (λ_i),

$$\mathcal{H}_\mathcal{Q} = \sum_i \lambda_i (\mathcal{Q}_i - 1) \tag{3.12}$$

we can forbid the double-occupancy on the f-level and arrive at the following single-particle mean-field Hamiltonian for the infinite-U PAM

$$\overline{\mathcal{H}} = \sum_{\mathbf{k},\sigma} \begin{bmatrix} c^\dagger_{\mathbf{k},\sigma} \\ f^\dagger_{\mathbf{k},\sigma} \end{bmatrix}^T \begin{bmatrix} \varepsilon^c_{\mathbf{k}} - \mu & \tilde{V} \\ \tilde{V}^* & \tilde{\varepsilon}^f_{\mathbf{k}} + \lambda \end{bmatrix} \begin{bmatrix} c_{\mathbf{k},\sigma} \\ f_{\mathbf{k},\sigma} \end{bmatrix} + N_f \lambda (b^2 - Q), \tag{3.13}$$

where $N_f = \sum_i n_{f,i}$ and we have also used the translation invariance property of the PAM to set

$$b_i \to b \quad \text{and} \quad \lambda_i \to \lambda,$$

and Fourier transformed the operators to momentum space $\left(f^\dagger_{\mathbf{k},\sigma} = \frac{1}{N_f} \sum_i f^\dagger_{i,\sigma} e^{\mathbf{k}\cdot\mathbf{x}_i} \right)$. Thus, the problem reduced to solving two self-consistent saddle-point equations for b and λ

$$\begin{cases} \langle \frac{\delta \overline{\mathcal{H}}}{\delta b} \rangle = 0 \to & \frac{1}{N_f} \sum_{\mathbf{k},\sigma} V \left(\langle c^\dagger_{\mathbf{k},\sigma} f_{\mathbf{k},\sigma} \rangle + \langle f^\dagger_{\mathbf{k},\sigma} c_{\mathbf{k},\sigma} \rangle \right) - \frac{1}{N_f} \sum_{\mathbf{k},\sigma} 2\, b\, \varepsilon^f_{\mathbf{k}} \langle f^\dagger_{\mathbf{k},\sigma} f_{\mathbf{k},\sigma} \rangle + 2\lambda b = 0 \\ \\ \langle \frac{\delta \overline{\mathcal{H}}}{\delta \lambda} \rangle = 0 \to & \frac{1}{N_f} \sum_{\mathbf{k},\sigma} \langle f^\dagger_{\mathbf{k},\sigma} f_{\mathbf{k},\sigma} \rangle + b^2 - Q = 0, \end{cases} \tag{3.14}$$

[2] This is the Kondo regime of the PAM.

which should be closed by the constraint enforced on the average charge per site $\langle \mathcal{Q} \rangle \leq 1$. In this way, at the saddle point, the f-electrons turns into a single-particle Hamiltonian of hybridized quasiparticles $(\gamma^{\dagger}_{\mathbf{k},\sigma}\,,\, \eta^{\dagger}_{\mathbf{k},\sigma})$

$$\gamma^{\dagger}_{\mathbf{k},\sigma} = u_{\mathbf{k}} c^{\dagger}_{\mathbf{k},\sigma} + v_{\mathbf{k}} f^{\dagger}_{\mathbf{k},\sigma}\,, \quad \eta^{\dagger}_{\mathbf{k},\sigma} = -v_{\mathbf{k}} c^{\dagger}_{\mathbf{k},\sigma} + u_{\mathbf{k}} f^{\dagger}_{\mathbf{k},\sigma} \quad \rightarrow \quad |\gamma_{\mathbf{k},\sigma}|^2 + |\eta_{\mathbf{k},\sigma}|^2 = 1,$$

with renormalized eigenvalues

$$E^{\pm}_{\mathbf{k}} = \frac{\varepsilon^{c}_{\mathbf{k}} + \tilde{\varepsilon}^{f}_{\mathbf{k}} + \lambda}{2} \pm \left[\left(\varepsilon^{c}_{\mathbf{k}} - \tilde{\varepsilon}^{f}_{\mathbf{k}} - \lambda \right)^2 + \tilde{V}^2 \right]^{1/2} \tag{3.15}$$

and eigenvectors

$$u_{\mathbf{k}},\, v_{\mathbf{k}} = \left[\frac{1}{2} \pm \frac{(\varepsilon^{c}_{\mathbf{k}} - \tilde{\varepsilon}^{f}_{\mathbf{k}} - \lambda)/2}{2\sqrt{(\varepsilon^{c}_{\mathbf{k}} - \tilde{\varepsilon}^{f}_{\mathbf{k}} - \lambda)^2 + \tilde{V}^2}} \right]^{1/2}. \tag{3.16}$$

Here, without loss of generality, we fixed the chemical potential to the Fermi level $(\mu = 0)$ and absorbed the bare f-level (ε^{f}) into its renormalized dispersion $(\tilde{\varepsilon}^{f}_{\mathbf{k}})$. In the case when the Fermi level lies inside the gap $\left(\Delta(\mathbf{k}) = E^{+}_{\mathbf{k}} - E^{-}_{\mathbf{k}}\right)$, a Kondo insulator is formed, and otherwise a correlated metal [80].

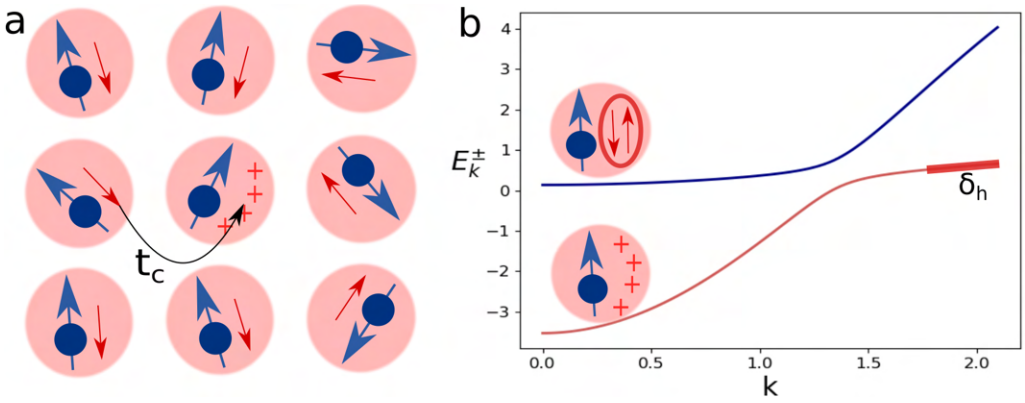

Figure 3.5: Quasiparticles of a Kondo insulator. **a** The cartoon illustrates how hole-doping a Kondo insulator at the strong coupling limit breaks a Kondo singlet, forming a hole quasiparticle, and opens a transport channel for the conduction electrons. (b) Electron and hole quasiparticle dispersion $(E^{\pm}_{k})$ of a Kondo insulator. The chemical potential of a Kondo insulator resides inside the narrow quasiparticle gap by holding 2 particles per site on average, and hence, it gives rise to no Fermi surface. A tiny amount of hole (δ_h) shifts the chemical potential downwards, leading to the crossing of the quasiparticle bands and amounts to a large Fermi surface with 2-δ_h electrons. The renormalized bands in (b) are obtained for $b = 0.63$, $\lambda = 0.28$ as the self-consistent solutions of the saddle-point equations, Eq.(3.14), for parameters: $T/D = 10^{-4}$, $V/D = 0.3$, and $t_f/D = 0.1$, where D is the bandwidth of the conduction electrons. (Adapted from [80])

3.6 The NTCDA Kondo Lattice: a heuristic picture

The paradigmatic understanding of the Kondo lattice and its QPT, developed in the last sections, has taken for granted the fact that there is a well-defined localized spin-$\frac{1}{2}$ atomic band with almost no spatial extension. This picture may need to be revised in the case of the molecular Kondo lattice where singly-occupied states host $\pi-$electrons with orbitals delocalized over several angstroms and directly and indirectly overlap with the neighboring electrons. Moreover, unlike above, where the conduction band comprises s-orbital electrons, the character of the itinerant electrons in many substrate-mediated molecular Kondo lattices is not fixed and, in fact, is a mixture of bulk and interface state electrons present at the surface of the substrate. This makes the expectation of a simple, well-defined local band under the Fermi level of a molecular Kondo lattice unrealistic. Here, we will investigate the fundamental scales of the NTCDA Kondo lattice and a few of its properties.

Observation of Kondo resonance on the self-assembled monolayer of 1,4,5,6-naphthalene tetracarboxylic acid dianhydride (NTCDA) on Ag(111) substrate [17] provided us with a playground to study the rich properties of electronic states and their excitations in the context of strongly correlated physics. As we have seen in Ch.(2), the NTCDA relaxed monolayer (r-ML) creates an atomically precise, highly organized 2D lattice of π-conjugated electrons. The molecules configure arrays of alternating bright and dark chains with drastically different properties, Fig.(3.6). On the bright chain, the molecules show a Kondo temperature of $T_{\mathrm{K1}} \sim 132\,\mathrm{K}$, and on the dark one $T_{\mathrm{K2}} \sim 350\,\mathrm{K}$. We relate the noticeable difference in the Kondo temperature of the two molecules to their different molecule-substrate distances. Generally, a shorter distance results in a larger hybridization between the local electron at the molecule with the conduction electrons of the substrate, giving a higher Kondo temperature and also a topographically darker appearance.

A noteworthy observation is the dramatic modification of the Kondo scale, from weak to the strong coupling limit, upon the formation of the lattice. As T. Esat and R. Temirov have shown[3], the single-ion Kondo temperature of an isolated NTCDA molecule on Ag(111) is much lower than the experimental temperature, and hence, no Kondo resonance appears at the Fermi level.

Moreover, at the summit of the Kondo peaks, we observed magnetic-dependent fine structures (see Fig.(2.7) and F.(2.8)), more pronounced on the dark molecules, that we relate to the inter-molecular magnetic interactions. These interactions are relatively long-ranged, mediated mainly by the LUMO of the molecules which have large ligands, and also, to a lower extent, by the residual surface states of the substrate[4]. We call it RKKY-like interaction[5] and assign a roughly $\tilde{J}_{\mathrm{RKKY}} \sim 7$ meV to it (see Sup.(A.1) for further information). This interaction induces magnetic instability, which decoheres the Kondo singlets formed

[3] Private communication.

[4] The silver substrate surface state is primarily destroyed and shifted in energy upon formation of the lattice (see Sec.(2.3.2)).

[5] We chose the name RKKY-like interaction to resemble the nomenclature in the KLM, but there is no necessity for it to take the same character as the original RKKY interaction. Realistically, this interaction can take a very complicated form in a molecular Kondo lattice.

at each lattice site, and as a result, produces depression of the density of states or a dented Kondo peak at the Fermi level, Fig.(3.6c top-inset). The depression of the density of states (pseudogap), which is associated with the strength of this interaction, does not turn into a full-fledged gap, essentially because of the strong background scattering with the metallic substrate and also due to the dominating Kondo scale on the molecules.

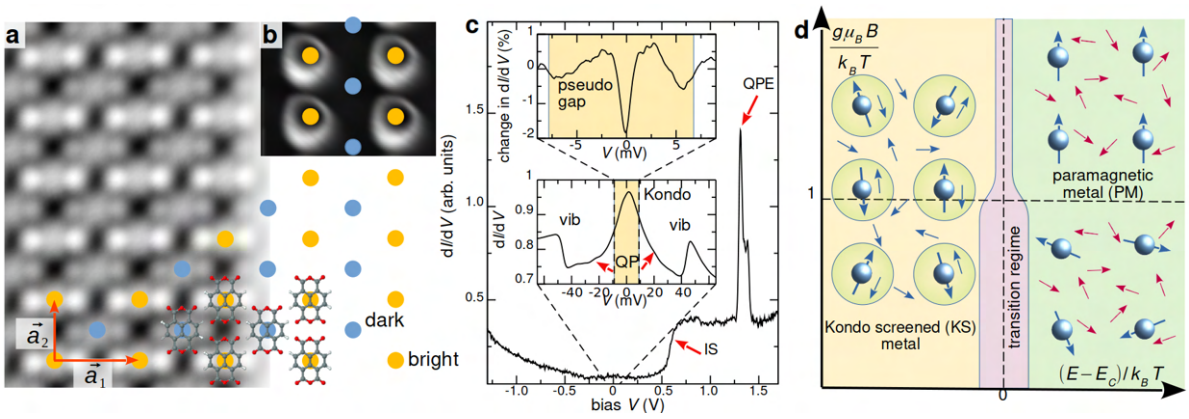

Figure 3.6: The molecular Kondo lattice. **a,** Constant-current gray-scale STM image ($V_b = 48\,\text{mV}, I_t = 1\,\text{nA}$) of a monolayer of NTCDA molecules on Ag(111) showing a brick-wall like structure consisting of molecules with higher (brighter) and lower (darker) appearance (yellow and blue circles, respectively). The apparent height difference is ≈ 30 pm. Superimposed are stick-and-ball models of the molecules and the lattice basis vectors $\mathbf{a_1}$ and $\mathbf{a_2}$ with lengths 1.5 and $1.16\,\text{nm}$. **b,** Constant-current gray-scale differential conductance (dI/dV) image measured at higher bias (setpoint: $V_b = 1.4\,\text{V}$, $I_t = 6\,\text{nA}$, $V_{\text{mod}} = 8\,\text{mV}$) reveals ring-like structures centered at each bright molecule. **c,** Differential conductance dI/dV spectrum (setpoint: $V_b = 2\,\text{V}$, $I_t = 4\,\text{nA}$, $V_{\text{mod}} = 8\,\text{mV}$) measured with the tip of the STM positioned above the center of a bright molecule (yellow dots) shows three prominent features: The interface state of the Ag(111) surface (IS), and a sharp peak at about $1.3\,\text{V}$ (QPE) which is at the origin of the ring-like structures seen in panel (b). The two insets show over the lattice averaged dI/dV spectra at biases close to the Fermi energy E_{F}. They reveal formation of a pseudogap at E_{F}, and also strong molecular vibrational modes (vib), a Kondo resonance and quasi-particle states (QP) introduced by the Kondo lattice. **d,** Schematic phase diagram of the Kondo lattice versus applied electric ($\mathbf{E}$) and magnetic ($\mathbf{B}$) field scaled by temperature. The Kondo screened (KS) metallic phase exists at low $\mathbf{E}$- and $\mathbf{B}$-field and undergoes a quantum phase transition to a paramagnetic metallic (PM) phase constituting free spins by tuning $\mathbf{E}$ and $\mathbf{B}$. The width of the transition regime (red area) where fluctuations dominates the system narrows by the applied $\mathbf{B}$-field. A quantum critical point expected to exist at the point where all phases merge at zero temperature.

The most outstanding spectroscopic feature of the NTCDA Kondo lattice is the prominent peak with a small shoulder at $V_b \sim 1.3\,\text{V}$, Fig.(3.6c), labeled as quasiparticle excitation (QPE). This peak shows up as ring-like feature in dI/dV maps at higher positive biases and can be obtained at the center of bright molecules while being irreproducible at the dark

ones and also at negative biases[6]. To understand the nature of this peak, we should remind that *ab initio* calculations of an isolated NTCDA on the Ag(111) predict partial occupation of the LUMO, close to a single-occupancy [49, 56]. This is also reflected in the Kondo peak, which is just by 2.7 meV off the E_{F} [17]. These observations bring us to an important conclusion that a moderate tip-induced electric field cannot lift the LUMO, which is located at $E_{\mathrm{LUMO}} \sim -0.5\,\mathrm{eV}$ all the way to E_{F}. This is a stark distinction from the systems studied in back-gated setups, which can compensate for this huge energy difference. Another scenario compatible exclusively with the impurity studies is to assume a single-particle level or a bound-state very close to E_{F}, associated with the impurity. This scenario is also ruled out in the NTCDA case by the DFT calculations and also experimentally by us, our collaborators, and also former studies on the NTCDA as no single-particle level or a bound-state is reported to exist near E_{F}. And finally, we disregard scenarios including a simple band-bending/lifting of the NTCDA LUMO state. This can be simply understood by considering that the NTCDA LUMO is a very broad satellite with a tail crossing the E_{F}, sitting 'directly' on Ag(111), which is a bath of free electrons. A continuous lifting of such a state should result in a fractional change in the density of states and not a sharp monumental peak in the differential conductance. We, therefore, more intuitively, explain it in the following in terms of charge quasiparticle excitations (QPE) of the Kondo lattice.

3.7 Electric field driven quantum phase transition

As explained in Sec.(3.1), below the Kondo temperature, the bare energy of the local electrons (ε_f), which was originally buried deep below E_{F} (typically in eV-order), shifts towards E_{F} (by amount λ) and forms a localized quasiparticle band there. As we have shown in our single-site analysis, Sec.(3.1), the low-lying charge excitation of such a quasiparticle state can be introduced in terms of breaking of a Kondo singlet via adding or removing an electron, which requires an energy of $\frac{3}{2}J_{\mathrm{K}}$. Following this scheme, in our measurement, we first demonstrated that the QPE has a discharging character[7] and its energy linearly depends on the applied electric fields (see Fig.(2.10) and Fig.(2.11)). More explicitly, we employ the tip's local electric field to wash away electrons at the molecule site and effectively hole-doping it. This, in turn, breaks the Kondo singlet and opens a lateral transport channel in the lattice, which lead to a step in the current channel, or equivalently, a sharp peak in the differential conductance. This process involves a change of ground state via tuning a non-thermal parameter (E-field) at a fixed temperature, and hence a QPT from a Kondo screened state to a state with unscreened spins.

The hallmark of such a QPT is imprinted on the magnetic properties of the initial and final states. As emphasized before, the Kondo peak of the bright molecule has a width of 28.5 meV, that even up to 14 T applied B-fields it remains intact, indicating a typical Pauli paramagnetic behavior deep in the Kondo regime. This behavior is in marked contrast with that of the QPE — for it dramatically sharpens with the applied B-field, Fig.(3.7f). Such behavior in the $B-T$ diagram can be seen as the freezing of the spin degree of freedom, that can be

[6] Using a bias voltage range that does not damage the lattice.

[7] We have used interchangeably the term 'discharging peak' for the QPE throughout this thesis.

oriented in every direction in the absence of the B-field and is polarized to the direction of the B-field as it is increased, which subsequently leads to the suppression of the thermal fluctuations.

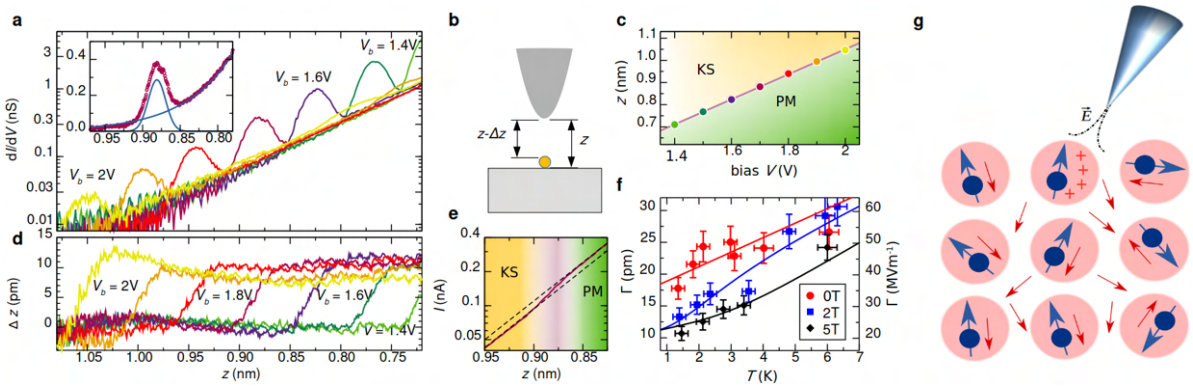

Figure 3.7: Signatures of the quantum phase transition. **a,** Logarithmic plot of the $dI/dV(z)$ signal above a bright molecule at constant V_b ranging from $1.4-2.0\,\mathrm{V}$ ($T = 1.4\,\mathrm{K}$, $B = 5\,\mathrm{T}$). The peaks mark the phase transition between the Kondo screened (KS) state and the paramagnetic metallic (PM) state. The inset shows exemplarily the $V_b = 1.7\,\mathrm{V}$ data in a linear plot and the corresponding least-squares fit of the data to the sum of an exponential and a Gaussian. **b,** Model of the effective tip-sample tunneling barrier z and its change to $z+\Delta z$. **c,** The extracted center of the Gauss-peaks shown in (a). The slope leads to a critical field $E_c = (1.77\pm0.02)\mathrm{GVm}^{-1}$. **d,** Extracted Δz of the effective tip-sample tunneling barrier from simultaneously measured $I(z)$ data in (a). **e,** Logarithmic plot of the $I(z)$ signal for the $V_b = 1.7\,\mathrm{V}$ data with exponential fits (dashed lines) separating the three regimes of the system. **f,** Half-width at half-maximum Γ of the phase transition at different fields and temperatures (dots), and least-square model of a paramagnetic metal with g-factor of 2 (solid lines). **g,** Cartoon illustrating an electric field driven QPT in a Kondo lattice. The tip's local E-field sweeps away electrons at the molecule site and effectively hole-dopes it, which leads to the breakdown of the Kondo singlet and releases a local moment.

3.8 Real-space manifestation of the NTCDA Kondo lattice

We unravel the real-space spectroscopic features of the quasiparticle states and also the Kondo resonance of the NTCDA lattice in the vicinity of E_F, Fig.(3.8). For this, we use the feature detection scanning tunneling spectroscopy [121] to efficiently sample the features for different energies buried in 58×58 dI/dV spectra spanning a 3 nm^2 area. The method allows us to extract tiny signals that are overwhelmed by the broad Kondo resonance and the strong metallic background, and further, disentangle their density of states from the topography of the lattice. In this way, our analysis reveals the presence of two low-lying features almost symmetrically appearing at ±21 mV that we relate to the hole and electron quasiparticle states, Fig.(3.8a, bottom panel). They are localized in the center

of molecules and extend along its long axis, Fig.(3.8 b, I and IV). Moreover, we resolve the Kondo resonance localized at CH sites of the LUMO, which also overlaps with the resonances originating from the neighboring molecules (see Sup.(A.1) and Sup.(A.2) for further information).

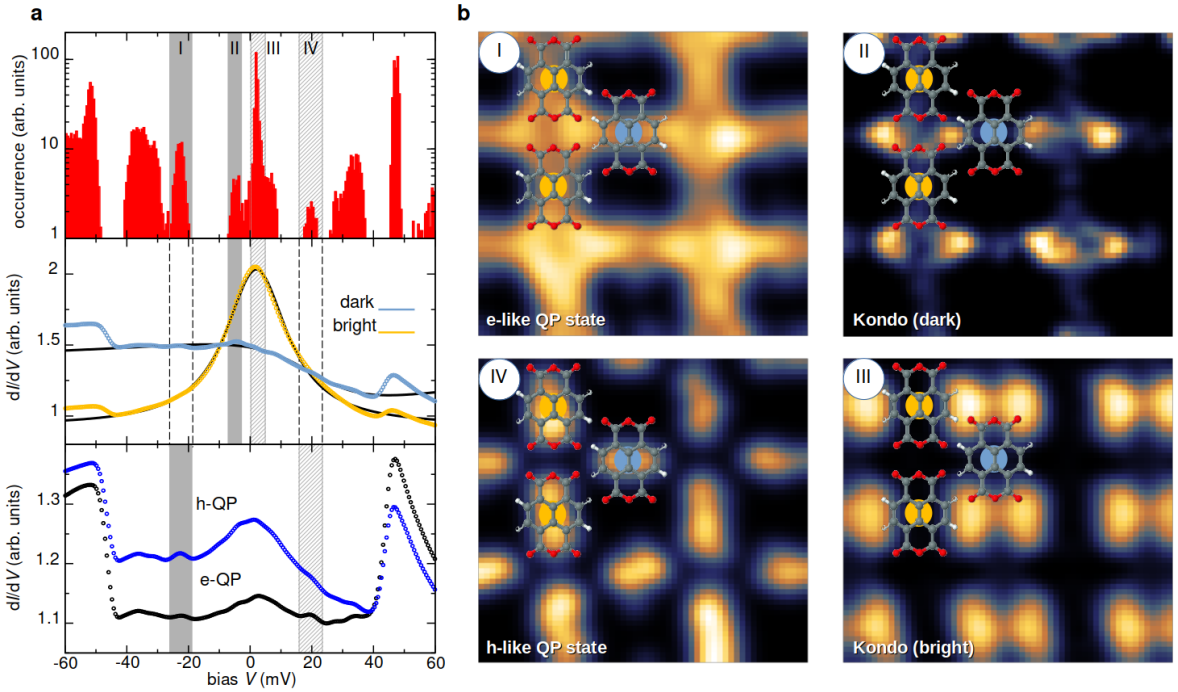

Figure 3.8: Low energy spectroscopic features of the Kondo lattice. **a,** Top panel: Energy distribution histogram of peaks in a map of 58×58 dI/dV spectra ($V_b = 70\,\mathrm{mV}$, $I_t = 1\,\mathrm{nA}$, $V_{\mathrm{mod}} = 0.2\,\mathrm{mV}$, $T = 4.24\,\mathrm{K}$) taken across the lattice. The full and hatched bars mark areas of interest at positive and negative bias ranges around E_{F}. Middle panel: Average spectra taken over the spectra in the interval specified by the full bar (labeled II) and hatched bar (labeled III), corresponding to the Kondo resonance at bright (gold dots) and dark (blue dots) molecules, with Frota fits (black full lines) ($\Gamma = 12.2\,(28.7)\,\mathrm{meV}$, $q > 300\,(= 1.2)$, $\varepsilon_0 = 2\,(21)\,\mathrm{meV}$, $T_{\mathrm{K}} = 132 \pm 5\,(340 \pm 20)\,\mathrm{K}$, where values in the brackets belong to the dark molecules. Bottom panel: Average spectra taken over the spectra in the interval specified by the full bar (labeled I) and hatched bar (labeled IV), corresponding to the hole (blue dots) and electron (black dots) quasiparticle states. **b,** Color-coded feature distribution maps of the peak intensity (dark: low, yellow: high) in the energy ranges marked in the histogram (**a**, top panel) with superimposed stick-and-ball model of the lattice (bright molecule: yellow circle, dark molecule: blue circle).

3.9 Cascade of quasiparticle excitations

Akin to their discharging (hole) character, the QPEs emerge in rings for large positive biases in $dI/dV\,(x, y)$ signals. However, in stark contrast to the impurity discharging events,

where they appear in ever-growing rings[8]; here, they manifest clear signatures of correlation and interactions, innate in their Kondo lattice traits. Starting from a point on the center of bright molecules, they gradually turn into in a ring as bias increases and when the tip goes off the discharging center. Once the rings reach the size of the unit cell, the QPEs interact with each other by creating a hybridization gap along the long molecule's axis ($\mathbf{a_1}$), and constructively superpose along the short one ($\mathbf{a_2}$): generating an intriguing portray of real-space quasiparticle interference Fig.(3.9).

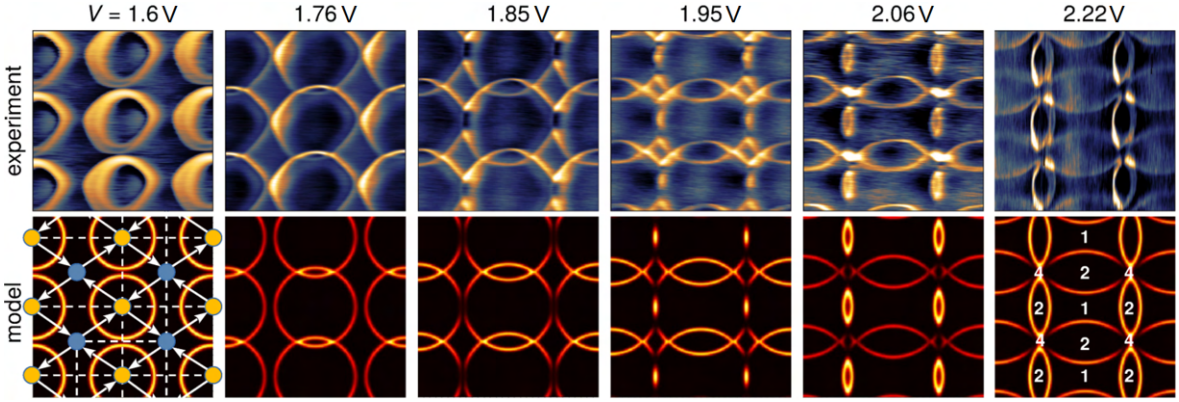

Figure 3.9: A portray of strongly correlated quasiparticle excitations. Top row: Color-coded plots of the dI/dV signal at constant V_b ranging from $1.6-2.22\,V$ measured in an area of approx. $1.5\times1.5\,\mathrm{nm}^2$ with a bright molecule in the centre (T = 1.4 K, B = −10 T). At increasing bias, i.e., increasing electric field, the transition rings cross along the short direction ($\mathbf{a_2}$) without strong interaction. Contrary, along the long direction ($\mathbf{a_1}$), in which the rings cross the bridge between two dark molecules, we observe an avoided crossing and the opening of a gap (V_b = 1.85 V). Bottom row: Tight-binding simulation of the discharging rings assuming a complex nearest-neighbor hybridization (arrows) between bright and dark molecules, as well as a next-nearest neighbor hoping (dashed line) between bright molecules, and different on-site energies (yellow: bright, blue: dark). The numbers in the last figure indicate the number of discharged molecules at the critical field E_c. The simulations reproduce the main features of the experimental data.

We further investigate the interference pattern of QPEs by using a tight-binding model Eq.(3.17) for a bipartite rectangular lattice and calculate the conductance between the tip and sample as the tip sweep the lattice. The model considers different on-site energies for each sublattice and also nearest-neighbor staggered hoppings inside a sublattice. Moreover, inspired by the seminal work of Haldane on Graphene, we assume a complex hybridization between the sublattices[9]. This assumption relies on the observation that an electron does not face the same energy landscape on the right and left sides while hopping forward and backward between the sublattices. In this model, the STM tip serves as a local top-gate

[8] Typically, there is an upper limit for the bias where rings disappear above it.

[9] We have to note that Haldane assumed a complex hopping between sites inside a sublattice, and a real-valued hopping between sublattices. This is the opposite setting of our model. Yet, we have borrowed his argument for justifying a complex hybridization.

that shifts the on-site energies, depending on their distance to the tip, besides its role in the junction for the electron tunneling to the sample. The model Hamiltonian follows as

$$\mathcal{H} = \sum_{i} \sum_{\nu=A,B} \sum_{\sigma} \left(E_\nu + U_i^{eff}\right) c^\dagger_{\nu,i\sigma} c_{\nu,i\sigma} - \sum_{\alpha=\mathbf{a_1},\mathbf{a_1}} \sum_{\sigma} \sum_{\langle\langle i,j\rangle\rangle} t_{\alpha,A} \left[c^\dagger_{A,i\sigma} c_{A,j\sigma} + h.c.\right] - \sum_{\langle i,j\rangle} \sum_{\sigma} \left[V_{AB} e^{i\theta_{i,j}}\, c^\dagger_{A,i\sigma} c_{B,j\sigma} + h.c.\right], \tag{3.17}$$

where $c^\dagger_{\nu,i\sigma}$ and $c_{\nu,i\sigma}$ are the creation and annihilation operators for $\nu = A$ and B sublattices with spin σ, E_ν is the on-site energies, $t_{\alpha,A}$ is the hopping amplitude along $\alpha = \mathbf{a_1}$ and $\mathbf{a_2}$ directions in the sublattice A, and V_{AB} is the hybridization amplitude between sublattices with phase $e^{i\theta_{ij}}$. The brackets $\langle i,j\rangle$ and $\langle\langle i,j\rangle\rangle$ in the sums stand for the nearest- and next-nearest- neighbors indices. The tip's local potential in Eq.(3.17) reads [77]

$$U_i^{eff} = \alpha \frac{eV_b}{1 + \epsilon_0 \frac{d_i}{r}} \quad \text{with} \quad d_i = \left((x_i - x_{\text{tip}})^2 + (y_i - y_{\text{tip}})^2\right)^{1/2}, \tag{3.18}$$

where α is the gating efficiency, ϵ_0 is the dielectric constant of the sample, r is the radius of the tip, and d_i is the tip-sample distance.

The direction of arrows in the superimposed lattice in Fig.(3.9, bottom row) shows the convention for a positive phase. Interestingly, such a non-interacting effective model with a minimal number of parameters is very predictive of the main features of the rings. In short, the main features comprise rings with certain broadening, which evolve with bias at different rates along $\mathbf{a_1}$ and $\mathbf{a_2}$ directions. Along $\mathbf{a_1}$, they grow faster and always constructively superpose. Along $\mathbf{a_2}$, they grow slower and form a hybridization gap, where at larger biases, they close the gap and further grow. The redistribution of the conductance intensity across the pattern comes from the fact that different part of the rings reaches the Fermi level at a different bias. We found that to match the conductance intensity in the simulation with the experimental results, fine-tuning the complex hybridization is crucial. For more information about the model and simulation consult with Ch.(5) and Sup.(B).

3.10 Conclusion

We close this chapter by recapitulating our understanding of the signal interpreted as a QPT in the Kondo lattice. Traditionally, the QPT has been studied along the trajectories in the phase diagram that joins the Kondo screened phase to the Néel ordered antiferromagnet. This is because to visit the interesting properties that happen in the neighborhood of QCP at very low temperatures, e.g., non-Fermi liquid behavior. In this study, we do not drive the ground state in this trajectory. The NTCDA Kondo lattice is in the strong coupling regime, even though there are low energy signatures of ordering in its density of states. Utilizing the tip's local electric field, we drive the ground state from the Kondo screened to the free spin regime of the phase diagram and probe the properties of the released spins by an applied magnetic field.

Naturally, the QPT in the Kondo lattice has been characterized mainly by means of measurements at the bulk (large) scale, elucidating the global properties of the ground state prior

to and after the phase transition. However, instrumentally, STM provides us with a tool to simultaneously probe and manipulate states at the local level. A unique chance to study the local properties of the QPT. In our investigation, we imaged a molecular Kondo lattice, and its spectroscopic features close to E_F, and showed that the QPT can be addressed in the 'real-space' and 'locally' in terms of low-lying charge quasiparticle excitations, which has ring-like representation and form long-range patterns of interference.

Last but not least, we have to mention that the interference pattern presented in Fig.(3.9, top panel) is not the only observed pattern. In fact, we have shown that the NTCDA lattice (relaxed monolayer and rippled phase) accommodate various other patterns that respect different symmetries. For more information consult with Ch.(4).

Chapter 4

Real-space quantum interference pattern

Quasiparticle interference (QPI) imaging is a powerful surface-sensitive technique to characterize the electronic structure of two-dimensional materials around the Fermi surface. It is based on electronic scattering of well-defined momentum states leading to interference patterns in the quasiparticle density of states that can be imaged with scanning tunneling spectroscopy. Practically, it is obtained by first Fourier-transforming the real-space interference map of the local density of states for a sufficiently large area, and then inverting it to yield the proportionate momentum gradient of energy. The patterns play a crucial role in revealing the type of interactions and correlations that determine the electronic ground state of the material. Here, without being faithful to the standard procedure of the QPI imaging, we merely look at the real-space interference patterns of the strongly correlated charge QPs of the NTCDA Kondo lattice. The intricate patterns are created by the constructive and destructive superposition of the discharging rings, which are induced by the local electric field of the STM tip. It is worth mentioning that similar patterns have also been observed as (dis)charging of impurities and defects at the surface of 2D materials and thin films [63, 64, 68, 70, 72, 73, 122–126], and also in molecules [74, 75, 127–130]. However, due to the complexity and novelty of the effects observed here, and also the limited number of available datasets, the thorough description of the underlying physics goes beyond the scope of this thesis and the above-mentioned works.

4.1 Discharging rings interference of NTCDA lattice

A flashback into the last chapter; we recall that in response to the tip's electric field which locally modifies the chemical potential of the lattice, a dot appears on the center of bright molecules and evolves into a growing ring as bias ramps up. The rings interfere once their radius is large enough to create a pattern of high and low intensity regions. Now, with sub-angstrom spectroscopic images Fig.(4.1), we can resolve the internal structures of the interference patterns and discuss their physical consequences.

4.1.1 Interference pattern (i): sample A, r-ML lattice

Let's first examine the pattern obtained for sample A and under 10 T magnetic field, Fig(4.1). The key features of this pattern are the non-trivial intertwining of rings along the molecule short axis, Fig(4.1 e), and formation of a hybridization gap at the intersection of the bright and dark molecules, Fig(4.1 f). We have to emphasize that these features are the product of interaction between the rings; otherwise, we would have observed ever-growing rings, as many groups have reported in impurities and defect studies. The non-trivial twist in the rings induces symmetry breaking and **handedness** (chirality) to the patterns. A property that is typically accompanied by systems with broken time-reversal symmetry. More importantly, the inter-locked rings create a topologically non-trivial object in real-space as one cannot separate them by smoothly deforming their manifold. Here, we have to be cautious of using common terminology since topology in physics is often refers to geometric properties of the momentum-space and not the real-space.

The meaning of chirality requires elaboration as the rings are not the trajectories of the electrons. For the sake of simplicity, consider the case of only two overlapping rings, Fig(4.1 e), originating from the nearest neighbouring bright molecules, which we call top and bottom. The overlaps with more rings in higher bias, Fig.(4.1 f-h), follows in the same way. The intersection of two consecutive rings has two special points, say left and right points, at equal distances from the center of both rings. As a result, once the tip is on these points and the bias is large enough, it can simultaneously discharge electrons of both molecules. So the intensity in these regions can be either summation (constructive) or subtraction (destructive) of rings. Surprisingly, the tip does not discharge both electrons at these points. Instead, once it is on the right point, it discharges the bottom molecule, and once it is on the left point, it discharges the top molecule: forming intertwined rings.

4.1.2 Interference pattern (ii): sample A, r-ML lattice

Repeating the measurement on the same sample but in a different area yielded a slightly different pattern, Fig.(4.2). The detail of this pattern is not as obvious as Fig.(4.1) because it was measured at 0 T B-field, and hence, the discharging peaks has an excessive width. Here, along the molecule's short axis the rings twist and along the long molecule's axis they take a fish scale structure.

4.1.3 Interference pattern (iii): sample B, r-ML lattice

A new set of observations were made on a completely different sample and at -10 T B-field. Most notably there are side rings, Fig.(4.3 a-c), which one can even spot them in the pattern (i), Fig.(4.1 d, e). The origin of the side rings is so far unclear, but it relates to the shoulder of the discharging peak (see Fig.(2.5)) that has been observed in many of the point dI/dV measurements. Moreover, at the center of each ring, Fig.(4.3 c, d), an additional feature appears and gradually takes an oval shape as bias increases. This feature is hardly visible in the other patterns[1]. One can attribute these features to the artifact of a double-tip. However, based on our personal experience, such an ordered pattern with sub-angstrom resolution cannot be achieved by a double or asymmetric tips.

Unlike pattern (i) which shows intertwining of rings along the molecule's short axis, here we see a fish scale structure, and therefore, it has no chirality and symmetry breaking along this direction. Along the long molecule's axis, it is very similar to the pattern (i) as both show the hybridization gap.

4.1.4 Interference pattern (iv): sample A, rippled lattice

Interestingly, we found that discharging rings are not exclusive to the r-ML lattice. We performed a similar measurement to the one we took on sample A and at 10 T B-field, but this time in the rippled phase and with a different tip. The topography of the lattice was previously presented in Fig.(2.4). Unfortunately, the tip was slightly asymmetric, and as a result, it deformed the rounded rings into broadened droplet shapes. This prevents us from resolving the intricate internal structures of the pattern. Nevertheless, based on this dataset, we can make general observations about the rippled phase.

As we said previously, in the rippled phase, bright and dark molecules periodically change character along their long and short axis, i.e., the bright molecule becomes dark, and vice versa [17]. Here, we see that discharging rings follow the same periodicity, Fig.(4.4). First, the bright molecules show the rings, and then gradually, as the bias increases, it extends to all over the lattice; even the darker-looking molecules in the transition regions show the discharging rings. It seems what is modulated across the lattice is the discharging energy of the molecules, which in turn modifies their bright and dark appearance and possibly even their Kondo temperature.

[1] In pattern (ii), it is not present, but visible in pattern (i), Fig.(4.1 g, h).

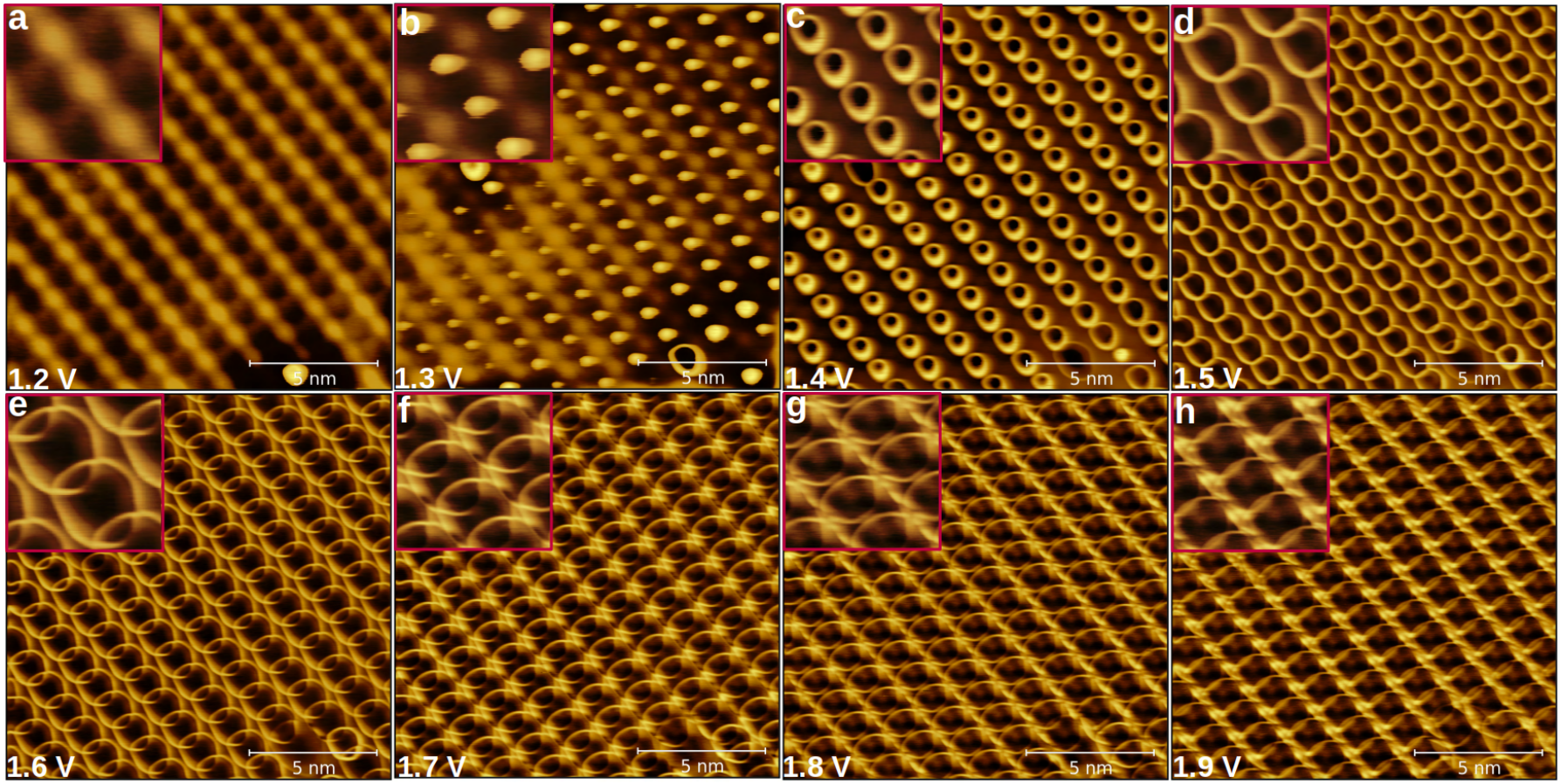

Figure 4.1: Interference pattern (i) of discharging rings of the NTCDA r-ML lattice. **a-h,** Constant-current dI/dV–maps of the r-ML lattice show interference pattern of intertwined rings measured with parameters $V_b \in \{1.2, 1.3, ..., 1.9\}$ V, I_t = 6 nA, T = 1.5 K, B = 10 T.

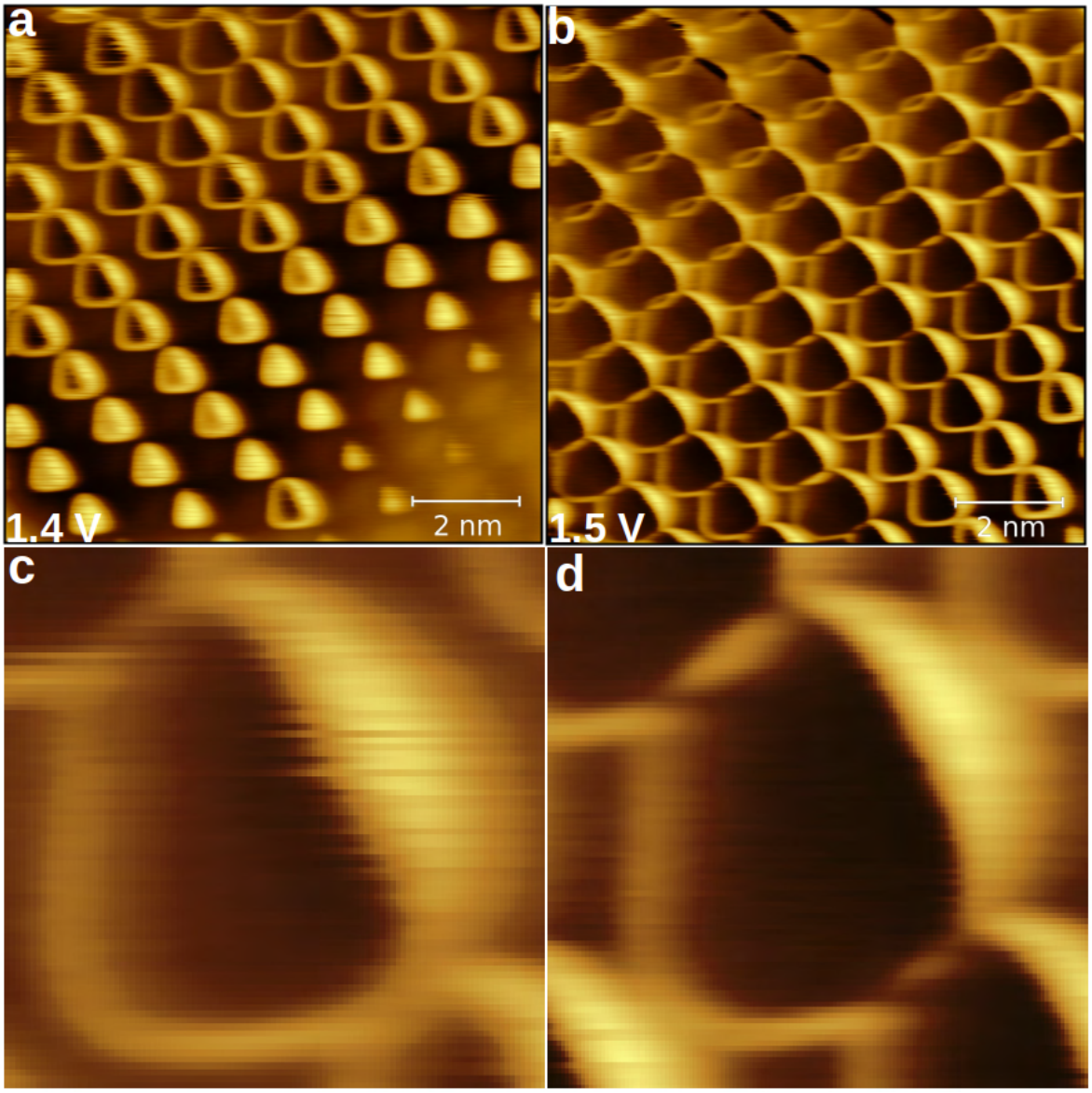

Figure 4.2: Interference pattern (ii) of discharging rings of the NTCDA r-ML lattice. **a, b,** Constant-current dI/dV–maps of the r-ML lattice show the interference pattern of discharging rings incorporating the intertwining and fish scale structure along different axis (V_b = 1.4 V and 1.5 V, I_t = 2 nA, T = 1.3 K, B = 0 T). **c** and **d** are zoom-in images of panel **a** and **b**, respectively.

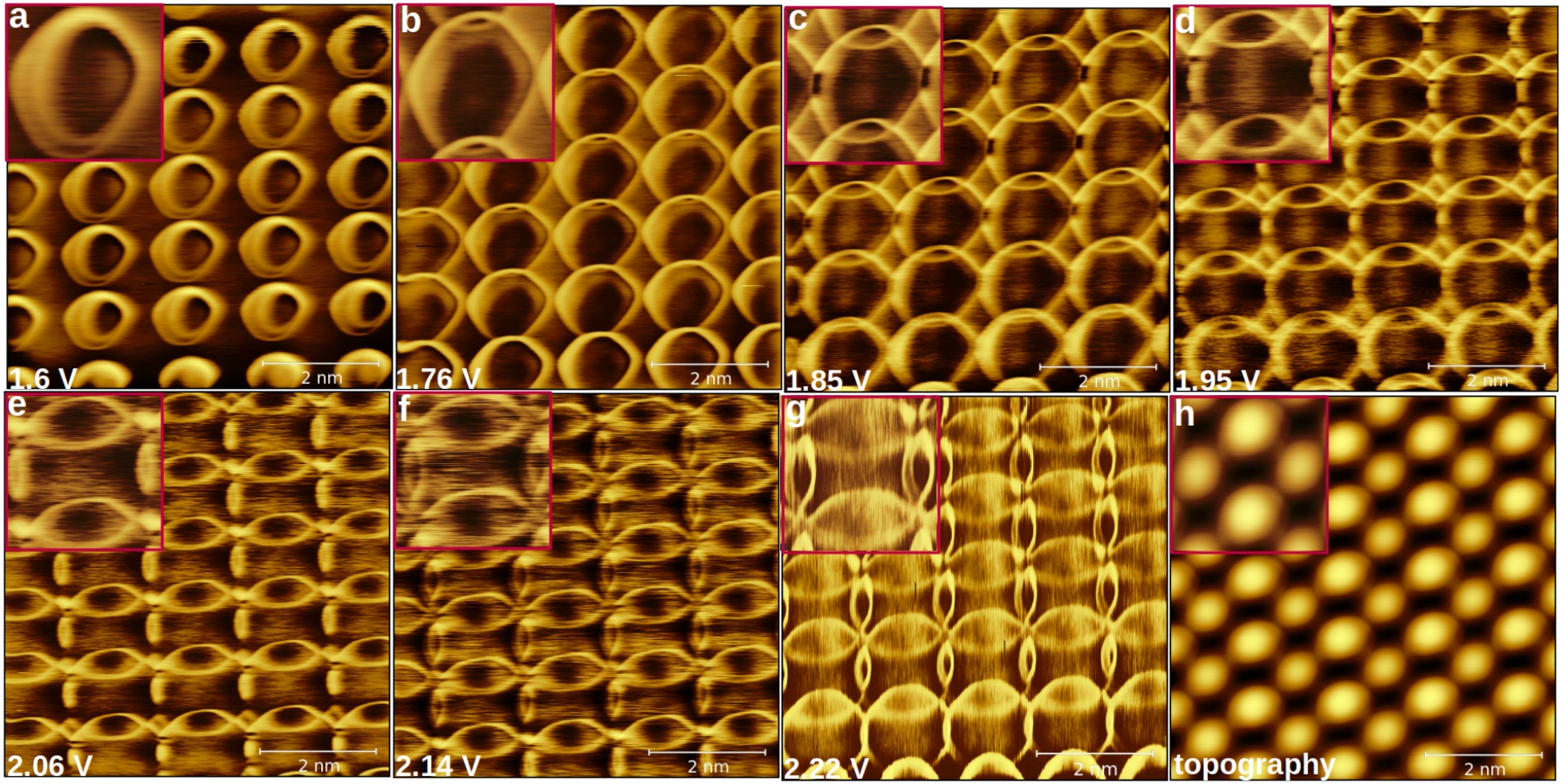

Figure 4.3: Interference pattern (iii) of discharging rings of the NTCDA r-ML lattice. **a-g,** Constant-current dI/dV–maps of the r-ML lattice show fish scale structure and hybridization of rings along different axis ($V_b \in \{1.6, 1.76, ..., 2.22\}$ V, I_t = 4.9 nA, T = 1.4 K, B = −10 T). **g,** Constant-current STM image (V_b = 1.6V, I_t = 4.9nA) acquired on the same region shows rounded topographic look of the bright and dark molecules that appear with different size.

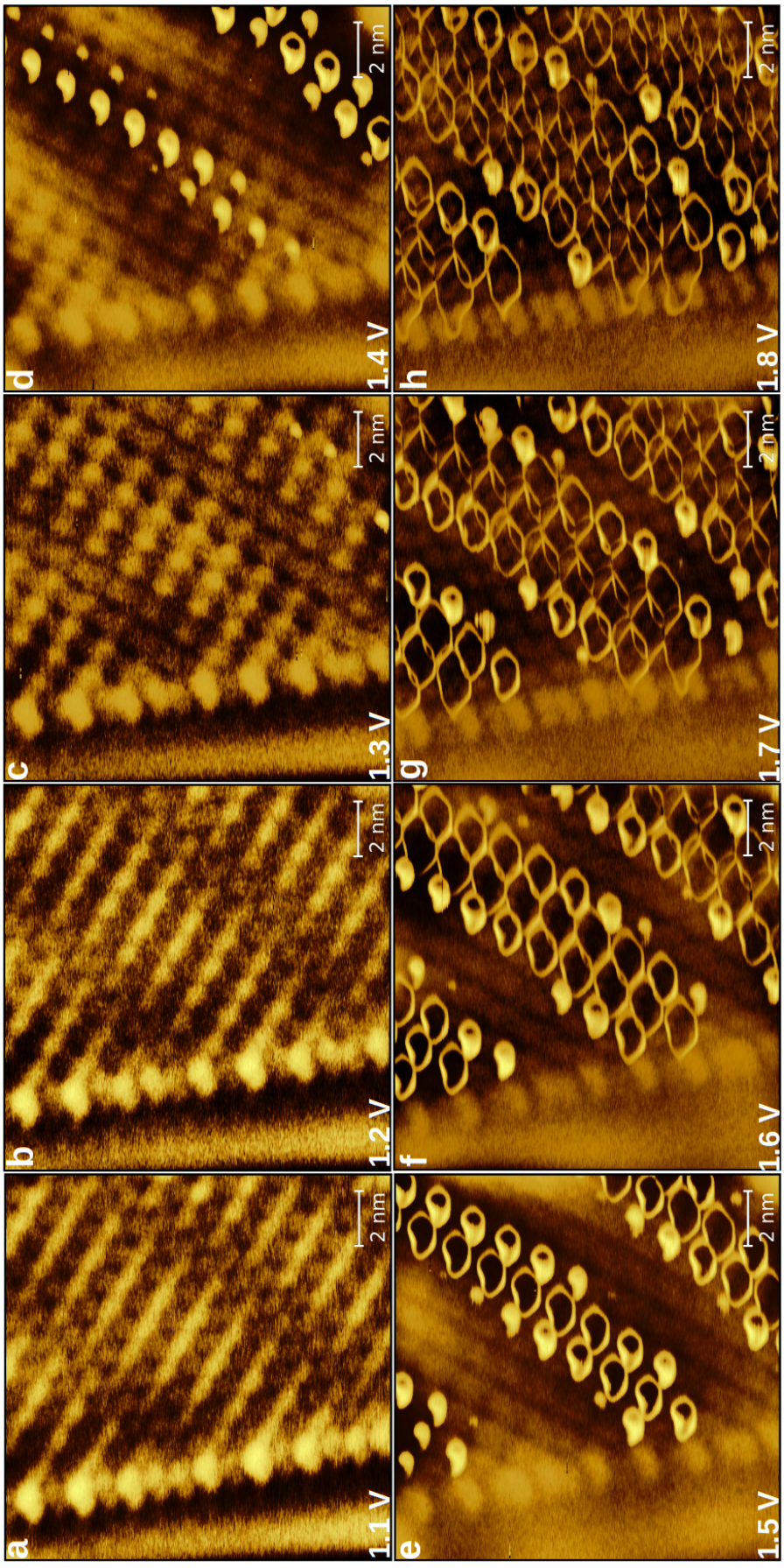

Figure 4.4: Interference pattern (iv) of discharging rings of the NTCDA rippled lattice. **a-h,** Constant-current dI/dV–maps of the rippled lattice show modulation of the discharging rings along the short and long molecule's axis ($V_b \in \{1.1, 1.2, ..., 1.8\}$ V, I_t = 4 nA, T = 1.5 K, B = 10 T).

4.2 Conclusion

We conclude this chapter by raising an important question about the patterns we have seen so far under different conditions. What drives the rings to develop a different pattern of interference? Is it encoded into the magnetic field, lattice type, sample preparation or the tip, since these are the apparent parameters vary among them[2]? Regarding the controversial role of magnetism, we have to consider the fact that the electron involved in the discharging process has an screened spin due to the Kondo effect ($T_K \sim 130$ K), which requires at least 15 T external magnetic field to show some signatures of magnetism. However, from other measurements[3], we know that the discharging peaks sharpens under applied magnetic field. A clear signature that over the discharging events the electron's spin is freed up from the Kondo singlet. Yet, one has to take into account that the discharging peaks occurs roughly around 1.5 eV, which is far beyond the reach of spin-related effects to play a significant role[4]. Therefore, the effect of magnetic field on the patterns, apart from sharpening of the rings, remains unclear and demands for further investigations.

As explained in Sec.(2.2), the NTCDA/Ag(111) is a substrate-mediated molecular lattice with various coverage-dependent phases. The lattice coverage controls the spacing between molecules, which in turn determines the strength of interaction between different entities, such as molecule-molecule and metal-molecule interactions. Consequently, the microscopic parameters such as hopping, hybridization, on-site energy, Coulomb repulsion, etc., could vary from lattice to lattice. Unfortunately, there are several technical barriers, computational and experimental, to gain realistic information about these microscopic quantities and how they impact the shape of the charging rings. From the theoretical side, this is due to the fact that the NTCDA/Ag(111) is a strongly correlated electron lattice system with a very large unit cell, and even though many of the single-molecule parameters are extracted [17, 49], *ab initio* calculations for the lattice problem are still missing. Similar blindness is also reflected in the experiments. From the experimental side, the control parameter to characterize the lattice is the molecular coverage which is determined by the deposition time and the substrate temperature during sample preparation, presuming that there are sufficiently large terraces on the silver substrate to deposit the molecule. Usually, this quantity is not sharply determined and has flexibility for a given phase, Tab.(2.2), which subsequently reserves a similar attitude in the above-mentioned microscopic parameters. Besides this, the STM tip, which we have little knowledge about its shape and symmetries, acts not only as a local probe but also modifies the parameters of the sample, such as the electron's on-site energy via its electric field. These discouraging myriad of unknowns impede a full characterization of the observed interference patterns, but nevertheless, in the next chapter, we will humbly approach the problem with the power of toy models!

[2] I have deliberately labeled each dataset by the sample (A,B), lattice type (r-ML, rippled), and the applied magnetic field so that one knows they are obtained under different conditions. Because in topographic images they are almost identical, except in r-ML and rippled phase.

[3] Not reported here.

[4] One caveat about the eV-energy scale of the discharging peaks is that, it is the energy needed to bring the electron to the Fermi level by the tip's electric field which acts like a local top-gate. Otherwise, it is not the intrinsic energy of the discharged electrons as they reside at the Fermi level of the sample.

Chapter 5

Tight-binding model of discharging rings

We present a class of single-particle model Hamiltonians tailored to simulate the measurements discussed before. Eventually, the aim is to calculate the tunneling conductance between the metallic tip and the lattice inside the STM junction over a given area in real-space, $\mathrm{dI/dV(x,y)}$. We start with a generic Hamiltonian and later add or drop terms based on their relevance to the experimental results. Therefore, not all scenarios discussed in this chapter can be realized in experiment. Unlike momentum-space, where calculations are fairly straightforward for periodic or infinite lattices, there are many subtleties to be noticed in real-space, especially for imposing periodic boundary conditions. Therefore, our strategy is to break the large real-space Hamiltonian matrix into a set of block matrices and provide a modular procedure to combine them. In this approach, even though the number of matrices to be constructed is large, the transparency and modularity of the method significantly help us to spot mistakes, and also modify them to make different models.

5.1 Model Hamiltonian

The model is presented schematically in Fig.(5.2). We start with the following Hamiltonian

$$\mathcal{H} = \mathcal{H}_A + \mathcal{H}_B + \mathcal{H}_{AB} + \mathcal{H}^G_{tip}, \tag{5.1}$$

where $\mathcal{H}_A$ describes the on-site energy (E_A) and staggered next-nearest-neighbour hopping $(t_{1A},\, t_{2A})$ of the electron between A-sites

$$\mathcal{H}_A = \sum_i \sum_{\sigma=\uparrow,\downarrow} E_A\, c^\dagger_{A,i\sigma} c_{A,i\sigma} - \sum_{\langle\langle i,j\rangle\rangle} \sum_{\sigma=\uparrow,\downarrow} [t_{1A}\, c^\dagger_{A,i\sigma} c_{A,j\sigma} + h.c.] - \sum_{\langle\langle i,j\rangle\rangle} \sum_{\sigma=\uparrow,\downarrow} [t_{2A}\, c^\dagger_{A,i\sigma} c_{A,j\sigma} + h.c.], \tag{5.2}$$

$\mathcal{H}_B$ describes only on-site energy (E_B) of the electron on B-sites (no hopping)

$$\mathcal{H}_B = \sum_i \sum_{\sigma=\uparrow,\downarrow} E_B\, c^\dagger_{B,i\sigma} c_{B,i\sigma}\,, \tag{5.3}$$

$\mathcal{H}_{AB}$ describes a complex nearest-neighbor hybridization (hopping) between A- and B-sites [34]

$$\mathcal{H}_{AB} = \sum_{\langle i,j\rangle} \begin{bmatrix} c^\dagger_{A,i\uparrow} \\ c^\dagger_{B,j\uparrow} \\ c^\dagger_{A,i\downarrow} \\ c^\dagger_{B,j\downarrow} \end{bmatrix}^T \begin{bmatrix} 0 & -V^{\uparrow\uparrow}_{AB} e^{i\theta} & 0 & 0 \\ -V^{\uparrow\uparrow}_{AB} e^{-i\theta} & 0 & 0 & 0 \\ 0 & 0 & 0 & -V^{\downarrow\downarrow}_{AB} e^{-i\theta} \\ 0 & 0 & -V^{\downarrow\downarrow}_{AB} e^{i\theta} & 0 \end{bmatrix} \begin{bmatrix} c_{A,i\uparrow} \\ c_{B,j\uparrow} \\ c_{A,i\downarrow} \\ c_{B,j\downarrow} \end{bmatrix} \tag{5.4}$$

and $\mathcal{H}^G_{tip}$ term describes the local tip-gating effect imposed on the electron at sites A and B

$$\mathcal{H}^G_{tip} = \sum_i \sum_{\sigma=\uparrow,\downarrow} U^{eff}_i\, c^\dagger_{A,i\sigma} c_{A,i\sigma} + \sum_i \sum_{\sigma=\uparrow,\downarrow} U^{eff}_i\, c^\dagger_{B,i\sigma} c_{B,i\sigma} \tag{5.5}$$

with the following band-bending electrostatic potential[1] [77, 131]

$$U^{eff}_i = \alpha \frac{eV_b}{1 + \epsilon_0 \frac{d_i}{r}} \quad \text{where} \quad d_i = \left((x_i - x_{\text{tip}})^2 + (y_i - y_{\text{tip}})^2\right)^{1/2}. \tag{5.6}$$

Here, $c^\dagger_{A,i\sigma}$ and $c_{A,i\sigma}$ are the creation and annihilation operators of an electron with spin σ at i–th site of the sublattice A and likewise in sublattice B. The brackets $\langle i,j\rangle$ and $\langle\langle i,j\rangle\rangle$ in the sums stand for nearest- and next-nearest- neighbors indices. The A-B hybridization matrix allows electrons with parallel and anti-parallel spins to have different Peierls phase $(e^{\pm i\theta})$, and therefore, hop in opposite directions in the unit cell [132–134]. This is inspired by Haldane's work on Graphene, which assumes a phase-dependent hopping between next-nearest neighbors, based on the assumption that electrons face different energy landscapes on the left and right sides while hopping forward and backward between the sites. Similarly, we can see that in the NTCDA lattice, an electron hopping from the dark to bright molecules faces the bridge-site on the right side, where the density of states is suppressed, while on the left side, it faces the CH-site, where the Kondo resonance is localized,

[1] The potential is modified by the prefactor α compared to Ref.[77] and Ref.[131], and also the constant $\mathcal{W}_0$ representing the difference in the work functions between the tip and sample in those references is absorbed by the shift of on-site energies.

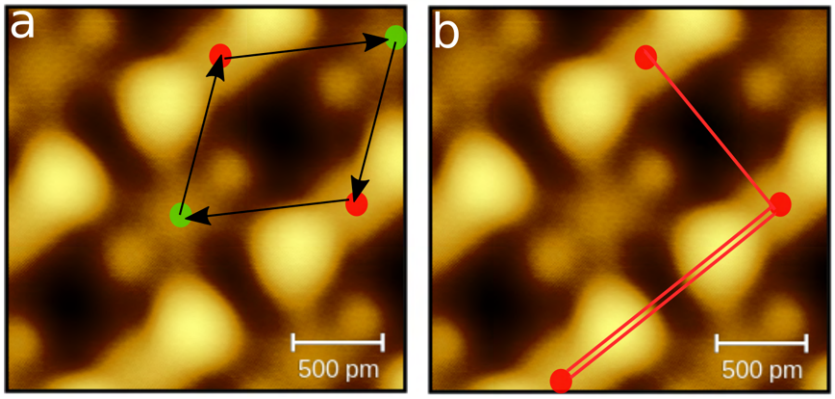

Figure 5.1: Inter-molecule phase-dependent hybridization and real hopping in the NTCDA lattice. a, Complex hybridization between bright and dark molecules with arrows indicating the positive phase convention. **b,** Staggered real hopping between bright molecules with single and double lines indicating the strong and weak bonds.

Fig.(7.1a). This argument does not hold for the hopping between two bright or two dark molecules as the left and right (top and bottom) environments are identical in those paths, Fig.(7.1b).

The STM tip plays the role of a local top-gate that shifts the onsite energy of electron at each lattice site by amount U_i^{eff}. The value of U_i^{eff} is determined by bias voltage between tip and sample (V_b), electric charge (e), gating efficiency (α), electrostatic dielectric constant of the sample (ϵ_0), tip radius (r), and the tip-sample distance (d_i).

To preserve the periodic boundary condition (PBC), the first and last sites must be connected to each other in each row and column. Applying this condition results in additional cells, which we shaded with light yellow color to distinguish them from the rest of the cells in the schematic lattice, Fig.(5.2). This is the consequence of having the nearest-neighbor hopping and hybridization in the Hamiltonian. In case there is a next-nearest neighbor hopping, the first and second sites in each row and column must be connected to the last and before the last ones, which requires appending one more cell. There is an important remark regarding the metric we use to evaluate the local gate potential in Eq.(5.6). Consider the tip is sweeping a row with n_x sites ($A_i \to B_{i+1} \to \cdots \to B_{n_x} \to A_i$) of a lattice with width $L_x = n_x\, a_x$. Due to PBC, there are two Euclidean distances between the tip and site i along the x-axis: $d_{i,x}^{(1)} = |x_i - x_{\text{tip}}|$, and $d_{i,x}^{(2)} = L_x - |x_i - x_{\text{tip}}|$. It is straightforward to check that $d_{i,x}^{(1)} < d_{i,x}^{(2)}$ before the tip reaches the middle of the row and $d_{i,x}^{(2)} \leq d_{i,x}^{(1)}$, otherwise. The same argument is true for a sweep along the y-axis for $d_{i,y}^{(1)}$ and $d_{i,y}^{(2)}$ distances. To compute the local gating potential U_i^{eff}, we choose the minimum distance along each axis.

$$\begin{cases} d_{i,x} = \min(d_{i,x}^{(1)},\, d_{i,x}^{(2)}) \\ \\ d_{i,y} = \min(d_{i,y}^{(1)},\, d_{i,y}^{(2)}) \end{cases} \quad \to \quad d_i = (d_{i,x}^2 + d_{i,y}^2)^{1/2}.$$

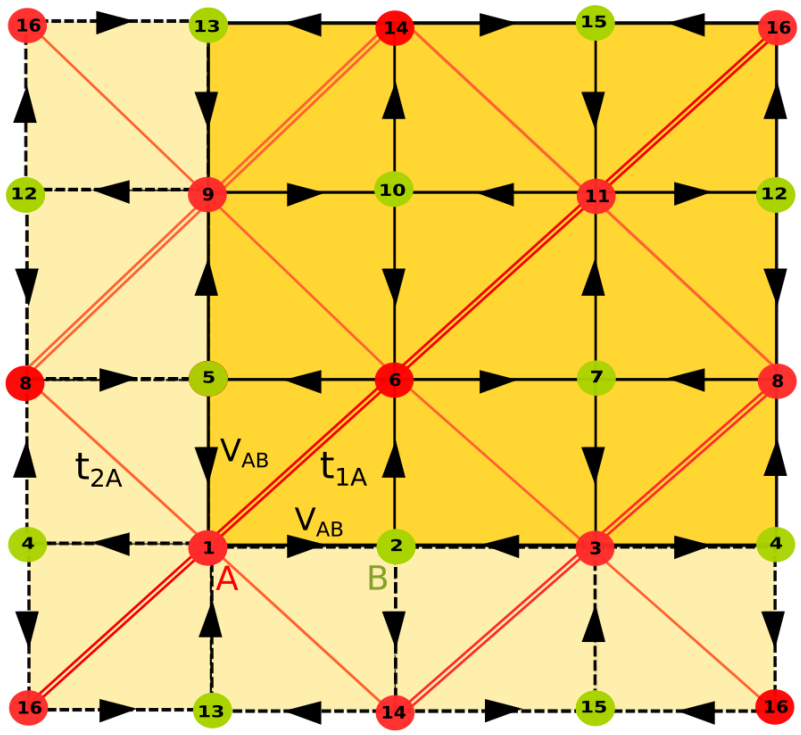

Figure 5.2: Schematic of a bipartite lattice comprises of sites A and B with staggered hopping and complex hybridization. Sublattices A and B are specified by red and green circles, which are separated by the lattice constant (a). The lattice constant of sublattice A and B is $(a\sqrt{2})$. The hopping is merely between A-sites and staggered by strong (double red line) and weak bond (single red line). The complex hybridization is between A- and B-sites (black line) with an arrow specifying the direction of the hybridization (phase). The light yellow cells impose periodic boundary conditions on the lattice. To compare this lattice with the arrays of bright and dark molecules in the NTCDA lattice, one should assign the A-sites (red: $1, 6, 11, ...$) to the chain of bright molecules and the B-sites (green: $2, 7, 12, ...$) to dark ones.

5.2 Matrix structure of the real-space Hamiltonian

This section can be used as a manual to follow our python source code provided at the supplement of this thesis, Sup.(B). The variable naming and matrix structure obey a similar style to make reading the code smoother. The Hamiltonian of the spin-$1/2$ electron, Eq.(5.1), can be decomposed into a $\mathcal{H}_{\text{spin}} \otimes \mathcal{H}_{\mathcal{A}-\mathcal{B}}$ space as

$$\mathcal{H} = \begin{bmatrix} \Psi_\uparrow \\ \Psi_\downarrow \end{bmatrix}^T \begin{bmatrix} \mathcal{H}_{\uparrow\uparrow} & \mathcal{H}_{\uparrow\downarrow} \\ \mathcal{H}_{\downarrow\uparrow} & \mathcal{H}_{\downarrow\downarrow} \end{bmatrix} \begin{bmatrix} \Psi_\uparrow \\ \Psi_\downarrow \end{bmatrix}$$

with the following basis

$$\Psi_\uparrow = \begin{bmatrix} \psi_{A1\uparrow} \\ \psi_{B2\uparrow} \\ \psi_{A3\uparrow} \\ \psi_{B4\uparrow} \\ \vdots \\ \psi_{BN\uparrow} \end{bmatrix} \qquad \text{and} \qquad \Psi_\downarrow = \begin{bmatrix} \psi_{A1\downarrow} \\ \psi_{B2\downarrow} \\ \psi_{A3\downarrow} \\ \psi_{B4\downarrow} \\ \vdots \\ \psi_{BN\downarrow} \end{bmatrix}$$

where indices running over flavor (A, B) and lattice site number ($i = 1, 2, ..., N$). The Hilbert space of the full Hamiltian has a $(2N \times 2N)$ size, where N can be decomposed into the number of sites in rows and columns ($N = n_x \times n_y$) of the lattice. All four blocks of the full Hamiltonian are **cyclic block tri-diagonal matrices** that will explore their structure in the following sections. Since there no spin mixing term in the Hamiltonian, we can already set $\mathcal{H}_{\uparrow\downarrow} = \mathcal{H}_{\downarrow\uparrow} = 0$.

5.2.1 Diagonal blocks: $\mathcal{H}_{\uparrow\uparrow}$ and $\mathcal{H}_{\downarrow\downarrow}$

We construct the full Hamiltonian matrix block by block, starting with $H_{\uparrow\uparrow}$,

$$\mathcal{H}_{\uparrow\uparrow} = \begin{bmatrix} \mathcal{D}_{1x\uparrow\uparrow} & \mathcal{O}_{1y\uparrow\uparrow} & 0 & 0 & 0 & \cdots & 0 & 0 & \mathcal{O}^\dagger_{2y\uparrow\uparrow} \\ \mathcal{O}^\dagger_{1y\uparrow\uparrow} & \mathcal{D}_{2x\uparrow\uparrow} & \mathcal{O}_{2y\uparrow\uparrow} & 0 & 0 & \cdots & 0 & 0 & 0 \\ 0 & \mathcal{O}^\dagger_{2y\uparrow\uparrow} & \mathcal{D}_{1x\uparrow\uparrow} & \mathcal{O}_{1y\uparrow\uparrow} & 0 & \cdots & 0 & 0 & 0 \\ 0 & 0 & \mathcal{O}^\dagger_{1y\uparrow\uparrow} & \mathcal{D}_{2x\uparrow\uparrow} & \ddots & \ddots & \ddots & \vdots & \vdots \\ 0 & 0 & 0 & \ddots & \ddots & \ddots & \ddots & 0 & 0 \\ \vdots & \vdots & \vdots & \ddots & \ddots & \mathcal{D}_{1x\uparrow\uparrow} & \mathcal{O}_{1y\uparrow\uparrow} & 0 & 0 \\ 0 & 0 & 0 & \ddots & \ddots & \mathcal{O}^\dagger_{1y\uparrow\uparrow} & \mathcal{D}_{2x\uparrow\uparrow} & \mathcal{O}_{2y\uparrow\uparrow} & 0 \\ 0 & 0 & 0 & 0 & 0 & 0 & \mathcal{O}^\dagger_{2y\uparrow\uparrow} & \mathcal{D}_{1x\uparrow\uparrow} & \mathcal{O}_{1y\uparrow\uparrow} \\ \mathcal{O}_{2y\uparrow\uparrow} & 0 & 0 & \cdots & 0 & 0 & 0 & \mathcal{O}^\dagger_{1y\uparrow\uparrow} & \mathcal{D}_{2x\uparrow\uparrow} \end{bmatrix}. \tag{5.7}$$

The PBC is automatically imposed on the blocks by satisfying the following conditions

$$\begin{cases} \left[\mathcal{H}_{\uparrow\uparrow}\right]_{1,N} = \left[\mathcal{H}_{\uparrow\uparrow}\right]^\dagger_{2,3} \\ \\ \left[\mathcal{H}_{\uparrow\uparrow}\right]_{N,1} = \left[\mathcal{H}_{\uparrow\uparrow}\right]^\dagger_{3,2} \end{cases}. \tag{5.8}$$

First, we find its diagonal blocks, $\mathcal{D}_{1x\uparrow\uparrow}$ and $\mathcal{D}_{2x\uparrow\uparrow}$, which generate the on-site energies and hybridization between A and B sites along the row of the lattice. The $\mathcal{D}_{1x\uparrow\uparrow}$ matrix follows as

$$\mathcal{D}_{1x\uparrow\uparrow} = \begin{bmatrix} E_A + U_1^{eff} & -V_{AB}^{\uparrow\uparrow} e^{i\theta} & 0 & 0 & 0 & \cdots & 0 & 0 & -V_{AB}^{\uparrow\uparrow} e^{i\theta} \\ -V_{AB}^{\uparrow\uparrow} e^{-i\theta} & E_B + U_1^{eff} & -V_{AB}^{\uparrow\uparrow} e^{-i\theta} & 0 & 0 & \cdots & 0 & 0 & 0 \\ 0 & -V_{AB}^{\uparrow\uparrow} e^{i\theta} & E_A + U_2^{eff} & -V_{AB}^{\uparrow\uparrow} e^{i\theta} & 0 & \cdots & 0 & 0 & 0 \\ 0 & 0 & -V_{AB}^{\uparrow\uparrow} e^{-i\theta} & E_B + U_2^{eff} & \ddots & \ddots & \vdots & \vdots & \vdots \\ 0 & 0 & 0 & \ddots & \ddots & \ddots & 0 & 0 & 0 \\ \vdots & \vdots & \vdots & \ddots & \ddots & E_A + U_{N-1}^{eff} & -V_{AB}^{\uparrow\uparrow} e^{i\theta} & 0 & 0 \\ 0 & 0 & 0 & \ddots & \ddots & -V_{AB}^{\uparrow\uparrow} e^{-i\theta} & E_B + U_{N-1}^{eff} & -V_{AB}^{\uparrow\uparrow} e^{-i\theta} & 0 \\ 0 & 0 & 0 & 0 & \ddots & 0 & -V_{AB}^{\uparrow\uparrow} e^{i\theta} & E_A + U_N^{eff} & -V_{AB}^{\uparrow\uparrow} e^{i\theta} \\ -V_{AB}^{\uparrow\uparrow} e^{-i\theta} & 0 & 0 & \cdots & 0 & 0 & 0 & -V_{AB}^{\uparrow\uparrow} e^{-i\theta} & E_B + U_N^{eff} \end{bmatrix}$$

where the PBC is imposed on the linking elements by satisfying the following conditions

$$\begin{cases} \left[\mathcal{D}_{1x\uparrow\uparrow}\right]_{1,n_x} = \left[\mathcal{D}_{1x\uparrow\uparrow}\right]_{2,1}^{*} \\ \left[\mathcal{D}_{1x\uparrow\uparrow}\right]_{n_x,1} = \left[\mathcal{D}_{1x\uparrow\uparrow}\right]_{1,2}^{*} \end{cases} . \tag{5.9}$$

One can track the alternating phase reversal in $\mathcal{D}_{1x\uparrow\uparrow}$ from site to site by following the arrows in Fig.(5.2). By convention, moving along the arrow is assigned to $e^{i\theta}$, and the opposite to $e^{-i\theta}$. Moreover, notice in Fig.(5.2) that from one row to the next, the starting site switches from A to B. This leads to the following elements for $\mathcal{D}_{2x\uparrow\uparrow}$ matrix

$$\mathcal{D}_{2x\uparrow\uparrow} = \begin{bmatrix} E_B + U_1^{eff} & -V_{AB}^{\uparrow\uparrow} e^{-i\theta} & 0 & 0 & 0 & \cdots & 0 & 0 & -V_{AB}^{\uparrow\uparrow} e^{-i\theta} \\ -V_{AB}^{\uparrow\uparrow} e^{i\theta} & E_A + U_1^{eff} & -V_{AB}^{\uparrow\uparrow} e^{i\theta} & 0 & 0 & \cdots & 0 & 0 & 0 \\ 0 & -V_{AB}^{\uparrow\uparrow} e^{-i\theta} & E_B + U_2^{eff} & -V_{AB}^{\uparrow\uparrow} e^{-i\theta} & 0 & \cdots & 0 & 0 & 0 \\ 0 & 0 & -V_{AB}^{\uparrow\uparrow} e^{i\theta} & E_A + U_2^{eff} & \ddots & \ddots & \vdots & \vdots & \vdots \\ 0 & 0 & 0 & \ddots & \ddots & \ddots & 0 & 0 & 0 \\ \vdots & \vdots & \vdots & \ddots & \ddots & E_B + U_{N-1}^{eff} & -V_{AB}^{\uparrow\uparrow} e^{-i\theta} & 0 & 0 \\ 0 & 0 & 0 & \ddots & \ddots & -V_{AB}^{\uparrow\uparrow} e^{i\theta} & E_A + U_{N-1}^{eff} & -V_{AB}^{\uparrow\uparrow} e^{i\theta} & 0 \\ 0 & 0 & 0 & 0 & \ddots & 0 & -V_{AB}^{\uparrow\uparrow} e^{-i\theta} & E_B + U_N^{eff} & -V_{AB}^{\uparrow\uparrow} e^{-i\theta} \\ -V_{AB}^{\uparrow\uparrow} e^{i\theta} & 0 & 0 & \cdots & 0 & 0 & 0 & -V_{AB}^{\uparrow\uparrow} e^{i\theta} & E_A + U_N^{eff} \end{bmatrix}.$$

The PBC of the $\mathcal{D}_{2x\uparrow\uparrow}$ is imposed similar to Eq.(5.9). We have to take into account that dimension of these two matrices are $(n_x \times n_x)$, where n_x is the number of sites in a row of the lattice. The $\mathcal{D}_{1x\uparrow\uparrow}$ and $\mathcal{D}_{2x\uparrow\uparrow}$ matrices sit alternately on the diagonal blocks of $\mathcal{H}_{\uparrow\uparrow}$ to capture the periodic reversal of flow and specie in successive rows (see Fig.(5.2)).

The off-diagonal blocks of $\mathcal{H}_{\uparrow\uparrow}$ consist of $\mathcal{O}_{1y\uparrow\uparrow}$ and $\mathcal{O}_{2y\uparrow\uparrow}$ matrices, and their complex transpose. They generate the staggered hopping (t_{1A}, t_{2A}) between two A-sites for a spin up electron, and also hybridization between A and B sites along the column of the lattice. The

$\mathcal{O}_{1y\uparrow\uparrow}$ matrix can be found as

$$\mathcal{O}_{1y\uparrow\uparrow} = \begin{bmatrix} -V_{AB}^{\uparrow\uparrow} e^{-i\theta} & -t_{1A} & 0 & 0 & 0 & \cdots & 0 & 0 & -t_{2A} \\ 0 & -V_{AB}^{\uparrow\uparrow} e^{i\theta} & 0 & 0 & 0 & \cdots & 0 & 0 & 0 \\ 0 & -t_{2A} & -V_{AB}^{\uparrow\uparrow} e^{-i\theta} & -t_{1A} & 0 & \cdots & 0 & 0 & 0 \\ 0 & 0 & 0 & -V_{AB}^{\uparrow\uparrow} e^{i\theta} & \ddots & \ddots & \ddots & \vdots & \vdots \\ 0 & 0 & 0 & -t_{2A} & \ddots & \ddots & 0 & 0 & 0 \\ \vdots & \vdots & \vdots & \ddots & \ddots & -V_{AB}^{\uparrow\uparrow} e^{-i\theta} & -t_{1A} & 0 & 0 \\ 0 & 0 & 0 & \ddots & \ddots & 0 & -V_{AB}^{\uparrow\uparrow} e^{i\theta} & 0 & 0 \\ 0 & 0 & 0 & \ddots & 0 & 0 & -t_{2A} & -V_{AB}^{\uparrow\uparrow} e^{-i\theta} & -t_{1A} \\ 0 & 0 & 0 & \cdots & 0 & 0 & 0 & 0 & -V_{AB}^{\uparrow\uparrow} e^{i\theta} \end{bmatrix}$$

and $\mathcal{O}_{2y\uparrow\uparrow}$ matrix as

$$\mathcal{O}_{2y\uparrow\uparrow} = \begin{bmatrix} -V_{AB}^{\uparrow\uparrow} e^{i\theta} & 0 & 0 & 0 & 0 & \cdots & 0 & 0 & 0 \\ -t_{2A} & -V_{AB}^{\uparrow\uparrow} e^{-i\theta} & -t_{1A} & 0 & 0 & \cdots & 0 & 0 & 0 \\ 0 & 0 & -V_{AB}^{\uparrow\uparrow} e^{i\theta} & 0 & 0 & \cdots & 0 & 0 & 0 \\ 0 & 0 & -t_{2A} & -V_{AB}^{\uparrow\uparrow} e^{-i\theta} & -t_{1A} & \ddots & \ddots & \vdots & \vdots \\ 0 & 0 & 0 & \ddots & \ddots & \ddots & 0 & 0 & 0 \\ \vdots & \vdots & \vdots & \ddots & \ddots & -V_{AB}^{\uparrow\uparrow} e^{i\theta} & 0 & 0 & 0 \\ 0 & 0 & 0 & \ddots & \ddots & -t_{2A} & -V_{AB}^{\uparrow\uparrow} e^{-i\theta} & -t_{1A} & 0 \\ 0 & 0 & 0 & \ddots & 0 & 0 & 0 & -V_{AB}^{\uparrow\uparrow} e^{i\theta} & 0 \\ -t_{1A} & 0 & 0 & \cdots & 0 & 0 & 0 & -t_{2A} & -V_{AB}^{\uparrow\uparrow} e^{-i\theta} \end{bmatrix}.$$

Their complex transpose reads

$$\mathcal{O}_{1y\uparrow\uparrow}^{\dagger} = \begin{bmatrix} -V_{AB}^{\uparrow\uparrow} e^{i\theta} & 0 & 0 & 0 & 0 & \cdots & 0 & 0 & 0 \\ -t_{1A} & -V_{AB}^{\uparrow\uparrow} e^{-i\theta} & -t_{2A} & 0 & 0 & \cdots & 0 & 0 & 0 \\ 0 & 0 & -V_{AB}^{\uparrow\uparrow} e^{i\theta} & 0 & 0 & \cdots & 0 & 0 & 0 \\ 0 & 0 & -t_{1A} & -V_{AB}^{\uparrow\uparrow} e^{-i\theta} & -t_{2A} & \ddots & \ddots & \vdots & \vdots \\ 0 & 0 & 0 & 0 & \ddots & \ddots & 0 & 0 & 0 \\ \vdots & \vdots & \vdots & \ddots & \ddots & -V_{AB}^{\uparrow\uparrow} e^{i\theta} & 0 & 0 & 0 \\ 0 & 0 & 0 & \ddots & \ddots & -t_{1A} & -V_{AB}^{\uparrow\uparrow} e^{-i\theta} & -t_{2A} & 0 \\ 0 & 0 & 0 & \ddots & 0 & 0 & 0 & -V_{AB}^{\uparrow\uparrow} e^{i\theta} & 0 \\ -t_{2A} & 0 & 0 & \cdots & 0 & 0 & 0 & -t_{1A} & -V_{AB}^{\uparrow\uparrow} e^{-i\theta} \end{bmatrix}$$

and

$$\mathcal{O}_{2y\uparrow\uparrow}^{\dagger} = \begin{bmatrix} -V_{AB}^{\uparrow\uparrow} e^{-i\theta} & -t_{2A} & 0 & 0 & 0 & \cdots & 0 & 0 & -t_{1A} \\ 0 & -V_{AB}^{\uparrow\uparrow} e^{i\theta} & 0 & 0 & 0 & \cdots & 0 & 0 & 0 \\ 0 & -t_{1A} & -V_{AB}^{\uparrow\uparrow} e^{-i\theta} & -t_{2A} & 0 & 0 & 0 & 0 & 0 \\ 0 & 0 & 0 & -V_{AB}^{\uparrow\uparrow} e^{i\theta} & 0 & \ddots & \vdots & \vdots & \vdots \\ 0 & 0 & 0 & -t_{1A} & \ddots & \ddots & 0 & 0 & 0 \\ \vdots & \vdots & \vdots & \ddots & \ddots & -V_{AB}^{\uparrow\uparrow} e^{-i\theta} & -t_{2A} & 0 & 0 \\ 0 & 0 & 0 & \ddots & \ddots & \ddots & -V_{AB}^{\uparrow\uparrow} e^{i\theta} & 0 & 0 \\ 0 & 0 & 0 & 0 & 0 & 0 & -t_{1A} & -V_{AB}^{\uparrow\uparrow} e^{-i\theta} & -t_{2A} \\ 0 & 0 & 0 & \cdots & 0 & 0 & 0 & 0 & -V_{AB}^{\uparrow\uparrow} e^{i\theta} \end{bmatrix}.$$

The size of these four matrices are $(n_y \times n_y)$, where n_y is the size of a column of the lattice. Without loss of generality, we choose $n_y = n_x$.

In a similar way, we construct $\mathcal{H}_{\downarrow\downarrow}$ as

$$\mathcal{H}_{\downarrow\downarrow} = \begin{bmatrix} \mathcal{D}_{1x\downarrow\downarrow} & \mathcal{O}_{1y\downarrow\downarrow} & 0 & 0 & 0 & \cdots & 0 & 0 & \mathcal{O}^{\dagger}_{2y\downarrow\downarrow} \\ \mathcal{O}^{\dagger}_{1y\downarrow\downarrow} & \mathcal{D}_{2x\downarrow\downarrow} & \mathcal{O}_{2y\downarrow\downarrow} & 0 & 0 & \cdots & 0 & 0 & 0 \\ 0 & \mathcal{O}^{\dagger}_{2y\downarrow\downarrow} & \mathcal{D}_{1x\downarrow\downarrow} & \mathcal{O}_{1y\downarrow\downarrow} & 0 & \cdots & 0 & 0 & 0 \\ 0 & 0 & \mathcal{O}^{\dagger}_{1y\downarrow\downarrow} & \mathcal{D}_{2x\downarrow\downarrow} & \ddots & \ddots & \ddots & \vdots & \vdots \\ 0 & 0 & 0 & \ddots & \ddots & \ddots & \ddots & 0 & 0 \\ \vdots & \vdots & \vdots & \ddots & \ddots & \mathcal{D}_{1x\downarrow\downarrow} & \mathcal{O}_{1y\downarrow\downarrow} & 0 & 0 \\ 0 & 0 & 0 & \ddots & \ddots & \mathcal{O}^{\dagger}_{1y\downarrow\downarrow} & \mathcal{D}_{2x\downarrow\downarrow} & \mathcal{O}_{2y\downarrow\downarrow} & 0 \\ 0 & 0 & 0 & 0 & 0 & 0 & \mathcal{O}^{\dagger}_{2y\downarrow\downarrow} & \mathcal{D}_{1x\downarrow\downarrow} & \mathcal{O}_{1y\downarrow\downarrow} \\ \mathcal{O}_{2y\downarrow\downarrow} & 0 & 0 & \cdots & 0 & 0 & 0 & \mathcal{O}^{\dagger}_{1y\downarrow\downarrow} & \mathcal{D}_{2x\downarrow\downarrow} \end{bmatrix}, \tag{5.10}$$

where the PBC for $\mathcal{H}_{\downarrow\downarrow}$ is imposed similar to Eq.(5.8). The $\mathcal{D}_{1x\downarrow\downarrow}$ matrix generates the on-site energies and the hybridization of electron with spin down between A and B sites along a row of the lattice. It reads

$$\mathcal{D}_{1x\downarrow\downarrow} = \begin{bmatrix} E_A + U_1^{eff} & -V_{AB}^{\downarrow\downarrow} e^{-i\theta} & 0 & 0 & 0 & \cdots & 0 & 0 & -V_{AB}^{\downarrow\downarrow} e^{-i\theta} \\ -V_{AB}^{\downarrow\downarrow} e^{i\theta} & E_B + U_1^{eff} & -V_{AB}^{\downarrow\downarrow} e^{i\theta} & 0 & 0 & \cdots & 0 & 0 & 0 \\ 0 & -V_{AB}^{\downarrow\downarrow} e^{-i\theta} & E_A + U_2^{eff} & -V_{AB}^{\downarrow\downarrow} e^{-i\theta} & 0 & \cdots & 0 & 0 & 0 \\ 0 & 0 & -V_{AB}^{\downarrow\downarrow} e^{i\theta} & E_B + U_2^{eff} & \ddots & \ddots & \vdots & \vdots & \vdots \\ 0 & 0 & 0 & \ddots & \ddots & \ddots & 0 & 0 & 0 \\ \vdots & \vdots & \vdots & \ddots & \ddots & E_A + U_{N-1}^{eff} & -V_{AB}^{\downarrow\downarrow} e^{-i\theta} & 0 & 0 \\ 0 & 0 & 0 & \ddots & \ddots & -V_{AB}^{\downarrow\downarrow} e^{i\theta} & E_B + U_{N-1}^{eff} & -V_{AB}^{\downarrow\downarrow} e^{i\theta} & 0 \\ 0 & 0 & 0 & 0 & \ddots & 0 & -V_{AB}^{\downarrow\downarrow} e^{-i\theta} & E_A + U_N^{eff} & -V_{AB}^{\downarrow\downarrow} e^{-i\theta} \\ -V_{AB}^{\downarrow\downarrow} e^{i\theta} & 0 & 0 & \cdots & 0 & 0 & 0 & -V_{AB}^{\downarrow\downarrow} e^{i\theta} & E_B + U_N^{eff} \end{bmatrix}$$

and for the next row, we use $\mathcal{D}_{2x\downarrow\downarrow}$

$$\mathcal{D}_{2x\downarrow\downarrow} = \begin{bmatrix} E_B + U_1^{eff} & -V_{AB}^{\downarrow\downarrow} e^{i\theta} & 0 & 0 & 0 & \cdots & 0 & 0 & -V_{AB}^{\downarrow\downarrow} e^{i\theta} \\ -V_{AB}^{\downarrow\downarrow} e^{-i\theta} & E_A + U_1^{eff} & -V_{AB}^{\downarrow\downarrow} e^{-i\theta} & 0 & 0 & \cdots & 0 & 0 & 0 \\ 0 & -V_{AB}^{\downarrow\downarrow} e^{i\theta} & E_B + U_2^{eff} & -V_{AB}^{\downarrow\downarrow} e^{i\theta} & 0 & \cdots & 0 & 0 & 0 \\ 0 & 0 & -V_{AB}^{\downarrow\downarrow} e^{-i\theta} & E_A + U_2^{eff} & \ddots & \ddots & \vdots & \vdots & \vdots \\ 0 & 0 & 0 & \ddots & \ddots & \ddots & 0 & 0 & 0 \\ \vdots & \vdots & \vdots & \ddots & \ddots & E_B + U_{N-1}^{eff} & -V_{AB}^{\downarrow\downarrow} e^{i\theta} & 0 & 0 \\ 0 & 0 & 0 & \ddots & \ddots & -V_{AB}^{\downarrow\downarrow} e^{-i\theta} & E_A + U_{N-1}^{eff} & -V_{AB}^{\downarrow\downarrow} e^{-i\theta} & 0 \\ 0 & 0 & 0 & 0 & \ddots & 0 & -V_{AB}^{\downarrow\downarrow} e^{i\theta} & E_B + U_N^{eff} & -V_{AB}^{\downarrow\downarrow} e^{i\theta} \\ -V_{AB}^{\downarrow\downarrow} e^{-i\theta} & 0 & 0 & \cdots & 0 & 0 & 0 & -V_{AB}^{\downarrow\downarrow} e^{-i\theta} & E_A + U_N^{eff} \end{bmatrix}.$$

where again one should notice that the A and B on-site energies, and the direction of flow has been switched from $\mathcal{D}_{1x\downarrow\downarrow}$ to $\mathcal{D}_{2x\downarrow\downarrow}$ matrix.
The off-diagonal blocks of $\mathcal{H}_{\downarrow\downarrow}$ consist of $\mathcal{O}_{1y\downarrow\downarrow}$ and $\mathcal{O}_{2y\downarrow\downarrow}$ matrices, and their complex transpose. They generate the staggered hopping $(t_{1A},\, t_{2A})$ of a spin down electron between two A-sites, and also the hybridization between A and B sites along the column of the lattice. The $\mathcal{O}_{1y\downarrow\downarrow}$ matrix can be found as

$$\mathcal{O}_{1y\downarrow\downarrow} = \begin{bmatrix} -V_{AB}^{\downarrow\downarrow}\, e^{i\theta} & -t_{1A} & 0 & 0 & 0 & \cdots & 0 & 0 & -t_{2A} \\ 0 & -V_{AB}^{\downarrow\downarrow}\, e^{-i\theta} & 0 & 0 & 0 & \cdots & 0 & 0 & 0 \\ 0 & -t_{2A} & -V_{AB}^{\downarrow\downarrow}\, e^{i\theta} & -t_{1A} & 0 & \cdots & 0 & 0 & 0 \\ 0 & 0 & 0 & -V_{AB}^{\downarrow\downarrow}\, e^{-i\theta} & \ddots & \ddots & \ddots & \vdots & \vdots \\ 0 & 0 & 0 & -t_{2A} & \ddots & \ddots & 0 & 0 & 0 \\ \vdots & \vdots & \vdots & \ddots & \ddots & -V_{AB}^{\downarrow\downarrow}\, e^{i\theta} & -t_{1A} & 0 & 0 \\ 0 & 0 & 0 & \ddots & \ddots & 0 & -V_{AB}^{\downarrow\downarrow}\, e^{-i\theta} & 0 & 0 \\ 0 & 0 & 0 & \ddots & 0 & 0 & -t_{2A} & -V_{AB}^{\downarrow\downarrow}\, e^{i\theta} & -t_{1A} \\ 0 & 0 & 0 & \cdots & 0 & 0 & 0 & 0 & -V_{AB}^{\downarrow\downarrow}\, e^{-i\theta} \end{bmatrix}$$

and $\mathcal{O}_{2y\downarrow\downarrow}$ matrix as

$$\mathcal{O}_{2y\downarrow\downarrow} = \begin{bmatrix} -V_{AB}^{\downarrow\downarrow} e^{-i\theta} & 0 & 0 & 0 & 0 & \cdots & 0 & 0 & 0 \\ -t_{2A} & V_{AB}^{\downarrow\downarrow} e^{i\theta} & -t_{1A} & 0 & 0 & \cdots & 0 & 0 & 0 \\ 0 & 0 & -V_{AB}^{\downarrow\downarrow} e^{-i\theta} & 0 & 0 & \cdots & 0 & 0 & 0 \\ 0 & 0 & -t_{2A} & -V_{AB}^{\downarrow\downarrow} e^{i\theta} & -t_{1A} & \ddots & \ddots & \vdots & \vdots \\ 0 & 0 & 0 & \ddots & \ddots & \ddots & 0 & 0 & 0 \\ \vdots & \vdots & \vdots & \ddots & \ddots & -V_{AB}^{\downarrow\downarrow} e^{-i\theta} & 0 & 0 & 0 \\ 0 & 0 & 0 & \ddots & \ddots & -t_{2A} & -V_{AB}^{\downarrow\downarrow} e^{i\theta} & -t_{1A} & 0 \\ 0 & 0 & 0 & \ddots & 0 & 0 & 0 & -V_{AB}^{\downarrow\downarrow} e^{-i\theta} & 0 \\ -t_{1A} & 0 & 0 & \cdots & 0 & 0 & 0 & -t_{2A} & -V_{AB}^{\downarrow\downarrow} e^{i\theta} \end{bmatrix}.$$

Their complex transpose reads

$$\mathcal{O}_{1y\downarrow\downarrow}^{\dagger} = \begin{bmatrix} -V_{AB}^{\downarrow\downarrow} e^{-i\theta} & 0 & 0 & 0 & 0 & \cdots & 0 & 0 & 0 \\ -t_{1A} & -V_{AB}^{\downarrow\downarrow} e^{i\theta} & -t_{2A} & 0 & 0 & \cdots & 0 & 0 & 0 \\ 0 & 0 & -V_{AB}^{\downarrow\downarrow} e^{-i\theta} & 0 & 0 & \cdots & 0 & 0 & 0 \\ 0 & 0 & -t_{1A} & -V_{AB}^{\downarrow\downarrow} e^{i\theta} & -t_{2A} & \ddots & \ddots & \vdots & \vdots \\ 0 & 0 & 0 & 0 & \ddots & \ddots & 0 & 0 & 0 \\ \vdots & \vdots & \vdots & \ddots & \ddots & -V_{AB}^{\downarrow\downarrow} e^{-i\theta} & 0 & 0 & 0 \\ 0 & 0 & 0 & \ddots & \ddots & -t_{1A} & -V_{AB}^{\downarrow\downarrow} e^{i\theta} & -t_{2A} & 0 \\ 0 & 0 & 0 & \ddots & 0 & 0 & 0 & -V_{AB}^{\downarrow\downarrow} e^{-i\theta} & 0 \\ -t_{2A} & 0 & 0 & \cdots & 0 & 0 & 0 & -t_{1A} & -V_{AB}^{\downarrow\downarrow} e^{i\theta} \end{bmatrix}$$

and

$$\mathcal{O}_{2y\downarrow\downarrow}^{\dagger} = \begin{bmatrix} -V_{AB}^{\downarrow\downarrow} e^{i\theta} & -t_{2A} & 0 & 0 & 0 & \cdots & 0 & 0 & -t_{1A} \\ 0 & -V_{AB}^{\downarrow\downarrow} e^{-i\theta} & 0 & 0 & 0 & \cdots & 0 & 0 & 0 \\ 0 & -t_{1A} & -V_{AB}^{\downarrow\downarrow} e^{i\theta} & -t_{2A} & 0 & 0 & 0 & 0 & 0 \\ 0 & 0 & 0 & -V_{AB}^{\downarrow\downarrow} e^{-i\theta} & 0 & \ddots & \vdots & \vdots & \vdots \\ 0 & 0 & 0 & -t_{1A} & \ddots & \ddots & 0 & 0 & 0 \\ \vdots & \vdots & \vdots & \ddots & \ddots & -V_{AB}^{\downarrow\downarrow} e^{i\theta} & -t_{2A} & 0 & 0 \\ 0 & 0 & 0 & \ddots & \ddots & \ddots & -V_{AB}^{\downarrow\downarrow} e^{-i\theta} & 0 & 0 \\ 0 & 0 & 0 & 0 & 0 & 0 & -t_{1A} & -V_{AB}^{\downarrow\downarrow} e^{i\theta} & -t_{2A} \\ 0 & 0 & 0 & \cdots & 0 & 0 & 0 & 0 & -V_{AB}^{\downarrow\downarrow} e^{-i\theta} \end{bmatrix}.$$

5.3 Lattice conductance

To compute the conductance (G) of the lattice we make use of Eq.(1.64),

$$G = e^2 \sum_{\mathbf{k},\sigma} \int \frac{d\xi}{2\pi} \frac{\Gamma^{\mathrm{L}}\Gamma^{\mathrm{R}}}{\Gamma^{\mathrm{L}} + \Gamma^{\mathrm{R}}} \mathcal{A}(d\mathbf{k}, \sigma, \xi) \left(-\frac{\partial n_{\mathrm{F}}(\xi)}{\partial \xi} \right)$$

that we derived in great detail in chapter 1. It is worth recalling that in this formula the dispersion of the metallic tip and substrate

$$\mathcal{H}_0 = \sum_{\mathbf{k},\sigma} \varepsilon_{\mathrm{sub},\mathbf{k}}\, c_{\mathrm{sub},\mathbf{k}\sigma}^{\dagger} c_{\mathrm{sub},\mathbf{k}\sigma} + \sum_{\mathbf{k},\sigma} \varepsilon_{\mathrm{tip},\mathbf{k}} c_{\mathrm{tip},\mathbf{k}\sigma}^{\dagger} c_{\mathrm{tip},\mathbf{k}\sigma},$$

the tunneling between the sample and substrate,

$$\mathcal{H}_{\mathrm{tunn.}}^{(1)} = \sum_{i} \sum_{\sigma=\uparrow,\downarrow} \left[\Gamma_1\, c_{\mathrm{sub},i\sigma}^{\dagger} d_{i\sigma} + h.c. \right]$$

and also the tunneling between the tip and sample

$$\mathcal{H}^{(2)}_{\text{tunn.}} = \sum_i \sum_{\sigma=\uparrow,\downarrow} \Big[\Gamma_2\, c^\dagger_{\text{tip},i\sigma} d_{i\sigma} + h.c.\Big].$$

are already accounted for small bias approximation (see chapter 1), and we only have to determine the sample spectral function $\mathcal{A}(d\mathbf{k}, \sigma, \xi)$, which is a simple task since the lattice Hamiltonian, Eq.(5.1), is quadratic and can be exactly diagonalized. Considering the definition of density of states in terms of spectral function

$$\rho(\xi) = \sum_{\mathbf{k},\sigma} \mathcal{A}(\mathbf{k}, \sigma, \xi) = |\Psi(\xi)|^2,$$

we compute the following quantity as the tip sweeps the lattice in discrete steps

$$G \sim \sum_\xi |\Psi(\xi)|^2 \left(-\frac{\partial n_{\text{F}}(\xi)}{\partial \xi}\right),$$

where ξ and $\Psi(\xi)$ are the eigenvalue and eigenstate of the lattice Hamiltonian which we obtain by diagonalization of the full Hamiltonian at each step.

5.4 Simulation of discharging rings interference pattern

Here, we systematically explore the parameter space of the full Hamiltonian. In each simulation, we variate only one parameter and keep the other parameters constant so that we can monitor the effect of that specific parameter on the discharging pattern without losing track. Since the size of the parameter space is relatively large, we restrict the simulations to six interesting collections of the most relevant intervals.

5.4.1 Pattern (1): a trivial pattern

The most straightforward discharging pattern is obtained by setting the hopping and hybridization amplitudes to zero and the sublattice on-site energies ($E_A,\ E_B$) to a finite value, Fig.(5.3). In this case, we can see that dots appear when the tip's local potential reaches the on-site energy of electrons at the sublattice A and turn into ever-growing rings as it ramps up. More importantly, rings always constructively interfere at the crossings in this setting.

5.4.2 Pattern (2): hybridized rings

We can see that intensity modulates around a ring when the A-B hybridization amplitudes take finite real values, Fig.(5.4). Similar to the trivial pattern, there is no gap opening at the crossing of the rings, but obviously, the intensity shifts more from the A-B axis to the A-A axis as the hopping amplitudes increases. This becomes more obvious when we show the line-cut of this pattern along the A-B axis.

5.4.3 Pattern (3): a complex pattern

A diverse number of effects emerges as the hybridization takes a finite phase ($\theta = \pi/2$) and when we allow the electrons to have a finite staggered hopping in the sublattice A-sites, Fig.(5.5). Most notably, the continuous symmetry of a ring reduces to a two-fold symmetry, and a gap opens at the crossings. This set of parameters is the most interesting case because it generates the closest patterns to the maps we have for the NTCDA/Ag(111) measurements.

5.4.4 Position dependence

Looking at the line-map of the three cases above side by side in Fig.(5.6), shows unambiguously how hybridization shifts the intensity and opens a small gap at the crossing point of two consecutive rings along the A-B axis and also a much larger gap opening along the bias axis once the staggered hopping amplitude becomes finite. Furthermore, we can discern a parabolic dependence of bias to (lateral) position in all cases.

5.4.5 Phase dependence

Changing phase of the complex hybridization in Fig.(5.7) makes a π-periodic modulation of the conductance intensity. It transfers the conductance from the oval shapes created by the intersection of two rings (two discharging events) to the small square regions created by the intersection of four rings (four discharging events). As a matter of fact, reproducing the pattern we see in measurements requires fine-tuning of the phase to obtain the correct intensity. Therefore, a real hybridization is insufficient.

5.4.6 Hopping amplitude dependence

Increasing the staggered hopping amplitudes (t_{1A}, t_{2A}) of the sublattice A, Fig.(5.8),[2] generates a gap along the hopping direction, for it pushes the electron energy level further below the Fermi level and thus harder to be gated[3]. This allows us to effectively make a hard and easy gating axis for the electrons, i.e., anisotropy. Besides, we can see that hopping broadens the linewidth of the rings.

[2] Without loss of generality, we set $t_{2A} = 0$ and only change t_{1A}.

[3] The electron hopping term (kinetic energy) in the real-space Hamiltonian comes with a minus sign convention which effectively lowers the on-site energy of the electron.

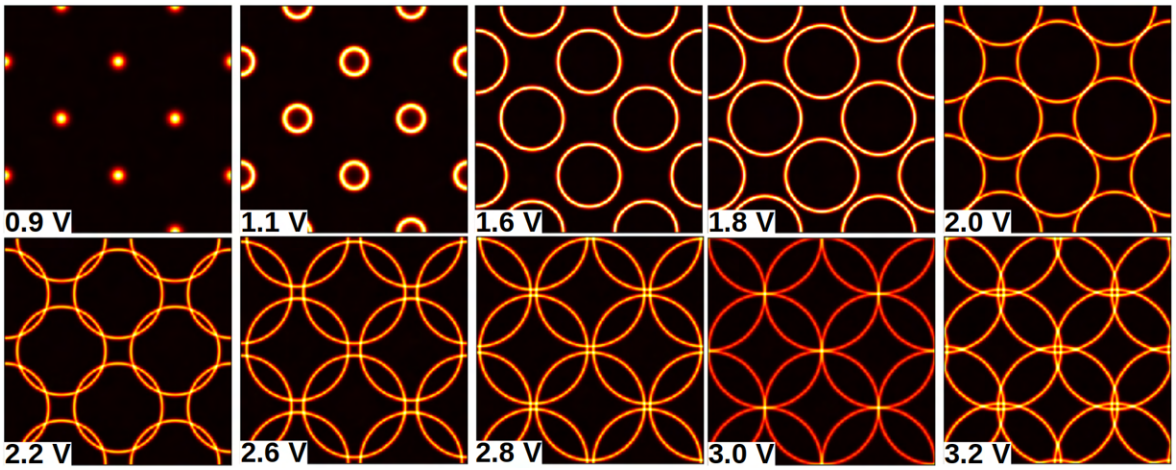

Figure 5.3: Evolution of discharging rings interference pattern (1) with increasing bias voltage. The 2D conductance map simulations are obtained with the following model parameters: $E_A = -0.5$ and $E_B = 3.0$ for the on-site energies of A and B sites, $t_{1A} = t_{2A} = 0$ for the staggered hopping amplitudes of the electron in the sublattice A, $V_{AB}^{\uparrow\uparrow} = V_{AB}^{\downarrow\downarrow} = 0.0$ for the hybridization amplitude of the spin up and down electrons between sublattice A and B, $\theta = 0$ for the complex phase of the hybridization, $T = 0.01$ for the temperature, $r = 1$, $\alpha = 0.5$, and $\epsilon_0 = 2$ for the radius of the tip apex, tip-gating efficiency, and sample dielectric constant, respectively.

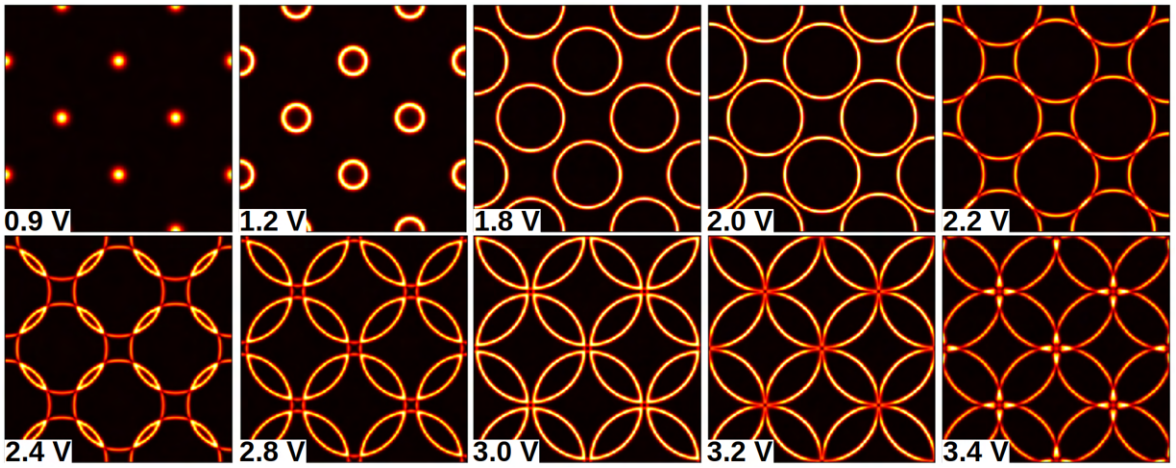

Figure 5.4: Evolution of discharging rings interference pattern (2) with increasing bias voltage. The 2D conductance map simulations are obtained with the following model parameters: $E_A = -0.5$ and $E_B = 3.0$ for the on-site energies of A and B sites, $t_{1A} = t_{2A} = 0$ for the staggered hopping amplitudes of the electron in the sublattice A, $V_{AB}^{\uparrow\uparrow} = V_{AB}^{\downarrow\downarrow} = 0.1$ for the hybridization amplitude of the spin up and down electrons between sublattice A and B, $\theta = 0$ for the complex phase of the hybridization, $T = 0.01$ for the temperature, $r = 1$, $\alpha = 0.5$, and $\epsilon_0 = 2$ for the radius of the tip apex, tip-gating efficiency, and sample dielectric constant, respectively.

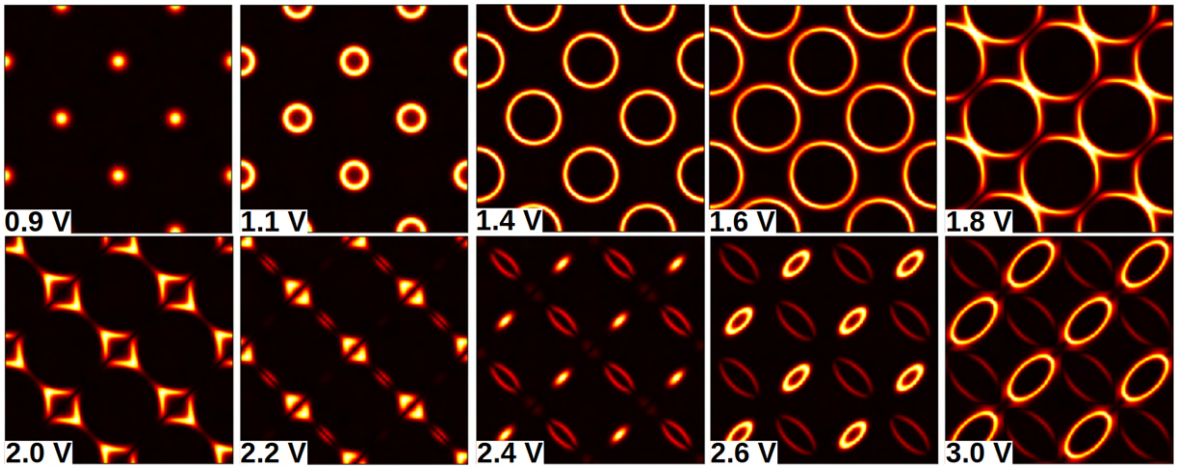

Figure 5.5: Evolution of discharging rings interference pattern (3) with increasing bias voltage. The 2D conductance map simulations are obtained with the following model parameters: $E_A = -0.5$ and $E_B = 3.0$ for the on-site energies of A and B sites, $t_{1A} = 0.1$ and $t_{2A} = 0$ for the staggered hopping amplitudes of the electron in the sublattice A, $V_{AB}^{\uparrow\uparrow} = V_{AB}^{\downarrow\downarrow} = 0.1$ for the hybridization amplitude of the spin up and down electrons between sublattice A and B, $\theta = \pi/2$ for the complex phase of the hybridization, $T = 0.01$ for the temperature, $r = 1$, $\alpha = 0.5$, and $\epsilon_0 = 2$ for the radius of the tip apex, tip-gating efficiency, and sample dielectric constant, respectively. The parameters are set to reveal the effect of complex hybridization amplitudes and staggered hopping on the patterns.

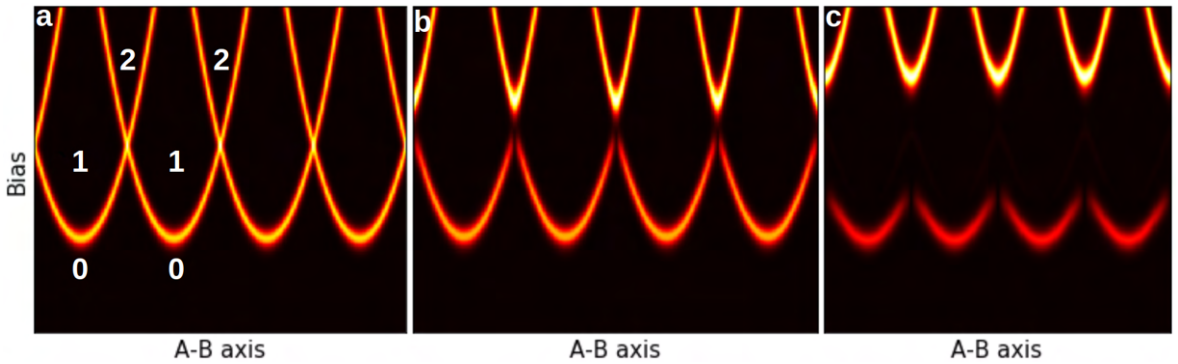

Figure 5.6: Position dependence of the discharging rings. The line-map simulations along the A-B axis of the bipartite lattice show parabolic modulation of the bias as a function of position, and also shift of intensity and gap opening at the crossing points of neighbouring rings. Panel **(a)**, **(b)**, and **(c)** are line-cuts of case (1), (2), and (3), respectively. The labels on panel **(a)** specify the number of discharging events.

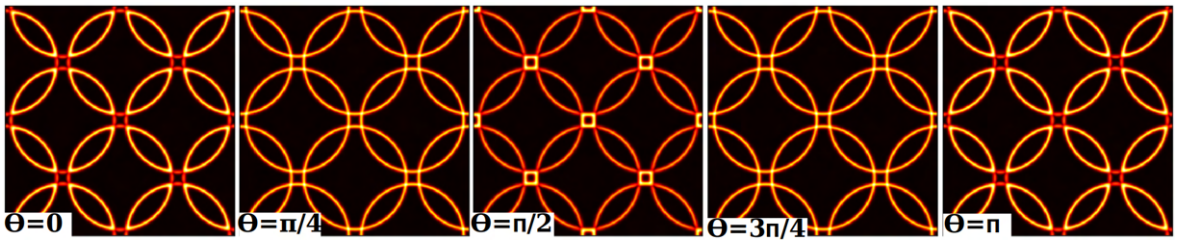

Figure 5.7: Phase dependence of the discharging rings. The 2D conductance map simulations are obtained while all parameters kept constant except the phase (θ) of the complex hybridization which is varied by a $\pi/4$ step. The constant parameters are: E_A = -0.5 and E_B = 3.0 for the on-site energies of A and B sites, V_b = 2.8 V for the bias, t_{1A} = t_{2A} = 0 for the staggered hopping amplitudes of the electron in the sublattice A, $V_{AB}^{\uparrow\uparrow}$ = $V_{AB}^{\downarrow\downarrow}$ = 0.1 for the hybridization amplitude of the spin up and down electrons between sublattice A and B, T = 0.01 for the temperature, r = 1, α = 0.5, and ϵ_0 = 2 for the radius of the tip apex, tip-gating efficiency, and sample dielectric constant, respectively.

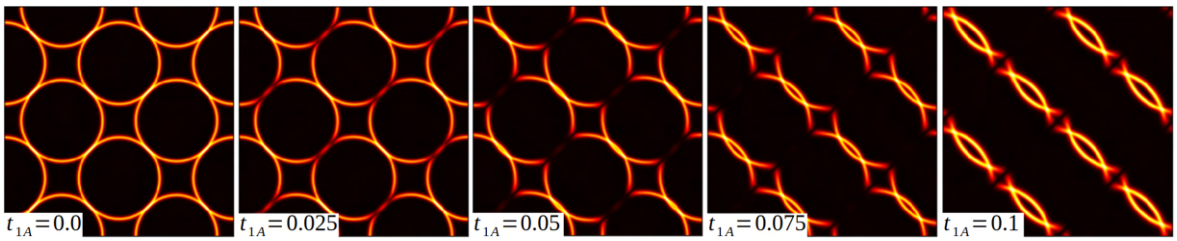

Figure 5.8: Hopping amplitude dependence of the discharging rings. The 2D conductance map simulations are obtained while all parameters kept constant except the staggered hopping amplitude (t_{1A}). The constant parameters are: E_A = -0.5 and E_B = 3.0 for the on-site energies of A and B sites, V_b = 2.0 V for the bias, t_{2A} = 0 for the staggered hopping amplitudes of the electron in the sublattice A, $V_{AB}^{\uparrow\uparrow}$ = $V_{AB}^{\downarrow\downarrow}$ = 0.1 for the hybridization amplitude of the spin up and down electrons between sublattice A and B, θ = $\pi/2$ for the complex phase of the hybridization, T = 0.01 for the temperature, r = 1, α = 0.5, and ϵ_0 = 2 for the radius of the tip apex, tip-gating efficiency, and sample dielectric constant, respectively.

5.5 Conclusion

We conclude this chapter by summarizing what we were able to simulate with this simple model. As a matter of fact, the rings are created as a direct consequence of the tip's local electric field that shifts the on-site energy of the electron to the Fermi level, which leads to a spike in the tunneling conductance. Considering the spatial dependence of the electric field, a ring is an equipotential line where the tip can discharge the electron located at its center. Naturally, as the electric potential increases, the size of the ring increases, meaning that the tip can discharge the electron at farther distances. Once the size of the rings surpasses the unit-cell size, they will interfere with each other and form new discharging patterns. In other words, the tip can be coupled to multiple charges located at different

lattice positions at the same time.

In the simplest version of the model, where the lattice Hamiltonian of A- and B-sites comprises only the on-site energies, the interference of the above-mentioned tunneling channels is always constructive, and therefore, the rings add up at the crossing points. However, once we let the electrons hop or hybridize between different sites and sublattices, new features appear on the discharging patterns. Most remarkably, hopping and hybridization shift the conductance intensity, broadens the ring's linewidth, and open up different gaps at the crossing points. Additionally, we have seen that a complex hybridization induces an alternating orbital current in the lattice, which leads to the redistribution of the conductance intensity between different discharging zones.

Last but not least, we have to be cautious that several important terms are missing in this model. Even though the relevance and substantiation of these terms goes beyond the scope of this thesis, very briefly, we will touch on them in the following. As we mentioned above, there are zones in the patterns where the tip is coupled to multiple charges[4] on the lattice. This means that the Coulomb interaction and correlation effect of these charges must be accounted for in the tunneling conductance. Moreover, even though we have included the spin degree of freedom in the single-particle Hamiltonian, it remains degenerate throughout the formalism. Upon the necessity, one can lift the spin degeneracy in various ways. The simplest way is to lift it along the z-axis with an applied magnetic field (B_z). This can be easily included in the Hamiltonian matrix as a Zeeman term $\left(g\mu_B B_z S_z\right)$ via the following substitution $\left(E_A \rightarrow E_A \pm g\mu_B B_z\right)$ for the spin-up $(+)$ and spin-down $(-)$ blocks. It results in the doubling of the rings. Another way to lift the S_z degeneracy is through the hybridization Hamiltonian, Eq.(5.4), by setting $V_{AB}^{\uparrow\uparrow} \neq V_{AB}^{\downarrow\downarrow}$.

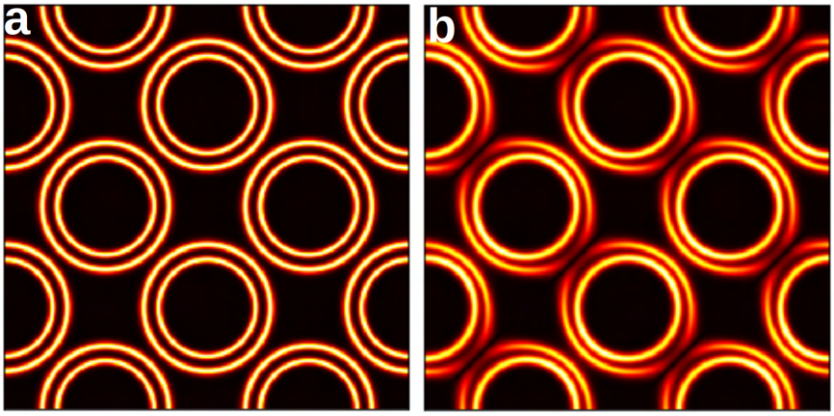

Figure 5.9: Lifting spin degeneracy giving rise to a double ring structure. Examples of lifting spin degeneracy: **a,** with an applied magnetic field ($B_z \neq 0$); and **b,** with the hybridization amplitudes $V_{AB}^{\uparrow\uparrow} \neq V_{AB}^{\downarrow\downarrow}$. The simulation **(a)** is performed with the same parameters as pattern (1), plus assuming $B_z = 0.05$, and simulation **(b)** with the same parameters as pattern (3), except for $V_{AB}^{\uparrow\uparrow} = 0.3$ and $V_{AB}^{\downarrow\downarrow} = 0.1$. Both simulations are obtained at $V_b = 1.6$.

[4] Zones with up to 4 discharges have been observed in our measurements.

In a similar way, one can also lift the degeneracy for S_x and S_y. One way is to introduce spin-flip terms $V_{AB}^{\uparrow\downarrow}$ and $V_{AB}^{\downarrow\uparrow}$ in the hybridization Hamiltonian, Eq.(5.4). Another way can be, for example, via the Dzyaloshinskii-Moriya interaction (DMI), which is an antisymmetric exchange interaction between neighboring spins (i, j)

$$\mathcal{H}_{\mathrm{DM}} = \sum_{i,j} \mathbf{D} \cdot \big(\vec{S}_{A,i} \times \vec{S}_{A,j}\big). \tag{5.11}$$

If we rewrite this term in the second quantization, it can be easily included into the Hamiltonian matrix. For the sake of simplicity, if we assume that the symmetry breaking happens only along the $y-$axis,

$$\mathbf{D} = (D_x,\, D_y,\, D_z) = (0,\, D_y,\, 0),$$

we can reduce Eq.(5.11) to

$$\begin{aligned}
\mathcal{H}_{\mathrm{DM}} &= \sum_{i,j} D_y \big(S_{A,i,z} S_{A,j,x} - S_{A,j,x} S_{A,i,z}\big) \\
&= \sum_{i,j} D_y \big[S_{A,i,z}\,,\, S_{A,j,x}\big] \\
&= \sum_{i,j} D_y (2i\,\hbar \delta_{i,j}\, S_{A,i,y}) \\
&= \sum_{i} 2i\hbar\, D_y\, S_{A,i,y}.
\end{aligned}$$

Now by setting $(\hbar = 1)$ and using the Abrikosov's pseudo-fermion representation of S_y spin operator

$$S_{A,i,y} = -\frac{i}{2}\big(c_{A,i,\uparrow}^{\dagger} c_{A,i,\downarrow} - c_{A,i,\downarrow}^{\dagger} c_{A,i,\uparrow}\big),$$

we find the second quantized $\mathcal{H}_{\mathrm{DM}}$ as

$$\mathcal{H}_{\mathrm{DM}} = D_y \sum_{i} \big(c_{A,i,\uparrow}^{\dagger} c_{A,i,\downarrow} - c_{A,i,\downarrow}^{\dagger} c_{A,i,\uparrow}\big). \tag{5.12}$$

The calculation follows analogously for the sublattice B. As we can see, the DMI is just another channel for the spin-flip process, which allows us to effectively break symmetry along the y-axis. Including these spin-flip terms (hybridization and DMI) into the Hamiltonian matrix is straightforward. One should only modify the diagonal elements of $\mathcal{H}_{\uparrow\downarrow}$ and $\mathcal{H}_{\downarrow\uparrow}$ with $\pm D_y$, and their off-diagonal elements with $V_{AB}^{\uparrow\downarrow}$ and $V_{AB}^{\downarrow\uparrow}$.

Chapter 6

Symmetry mediated tunable molecular magnetism on a 2D material

It reminds Hollywood movies where a tiny turn of the head traverses you from the classical to the quantum world. In nanoscale, however, owing to the magic of symmetry; it is part of reality. This chapter explores the impact of symmetry and adsorption geometry on the ground state of a metal-organic molecule adsorbed on a transition metal dichalcogenide, a van der Waals 2D superconductor. Namely, we identify two fundamentally different spin-related ground states by means of applied magnetic fields and their apparent planar symmetries in STM images. The two ground states are tunable by a small voltage pulse from the STM tip altering the twist angle between the molecule and the underlying substrate. One of the ground states is driven by a sizeable non-collinear Dzyaloshinskii–Moriya interaction between two electron spins on the molecule, which originates from the spin-orbit coupling in the van der Waals 2D material with broken mirror symmetries. On

the other ground state, we observe Yu-Shiba-Rusinov bound states, a genuinely quantum mechanical entity, formed due to partial screening of molecular spin by Cooper pairs from the superconducting substrate.
This chapter is adapted from our publication [135]:
Wang, Y., Arabi, S., Kern, K. and Ternes, M. Symmetry mediated tunable molecular magnetism on a 2D material. Commun Phys 4, 103 (2021).

6.1 Introduction

The emergence of strong electronic correlations in condensed matter physics as a result of modifying angle was initially introduced by twisted bilayer graphene, where a tiny angle mismatch between graphene layers dramatically changes the ground state at macroscopic scale and gives rise to unconventional superconductivity [136]. Here, we adopt a methodologically similar approach and resolve the changes of the ground state properties of a molecule-superconductor hybrid system (CoPc/2H-$NbSe_2$) at the nanoscale by means of a low-temperature scanning probe microscope.

The Cobalt phthalocyanine (CoPc) is an effective spin-1/2 system in the gas phase. Upon adsorption on the surface of an 2H-phase $NbSe_2$, it is found in two possible ground states: (i) a magnetic state with Yu-Shiba-Rusinov (YSR) bound states around the Fermi level, and (ii) a non-magnetic singlet ground state with a triplet excited state. We attribute the origin of the first ground state to the partial Kondo screening of the spin located on the central metallic ion of the molecule by the Cooper pairs, while the other to the quench of the central spin due to an in-plane antiferromagnetic interaction with a distributed magnetic moment on the molecular ligands.

The key idea to understand the stark deviation in magnetic properties of the two ground states is embedded in the significant non-collinear Dzyaloshinskii–Moriya interaction (DMI) induced by the 2D superconducting substrate [137, 138]. The DMI stems from the broken in-plane inversion symmetry in 2H-$NbSe_2$ and the significant spin-orbit coupling of the substrate induced by the heavy metal ion [139, 140].

6.2 Adsorption geometries of CoPc/2H-$NbSe_2$

CoPc is a flat-lying metal-organic molecule with two possible adsorption sites on the surface of 2H-$NbSe_2$ that shows different in-plane symmetries. The mirror planes of the molecule are found either aligned or twisted by $15°$ with respect to the three high symmetry planes of the surface, Fig.(6.1). The two different adsorption geometries can be explained by considering the point group symmetries of the molecule and the substrate. Upon adsorption, the surface of 2H-$NbSe_2$ acquire a $C_{3\nu}$ cyclic symmetry, with three identical mirror planes, and the CoPc a $C_{4\nu}$ symmetry, with in-equivalent pairs of σ_ν and σ_d mirror planes. The symmetries of these two entities must conform, and as a result, all rotational symmetries are broken, and only mirror planes survive. Therefore, the hybrid system can obtain the maximum symmetry if one of the three σ_ν mirror planes of the substrate aligns with one of the σ_ν of the CoPc, or otherwise with one of its σ_d mirror planes; resulting in only two distinct configurations which are off by $15°$ in-plane rotation. We observe that those molecules where their σ_d are aligned with the substrate's σ_ν have magnetic properties similar to the gas-phase CoPc, showing an effective spin $S = 1/2$ system [141]. We acronymize these molecules as $CoPc_\mathrm{d}$. And respectively, those molecules in which their σ_ν match with that of the substrate show charge transfer [142–144], and acquire a non-magnetic ground state. We accordingly acronymize them as $CoPc_\nu$.

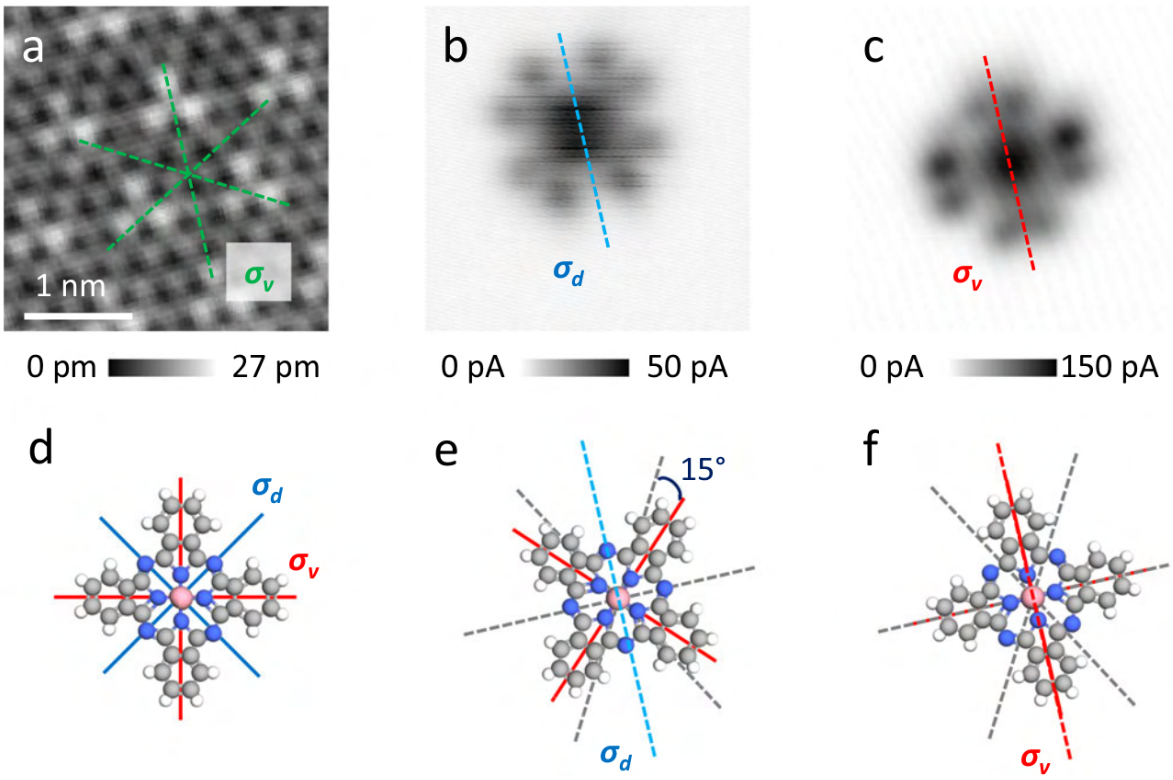

Figure 6.1: Absorption symmetry and spectral fingerprint of Cobalt phthalocyanine (CoPc) molecules on 2H-$NbSe_2$. Constant current image of the 2H-$NbSe_2$ surface showing the 3×3 charge-density wave superstructure ($V_b = -10$ mV, $I_p = 1$ nA). **b, c,** Constant-height scanning tunneling microscopy images of two CoPc molecules ($V_b = 400$ mV) adsorbed in different orientations. Colored dashed lines in **a-c** mark the different mirror planes of the CoPc molecules and the 2H-$NbSe_2$ surface. **d,** Model of the CoPc molecule with its vertical σ_ν (red lines) and diagonal σ_d (blue lines) mirror plane symmetries. **e, f,** Absorption models of CoPc molecules on 2H-$NbSe_2$. While the molecule in (**e**) is rotated by $15°$ with respect to one of the three principal axes of the substrate (gray dashed lines), the molecule in (**f**) is aligned (Taken from [135]).

6.3 Group theory of CoPc/2H-$NbSe_2$

The two adsorption geometries of the CoPc molecules on the 2H-$NbSe_2$ substrate can be understood using point-group theory. The gas-phase CoPc molecule has a D_{4h} symmetry, which, upon adsorption reduces due to the presence of the surface. Neglecting the charge density wave at sufficiently low temperatures, the symmetry of 2H-$NbSe_2$ surface reduces from the D_{3h} to the C_{3v} point group [145]. Combining these two high symmetry groups reduces the possible symmetry operations drastically. In particular, all non-trivial cyclic operations, i.e., rotations by $360°$, are broken due to the incommensurability of the allowed C_4 operations of the molecule with the C_3 operations of the substrate. Additionally, the inversion symmetry operation is also broken, leaving mirror symmetries as the only symmetry of the system.

The surface with $C_{3\nu}$ point group contains three mirror planes (σ_ν) (see Fig. 6.2a), while the CoPc molecule with $C_{4\nu}$ symmetry has four mirror planes: two vertical σ_ν and two dihedral σ_d planes, which have $45°$ angle mismatch (see Fig. 6.2b). To minimize the energy, the CoPc prefers high symmetry adsorption sites. Therefore, we find the following two configuration sites where one of the substrate's σ_ν planes is either aligned with one of the molecule's σ_v planes (Fig. 6.2c), or with one of the molecule's σ_d planes (Fig. 6.2d). The former symmetry describes the nonmagnetic CoPc_ν, while the latter in which the molecule is $15°$ rotated describes the doubly degenerate ($S = 1/2$) system, CoPc_d.

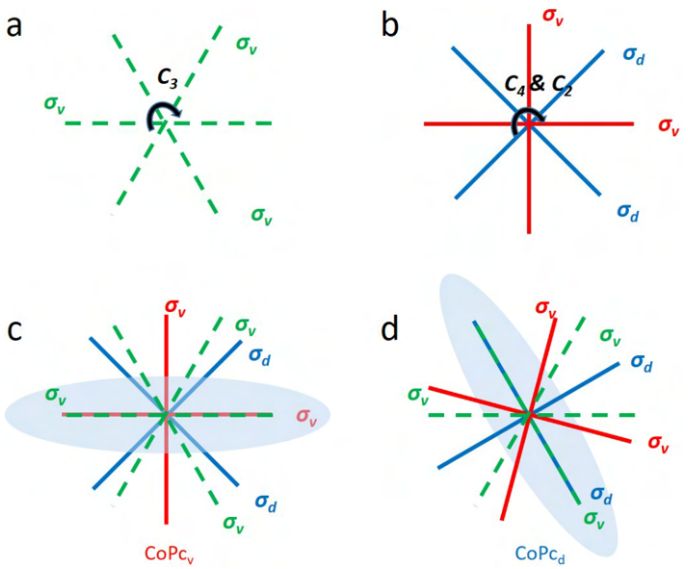

Figure 6.2: Symmetry conformation of CoPc/$NbSe_2$. **a, b**, The symmetry elements of $C_{3\nu}$ and $C_{4\nu}$ point group of the $NbSe_2$ surface and the adsorbed CoPc molecule. **c, d**, Sketch of the high symmetry conformation of the symmetry elements of the $C_{3\nu}$ and $C_{4\nu}$ point groups.

6.4 Kelvin probe force microscopy of CoPc molecules

To identify different charge states of the CoPc molecules, we performed the Kelvin probe force microscopy (KPFM) on them. Our data, Fig.(6.3), shows a remarkable difference between the energies of the dips on CoPc_d and CoPc_ν, allowing us to assign different charge states to them [146]. Evidently, the KPFM parabola of the CoPc_ν has a very broad dip around -3.25 eV, meaning that the charge is delocalized over the ligands of the molecule, leading to a negligible shift of the local work function. On the contrary, the CoPc_d shows a sharper dip at about -1.2 eV, implying that the charge is localized at Co^{2+} ion. We repeated the measurements over the ligands and obtained similar results. To eliminate the possibility of hydrogenation of the molecules as the origin of their different spin states, rather than the charge transfer that we proved above, we compared the topography and constant-height frequency shift measurement of CoPc_d, CoPc_ν, and H-CoPc in Fig.(6.4). The hydrogenated molecule indicates a different appearance from the other two.

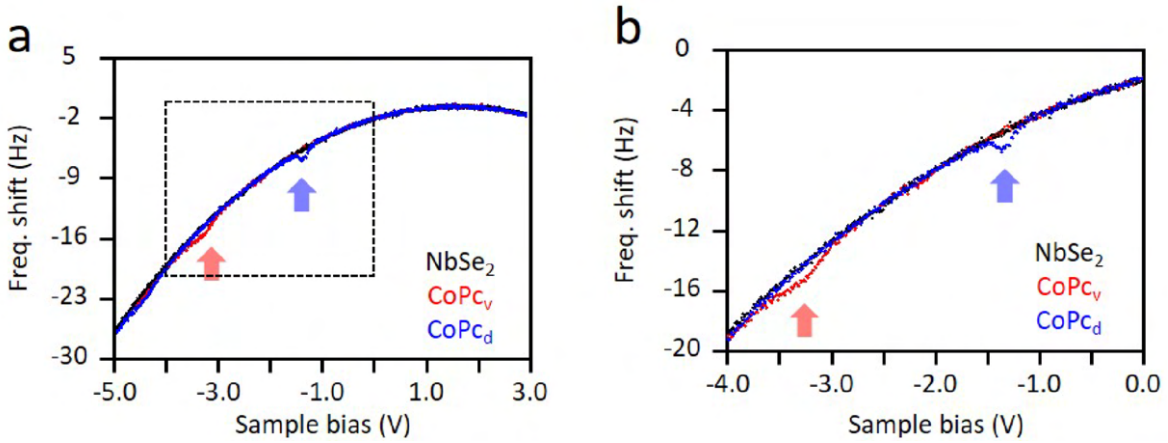

Figure 6.3: Kelvin probe force microscopy on CoPc molecules. **a**, Kelvin probe force microscopy data obtained on the $NbSe_2$ surface (black) and on the adsorbed CoPc molecules (red and blue), respectively. **b**, A zoom-in as marked in **a**. All spectra were measured with the same tip at the tip-sample distance. Dips on-top of the general parabolic spectra indicates the charging of $CoPc_\nu$ ($CoPc^0_\nu \rightarrow CoPc^+_\nu$) and $CoPc_d$ ($CoPc^0_d \rightarrow CoPc^+_d$), respectively.

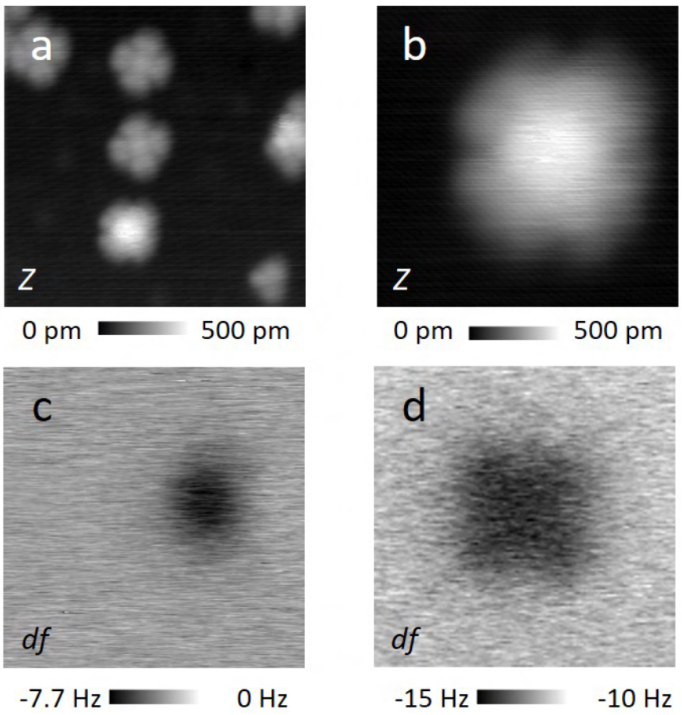

Figure 6.4: Hydrogenated CoPc. **a**, Constant-current SPM image (size 10×10 nm^2) of several CoPc molecules and one H-CoPc complex (lower left molecule). **b**, Zoom-in SPM image of the H-CoPc complex ($V = -500$ mV, $I = 10$ pA). **c, d**, Constant height df image of a H-CoPc (**c**) and a bare $CoPc_\nu$ molecule (**d**). Both molecules have a $S = 0$ ground state but a significant difference in the topographical appearance. Setpoint parameters at molecular center of the H-CoPc complex: $V = -500$ mV $I = 10$ pA. Set point parameters at molecular center of the bare $CoPc_\nu$ are $V = -20$ mV, $I = 20$ pA.

6.5 YSR states on $CoPc_d$ molecules

Magnetic impurities induce subgap bound states on the surface of a s-wave superconductor, due to interaction of the unscreened impurity spin with the Andreev reflected electrons or holes, which can penetrates to the superconductor for several nanometers. The phenomenon was independently discovered by Yu, Shiba and Rusinov in the late 1960s and have been observed in numerous measurements since then [147–149]. Here we investigate it in a molecular spin which is placed in a superconducting tunnel junction by means of a lead coated tip [150], i.e., tip and substrate are both superconductors. The effective superconducting gap of the tip is $\Delta_T \approx 1.15$ meV and of the substrate is $\Delta_S \approx 1.3$ meV. The YSR states appear in a particle-hole (PH) pair at $\approx \pm 1.8$ mV on the molecule, with an asymmetric intensities indicating PH symmetry breaking, Fig.(6.5 a, b). The origin of this symmetry breaking is attributed to the nonmagnetic background Coulomb scattering [151], which we estimate to $\pi\rho_S U = 0.28 \pm 0.02$.

Denoting the origin of the YSR states allows us to extract the fundamental scales of the problem from the magnetic-dependent measurements. As we stated earlier, they can be merely created in the weak Kondo coupling regime where normal conducting electrons are depleted at the superconducting gap, leading to a partial Kondo screening of the impurity spin. This requires that the Kondo temperature to be smaller than the Cooper pair binding energy ($\Delta_S > k_B T_K$) [152]. In other words, the local magnetic field of the unscreened spin is not strong enough to break the Cooper pairs and locally collapse the superconducting gap. Therefore, to see the Kondo splitting of the magnetic moment, one needs first to quench the superconductivity, which naturally has a critical value.

Upon quenching superconductivity, the gap fills with normal electrons and subsequently allows the impurity spin to antiferromagnetically couple to them and produce a Kondo resonance at the Fermi level. Based on our results, a magnetic field of $B \geq 5$ T normal to the sample surface is sufficient to quench the superconductivity of both tip and sample and reveal the unscreened spin of the $CoPc_d$. Fig.(6.5c) shows that the Zeeman energy ($E_Z = g\mu_B B$) of 5 T is not only enough to quench the superconductivity but also split the Kondo peak ($E_Z \geq k_B T_K$) with equal intensity around zero bias, accounting for its $S = 1/2$ state. By treating the molecule as a classical spin-1/2 system, we can approximate its effective magnetic moment as

$$1/2\pi\rho_S J_S S = -0.60 \pm 0.02 \tag{6.1}$$

where J_S is the antiferromagnetic coupling of the molecule spin to the normal electrons in the substrate with local density of state ρ_S. Usually, the antiferromagnetic exchange coupling strength cannot be measured directly, even though it controls the Kondo resonances and also the YSR states energies. The detail of the perturbative model we used to calculate the energies of the YSR states in Fig.(6.5 a) is presented in the next section.

We extract a Landé g-factor of 1.54 ± 0.02 from the linear regression of the Zeeman splitting, Fig.(6.5d), which is smaller than the one for a free electron. Furthermore, the interception of the linear fit with the abscissa gives the minimum magnetic field required to split the Kondo peak, amounting to $B_K = 0.67 \pm 0.19$ T. One has to take into account that this is a very naive

estimation of B_K as it typically plays a very complicated role with the Kondo singlets [153, 154]. However, from this two quantities (g, B_K) we can estimate the Kondo temperature of $T_K \approx g\mu_B B_K/k_B = 0.77 \pm 0.24\,\mathrm{K}$, lying perfectly in the weak coupling regime. Historically, the formalism of the weak-coupling Kondo effect developed by Anderson and Appelbaum [155, 156]. It is a second-order perturbation theory also known as $s-d$ exchange model, to explain the zero bias tunneling anomaly which was observed in various $p-n$ junctions and insulating oxide layers.

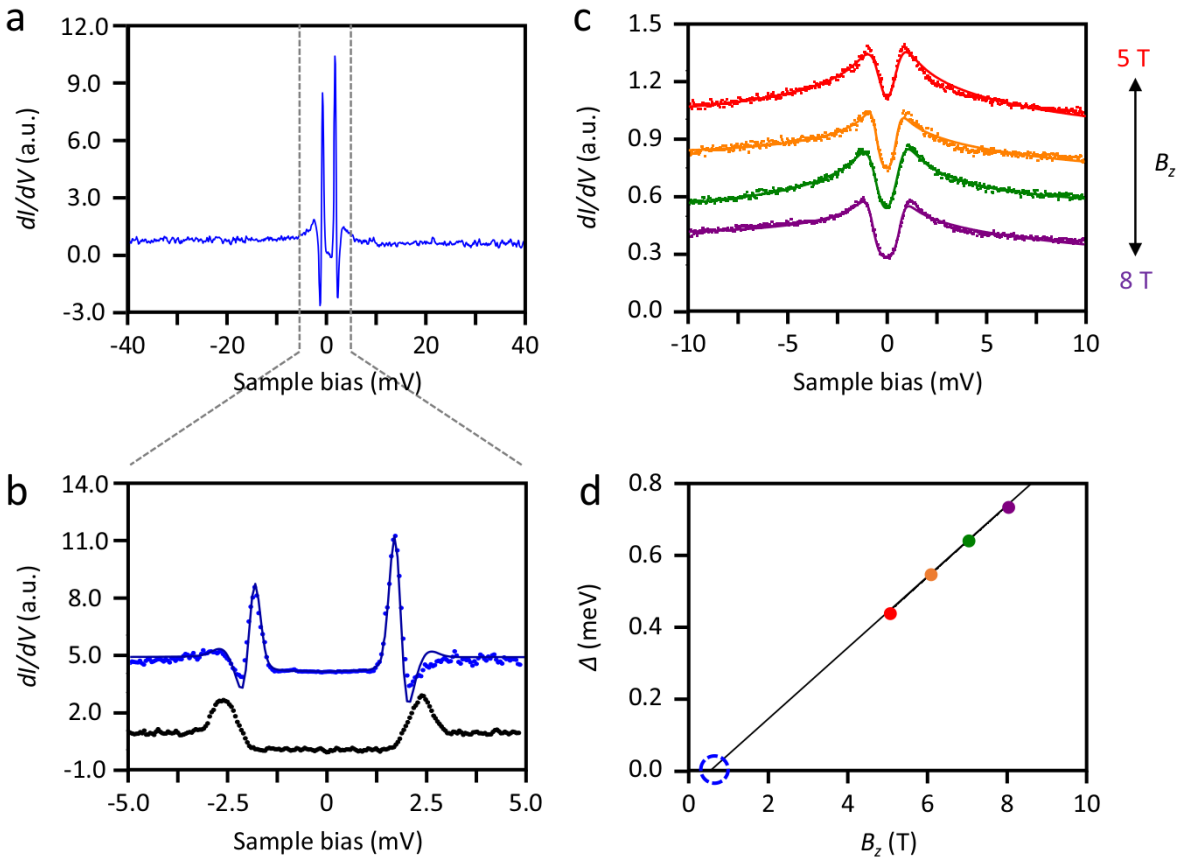

Figure 6.5: Spectral features of a Cobalt phthalocyanine molecule with diagonal σ_d mirror plane symmetry ($CoPc_d$). **a, b,** Differential conductance (dI/dV) spectra measured on the bare $NbSe_2$ sample (black dots) and the center of a $CoPc_d$ molecule (blue dots) by using a superconducting tip ($V_b = -40$ mV, $I_p = 40$ pA in **a**; $V_b = -5$ mV, $I_p = 50$ pA in **b**). Full line in **b** is a least-square fit to a scattering model in which the magnetic impurity is treated classically. **c,** Differential conductance spectra measured on $CoPc_d$ at magnetic fields large enough to suppress superconductivity (dotted lines, $V_b = -10$ mV, $I_p = 100$ pA) and least-square fits using a perturbative scattering model (full lines). Curves are vertically offset for clarity. **d,** Extracted splitting Δ of the peaks in **c** and linear regression (full line). The dashed circle marks the crossing of the regression with the abscissa.

6.6 Simulation of YSR states in a superconducting tunnel junction

In superconducting tunnelling junction, both tip and sample are superconductors with a quasiparticle excitation spectrum described in the framework of the Bardeen-Cooper-Schrieffer (BCS)-theory of superconductivity as

$$\rho_{\mathrm{BCS}}(\varepsilon) = \rho_{\mathrm{S}}\,\mathrm{Im}\left(\frac{\varepsilon + \mathrm{i}\Gamma}{\sqrt{\Delta^2 - (\varepsilon + \mathrm{i}\Gamma)^2}}\right), \tag{6.2}$$

where Δ is the superconducting gap width of either sample or tip, $i\Gamma$ is a small imaginary number accounting for the finite lifetime effects of the quasiparticles around the gap edge ($\Gamma \ll \Delta$), and ρ_{S} is the density of states of the sample at Fermi energy in the normal conducting state [157]. The differential conductance (dI/dV) for tunneling between superconducting tip and sample reads

$$\frac{dI}{dV}(V) \propto \frac{d}{dV}\int_{-\infty}^{+\infty} \rho_{\mathrm{BCS_S}}(\varepsilon)\rho_{\mathrm{BCS_T}}(\varepsilon - eV)\big[f(\varepsilon) - f(\varepsilon - eV)\big]d\varepsilon, \tag{6.3}$$

with $f(\varepsilon) = [1 + \exp(\varepsilon/k_{\mathrm{B}}T)]^{-1}$ being the Fermi–Dirac distribution, k_{B} the Boltzmann constant, and T the effective temperature.
The interaction between the superconducting Cooper pairs and the unscreened spin leads to a pair of YSR peaks around the Fermi energy. By approximating the spin as a classical magnetic moment, the energy (E_{YSR}) and intensities ($I_{\pm}$) of the peaks reads [151, 158, 159]:

$$E_{\mathrm{YSR}} = \Delta_{\mathrm{S}}\frac{1 - w^2 + u^2}{\sqrt{(1 - w^2 + u^2)^2 + 4w^2}}, \tag{6.4}$$

$$I_{\pm} = -\rho_{\mathrm{S}}\frac{2w(1 + (w \mp u)^2)}{\left((1 - w^2 + u^2)^2 + 4w^2\right)^{3/2}}, \tag{6.5}$$

where Δ_{S} is the effective superconducting gap of the 2H-$NbSe_2$ substrate, S is the local impurity spin, J_{S} is the antiferromagnetic exchange coupling, U is the local Coulomb potential, and w and u are the dimensionless parameters defined as

$$w = \frac{1}{2}\pi\rho_{\mathrm{S}}J_{\mathrm{S}}S < 0\,, \qquad u = \pi\rho_{\mathrm{S}}U.$$

The quasiparticle excitation spectrum of the magnetic impurity then reads

$$\rho^{nn}_{\mathrm{YSR}}(\varepsilon) = -\frac{1}{\pi}\mathrm{Im}G^{R,nn}(\varepsilon), \tag{6.6}$$

where $\rho^{nn}_{\mathrm{YSR}}(\varepsilon)$s are the diagonal elements of the spectral function with $n = (1, 2)$ superscript addressing electron ($n = 1$) and hole ($n = 2$) components of the YSR state.
The full retarded Green's function at finite temperature $G^R(\varepsilon)$ is defined in terms of the Dyson equation as

$$G^R(\varepsilon) = G^R_0(\varepsilon) + G^R_0(\varepsilon)VG^R(\varepsilon)\,, \quad G^R(\varepsilon)^{-1} = G^R_0(\varepsilon)^{-1} - \Sigma,$$

where $G_0^R(\varepsilon)$ is the free Green's function

$$G_0^R(\varepsilon) = \frac{-\pi\rho_S}{\sqrt{\Delta_S^2 - (\varepsilon + i\Gamma)^2}} \begin{pmatrix} \varepsilon + i\Gamma & \Delta_S \\ \Delta_S & \varepsilon + i\Gamma \end{pmatrix},$$

and Σ is the impurity self-energy matrix

$$\Sigma = \frac{1}{\pi\rho_S} \begin{pmatrix} w + u & 0 \\ 0 & w - u \end{pmatrix}.$$

The differential conductance of the superconducting tunneling junction with YSR states is then the convolution of Eq.(6.2) and Eq.(6.6), which we additionally broaden them by a Gaussian distribution function $g(\varepsilon) = \frac{1}{\sqrt{\pi}\gamma} e^{-\left(\frac{\varepsilon}{\gamma}\right)^2}$ [160],

$$\begin{aligned} \frac{dI}{dV}(V) \propto \frac{d}{dV} \int_{-\infty}^{+\infty} \int_{-\infty}^{+\infty} \Big[& \rho_{\mathrm{BCS_T}}(\varepsilon) \rho_{\mathrm{YSR}}^{11}(\varepsilon' - eV)(f(\varepsilon) - f(\varepsilon' - eV)) \\ & + \rho_{\mathrm{BCS_T}}(\varepsilon' - eV) \rho_{\mathrm{YSR}}^{22}(\varepsilon)(f(\varepsilon' - eV) - f(\varepsilon)) \Big] g(\varepsilon - \varepsilon') d\varepsilon' d\varepsilon. \end{aligned} \tag{6.7}$$

6.7 Singlet–triplet transition in $CoPc_v$ molecules

There is a strikingly dissimilar physics ruling over the $CoPc_\nu$ molecules. On the one hand, we observe no subgap YSR states or other signatures of magnetism, such as Kondo resonance or zero-bias peak splitting at the Fermi level. On the other hand, these molecules show very strong, symmetric, inelastic steps at $|V_b| \approx 23$ mV. We attribute these steps to a singlet-triplet (ST) transition, Fig.(6.6a, b), accompanied by a *normal* singlet ground state[1]. We interrogate the magnetism of the ST transition by applying magnetic fields perpendicular to the sample, resulting in the splitting of the steps, which unequivocally corroborate its magnetic nature [161].

[1] Here, we used the term normal singlet (drop the normal henceforth) to discriminate it from a Kondo singlet.

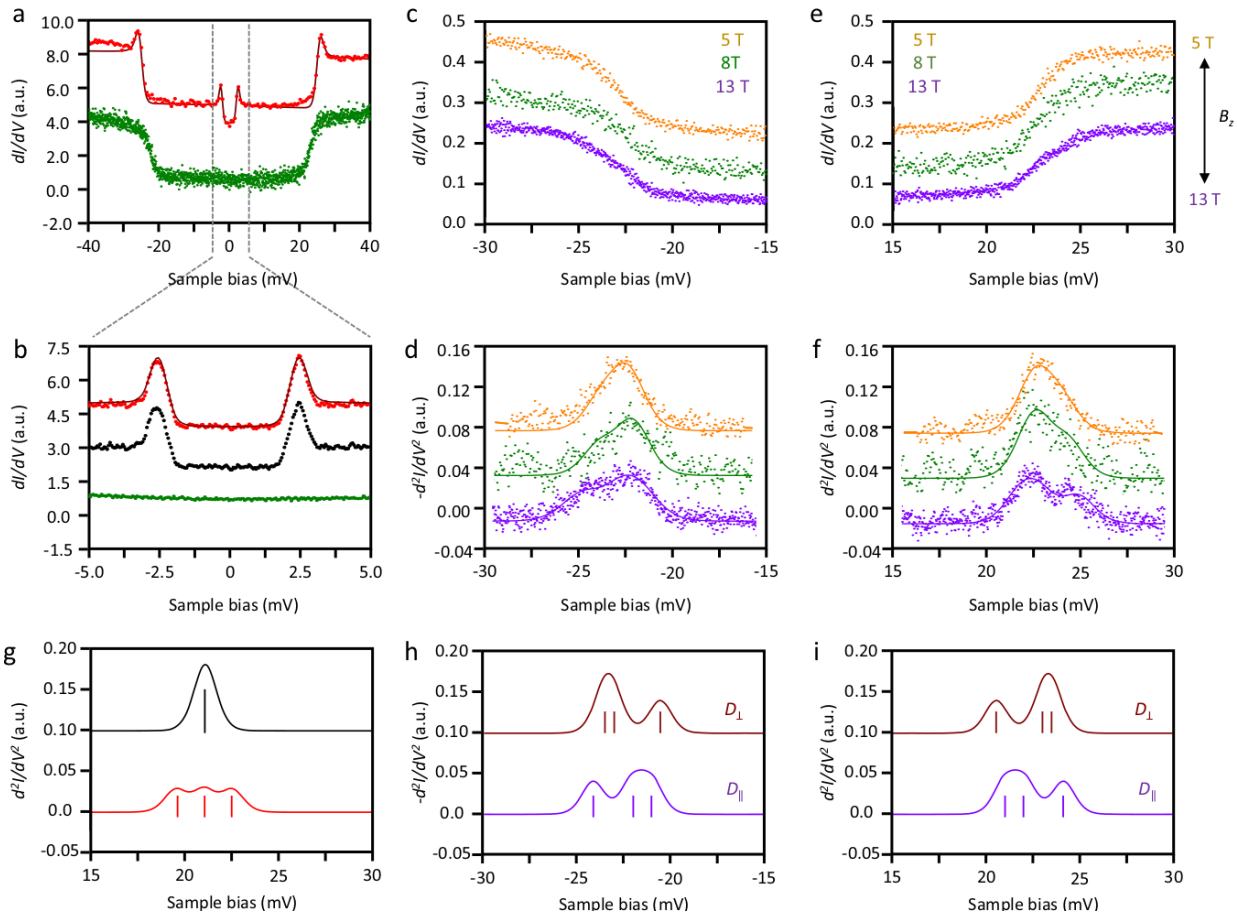

Figure 6.6: The singlet-triplet transition in a Cobalt phthalocyanine molecule with vertical σ_ν mirror plane symmetry (CoPc$_\nu$). a, Differential conductance (dI/dV) spectra measured on CoPc$_\nu$ at $B = 0$ (red dots) and at $B = 8$ T, where superconductivity is suppressed (green dots). Here, B is the magnetic field perpendicular to the sample surface. The full line at $B = 0$ is a least-square fit to a model, which accounts for the superconducting gaps in tip and sample and the spin excitation. **b,** Detail of the curves in a (red and green dots) and spectrum measured on the bare $NbSe_2$ surface (black dots), showing that neither Yu-Shiba-Rusinov states nor a Kondo peak can be detected on the molecule ($V = -5$ mV, $I = 50$ pA). The dark red line is a fit to a superconducting tunneling model. **c–f,** dI/dV and numerically derived d^2I/dV^2 spectra measured on CoPc$_\nu$ at $B = 5, 8$ and 13 T, respectively. Full lines in (**d, f,**) are least-square fits to a perturbative transport model. The spectra reveal an asymmetric splitting of the inelastic excitation at $\approx \pm 23$ mV in magnetic field. **g,** Expected splitting of a triplet excitation at $B = 13$ T (red line) if only Heisenberg exchange interaction between both spins is taken into account. **h, i,** Accounting for an additional non-collinear Dzyaloshinskii–Moriya (DM) interaction rationalized the observation of the DM vector lies in the surface plane ($D_\parallel$). A DM vector pointing out of surface ($D_\perp$) would reverse the intensity order. Curves in all panels are vertically offset for clarity.

6.8 Non-collinear intra-molecular spin-spin interaction

We attribute the observed symmetry reduction in the $CoPc_\nu$ to a charge transfer from the substrate and demonstrate it by taking Kelvin probe force microscope (KPFM) measurements on both kinds of molecules. The KPFM result of $CoPc_\nu$ Fig.(6.3) shows that the central ion strongly couples to the substrate and, therefore, has only a minor change in the local work function. This suggests that the transferred electron is distributed in the large ligand of the molecule and makes only a tiny dip on the KPFM parabola, in contrast to a localized charge that typically creates a more significant signal. The transferred charge induces an additional magnetic moment, which interacts antiferromagnetically with the moment localized at the Co^{2+} ion and leads to a singlet ground state with a triplet excited state. In principle, under a magnetic field the degeneracy of the triplet state is lifted, and it splits into three identical peaks, Fig.(6.6g). Surprisingly, when we apply a magnetic field along z-axis, the ST transition split into only two peaks of different heights with approximately 2:1 ratio Fig.(6.6 d, f). We relate this to the presence of a non-collinear interaction between spins, which induces an in-plane magnetic moment by decanting the spin towards the surface Fig.(6.9g).

Different magnetic interactions in $CoPc_\nu$ are summarized in the following Hamiltonian

$$H_{\mathrm{CoPc}_\nu} = \sum_{i=1,2} g\mu_B S_z^i B + J_{ST}\,\mathbf{S}_1 \cdot \mathbf{S}_2 + \mathbf{D_{ST}} \cdot (\mathbf{S}_1 \times \mathbf{S}_2). \tag{6.8}$$

We consider a Zeeman splitting for both magnetic moments on the molecule under an applied magnetic field along the z-axis, introduced in the first term. Moreover, we allow the spins to interact with each other inside the molecule in two ways: an isotropic Heisenberg-type interaction (J_{ST}), which is captured in the second term, and a non-collinear DM interaction ($\mathbf{D_{ST}}$), the last term [137, 138]. Subsequently, we use a perturbative tunneling model based on the above model Hamiltonian Eq.(6.8) to simulate the measured results [161]. In this manner, the Heisenberg coupling strength is found as $J_{ST} = 21.6 \pm 0.5$ meV and the DM vector, which lies mainly in the substrate plane, as $|\mathbf{D_{ST}}| = (0.45 \pm 0.1) \times J_{ST}$, Fig.(6.6d, f). The possibility of having a significant out-of-plane DM vector ($\mathbf{D}_\perp$) is ruled out as it reverses the order of peaks compared to the experimental measurements (check Fig.(6.6 h, i).

6.9 Simulation of Heisenberg models with DM interaction

The Hamiltonian of $CoPc_\nu$, Eq.(6.8), can be rewritten as

$$H_{\mathrm{CoPc}_\nu} = \sum_{i=1,2} g_i \mu_{\mathrm{B}} \hat{S}_z^i B + \mathbf{S}^1 \mathcal{T} \mathbf{S}^2, \tag{6.9}$$

where $\mathcal{T} = \begin{pmatrix} J_x & D_z & D_y \\ -D_z & J_y & -D_x \\ -D_y & D_x & J_z \end{pmatrix}$ is the coupling matrix incorporating both Heisenberg and DM interactions. The general form of Eq.(6.9) allows us to discuss different terms of the Hamiltonian and exclude possible interaction schemes based on the evolution of their eigenvalues in the external magnetic field, compared to the experimental result.

First, we consider an isotropic Heisenberg model with exchange couplings: $J_x = J_y = J_z = J_{\mathrm{ST}} = 21.6$ meV and g-factors $g_1 = g_2 = 2$, neglecting any DM interaction ($\mathbf{D}_{\mathrm{ST}} = \vec{0}$). Fig.(6.7 a) shows the evolution of its eigenvalues versus B-field. At zero field only transitions at an energy of J_{ST} between $(S, S_z) = \langle 0, 0\rangle$ singlet and the three degenerate triplet states $(S, S_z) = \langle 1, 0\rangle$ and $(S, S_z) = \langle 1, \pm 1\rangle$ are possible, while at large enough B-field the triplet state splits in three independent states with equal excitation amplitude. The calculated dI^2/d^2V spectra of this model is shown in Fig.(6.6g). This model is obviously incompatible with the experimental data.

Second, we consider the isotropic Heisenberg model with an in-plane DM interaction. Fig.(6.7b) shows the evolution of its eigenvalues using the same isotropic exchange coupling terms as in Fig.(6.7a), and an additional in-plane DM term with coupling $D_x = 0.45\, J_{\mathrm{ST}}$, $D_y = D_z = 0$. Here, the colored dots correspond to the energies of the simulated d^2I/dV^2 peaks in Fig.(6.6 d, f). This model fits our observed spectroscopic data well. Experimentally, since the relatively short lifetime of the excitations leads to a significant broadening at $B = 0$ all three excitations merge to only one detectable peak and at $B \geq 5$ T they appear in two peaks with $\approx 1:2$ intensity ratio.

Even though the second coupling scheme fits our experimental data well, it is not evident that it is the physically only possible solution. Therefore, in the following, we will discuss other coupling schemes, which, as it becomes clear, do not lead to a description consistent with our observations. Note that due to the inherent symmetry of the molecule, we restrict our search to cases where the intramolecular in-plane coupling constants J_x and J_y are identical.

Therefore, we now assume Ising-like couplings $J_x = J_y = 0$, $J_z = J_{\mathrm{ST}}$. At zero magnetic field the eigenstates are doubly-degenerate with $|\uparrow\downarrow\rangle$ and $|\downarrow\uparrow\rangle$ as the ground state, and $|\uparrow\uparrow\rangle$ and $|\downarrow\downarrow\rangle$ as the excited state. While the doublet ground state is not influenced by the magnetic field so long as $g_1 = g_2$, the excited states split, Fig.(6.7c), leading to two excitations with equal intensity which does not correspond to the experimental observations, Fig.(6.7e).

Because the molecule is highly symmetric in its plane, next we check whether an exclusively planar coupling of the form $J_x = J_y = J_{\mathrm{ST}}$, $J_z = 0$ could be a reasonable description of the spin system. As Fig.(6.7d) illustrates, such couplings lead to a $(S, S_z) = \langle 0, 0\rangle$ ground state, and a doubly-degenerate excited state $(S, S_z) = \langle 1, \pm 1\rangle$ at energy of $J_{\mathrm{ST}}/2$, which splits in finite magnetic field, and an additional excited state $(S, S_z) = \langle 1, 0\rangle$ at energy of J_{ST}, which does not react to the magnetic field. Contrary to our observation, at $B = 0$, this coupling scheme results into two excitations from the ground state, Fig.(6.7f).

From the above discussed scenarios, we conclude that any XXZ and XYZ Heisenberg models with arbitrary values of $J_x = J_y$ and J_z, and also Ising model, can not describe our observations. This further points to the proposed model discussed before: an isotropic Heisenberg model with an additional non-collinear DM interaction.

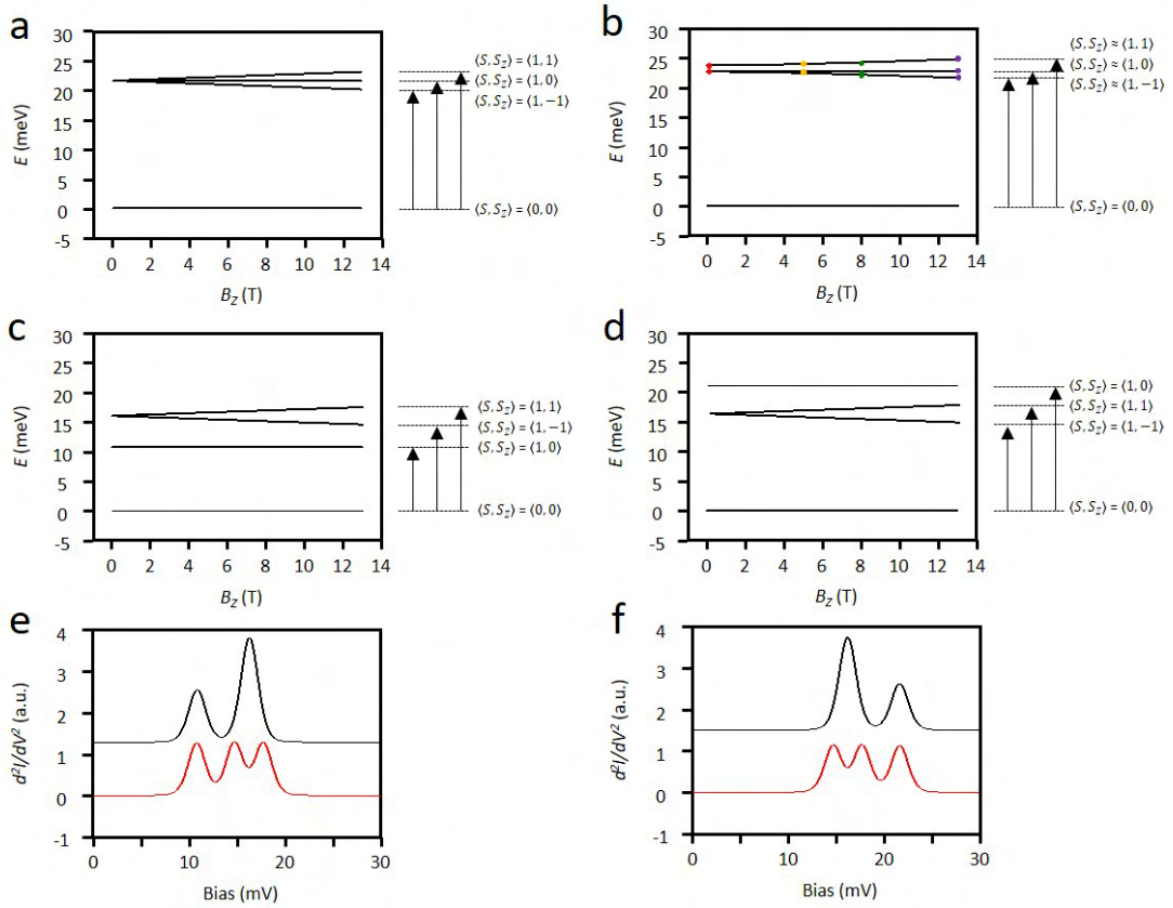

Figure 6.7: Simulation of the spin excitations under magnetic fields and the corresponding $\mathbf{d^2I/dV^2}$ spectra. a, The eigenvalues and eigenstates versus out-of-plane magnetic field strength of an isotropic Heisenberg model with couplings $J_x = J_y = J_z = J_{\mathrm{ST}} = 21.6$ meV. **b**, The eigenvalues and eigenstates versus out-of-plane magnetic field strength of an isotropic Heisenberg model with the same couplings as **(a)** and an additional in-plane DM interaction with $|\mathbf{D}_{\parallel}| = 0.45 \times J_{\mathrm{ST}}$. The colored dots are the energies of the peaks of the calculated d^2I/dV^2 in Fig.(6.6). **c, d**, Same as **(a)** for an anisotropic Heisenberg exchange coupling with $J_x = J_y = 0$ and $J_z = 21.6$ meV (**c**) and $J_x = J_y = 21.6$ meV and $J_z = 0$ (**d**), respectively. **e, f**, Modelled d^2I/dV^2 spectra for the simulations in (**c**) and (**d**), without magnetic field (black line) and with $B = 13$ T (red line), respectively. The arrows on the right-hand side of the panels (**a-d**) mark the possible transition between the energy levels labeled with the total spin (S) and its z-axis projection (S_z).

6.10 Tunneling conductance of the singlet-triplet transition on $CoPc_\nu$

The total tunneling current through the singlet-triplet transition on $CoPc_v$ can be calculated by decomposing it into its elastic and inelastic parts ($I = I_{\text{el.}} + I_{\text{inel.}}$). The elastic tunneling current follows as

$$\begin{aligned} I_{\text{el.}} =& \sigma_{\text{el.}} \int_{-\infty}^{+\infty}\int_{-\infty}^{+\infty} \Big[\rho_{\text{BCS}_\text{S}}(\varepsilon' - eV)\, \rho_{\text{BCS}_\text{T}}(\varepsilon) f(\varepsilon' - eV)\,(1 - f(\varepsilon)) \\ &+ \rho_{\text{BCS}_\text{S}}(\varepsilon)\, \rho_{\text{BCS}_\text{T}}(\varepsilon' - eV) f(\varepsilon)\,(1 - f(\varepsilon' - eV)) \Big] g(\varepsilon - \varepsilon') d\varepsilon d\varepsilon', \end{aligned} \tag{6.10}$$

and the inelastic current as

$$\begin{aligned} I_{\text{inel.}} =& \sum_{i=1}^{3} \frac{1}{3} \sigma_{\text{inel.}} \int_{-\infty}^{+\infty}\int_{-\infty}^{+\infty}\int_{-\infty}^{+\infty} \Big[\rho_{\text{BCS}_\text{S}}(\varepsilon'' - eV + V_{\text{ST}}^i) \rho_{\text{BCS}_\text{T}}(\varepsilon) f(\varepsilon'' - eV + V_{\text{ST}}^i) \\ &\times (1 - f(\varepsilon)) + \rho_{\text{BCS}_\text{S}}(\varepsilon)\, \rho_{\text{BCS}_\text{T}}(\varepsilon'' - eV - V_{\text{ST}}^i) f(\varepsilon) \\ &\times \left(1 - f(\varepsilon'' - eV - V_{\text{ST}}^i)\right) \Big] g(\varepsilon - \varepsilon') h(\varepsilon' - \varepsilon'') d\varepsilon d\varepsilon' d\varepsilon''. \end{aligned} \tag{6.11}$$

Here, $\rho_{\text{BCS}_\text{S}}(\varepsilon)$ and $\rho_{\text{BCS}_\text{T}}(\varepsilon)$ are density of states of the superconducting tip and sample, V_{ST}^i is the threshold voltage of the three possible spin excitations, $V_{\text{ST}}^1 = V_{\text{ST}}^2 < V_{\text{ST}}^3$ in zero magnetic field. An additional Cauchy-Lorentz distribution $h(\varepsilon) = (\pi\delta)^{-1}\left[1 + 2^{(\varepsilon/\delta)}\right]^{-1}$ is added to account for a finite lifetime of the excited state [162]. We found $\delta = 0.30$ meV corresponding to a lifetime of $\tau = h/\delta \approx 14$ ps, (h, Planck constant). The fitting in Fig.(6.6a) results in the threshold voltage of the spin excitation as $V_{\text{ST}}^1 = V_{\text{ST}}^2 = 22.7$ meV and $V_{\text{ST}}^3 = 23.8$ meV. They correspond to an intramolecuar Heisenberg coupling of $J_{\text{ST}} = 21.7$ meV, and a DMI coupling of $|\,\mathbf{D}_{\text{ST}}\,| = 0.45 \times J_{\text{ST}}$.

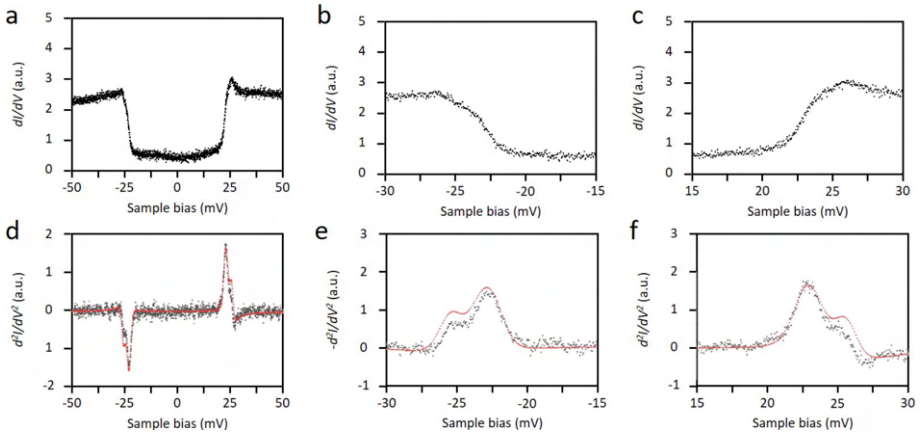

Figure 6.8: Measured and modeled spin excitation spectra of $CoPc_\nu$ at $B_z = 13$ T. a, dI/dV measurement acquired at the ligands of a $CoPc_\nu$ molecule. **b,** Zoom-in of the left step of the spectrum in (a). **c**, Zoom-in of the right step. **d,** Measured d^2I/dV^2 (black dots) and modelled d^2I/dV^2 spectrum (red dots). **e,** Zoom-in of the left peak. **f,** Zoom-in of the right peak. The extracted couplings are $J_{\text{ST}} = 22.4$ meV, and $|\,\mathbf{D}_{\text{ST}}\,| = 0.45 \times J_{\text{ST}}$.

6.11 Spatial distribution of the spin excitation over $CoPc_\nu$

Spatially resolved inelastic electron tunneling spectroscopy further reveals the existence of only a mirror plane on the $CoPc_\nu$ molecule. We take dI/dV measurement on a grid of 45×45 pixels where at each pixel we determine the energy ε or equivalently J_{ST}, and the inelastic differential conductance relative to the total conductance, $A = \sigma_{\text{inel.}}/(\sigma_{\text{el.}} + \sigma_{\text{inel.}})$ of the molecule Fig.(6.9 a, b). In the ε-map, Fig.(6.9 a), we restrict ourselves to the spatial distribution of the spin excitation energies, $20\,\text{mV} < \varepsilon < 23\,\text{mV}$, for a fixed differential conductance. It is evident that the ε-map retains a four-fold symmetry, which means that the Heisenberg coupling J_{ST} is identical along x and y axis. In the A-map, however, we look at the spatial distribution of the relative spin excitation intensity at the ST transition energy. We can clearly see that the A-map has a two-fold symmetry. We further prove this by comparing each map from an enforced four-fold symmetry Fig.(6.9 e, f), where the ε-map deviates only by a few percent from it but the A-map up to 40 percent.

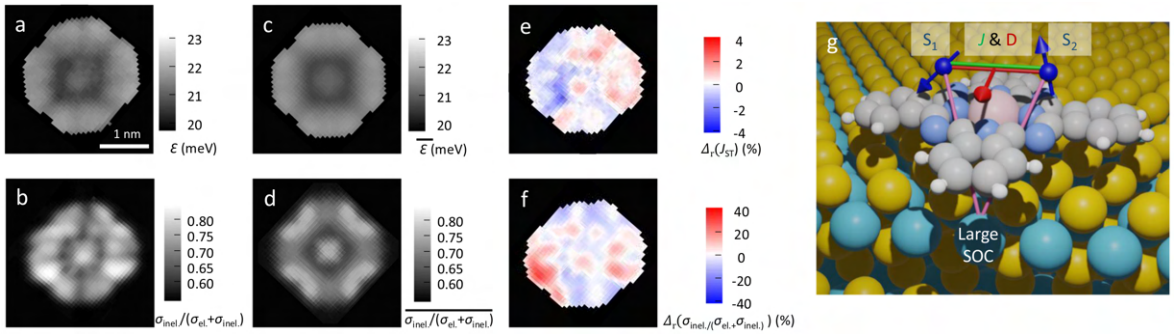

Figure 6.9: Spin excitation map of a Cobalt phthalocyanine molecule with vertical σ_ν mirror plane symmetry ($CoPc_\nu$). a, b, Maps of 45×45 points covering an area of 3×3 nm^2 on which differential conductance spectra (setpoint: $V_b = -50$ mV, $I = 500$ pA) were taken and **(a)** the spin excitation energy ε and **(b)** the intensity $A = \sigma_{inel.}/(\sigma_{inel.} + \sigma_{el.})$ were extracted. Here, $\sigma_{inel.}$ is the inelastic conductance, and $(\sigma_{inel.} + \sigma_{el.})$ is the total conductance. While the ε map shows mainly fourfold symmetry, the A-map clearly reveals the mirror plane, which cuts approximately vertical through the image. **c, d,** Averaged images of $\overline{\varepsilon}$ and $\overline{\sigma_{inel.}/(\sigma_{inel.} + \sigma_{el.})}$ with enforced $C_{4\nu}$ symmetry derived from (**a**) and (**b**), respectively. **e, f,** The relative difference Δ_r between the measured and averaged maps, respectively. **g,** Schematic ball model of the $CoPc_\nu$ and its interactions. Gray, white, light blue, and pink spheres correspond to C, H, N, and Co atoms, on the molecule, respectively. Yellow and turquoise spheres correspond to Se and Nb atoms of the surface. Blue arrows indicate the two spins and the red arrow the Dzyaloshinskii-Moriya vector.

6.12 Experimental procedure

The 2H-$NbSe_2$ single crystal was cleaved by attaching an adhesive Kapton polyimide tape to the crystal surface and pulling it off at a base pressure of $p \leq 10^{-8}$ mbar. CoPc molecules were then deposited from a Knudsen cell evaporator held at 410 C° onto the freshly cleaved

2H-$NbSe_2$ at room temperature and $p \leq 10^{-9}$ mbar. The SPM experiments were performed using a home-built combined scanning tunneling and atomic force microscope operating in ultrahigh vacuum ($p \leq 10^{-10}$ mbar), at fields perpendicular to the sample surface of up to 14 T, and at a base temperature of 1.2 K. The dI/dV spectra were detected by modulating the bias voltage V_b with a sinusoidal of $0.05 - 0.2$ mV amplitude and 617 Hz frequency utilizing a lock-in amplifier. We functionalized the bare Pt/Ir tip by indenting it into a Pb surface by several hundreds of nm repeatedly until it showed a bulk-like superconducting gap. The tip is mounted on a quartz tuning fork with a resonance frequency of $f_0 = 29,067$ Hz, a stiffness of $k = 1800$ N/m, and a Q-factor of $\approx 60,000$. Tuning fork oscillation amplitudes of 50 pm were used to measure the forces acting between tip and sample by detecting the frequency shift df of the tuning fork.

6.13 Conclusion

To summarize this chapter, we have studied in great detail the change of ground state by modifying the twist angle between the molecule mirror plane and the substrate. Evidently, the angle mismatch between the two controls the symmetry of the adsorbed molecule and as a result the nature of involved interactions. In one molecule, the localized spin on Co^{2+} strongly interacts with the superconducting substrate and renders subgap YSR states, and in the other, the molecule-substrate interaction is suppressed, and instead, intra-molecular spin-spin interactions determine the ground state. In this case, the spin-spin interactions take an isotropic Heisenberg-type plus a significant non-collinear DM character, which is presumably due to the coupling between the magnetic moments in the CoPc and the Nb d-orbitals of the 2H-$NbSe_2$ [163, 164].

Chapter 7

Conclusions

In this thesis, we studied in great detail the properties of the NTCDA Kondo lattice using a low-temperature scanning tunneling microscope. We observed that the NTCDA molecules adsorbed on the surface of Ag(111) show two visually different appearances, labeled as bright and dark molecules. They collaboratively form a self-assembled Kondo lattice in the relaxed monolayer phase with two dramatically different Kondo scales. Moreover, we identified another scale in the lattice (much smaller than the Kondo scale) generated by the long-range RKKY-like interaction between the local moments that favors ordering them and breaking the Kondo singlets, resulting in the opening of a small gap or a dented Kondo peak at the Fermi level.

Employing the feature detection scanning tunneling spectroscopy, we extracted the small dI/dV signals related to the low energy features of the NTCDA Kondo lattice and imaged them in real space. We have also shown that STM as a local probe allows us to study the QPT of the Kondo lattice from a local perspective. In this way, by utilizing the tip's electric field, we induced the charge QPE of the Kondo lattice and simultaneously interrogated their magnetic properties to track the change of the ground state. We observed that they appear as a train of discharging peaks in the dI/dV signal running towards the Fermi level at sufficiently large biases.

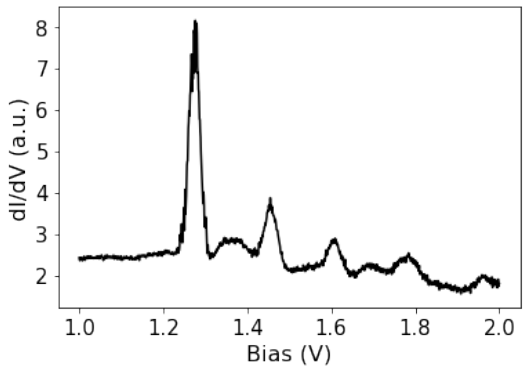

Figure 7.1: Discharging cascade of the NTCDA Kondo lattice.

Moreover, we have shown via our dI/dV mappings that these QPEs have ring-like features in the real space, which grow in size with increasing bias and interact with each other, forming various interference patterns. The patterns contain interesting sub-angstrom features such as a twist at the intersection of the rings and a hybridization gap. These patterns respect different symmetries and are not exclusive to the relaxed monolayer phase. In fact, we have observed similar patterns in the rippled phase, too. We complemented our understanding by developing a tight-binding model to simulate the conductance maps of the NTCDA lattice in the STM junction under different conditions. Interestingly, we observed that the simulations predicts many features of the patterns.

In order to further improve this work, there are still questions pending to be answered, such as

- Why does the r-ML NTCDA lattice show a variety of discharging patterns, and which parameter in the lattice controls it?
- What effect is responsible for the twist of the rings? Is it an artifact of the tip, or is there a more profound underlying effect?
- Is the discharging pattern of the rippled phase similar to the ones in the r-ML phase?
- How does the Coulomb interaction and strong correlation between several discharged molecules play a role?
- How does the substrate play a role in the formation of such spatially extended patterns? Are these patterns exclusive to the Ag(111) substrate?
- Does the NTCDA lattice at its border with the substrate host a low energy edge state?

This thesis also recapitulated our published work on the tuning of the molecular magnetism in the superconducting tunneling junction studied by STM and AFM methods. In this work, we have shown that the CoPc molecule has two stable adsorption sites on the 2H-$NbSe_2$, which are mismatched by 15° angle. The magnetic properties of the molecule at each of these sites are markedly different. In one of them, the molecule shows in-gap YSR bound states with partially screened spins, and in the other shows a singlet ground state with a triplet excited. In the latter, we have also observed signatures of a significant Dzyaloshinskii-Moriya interaction originating from the superconducting substrate.

Appendix A

Scanning tunneling spectroscopy

Scanning tunneling spectroscopy (STS) mapping is a versatile technique joining the sub-atomic spatial resolution of STM and energy-resolved differential conductance spectroscopy, providing us with a powerful tool to measure the local density of states of single atoms and molecules [18, 165–167]. STS is typically acquired by measuring the differential conductance under open feedback-loop condition by adding a small AC modulation with specific frequency ω_{mod} on the bias voltage $\mathrm{V_b}$, which is sufficiently far from the low-frequency noises in the STM junction, and then extracting the corresponding $\mathrm{dI/dV}$ signal via a lock-in technique. The procedure is repeated on a given area pixel-by-pixel, while the feedback loop is closed after recording each measurement, to prepare a tuple of data $(\mathrm{x}, \mathrm{y}, \mathrm{dI/dV})$. Subsequently, the spatial distribution of the local density of states can be extracted from the dataset in terms of $\mathrm{dI/dV}$–maps for a chosen bias voltage.

In this supplement, we compile several $\mathrm{dI/dV}$–maps of the NTCDA/Ag(111) r-ML and rippled phase for different bias ranges. The aim is to give us a general understanding of the system by listing out the essential features of the two lattices in real-space. Therefore, unavoidably, the text takes a monotonous repetitive language.

A.1 STS of NTCDA r-ML (I):$\mathbf{V_b \in [-8.0,\ 8.0]\ mV}$

The constant current dI/dV –maps in Fig.(A.1) resolves the spatial dependence and spectroscopic evolution of the Fermi level of NTCDA/Ag(111) r-ML for different bias in $[-8.0,\ 8.0]$ mV. In this range, three representative bias intervals can be distinguished based on the apparent contrast[1]:

$\mathbf{V_b \in [-8.0,\ -0.4)\ mV}$

In this interval, alternating bright and dark chains appear along the bright and dark molecules. The apparent contrast is mainly due to the periodic modulation of the Kondo resonance across the lattice, demonstrating a spatially extended Kondo cloud. Withing a bright molecule, the Kondo resonance takes its maximum intensity at the CH and bridge site[2] and drops significantly at the naphthalene core. The relatively sharp contrast between bright and dark molecules gradually smears as the bias approaches -0.4 mV.

$\mathbf{V_b \in [-0.4,\ 7.2)\ mV}$

In this interval, the contrast almost completely disappears across the lattice. Moreover, on the point dI/dV spectrum two dips appear within this range most prominent on the dark molecule CH- and bridge-site. One of them is precisely located at zero bias and the other between $3-4$ mV. The inhomogeneous distribution of the differential conductance, together with the observation of the dips, signifies the formation of an asymmetric *pseudogap* of approximately 7 mV width at the Fermi level. The pseudogap does not evolve into a full-gap most presumably due to the presence of the strong background scattering of the tunneling electron with the silver substrate around the Fermi level. Besides, we have to consider the marginal effect of the instrumental broadening in the lock-in detection scheme[3] and the finite temperature broadening,[4].

$\mathbf{V_b \in [7.2,\ 8]\ mV}$

In this interval, the alternating bright and dark chains reappear, with a minor difference compared to the first interval. Unlike the negative bias where contrast is homogeneously distributed along the chains, here the intensity is predominantly localized at the CH and bridge sites, with negligible contribution from the naphthalene cores.

[1] One has to take into account that the tip had a slight lateral drift in this measurement.
[2] The bridge between two bright molecules.
[3] An AC modulation amplitude of $200\mu V$ was used in the lock-in amplifier.
[4] The measurement was carried out at T = 1.5 K.

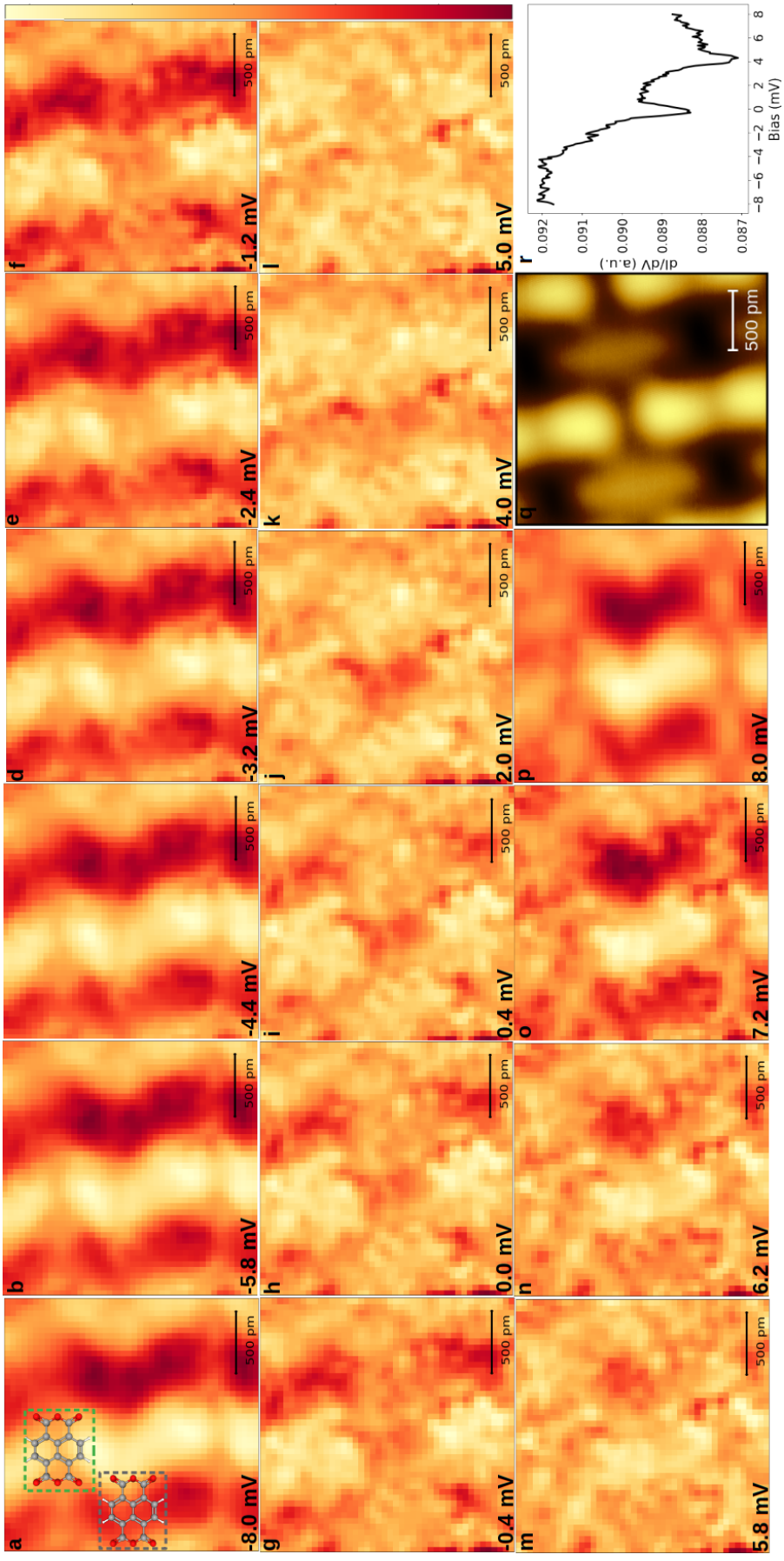

Figure A.1: Spatially resolved local density of state of the NTCDA/Ag(111) r-ML around the Fermi energy. Panel **a,** to **p,** are $dI/dV-$maps of the lattice for $\mathbf{V_b} \in [-8.0, 8.0]$ mV. The $dI/dV-$maps were measured with parameters $I_t = 1\,\mathrm{nA}$, $V_{\mathrm{mod}} = 200\,\mu V$, $T = 1.51\,\mathrm{K}, B = 10\,\mathrm{T}$. **q,** Constant-current STM image ($V_b = 10\mathrm{mV}, I_t = 500\,\mathrm{pA}$) acquired on the same region where the $dI/dV-$maps were measured. **r,** A typical dI/dV spectrum extracted from the same dataset. The graphical representation of an NTCDA molecule is overlaid on the bright molecule with a green and on the dark molecule with a gray dashed frame.

A.2 STS of NTCDA r-ML (II):$\mathbf{V_b \in [-70,\ 70]\ mV}$

The constant-current dI/dV–maps in Fig.(A.2) resolves the spatial dependence and spectroscopic evolution of various low energy features of the NTCDA/Ag(111) r-ML for different bias in $[-70,\ 70]$ mV range. It includes vibronic states, which are mainly localized at the center of molecules and the Kondo states, which are localized at CH- and bridge-site. In this range, five representative bias intervals can be distinguished based on the apparent contrast:

$\mathbf{V_b \in [-70,\ -43)\ mV}$

In this interval, the vibronic states localized at the center of bright molecule (naphthalene core) shows the maximum LDOS. On the dark molecule, however, the central area is much less pronounced, despite the fact they are identical molecules. This suggests that in the negative bias, the out-of-plane vibrational modes on the bright molecules are more susceptible to scatter off the tunneling electrons than the dark ones. Surprisingly, the bridge between two bright molecules which also accommodates the Kondo state at the Fermi level (see Sec.(A.1)), shows a noticeable intensity.

$\mathbf{V_b \in [-43,\ -14)\ mV}$

In this interval, a 'dumbbell-like' feature appears on the dark molecule CH- and bridge-site. This feature should be related to the Kondo state of the dark molecules.

$\mathbf{V_b \in [-14, 28)\ mV}$

In this interval, as we approach the Fermi level, the 'dumbbell-like' feature originating from the dark molecule consistently overlaps with the feature from the Kondo state on the bright molecule, and create a (quasi-)1D Kondo chain.

$\mathbf{V_b \in [28,\ 35]\ mV}$

In this interval, the contrast almost completely disappears.

$\mathbf{V_b \in (35,\ 70]\ mV}$

Throughout this interval, the contrast almost remains unchanged. The vibronic states reappear with maximum LDOS localized at the center of bright and dark molecules. The CH-sites hosting the Kondo states shows the minimum LDOS.

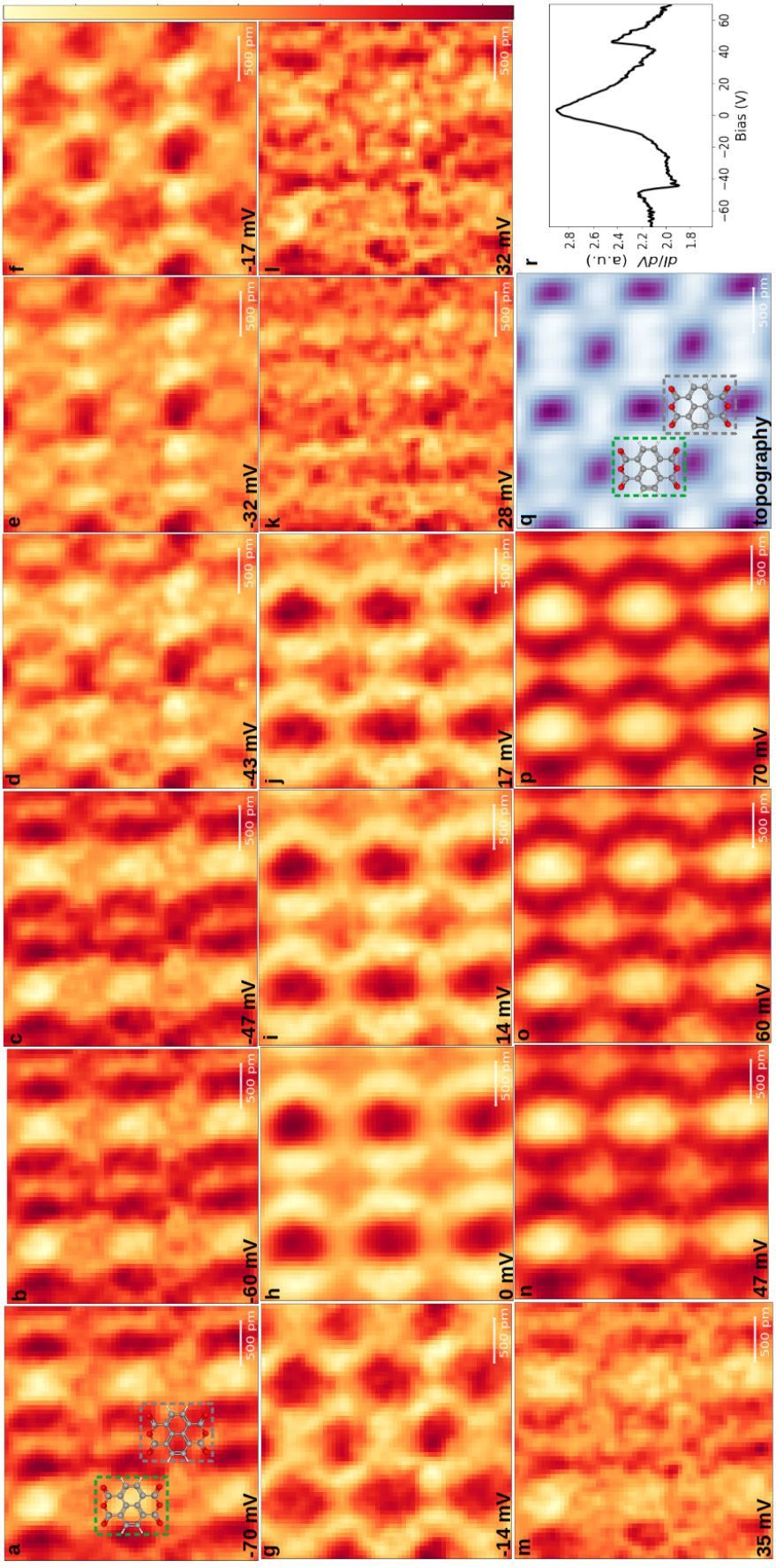

Figure A.2: Spatially resolved local density of state of the NTCDA/Ag(111) r-ML around the Fermi energy. Panel **a,** to **p,** are dI/dV−maps of the lattice for $V_b \in [-70,\ 70]$ mV. The dI/dV−maps were measured with parameters $I_t = 1$ nA, $V_{\text{mod}} = 1$ mV, $T = 4.25$ K, $B = 10$ T. **q,** Simultaneously recorded constant-current STM image of the region where the dI/dV−maps were acquired. **r,** A typical dI/dV spectrum extracted from the same dataset. The graphical representation of an NTCDA molecule is overlaid on the bright molecule with a green and on the dark one with a gray dashed frame.

A.3 STS of NTCDA r-ML (III):$\mathbf{V_b \in [300, 790]\ mV}$

The constant-current dI/dV–maps in Fig.(A.3) resolves the spatial dependence and spectroscopic evolution of the interface state of the NTCDA/Ag(111) r-ML lattice within $[300, 790]$ mV bias range. In this range, three representative bias intervals can be distinguished based on the apparent contrast[5]:

$\mathbf{V_b \in [300, 515)\ mV}$

In this interval, all molecules on the lattice appear with similar contrast. As we increase the bias, the LDOS is redistributed such that the bright molecules takes more weight and gradually extend along the short axis of the molecule (H-C_{core}-H). Denoting that in this energy range, the tunneling electron is sufficiently away from the spectroscopic features around the Fermi level, makes the interface state a suitable place to extract the surface potential profile of the lattice[6]. The surface potential profile provides us with a powerful tool to determine the location of electrostatic charges[7]. An electrostatic charge naturally prefers the lower potential, and therefore, the naphthalene cores which have the maximum intensities in this map are the charge centers.

$\mathbf{V_b \in [515, 590]\ mV}$

In this interval, as we approach 560 mV, which is the approximate energy of the interface state, the bright molecules create a chain along the molecule's short axis.

$\mathbf{V_b \in [605, 790]\ mV}$

In this interval, the bright chains gradually smears out and the intensity evens out in the entire lattice.

[5] One has to take into account that the tip had a slight lateral drift in this measurement.

[6] In fact, this map does not accurately address the surface potential. Because it is a constant current map which means tip-sample distance changes pixel by pixel, and therefore, the spectroscopic features are convoluted with topography. A better way to extract the surface potential profile is through the constant bias $dI/dV(Z)$-map at energies sufficiently away from the Fermi level.

[7] In principle, a lattice can be conceived as a periodic array of parabolic electrostatic potentials.

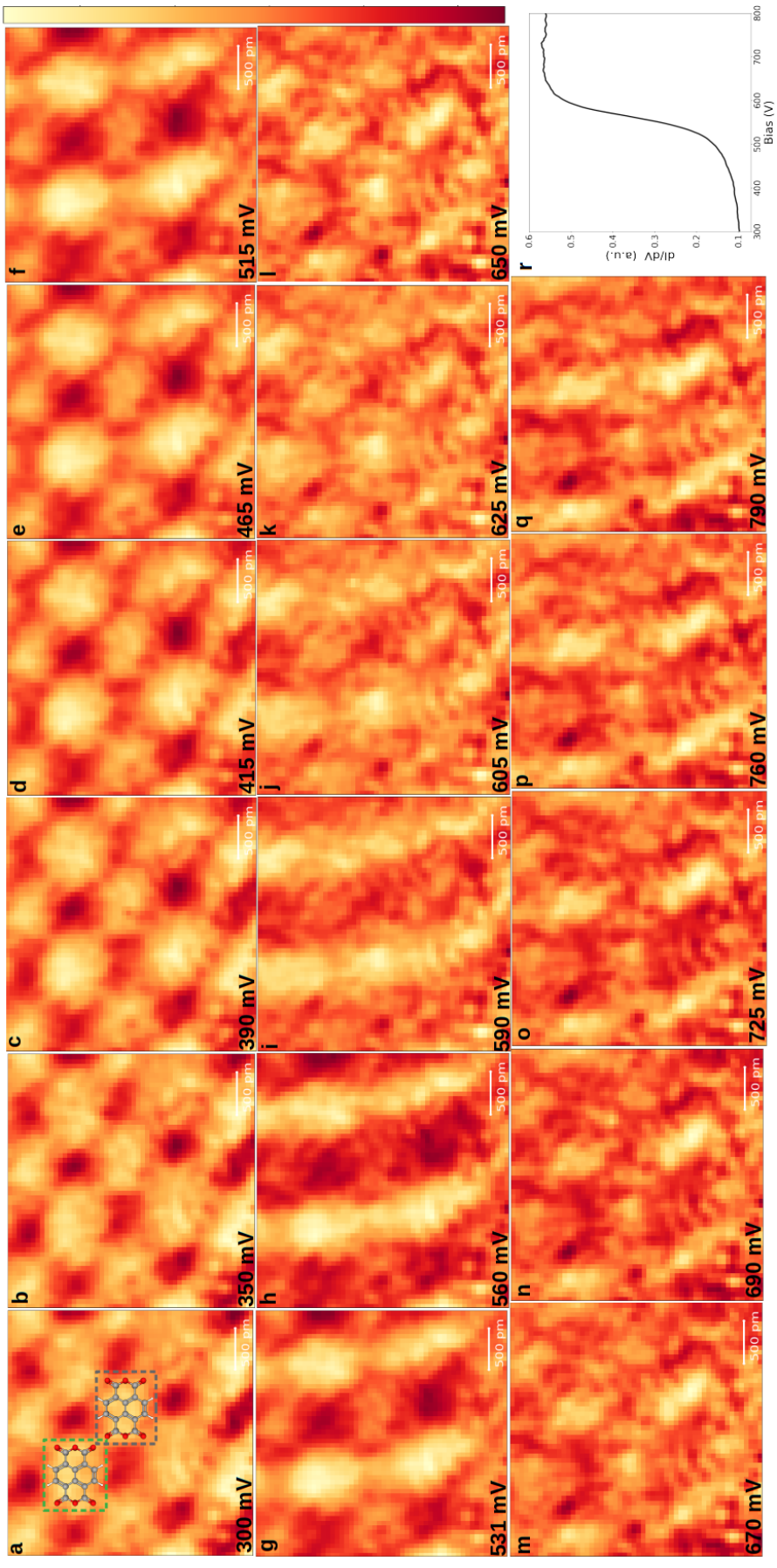

Figure A.3: Spatially resolved local density of state of the NTCDA/Ag(111) r-ML around the interface state. Panel **a,** to **q,** are dI/dV−maps of the lattice for $V_b \in [300, 790]$ mV measured with parameters $I_t = 1\,\mathrm{nA}$, $V_{\mathrm{mod}} = 5\,\mathrm{mV}$, $T = 4.25\,\mathrm{K}$, $B = 10\,\mathrm{T}$. **r,** A typical dI/dV point spectrum extracted from the same dataset. The graphical representation of an NTCDA molecule is overlaid on the bright molecule with a green and on the dark one with a gray dashed frame.

A.4 STS of NTCDA r-ML (VI): $\mathbf{V_b \in [1.0,\ 1.27]\ V}$

The constant-current dI/dV–maps in Fig.(A.4) resolves the spatial dependence and spectroscopic evolution of a charge quasiparticle excitation on the NTCDA/Ag(111) r-ML. In this range, two representative bias intervals can be distinguished based on the apparent contrast:

$\mathbf{V_b \in [1.0,\ 1.20]\ V}$

In this interval, bright and dark chains features appear smeared and blurry. It is because the bias is far from the Fermi level, and there is no intrinsic state in this range on the molecule to be probed.

$\mathbf{V_b \in (1.20,\ 1.27]\ V}$

In this interval, the background contrast between bright and dark chains abruptly disappears, and a dot emerges on the center of bright molecules[8]. This announces the arrival of a new tunneling channel to the Fermi level, which masks all the underlying spectroscopic features in the background. As the bias increases and the tip goes off the center, the dot evolves into a growing ring. There is a crucial consideration here. There is no intrinsic molecular state at 1.20 V on the adsorbed NTCDA, neither reported by DFT calculations nor have it been probed in various experiments[9]. It's worth mentioning that a similar feature, a growing ring[10], has been observed in numerous defect and impurity studies in 2D materials and back-gated heterostructures, where sufficient control over the local state and decoupling from the charge reservoir (substrate) can be exerted. In these studies, the ring is attributed to (dis)charging of a *gated local state* at the Fermi level. This picture, however, needs to be modified for the NTCDA case since based on the DFT calculations, the nearest *electronic* state to the Fermi level belongs to the partially filled LUMO, which is a very broad satellite centered around 500 meV immersed in a sea of the substrate's conduction electrons. The tip-gating of such a broad energetic level cannot result in an abrupt step-like jump in the current channel. Therefore, presence of a small local state on the molecule in the vicinity of the Fermi level is necessary to justify this picture. As it becomes more apparent later, we interpret this abrupt change in the local density of states at the Fermi level as the excitation of charged quasiparticles of the NTCDA Kondo lattice by means of tip's electric field[11], rather than a simple (dis)charging event as a result of the tip-gating effect.

[8] In this map, the dot is slightly off the center and deformed because the tip is asymmetric.

[9] The fact that it emerges only on the bright molecules and not on the dark ones excludes the possibility of probing an intrinsic molecular state at approximately 1.2 V, as both bright and dark molecules are identical.

[10] The ring is the equipotential line of the electrostatic field when the tip is off the charging center.

[11] The presumption here is that the partially filled LUMO of individual molecules overlaps and forms a band, which energetically shifts to the vicinity of the Fermi level.

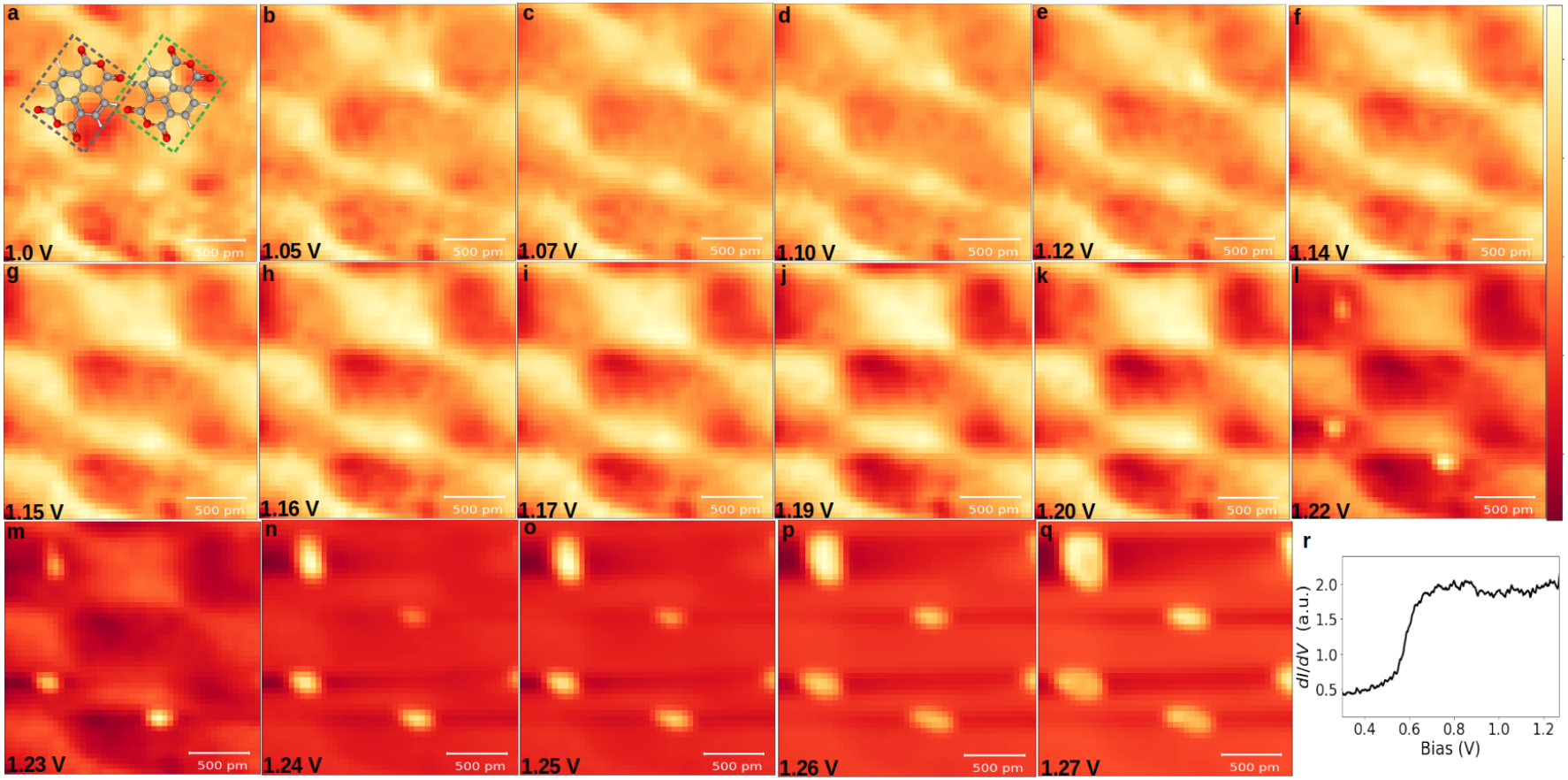

Figure A.4: Spatially resolved local density of state of the NTCDA/Ag(111) r-ML around the charging resonance. Panel **a,** to **q** are dI/dV-maps of the lattice for $V_b \in [1.0, 1.27]$ mV measured with parameters $I_\mathrm{t} = 6\,\mathrm{nA}$, $V_\mathrm{mod} = 10\,\mathrm{mV}$, $T = 1.51\,\mathrm{K}, B = 10\,\mathrm{T}$. **r,** A typical dI/dV point spectrum extracted from the same dataset. The graphical representation of an NTCDA molecule is overlaid on the bright molecule with a green and on the dark one with a gray dashed frame.

A.5 STS of NTCDA r-ML (VI): $\mathbf{V_b \in [1.28,\ 1.96]\ V}$

The constant-current dI/dV–maps in Fig.(A.5) resolves the spatial dependence and spectroscopic evolution of a *real-space quasiparticle interference pattern*[12] on the NTCDA/Ag(111) r-ML lattice. In this range, three representative bias intervals can be distinguished based on the apparent contrast:

$\mathbf{V_b \in [1.28,\ 1.64]\ V}$

In this interval, the ring's size grows as bias increases with a much faster rate along the molecule's short axis (H-C_{core}-H) than the long one (O_{anhy}–C_{core}–O_{anhy}). Above 1.5 V, the ring has already surpassed the size of the molecule[13], and interfere (overlap) with other rings approaching from the neighboring sites. Considering the size of the molecule and the typical range of quantum tunneling distance[14], this is strong evidence for the existence of a molecular band, which allows the tip to excite the quasiparticle several nanometers away from the charge center.

$\mathbf{V_b \in (1.64,\ 1.71]\ V}$

In this interval, the interference pattern shows two distinct features: (i) Formation of a hybridization gap (dark segments) of about 50 meV when rings overlap at the oxygen groups, and (ii) propagation and twisting when they cross at the CH-sites[15]. This observation also approves that the quasiparticles have a 1D physics in this energy range. Furthermore, we can see *inhomogeneity* in the lattice in terms of variation in the growth rate of different rings and the evolution of real-space gaps [16].

$\mathbf{V_b \in (1.71,\ 1.96]\ V}$

In this interval, the hybridization gap closes, and the ring penetrates to the next molecule. It is worth mentioning that propagation of rings continues as bias increases until the tip's electric field destroys the lattice. Typically, above 2.3 V the NTCDA lattice is washed away by the intense electric field of the tip.

[12] In STM, the term quasiparticle interference is typically used for the scattering of quasiparticles in momentum space, and is obtained by Fourier-transforming then inverting the real-space interference patterns, which contains information about the wavefunction of the of the quasiparticles $\left(dI/dV \sim \sum_{\mathbf{k}} |\Psi_{\mathbf{k}}(r)|^2\right)$. Here, in real space, the interference pattern is produced by the overlap of the rings at different lattice sites.

[13] The size of the molecule is 11.57×15.04 Å^2.

[14] A typical range for the quantum tunneling is less than 1 nm.

[15] The delicate features in this map and their profound physical consequences demand a higher resolution result. Therefore, this result will be repeated later with extraordinary quality.

[16] The coupling between molecules slightly varies among different unit cells.

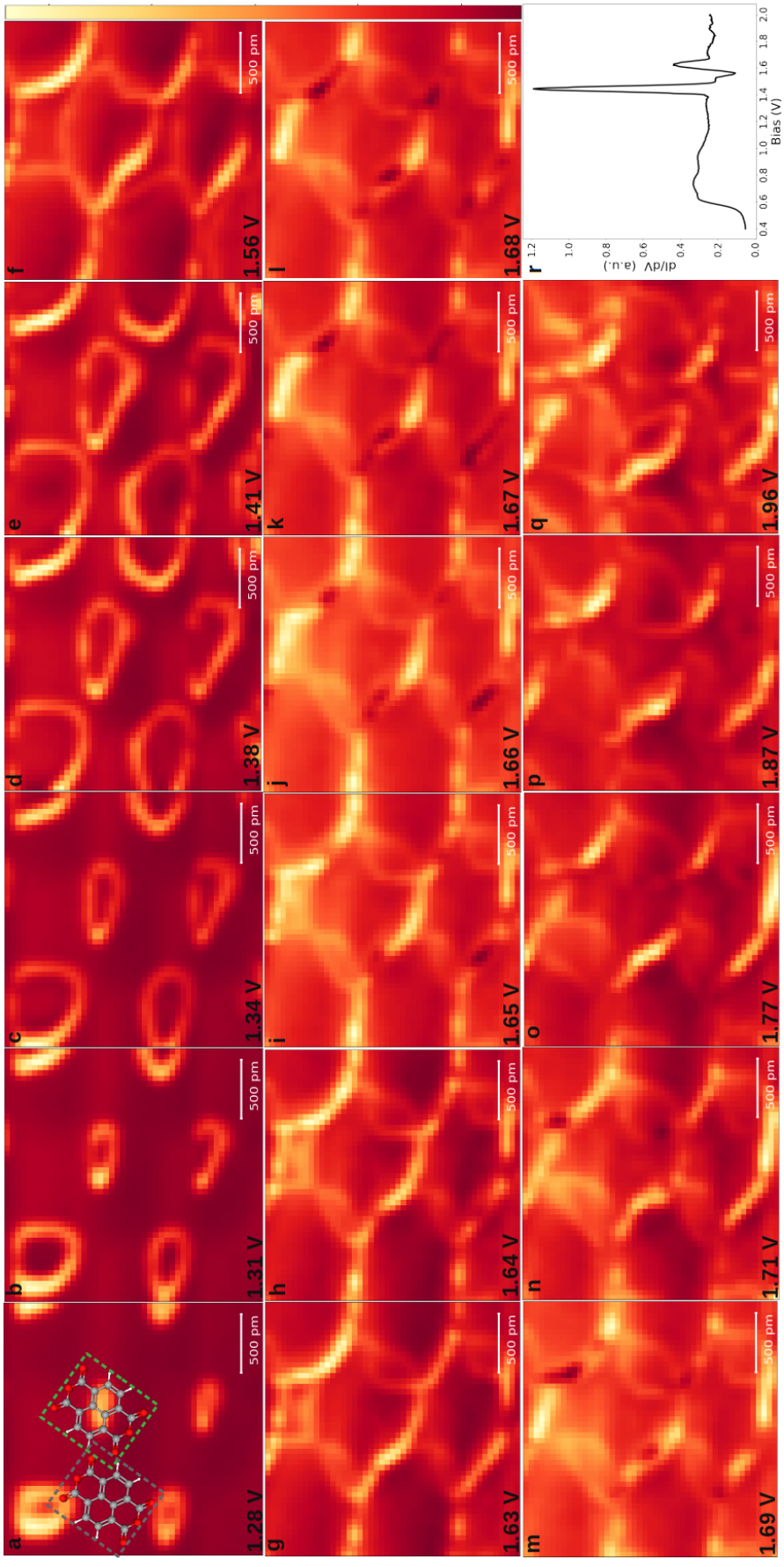

Figure A.5: Spatial and spectroscopic evolution of the charging resonance on the NTCDA/Ag(111) r-ML. Panel **a,** to **q** are dI/dV-maps of the lattice for $V_b \in [1.28, 1.96]$ mV measured with parameters $I_t = 6\,\mathrm{nA}$, $V_{\mathrm{mod}} = 10\,\mathrm{mV}$, $T = 1.51\,\mathrm{K}$, $B = 10\,\mathrm{T}$. **r,** A typical dI/dV point spectrum extracted from the same dataset. The graphical representation of an NTCDA molecule is overlaid on the bright molecule with a green and on the dark one with a gray dashed frame.

A.6 STS of NTCDA r-ML at the border: $\mathbf{V_b \in [-100,\ 100]\ mV}$

The constant-current dI/dV−maps in Fig.(A.6) resolves the spatial dependence and spectroscopic evolution of the NTCDA/Ag(111) r-ML around the rim. The major features of this map are qualitatively the same as the maps in the middle of the lattice, except the observation of an *edge state* and creation of several *low energy peaks* at the Fermi level. In this range, five representative bias intervals can be distinguished based on the apparent contrast:

$\mathbf{V_b \in [-100,\ -40)\ mV}$

In this interval, the vibronic states localized at the center of bright molecules, and to a lower extent, on the dark ones, appear with the maximum LDOS, while the CH-sites show the minimum. On the bare Ag(111), away from the lattice, the intensity remains homogeneous and perceptibly drops adjacent to the lattice border.

$\mathbf{V_b \in [-40,\ -10)\ mV}$

The dumbbell-like features appear at the dark molecule CH- and bridge sites in this interval. Additionally, as we further approach the Fermi level, a new state emerges precisely at the lattice border with Ag(111).

$\mathbf{V_b \in [-10,\ 30)\ mV}$

In this interval, the Kondo state on CH- and bridge-sites appear with the maximum intensity, while the centers show the minimum. Moreover, looking more closely at the point spectra extracted from the same dataset shows several low energy peaks at the edge, most notably a split state precisely at the Fermi energy, which penetrates several angstroms into the bare Ag(111) and decays at far distances.

$\mathbf{V_b \in [30,\ 40]\ mV}$

The contrast between the substrate and the lattice almost completely disappears in this interval.

$\mathbf{V_b \in (40,\ 100]\ mV}$

In this interval, the vibronic states localized at the center of molecules reappear with the maximum intensity, while the CH- and bridge-sites show the minimum.

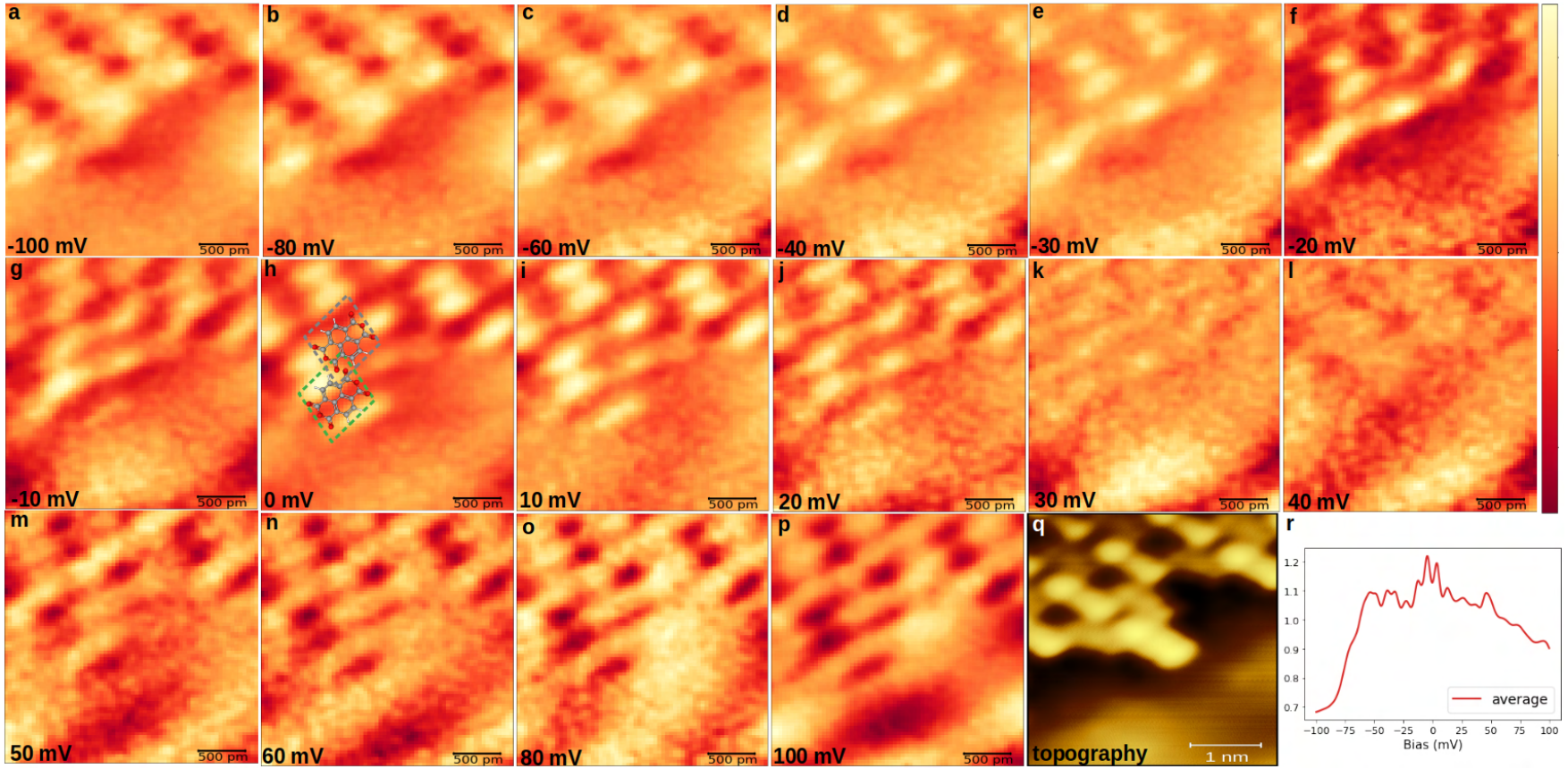

Figure A.6: Spatially resolved local density of state of the NTCDA/Ag(111) r-ML around the border of lattice. Panel **a,** to **p,** are dI/dV−maps of the lattice for $V_b \in [-100, 100]$ mV. The dI/dV−maps were measured with parameters $I_t = 700\,\text{pA}$, $V_{\text{mod}} = 1\,\text{mV}$, $T = 4.24\,\text{K}$, $B = 10\,\text{T}$. **r,** The average dI/dV spectrum of 65×82 spectra across the border of lattice, extracted from the same dataset. The graphical representation of an NTCDA molecule is overlaid on the bright molecule with a green and on the dark one with a gray dashed frame.

A.7 STS of NTCDA rippled phase (I): $\mathbf{V_b \in [-60,\, 60]\ mV}$

The constant-current dI/dV−maps in Fig.(A.7) resolves the spatial dependence and spectroscopic evolution of the NTCDA/Ag(111) rippled phase in the smooth *transition region* of the lattice[17] for different bias in $[-60,\, 60]$ mV range. The major features of this map are shared with the one for the r-ML lattice except an apparent *inhomogeneity*. In this range, five representative bias intervals can be distinguished based on the apparent contrast:

$\mathbf{V_b \in [-60,\, -39)\ V}$

In this interval, the vibronic states localized at the center of bright molecule takes the maximum LDOS. It also appears on the center of the dark molecule, though with much less intensity. Furthermore, the bright molecule CH-sites have a noticeable weight in this range.

$\mathbf{V_b \in [-39,\, -12]\ V}$

In this interval, the maximum LDOS is located on the dark molecule CH-sites in a spherical shape[18], and on the bright molecule bridge-sites in a rectangular shape.

$\mathbf{V_b \in (-12,\, 22)\ V}$

In this interval, as we further approach the Fermi level, the spherical features on the dark molecule CH-sites fade away and the bright molecule CH-sites, where the Kondo state is located, takes the maximum LDOS in a slightly distorted rectangular shape.

$\mathbf{V_b \in [22,\, 33)\ V}$

The contrast almost completely disappears in this interval, exhibiting a roughly 10 meV pseudogap, which is slightly larger than the gap in the r-ML lattice.

$\mathbf{V_b \in [33,\, 60]\ V}$

In this interval, the vibronic states localized at the center of bright and dark molecules reappear with the maximum intensity, while the Kondo state at CH-sites shows the minimum.

[17] Recall that, roughly speaking, the rippled phase is comprised of two regions [17]. A region where there is a smooth transition from the bright to the dark molecule and vice versa, and a region where all molecules are identical. This map resolves the former.

[18] In the r-ML lattice, the nearest neighbor spherical shapes connect and form a dumbbell-like-feature.

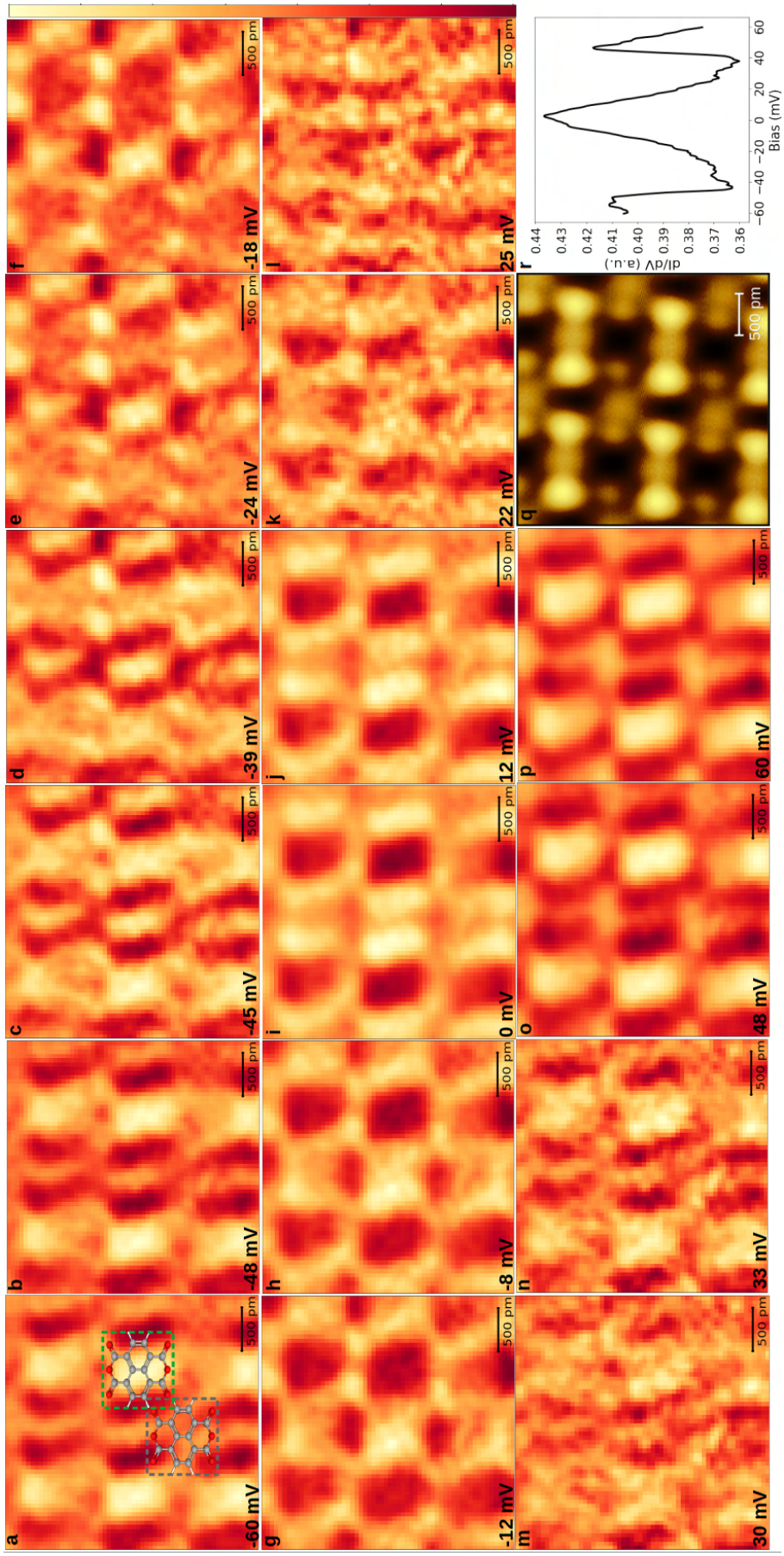

Figure A.7: Spatially resolved local density of state of the NTCDA/Ag(111) rippled phase in the transition region around the Fermi energy. Panel **a,** to **p,** are dI/dV–maps of the lattice for $V_b \in [-60, 60]$ mV. The dI/dV–maps were measured with parameters $I_t = 1\,\mathrm{nA}$, $V_{\mathrm{mod}} = 2\,\mathrm{mV}$, $T = 1.48\,\mathrm{K}$, $B = 10\,\mathrm{T}$. **q,** Constant-current STM image ($V_b = 20\mathrm{mV}, I_t = 300\mathrm{pA}$) acquired on the same region where the dI/dV–maps were measured. **r,** A typical dI/dV point spectrum extracted from the same dataset. The graphical representation of an NTCDA molecule is overlaid on the bright molecule with a green and on the dark one with a gray dashed frame.

A.8 STS of NTCDA rippled phase (II): $\mathbf{V_b \in [-60,\ 60]\ mV}$

The constant-current dI/dV−maps in Fig.(A.8) resolves the spatial dependence and spectroscopic evolution of the NTCDA/Ag(111) rippled phase in the region where all molecules are topographically *identical*. The major features of this map *qualitatively differs* from the r-ML phase. In this range, five representative bias intervals can be distinguished based on the apparent contrast:

$\mathbf{V_b \in [-60,\ -44)\ V}$

In this interval, the vibronic states localized at the center of bright and dark molecules show the maximum LDOS in a rectangular shape. Unlike the r-ML lattice, in which the bright molecule CH-sites are also present in this interval, here they are absent (see rectangular dark regions).

$\mathbf{V_b \in [-44,\ -19)\ V}$

In this interval, the contrast smears out inhomogeneously across the lattice, which may be interpreted as the creation of a pseudogap. Comparatively, in the same interval, the r-ML lattice shows dumbbell-like features at the dark molecule CH-sites.

$\mathbf{V_b \in [-19,\ 22]\ V}$

In this interval, the CH- and bridge-sites on both molecules show the maximum LDOS, and the centers show the minimum, creating a checkerboard rectangular lattice. As we have seen it before, this interval in the r-ML lattice host the Kondo state which takes a qualitatively different shape from here.

$\mathbf{V_b \in (22,\ 33]\ V}$

The contrast almost completely disappears in this interval.

$\mathbf{V_b \in (33,\ 60]\ V}$

In this interval, the vibronic states localized at the center of molecules reappear with the maximum intensity, while the CH- and bridge-sites show the minimum.

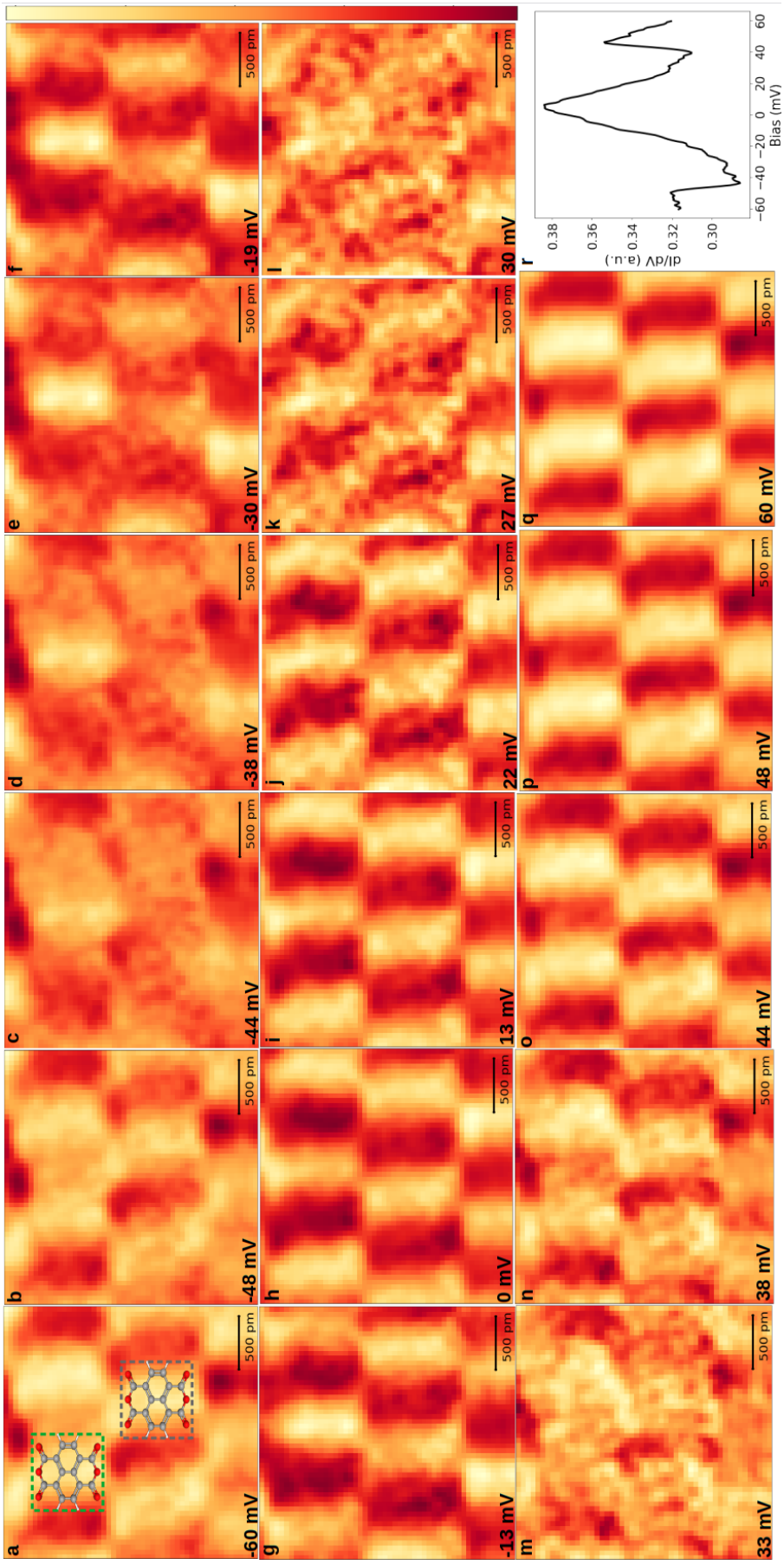

Figure A.8: Spatially resolved local density of state of the NTCDA/Ag(111) rippled phase around the Fermi energy. Panel **a,** to **q,** are dI/dV–maps of the lattice for $V_b \in [-60, 60]$ mV. The dI/dV–maps were measured with parameters $I_t = 1\,\mathrm{nA}$, $V_{\mathrm{mod}} = 1.5\,\mathrm{mV}$, $T = 1.48\,\mathrm{K}$, $B = 10\,\mathrm{T}$. A typical dI/dV point spectrum extracted from the same dataset. The graphical representation of an NTCDA molecule is overlaid on the bright molecule with a green and on the dark one with a gray dashed frame.

A.9 Conclusion

We close this chapter by summarizing the significant observations made in the dI/dV–maps.

- The vibronic states (± 47 meV) are localized at the center of bright and dark molecules. The spatial distribution of the contrast for positive and negative peaks is not identical, implying the presence of fermionic states in their vicinity.
- The Kondo state on the bright molecule is localized at the CH- and bridge-sites and creates a 'butter-fly-shape' in the real space.
- The Kondo state on the dark molecule is located further below the Fermi level and localized at the CH-sites, creating a 'dumbbell-like shape' in the real space.
- Overlap of Kondo states on different molecules forms alternating bright and dark chains at the Fermi level.
- There is a roughly 7 meV pseudogap at the Fermi level.
- The interface state creates alternating bright and dark chains very similar to the one created by the Kondo state at the Fermi level.
- A charging resonance occurs about 1.3 eV at the center of bright molecules and turns into a growing ring at a larger bias, when the tip is off the center. The rings mix (interfere) at different locations and create intricate patterns in real space.
- The rippled phase is comprised of two regions. A region where both molecules look identical, and a region where bright molecules smoothly turn into a dark one and vice versa. There are qualitative differences among the maps of the former and r-ML lattice, including an apparent spectral inhomogeneity.
- At the lattice border, there is an edge state with onset energy of about -20 meV, and also several low-energy peaks around the Fermi level, including a split state that penetrates the bare silver.

Appendix B

Python source code

```
##########################################################################
#################### Packages & Libraries ################################
##########################################################################
from numpy import lib, pad, shape, resize , tanh, minimum, pi, cos, sqrt ,\
                  clip , zeros, ones, empty, nonzero, vstack, array, exp,\
                  arange, newaxis, fill_diagonal , set_printoptions , load, save

from scipy.linalg import eigh, norm
from scipy.sparse import diags
import matplotlib.pyplot as plt
import os
import time
##########################################################################
######################### Saving path ####################################
##########################################################################

saving_path = "Give your saving path"

##########################################################################
#################### Parameters and setting ##############################
##########################################################################
t0 = time.time() # Execution time: Start

# Sublattice A parameters:
E_A = -0.5     # On-site energy of the A-site
t_1A = 0.1     # Staggered nearest-neighbor hopping amplitude between A-sites
t_2A = 0.0     # Staggered nearest-neighbor hopping amplitude between A-sites

# Sublattice B parameters:
E_B = 3.0      # On-site energy of the B-site

# STM tip parameters:
alpha = 0.5          # Tip-gating efficiency
epsilon0 = 2         # Sample dielectric constant
r = 1                # Tip apex radius

# Common parameters:
V_AB_upup = 0.1          # Hybridization amplitude between A and B sublattice preserving spin-up
V_AB_downdown = 0.1      # Hybridization amplitude between A and B sublattice preserving spin-down
Theta = pi/2             # A-B hybridization phase
W_dim = 4                # Width of the lattice
kB = 1                   # Boltzman constant
T = 0.01                 # Temperature
```

```
##############################################################################
############################### Functions ####################################
##############################################################################
def deriv_Fermi_Dirac(E):
    ## Numerics friendly analytic expression for
    ## the derivative of the Fermi-Dirac function.

    dF_list = []
    for e in E:
        dF = 1/(2*T)*(tanh( e/(2*kB*T) ))**2 - 1/(2*T)
        dF_list.append(dF)
    return dF_list

def distance(x, y, x_tip, y_tip):
    ## Calculate the distance of a given point on the lattice
    ## to the tip's position (real-valued)

    L_x1 = abs(x_tip - x)
    L_x2 = W_dim - abs(x_tip - x)
    L_y1 = abs(y_tip - y)
    L_y2 = W_dim - abs(y_tip - y)

    L_xmin = minimum(L_x1, L_x2)
    L_ymin = minimum(L_y1, L_y2)
    r = (L_xmin**2 + L_ymin**2)**0.5
    return r

def Eff_pot(x, y, x_tip, y_tip):
    ## Assign the tip's effective potential to a given point on the lattice.

    U_eff = alpha*(1 + (epsilon0/r)*distance(x, y, x_tip , y_tip)**2 )**(-1)
    return U_eff

def H_gate(x_tip, y_tip):
    ## Generate a lattice in real space and assign a gating potential
    ## to each discrete point.

    h_gating = zeros((W_dim*W_dim, W_dim*W_dim))
    for I in arange(0, W_dim,1):
        for J in arange(0, W_dim,1):
            h_gating[(I-1)*W_dim + J, (I-1)*W_dim + J] = Eff_pot(I, J, x_tip, y_tip)

    H_upup_tip_block = lib.pad(h_gating, ((0, W_dim*W_dim),(0, W_dim*W_dim)), \
                               'constant', constant_values=(0))
    H_downdown_tip_block = lib.pad(h_gating, ((W_dim*W_dim,0),(W_dim*W_dim,0)),\
                                   'constant', constant_values=(0))

    return (h_gating, H_upup_tip_block, H_downdown_tip_block)
##############################################################################
######################## Creating blocks of the H_upup ######################
##############################################################################

##############################################################################
#                              D1x_upup matrix
##############################################################################
D1x_upup_array = [resize([-V_AB_upup*exp(1j*Theta), -V_AB_upup*exp(-1j*Theta)], W_dim-1), \
                  resize([E_A, E_B], W_dim), \
                  resize([-V_AB_upup*exp(-1j*Theta), -V_AB_upup*exp(1j*Theta)], W_dim-1)]
offset_D1x_upup = [1,0,-1]
D1x_upup_matrix = diags(D1x_upup_array, offset_D1x_upup, dtype=complex).toarray()
D1x_upup_matrix[0][W_dim-1] = -V_AB_upup*exp(1j*Theta)          # PBC
D1x_upup_matrix[W_dim-1][0] = -V_AB_upup*exp(-1j*Theta)         # PBC
```

```
##############################################################################
#                                D2x_upup matrix
##############################################################################
D2x_upup_array = [resize([-V_AB_upup*exp(-1j*Theta), -V_AB_upup*exp(1j*Theta)], W_dim-1 ), \
                  resize ([E_B, E_A], W_dim), \
                  resize ([-V_AB_upup*exp(1j*Theta), -V_AB_upup*exp(-1j*Theta)], W_dim-1)]
offset_D2x_upup =  [1,0,-1]
D2x_upup_matrix = diags(D2x_upup_array, offset_D2x_upup, dtype=complex).toarray()
D2x_upup_matrix[0][W_dim-1] = -V_AB_upup*exp(-1j*Theta)  # PBC
D2x_upup_matrix[W_dim-1][0] = -V_AB_upup*exp(1j*Theta)   # PBC
##############################################################################
#                                O1y_upup matrix
##############################################################################
O1y_upup_array = [resize([-t_1A,  0],  W_dim-1), \
                  resize ([-V_AB_upup*exp(-1j*Theta), -V_AB_upup*exp(1j*Theta)], W_dim), \
                  resize ([0,  -t_2A],  W_dim-1)]
offset_O1y_upup =  [1,0,-1]
O1y_upup_matrix = diags( O1y_upup_array , offset_O1y_upup,  dtype=complex ).toarray()
O1y_upup_matrix[0][W_dim-1] = -t_2A                                    # PBC
##############################################################################
#                                O1y_dagger_upup matrix
##############################################################################
O1y_dagger_upup_array = [resize ([0,  -t_2A],  W_dim-1), \
                  resize ([-V_AB_upup*exp(1j*Theta), -V_AB_upup*exp(-1j*Theta)], W_dim), \
                  resize ([-t_1A,  0],  W_dim-1)]
offset_O1y_dagger_upup =  [1,0,-1]
O1y_dagger_upup_matrix = diags(O1y_dagger_upup_array, offset_O1y_dagger_upup, dtype=complex).toarray()
O1y_dagger_upup_matrix[W_dim-1][0] = -t_2A       # PBC
##############################################################################
#                                O2y_upup matrix
##############################################################################
O2y_upup_array = [resize ([0,  -t_1A],  W_dim-1), \
                  resize ([-V_AB_upup*exp(1j*Theta), -V_AB_upup*exp(-1j*Theta)], W_dim), \
                  resize ([-t_2A,  0],  W_dim-1)]
offset_O2y_upup =  [1,0,-1]
O2y_upup_matrix = diags( O2y_upup_array , offset_O2y_upup,  dtype=complex ).toarray()
O2y_upup_matrix[W_dim-1][0] = -t_1A                 # PBC
##############################################################################
#                                O2y_dagger_upup matrix
##############################################################################
O2y_dagger_upup_array = [resize([-t_2A,  0],  W_dim-1), \
                  resize ([-V_AB_upup*exp(-1j*Theta), -V_AB_upup*exp(1j*Theta) ], W_dim), \
                  resize ([0,  -t_1A],  W_dim-1)]
offset_O2y_dagger_upup =  [1,0,-1]
O2y_dagger_upup_matrix = diags(O2y_dagger_upup_array, offset_O2y_dagger_upup, dtype=complex).toarray()
O2y_dagger_upup_matrix[0][W_dim-1] = -t_1A       # PBC
##############################################################################
######################### Creating blocks of the H_downdown ##################
##############################################################################

##############################################################################
#                                D1x_downdown_matrix
##############################################################################
D1x_downdown_array = [resize([-V_AB_downdown*exp(-1j*Theta), -V_AB_downdown*exp(1j*Theta)], W_dim-1), \
                  resize ([E_A, E_B],  W_dim), \
                  resize ([-V_AB_downdown*exp(1j*Theta), -V_AB_downdown*exp(-1j*Theta)], W_dim-1)]
offset_D1x_downdown = [1,0,-1]
D1x_downdown_matrix = diags(D1x_downdown_array, offset_D1x_downdown, dtype=complex).toarray()
D1x_downdown_matrix[0][W_dim-1] = -V_AB_downdown*exp(-1j*Theta) # PBC
D1x_downdown_matrix[W_dim-1][0] = -V_AB_downdown*exp(1j*Theta) # PBC
```

```
##############################################################################
#                                D2x_downdown_matrix
##############################################################################
D2x_downdown_array = [resize([-V_AB_downdown*exp(1j*Theta), -V_AB_downdown*exp(-1j*Theta)], W_dim-1), \
                      resize ([E_B, E_A], W_dim), \
                      resize ([-V_AB_downdown*exp(-1j*Theta), -V_AB_downdown*exp(1j*Theta)], W_dim-1)]
offset_D2x_downdown = [1,0,-1]
D2x_downdown_matrix = diags(D2x_downdown_array, offset_D2x_downdown, dtype=complex).toarray()
D2x_downdown_matrix[0][W_dim-1] = -V_AB_downdown*exp(1j*Theta) # PBC
D2x_downdown_matrix[W_dim-1][0] = -V_AB_downdown*exp(-1j*Theta) # PBC
##############################################################################
#                                O1y_downdown matrix
##############################################################################
O1y_downdown_array = [resize([-t_1A, 0], W_dim-1), \
                      resize ([-V_AB_downdown*exp(1j*Theta), -V_AB_downdown*exp(-1j*Theta)], W_dim), \
                      resize ([0, -t_2A], W_dim-1)]
offset_O1y_downdown = [1,0,-1]
O1y_downdown_matrix = diags(O1y_downdown_array, offset_O1y_downdown, dtype=complex ).toarray()
O1y_downdown_matrix[0][W_dim-1] = -t_2A                 # PBC
##############################################################################
#                                O1y_dagger_downdown matrix
##############################################################################
O1y_dagger_downdown_array = [resize( [0, -t_2A ], W_dim-1), \
                      resize ([-V_AB_downdown*exp(-1j*Theta), -V_AB_downdown*exp(1j*Theta) ], W_dim), \
                      resize ([-t_1A, 0], W_dim-1)]
offset_O1y_dagger_downdown = [1,0,-1]
O1y_dagger_downdown_matrix = diags(O1y_dagger_downdown_array, offset_O1y_dagger_downdown, dtype=complex).toarray()
O1y_dagger_downdown_matrix[W_dim-1][0] = -t_2A          # PBC
##############################################################################
#                                O2y_downdown matrix
##############################################################################
O2y_downdown_array = [resize([0, -t_1A], W_dim-1), \
                      resize ([-V_AB_downdown *exp(-1j*Theta), -V_AB_downdown*exp(1j*Theta)], W_dim), \
                      resize ([-t_2A, 0], W_dim-1)]
offset_O2y_downdown = [1,0,-1]
O2y_downdown_matrix = diags(O2y_downdown_array, offset_O2y_downdown, dtype=complex).toarray()
O2y_downdown_matrix[W_dim-1][0] = -t_1A                  # PBC
##############################################################################
#                                O2y_dagger_downdown matrix
##############################################################################
O2y_dagger_downdown_array = [resize([-t_2A, 0], W_dim-1), \
                      resize ([-V_AB_downdown *exp(1j*Theta), -V_AB_downdown*exp(-1j*Theta) ], W_dim), \
                      resize ([0, -t_1A ], W_dim-1)]
offset_O2y_dagger_downdown = [1,0,-1]
O2y_dagger_downdown_matrix = diags(O2y_dagger_downdown_array, offset_O2y_dagger_downdown, dtype=complex).toarray()
O2y_dagger_downdown_matrix[0][W_dim-1] = -t_1A          # PBC
##############################################################################
##############################################################################
############ Generating H_upup, H_downdown, H_updown, and H_downup matrices ############
##############################################################################
##############################################################################
H_upup_matrix = zeros((W_dim*W_dim, W_dim*W_dim), dtype=complex)
H_downdown_matrix = zeros((W_dim*W_dim, W_dim*W_dim), dtype=complex)


for I in range(W_dim):
        for J in range(W_dim):
                if (I == J-1):
                        if (I%2==0):
                                for m in range(W_dim):
                                        for n in range(W_dim):
                                                H_upup_matrix[I*W_dim+m,J*W_dim + n]=O1y_upup_matrix[m,n]
                                                H_downdown_matrix[I*W_dim+m,J*W_dim+n]=O1y_downdown_matrix[m,n]
```

```
                else:
                    for m in range(W_dim):
                        for n in range(W_dim):
                            H_upup_matrix[I*W_dim+m,J*W_dim+n]=O2y_upup_matrix[m,n]
                            H_downdown_matrix[I*W_dim+m,J*W_dim+n]=O2y_downdown_matrix[m,n]

            elif (I == J):
                if (I%2==0):
                    for m in range(W_dim):
                        for n in range(W_dim):
                            H_upup_matrix[I*W_dim+m,J*W_dim+n]=D1x_upup_matrix[m,n]
                            H_downdown_matrix[I*W_dim+m,J*W_dim+n]=D1x_downdown_matrix[m,n]

                else:
                    for m in range(W_dim):
                        for n in range(W_dim):
                            H_upup_matrix[I*W_dim + m,J*W_dim+n]=D2x_upup_matrix[m,n]
                            H_downdown_matrix[I*W_dim+m,J*W_dim+n]=D2x_downdown_matrix[m,n]


            elif (I == J+1):
                if (I%2==1):
                    for m in range(W_dim):
                        for n in range(W_dim):
                            H_upup_matrix[I*W_dim+m,J*W_dim+n]=O1y_dagger_upup_matrix[m,n]
                            H_downdown_matrix[I*W_dim+m,J*W_dim+n]=O1y_dagger_downdown_matrix[m,n]


                else:
                    for m in range(W_dim):
                        for n in range(W_dim):
                            H_upup_matrix[I*W_dim+m,J*W_dim + n]=O2y_dagger_upup_matrix[m,n]
                            H_downdown_matrix[I*W_dim+m,J*W_dim+n]=O2y_dagger_downdown_matrix[m,n]


            # Fulfill PBC for the top-right triangle of the upup and downdown blocks:
            elif (I==0 and J == W_dim-1):
                for m in range(W_dim):
                    for n in range(W_dim):
                        H_upup_matrix[I*W_dim+m,J*W_dim+n]=O2y_dagger_upup_matrix[m,n]
                        H_downdown_matrix[I*W_dim+m,J*W_dim+n]=O2y_dagger_downdown_matrix[m,n]


            # Fulfill PBC for the bottom-left triangle of the upup and downdown blocks:
            elif (I==W_dim-1 and J == 0):
                for m in range(W_dim):
                    for n in range(W_dim):
                        H_upup_matrix[I*W_dim+m,J*W_dim+n]=O2y_upup_matrix[m,n]
                        H_downdown_matrix[I*W_dim+m,J*W_dim+n]=O2y_downdown_matrix[m,n]
################################################################################
################################################################################
######################### Constructing the Full Hamiltonian ####################
################################################################################
################################################################################
# Placing each block into its corresponding place in the full Hamiltonian matrix:

H_upup_block = lib.pad(H_upup_matrix, ((0, W_dim*W_dim),(0, W_dim*W_dim)), \
                       'constant', constant_values=(0))

H_downdown_block = lib.pad(H_downdown_matrix, (( W_dim*W_dim,0),( W_dim*W_dim,0)), \
                       'constant', constant_values=(0))

## NOTE: H_tip has not yet included! It is added in the main for-loop.
H_full0 = H_upup_block + H_downdown_block
```

```
#############################################################################################
################### Main For-loop: Generating conductance map ########################
#############################################################################################
##  Within the main loop, the full Hamiltonian is updated and digonalized as the tip
##  sweep the lattice . Subsequently, the eigenvalues and eigenstates of the Hamiltonian
##  is used to compute the conductance.

 tip_x_list  = arange(0, W_dim, 0.01)              # STM tip sweep line along the x-axis
 tip_y_list  = arange(0, W_dim, 0.01)              # STM tip sweep line along the y-axis
 bias_list  = [2.7]
conductance1 = zeros((len( tip_x_list ) , len( tip_y_list )))
for bias in  bias_list :
    for W_x, pos_x in enumerate( tip_x_list ):
        for W_y, pos_y in enumerate( tip_y_list ):
            H_full = H_full0 + bias*(H_gate(x_tip = pos_x , y_tip = pos_y)[1] \
                              + H_gate( x_tip = pos_x , y_tip = pos_y)[2])
            eigenval1, eigenvec1 = eigh(H_full)
            Dn_F1 = deriv_Fermi_Dirac(eigenval1)
            weighted_Dn_F1 = sum(Dn_F1*eigenvec1)
            conductance1[W_x, W_y] = norm(weighted_Dn_F1)

    # Saving the simulation data with all parameters stored in a separarate file as a dictionary:
    filename = "conductance_map" + str(bias) + "V"
    params_name = "conductance_map"+ str(bias) + "V_Params"
    params = {"E_A": E_A, "t_1A": t_1A, "t_2A": t_2A,\
              "E_B": E_B, "alpha": alpha, "epsilon0": epsilon0 ,\
              "V_AB_upup": V_AB_upup, "V_AB_downdown": V_AB_downdown,
              "Theta": Theta, "W_dim": W_dim, "kB" : kB, "T":T}

    save(saving_path + params_name, params)
    save(saving_path + filename, conductance1)
#############################################################################################
################ Main For-loop: Generating conductance line-map ########################
#############################################################################################
##  Within the main loop, the full Hamiltonian is updated and digonalized as the tip
##  sweep a line along the A-B bond. Subsequently, the eigenvalues and eigenstates of
##  the Hamiltonian is used to compute the conductance as a function of the tip effective
##  potential and tip position.

Bias_range = arange(0.0, 4.5, 0.01)
tip_pos_A_B_range = arange(0, W_dim, 0.01)
conductance2 = zeros((len(Bias_range), len(tip_pos_A_B_range)))

for bias_index, bias_val in enumerate(Bias_range[::-1]):
    for W_y, pos_y in enumerate(tip_pos_A_B_range):
        H_full = H_full0 + bias_val*( H_gate( x_tip = pos_y, y_tip = pos_y )[1] \
                                    + H_gate( x_tip = pos_y , y_tip = pos_y )[2])

        eigenval2, eigenvec2 = eigh(H_full)
        Dn_F2 = deriv_Fermi_Dirac(eigenval2)
        weighted_Dn_F2 = sum(Dn_F2*eigenvec2)
        conductance2[ bias_index, W_y ] = norm(weighted_Dn_F2)

# Saving the simulation data with all parameters stored in a dictionary:
filename = "line_map"
params_name = 'Params_line_map'
params = {"E_A": E_A, "t_1A": t_1A , "t_2A": t_2A ,\
          "E_B": E_B, "alpha": alpha , "epsilon0": epsilon0 , \
          "V_AB_upup": V_AB_upup, "V_AB_downdown": V_AB_downdown,
          "Theta": Theta, "W_dim": W_dim, "kB": kB , "T":T}

save(saving_path + params_name , params)
save(saving_path + filename , conductance2)
```

The simulation data are saved in the folder you gave the path at the beginning of the code with a numpy format (".npy"). It can be opened by executing the following snippet

```
data = load(saving_path + "FILENAME.npy")
fig1 ,ax1 = plt . subplots ()
Conductance_map = ax1.imshow( data, cmap="hot", interpolation ='nearest' )
fig1 . colorbar (Conductance_map)
plt . xticks ([])
plt . yticks ([])
plt .show()
```

Acknowledgements

Sadly, time flies so fast .... I would like to take advantage of this moment and express my gratitude to whom I shared an important part of my life.

In the beginning, I would like to express my deepest gratitude to **Prof. Markus Ternes** for supervising my doctorate. His trust in me and humble, pedagogical attitude were heart-warming to jump into a new world and start from zero in the experiment. It was an amazing journey. Thank you!

I would like to thank **Prof. Klaus Kern** for giving me the opportunity to join the Nanoscale Science Department at the Max Planck Institute for Solid State Research in Stuttgart as a PhD student and provided me with a fantastic lab.

I would like to thank **Dr. Yuqi Wang**, my former labmate who patiently passed me his knowledge in STM for more than two years.

I would like to thank **Prof. Ruslan Temirov** for kindly sharing his deep knowledge in STM and the NTCDA system and, more importantly, dragging me into the X-peak story. This fantastic story would not have started without him.

I would like to thank **Dr. Cedric Weber** for our collaboration and a lot of theory insights I gained from him in our discussions.

I would like to thank **Prof. Stefan Tautz** for our collaboration and the exciting discussions about the X-peak story.

I would like to thank **Dr. Taner Esat** for our collaboration and his keen eye in catching my mistakes in the measurements.

I would like to thank **Dr. Ammar Nejati** for sharing his profound intuition with me and also for the many friendly pieces of advice.

I would like to thank **Dr. Klaus Kunke** and **Mr. Abhishek Grewal** for kindly helping me and sharing their equipment and experience.

I would like to thank **Dr. Soon Jung Jung** for kindly borrowing me her molecule evaporator and other equipment when I needed it.

I would like to thank **Dr. Christopher Leon** for discussing his paper with me and his fruitful pieces of advice at the beginning of my research.

I would like to thank **Prof. Christian Ast** for the many deep discussions we had together with Markus.

I would like to thank **Mr. Hovan Lee** for reviewing my python code and his fruitful suggestions in our meetings.

I would like to thank **Ms. Birgit King**, **Dr. Michael Eppard**, **Mr. Frank Gottschalk** for their invaluable helps with my visa extensions and paper works in Germany.

I would like to thank **Ms. Sabine Birtel** for helping me with the administration and organizational works.

I would like to thank engineers in our department, **Ms. Isabel Wolf, Mr. Wolfgan Stiepany**, **Mr. Peter Andler**, and **Mr. Marco Memmler** for their technical assists.

I would like to thank all other members of the Precision Lab, specially **Mr. Janis Siebrecht**, **Dr. Haonan Huang**, **Dr. Sven Szilagyi**, **Dr. Tomasz Michnowicz**, **Dr. Anna Rosławska**, **Dr. Xu Wu**, **Dr. Manish Garg** for their assist and advice.

I would like to dedicate this work to my wonderful, loving **parents** for all their unconditional supports, and also thank my sister, **Sahar**, and my aunt, **Farah**, for their care and kindness.

Stuttgart, June 2, 2022 **Soroush Arabi**

Bibliography

1. Figgins, J. *et al.* Quantum engineered Kondo lattices. *Nature Communications* **10,** 55–88 (2019).
2. Drost, R., Ojanen, T., Harju, A. & Liljeroth, P. Topological states in engineered atomic lattices. *Nature Physics* **13,** 668–671 (2017).
3. Slot, M. R. *et al.* Experimental realization and characterization of an electronic Lieb lattice. *Nature Physics* **13,** 672–676 (2017).
4. Gomes, K. K., Mar, W., Ko, W., Guinea, F. & Manoharan, H. C. Designer Dirac fermions and topological phases in molecular graphene. *Nature* **483,** 306–310 (2012).
5. Bloch, I. Ultracold quantum gases in optical lattices. *Nature Physics* **1,** 23–30 (2005).
6. Ternes, M. *et al.* Scanning-Tunneling Spectroscopy of Surface-State Electrons Scattered by a Slightly Disordered Two-Dimensional Dilute “Solid": Ce on Ag(111). *Phys. Rev. Lett.* **93,** 146805 (2004).
7. Silly, F. *et al.* Creation of an Atomic Superlattice by Immersing Metallic Adatoms in a Two-Dimensional Electron Sea. *Phys. Rev. Lett.* **92,** 016101 (2004).
8. Jiang, Y., Zhang, Y. N., Cao, J. X., Wu, R. Q. & Ho, W. Real-Space Imaging of Kondo Screening in a Two-Dimensional O_2 Lattice. *Science* **333,** 324–328 (2011).
9. Kouwenhoven, L. & Marcus, C. Quantum dots. *Physics World* **11,** 35–40 (1998).
10. Lee, T. *et al.* Controlling the dimension of the quantum resonance in CdTe quantum dot superlattices fabricated via layer-by-layer assembly. *Nature Communications* **11,** 5471 (2020).
11. Springholz, G., Holy, V., Pinczolits, M. & Bauer, G. Self-Organized Growth of Three-Dimensional Quantum-Dot Crystals with fcc-Like Stacking and a Tunable Lattice Constant. *Science* **282,** 734–737 (1998).
12. Blatt, R. & Roos, C. F. Quantum simulations with trapped ions. *Nature Physics* **8,** 277–284 (2012).
13. Houck, A. A., Türeci, H. E. & Koch, J. On-chip quantum simulation with superconducting circuits. *Nature Physics* **8,** 292–299 (2012).
14. Singha, A. *et al.* Two-Dimensional Mott-Hubbard Electrons in an Artificial Honeycomb Lattice. *Science* **332,** 1176–1179 (2011).
15. Kirchner, S. *et al.* Colloquium: Heavy-electron quantum criticality and single-particle spectroscopy. *Rev. Mod. Phys.* **92,** 011002 (1 2020).
16. Stahl, U., Gador, D., Soukopp, A., Fink, R. & Umbach, E. Coverage-dependent superstructures in chemisorbed NTCDA monolayers: a combined LEED and STM study. *Surface Science* **414,** 423–434 (1998).

17. Eickhoff, F. *et al.* Inelastic electron tunneling spectroscopy for probing strongly correlated many-body systems by scanning tunneling microscopy. *Phys. Rev. B* **101,** 125–405 (2020).

18. Binnig, G. & Roher, H. Scanning tunneling microscopy. *Helvetica Physica Acta* **55,** 726–735 (1982).

19. Herden, T. *Combined Scanning Tunneling and Atomic Force Microscopy and Spectroscopy on Molecular Nanostructures,* PhD thesis (Universität Konstanz, Konstanz, 2014).

20. Muenks, M. *Scanning Tunneling Microscopy and Atomic Force Microscopy Measurements on Correlated Systems,* PhD thesis (Universität Konstanz, Konstanz, 2017).

21. Bruus, H. & Flensberg, K. *Many-body quantum theory in condensed matter physics* (Oxford University Press, Oxford, 2004).

22. Sólyom, J. *Fundamentals of the Physics of Solids, Volume 3* (Springer, Berlin, Heidelberg, 2010).

23. Haug, H. & Jauho, A.-P. *Quantum Kinetics in Transport and Optics of Semiconductors* (Springer, Berlin, Heidelberg, 2008).

24. Bardeen, J. Tunnelling from a Many-Particle Point of View. *Phys. Rev. Lett.* **6,** 57–59 (1961).

25. Gamow, G. Zur Quantentheorie des Atomkernes. *Zeitschrift für Physik* **51,** 204–212 (1928).

26. Tersoff, J. & Hamann, D. R. Theory of the scanning tunneling microscope. *Phys. Rev. B* **31,** 805–813 (1985).

27. Meir, Y. & Wingreen, N. S. Landauer formula for the current through an interacting electron region. *Phys. Rev. Lett.* **68,** 2512–2515 (1992).

28. Dobrovitski, V., Fuchs, G., Falk, A., Santori, C. & Awschalom, D. Quantum control over single spins in diamond. *Annual Review of Condensed Matter Physics* **4,** 23–50 (2013).

29. Loth, S. *et al.* Controlling the state of quantum spins with electric currents. *Nature Physics* **6,** 340–344 (2010).

30. Jezouin, S. *et al.* Controlling charge quantization with quantum fluctuations. *Nature* **536,** 58–62 (2016).

31. Arute, F. *et al.* Quantum supremacy using a programmable superconducting processor. *Nature* **574,** 505–510 (2019).

32. Ladd, T. D. *et al.* Quantum computers. *Nature* **464,** 45–53 (2010).

33. Yin, J.-X., Pan, S. H. & Zahid Hasan, M. Probing topological quantum matter with scanning tunnelling microscopy. *Nature Reviews Physics* **3,** 249–263 (2021).

34. Hasan, M. Z. & Kane, C. L. Colloquium: Topological insulators. *Rev. Mod. Phys.* **82,** 3045–3067 (4 2010).

35. Takagi, H., Takayama, T., Jackeli, G., Khaliullin, G. & Nagler, S. E. Concept and realization of Kitaev quantum spin liquids. *Nature Reviews Physics* **1,** 264–280 (2019).

36. Novoselov, K. S. *et al.* A roadmap for graphene. *Nature* **490,** 192–200 (2012).

37. Manzeli, S., Ovchinnikov, D., Pasquier, D., Yazyev, O. V. & Kis, A. 2D transition metal dichalcogenides. *Nature Reviews Materials* **2,** 17033 (2017).

38. Choi, W. *et al.* Recent development of two-dimensional transition metal dichalcogenides and their applications. *Materials Today* **20,** 116–130. ISSN: 1369–7021 (2017).

39. Brune, H., Giovannini, M., Bromann, K. & Kern, K. Self-organized growth of nanostructure arrays on strain-relief patterns. *Nature* **394,** 451–453 (1998).

40. Kern, K. *et al.* Long-range spatial self-organization in the adsorbate-induced restructuring of surfaces: Cu{100}-(2 × 1)O. *Phys. Rev. Lett.* **67,** 855–858 (1991).

41. Röder, H., Hahn, E., Brune, H., Bucher, J.-P. & Kern, K. Building one- and two-dimensional nanostructures by diffusion-controlled aggregation at surfaces. *Nature* **366,** 141–143 (1993).

42. Choi, D.-J. *et al.* Colloquium: Atomic spin chains on surfaces. *Rev. Mod. Phys.* **91,** 041001 (2019).

43. Paul, W. *et al.* Control of the millisecond spin lifetime of an electrically probed atom. *Nature Physics* **13,** 403–407 (2017).

44. Natterer, F. D. *et al.* Reading and writing single-atom magnets. *Nature* **543,** 226–228 (2017).

45. Fink, R., Gador, D., Stahl, U., Zou, Y. & Umbach, E. Substrate-dependent lateral order in naphthalene-tetracarboxylic-dianhydride monolayers. *Phys. Rev. B* **60,** 2818–2826 (1999).

46. Kilian, L. *et al.* The commensurate-to-incommensurate phase transition of an organic monolayer: A high resolution LEED analysis of the superstructures of NTCDA on Ag(111). *Surface Science* **602,** 2427–2434 (2008).

47. Braatz, C. *et al.* Switching orientation of adsorbed molecules: Reverse domino on a metal surface. *Surface Science* **643,** 98–107 (2016).

48. Eschmann, L. *et al.* Coverage-dependent anisotropy of the NTCDA/Ag(111) interface state dispersion. *Phys. Rev. B* **100,** 125–155 (2019).

49. Tonner, R., Rosenow, P. & Jakob, P. Molecular structure and vibrations of NTCDA monolayers on Ag(111) from density-functional theory and infrared absorption spectroscopy. *Phys. Chem. Chem. Phys.* **18,** 6316–6328 (2016).

50. Bendounan, A. *et al.* Electronic structure of 1ML NTCDA/Ag(111) studied by photoemission spectroscopy. *Surface Science* **601,** 4013–4017 (2007).

51. Ziroff, J. *et al.* Low-energy scale excitations in the spectral function of organic monolayer systems. *Phys. Rev. B* **85,** 161–404 (2012).

52. Alkauskas, A., Baratoff, A. & Bruder, C. Site-selective adsorption of naphthalene-tetracarboxylic-dianhydride on $\mathrm{Ag}(110)$: First-principles calculations. *Phys. Rev. B* **73,** 165–408 (2006).

53. Liu, Z.-F., Egger, D. A., Refaely-Abramson, S., Kronik, L. & Neaton, J. B. Energy level alignment at molecule-metal interfaces from an optimally tuned range-separated hybrid functional. *The Journal of Chemical Physics* **146,** 092–326 (2017).

54. Schöll, A. *et al.* Disordering of an organic overlayer on a metal surface upon cooling. *Science* **329,** 303–305 (2010).

55. Jackson, A. G. *Handbook of crystallography For electron microscopists and others* **5** (Springer, New York, NY, 1991).

56. Jakob, P. *et al.* Adsorption geometry and interface states: Relaxed and compressed phases of NTCDA/Ag(111). *Phys. Rev. B* **94,** 125–436 (2016).

57. Stadtmüller, B. *et al.* Unexpected interplay of bonding height and energy level alignment at heteromolecular hybrid interfaces. *Nature Communications* **5,** 36–85 (2014).

58. Zojer, E., Taucher, T. C. & Hofmann, O. T. The impact of dipolar layers on the electronic properties of organic/inorganic hybrid interfaces. *Advanced Materials Interfaces* **6,** 1900581 (2019).

59. Riss, A. *et al.* Imaging and tuning molecular levels at the surface of a gated graphene device. *ACS Nano* **8,** 5395–5401 (2014).

60. Fano, U. Effects of configuration interaction on intensities and phase shifts. *Phys. Rev.* **124,** 1866–1878 (1961).

61. Temirov, R., Soubatch, S., Luican, A. & Tautz, F. S. Free-electron-like dispersion in an organic monolayer film on a metal substrate. *Nature* **444,** 350–353 (2006).

62. Sabitova, A. *Engineering of extended two-dimensional electronic states at a molecule-metal interface with low-temperature STM.* (Unpublished PhD Thesis).

63. Stolyarov, V. S. *et al.* Double Fe-impurity charge state in the topological insulator Bi_2Se_3. *Applied Physics Letters* **111,** 251601 (2017).

64. Cui, Y. *et al.* Controlling the charge state of single Mo dopants in a CaO film. *Phys. Rev. B* **88,** 205–421 (2013).

65. Zhang, R., Clark, G., Xu, X., Darancet, P. T. & Guest, J. R. Observation of single-electron transport and charging on individual point defects in atomically thin WSe2. *The Journal of Physical Chemistry C* **125,** 14056–14064 (2021).

66. Qiu, Z. *et al.* Resolving the spatial structures of bound hole states in black phosphorus. *Nano Letters* **17,** 6935–6940 (2017).

67. Velasco, J. *et al.* Visualization and control of single-electron charging in bilayer graphene quantum dots. *Nano Letters* **18,** 5104–5110 (2018).

68. Pörtner, M. *et al.* Charge state control of F16CoPc on h-BN/Cu(111). *Advanced Materials Interfaces* **7,** 2000080 (2020).

69. Lee, D., Gohlke, D., Benjamin, A. & Gupta, J. A. Influence of the local environment on Mn acceptors in GaAs. *Journal of Physics: Condensed Matter* **27,** 154–202 (2015).

70. Wong, D. *et al.* Characterization and manipulation of individual defects in insulating hexagonal boron nitride using scanning tunnelling microscopy. *Nature Nanotechnology* **10,** 949–953 (2015).

71. Eom, D., Seo, E. & Koo, J.-Y. Surface-sensitive measurement of dielectric screening via atom and electron manipulations. *Phys. Rev. B* **94,** 195–308 (2016).

72. Nguyen, G. D. *et al.* 3D imaging and manipulation of subsurface selenium vacancies in $PdSe_2$. *Phys. Rev. Lett.* **121,** 086–101 (2018).

73. Li, H. *et al.* Imaging local discharge cascades for correlated electrons in WS2/WSe2 moiré superlattices. *Nature Physics* **17,** 1114–1119 (2021).

74. Mohammed, M. S. G. *et al.* Electronic decoupling of polyacenes from the underlying metal substrate by sp3 carbon atoms. *Communications Physics* **3,** 159 (2020).

75. Fernández-Torrente, I., Kreikemeyer-Lorenzo, D., Stróżecka, A., Franke, K. J. & Pascual, J. I. Gating the charge state of single molecules by local electric fields. *Phys. Rev. Lett.* **108,** 036–801 (2012).

76. Leon, C. C., Kuhnke, K. & Gunnarsson, O. Band Bending and Beyond. *The Journal of Physical Chemistry C* **125,** 3206–3214 (2021).

77. Battisti, I. *et al.* Poor electronic screening in lightly doped Mott insulators observed with scanning tunneling microscopy. *Phys. Rev. B* **95,** 235141 (2017).

78. Stadler, C *et al.* Molecular distortion of NTCDA upon adsorption on Ag(111): a normal incidence x-ray standing wave study. *New Journal of Physics* **9,** 50 (2007).

79. Varma, C. M. Colloquium: Linear in temperature resistivity and associated mysteries including high temperature superconductivity. *Rev. Mod. Phys.* **92,** 031001 (2020).

80. Coleman, P. *Introduction to Many-Body Physics* (Cambridge University Press, 2015).

81. Matthias, B. T. *et al.* Magnetic Moment of Transition Metal Atoms in Dilute Solution and Their Effect on Superconducting Transition Temperature. *Phys. Rev. Lett.* **5,** 542–544 (1960).

82. Clogston, A. M. *et al.* Local Magnetic Moment Associated with an Iron Atom Dissolved in Various Transition Metal Alloys. *Phys. Rev.* **125,** 541–552 (1962).

83. Kondo, J. Resistance minimum in dilute magnetic alloys. *Progress of Theoretical Physics* **32,** 37–49 (1964).

84. Hewson, A. C. *The Kondo Problem to Heavy Fermions* (Cambridge University Press, 1993).

85. Anderson, P. W. Localized Magnetic States in Metals. *Phys. Rev.* **124,** 41–53 (1961).

86. Friedel, J. The distribution of electrons round impurities in monovalent metals. *The London, Edinburgh, and Dublin Philosophical Magazine and Journal of Science* **43,** 153–189 (1952).

87. Friedel, J. On some electrical and magnetic properties of metallic solid solutions. *Canadian Journal of Physics* **34,** 1190–1211 (1956).

88. Barzykin, V. & Affleck, I. The Kondo Screening Cloud: What Can We Learn from Perturbation Theory? *Phys. Rev. Lett.* **76,** 4959–4962 (1996).

89. Affleck, I. *The Kondo screening cloud: what it is and how to observe it* 2009.

90. Doniach, S & Sondheimer, E. H. *Green's Functions for Solid State Physicists* (Published by imperial college press and distributed by world scientific publishing co., 1998).

91. Schrieffer, J. R. & Wolff, P. A. Relation between the Anderson and Kondo Hamiltonians. *Phys. Rev.* **149,** 491–492 (1966).

92. Abrikosov, A. A. Electron scattering on magnetic impurities in metals and anomalous resistivity effects. *Physics Physique Fizika* **2,** 5–20 (1965).

93. Suhl, H. Dispersion Theory of the Kondo Effect. *Phys. Rev.* **138,** A515–A523 (1965).

94. Grüner, G. & Zawadowski, A. Magnetic impurities in non-magnetic metals. *Reports on Progress in Physics* **37,** 1497–1583 (1974).

95. Grüner, G. & Zawadowski, A. *Low temperature properties of Kondo alloys* 591–647 (Elsevier, 1978).

96. Anderson, P. W., Yuval, G. & Hamann, D. R. Exact Results in the Kondo Problem. II. Scaling Theory, Qualitatively Correct Solution, and Some New Results on One-Dimensional Classical Statistical Models. *Phys. Rev. B* **1,** 4464–4473 (1970).

97. Paschen, S. & Si, Q. Quantum phases driven by strong correlations. *Nature Reviews Physics* **3,** 9–26 (2021).

98. Steglich, F. & Wirth, S. Foundations of heavy-fermion superconductivity: lattice Kondo effect and Mott physics. *Reports on Progress in Physics* **79,** 084502 (2016).

99. Seiro, S. *et al.* Evolution of the Kondo lattice and non-Fermi liquid excitations in a heavy-fermion metal. *Nature Communications* **9,** 3324 (2018).

100. Affleck, I. Non-Fermi Liquid Behavior in Kondo Models. *Journal of the Physical Society of Japan* **74,** 59–66 (2005).

101. Stewart, G. R. Non-Fermi-liquid behavior in d- and f-electron metals. *Rev. Mod. Phys.* **73,** 797–855 (2001).

102. Doniach, S. The Kondo lattice and weak antiferromagnetism. *Physica B+C* **91,** 231–234 (1977).

103. Ruderman, M. A. & Kittel, C. Indirect Exchange Coupling of Nuclear Magnetic Moments by Conduction Electrons. *Phys. Rev.* **96,** 99–102 (1954).

104. Kasuya, T. A Theory of Metallic Ferro- and Antiferromagnetism on Zener's Model. *Progress of Theoretical Physics* **16,** 45–57 (1956).

105. Yosida, K. Magnetic Properties of Cu-Mn Alloys. *Phys. Rev.* **106,** 893–898 (1957).

106. Schröder, A. *et al.* Onset of antiferromagnetism in heavy-fermion metals. *Nature* **407,** 351–355 (2000).

107. Vojta, M. Quantum phase transitions. *Reports on Progress in Physics* **66,** 2069–2110 (2003).

108. Si, Q. & Paschen, S. Quantum phase transitions in heavy fermion metals and Kondo insulators. *physica status solidi (b)* **250,** 425–438 (2013).

109. Zhu, J.-X., Grempel, D. R. & Si, Q. Continuous Quantum Phase Transition in a Kondo Lattice Model. *Phys. Rev. Lett.* **91,** 156404 (2003).

110. Si, Q. & Steglich, F. Heavy Fermions and Quantum Phase Transitions. *Science* **329,** 1161–1166 (2010).

111. Si, Q., Zhu, J.-X. & Grempel, D. R. Magnetic quantum phase transitions in Kondo lattices. *Journal of Physics: Condensed Matter* **17,** R1025–R1040 (2005).

112. Stockert, O. & Steglich, F. Unconventional Quantum Criticality in Heavy-Fermion Compounds. *Annual Review of Condensed Matter Physics* **2,** 79–99 (2011).

113. Trovarelli, O. *et al.* $YbRh_2Si_2$: Pronounced Non-Fermi-Liquid Effects above a Low-Lying Magnetic Phase Transition. *Phys. Rev. Lett.* **85,** 626–629 (2000).

114. Custers, J. *et al.* The break-up of heavy electrons at a quantum critical point. *Nature* **424,** 524–527 (2003).

115. Goh, S. K. *et al.* Fermi-Surface Reconstruction in $CeRh_{1-x}Co_xIn_5$. *Phys. Rev. Lett.* **101,** 056402 (2008).

116. Mathur, N. D. *et al.* Magnetically mediated superconductivity in heavy fermion compounds. *Nature* **394,** 39–43 (1998).

117. Raymond, S., Knafo, W., Flouquet, J., Bourdarot, F. & Lejay, P. Quantum criticality of $Ce_{1-x}La_xRu_2Si_2$: The magnetically ordered phase. *physica status solidi (b)* **247,** 700–702 (2010).

118. Löhneysen, H. v. *et al.* Non-Fermi-liquid behavior in a heavy-fermion alloy at a magnetic instability. *Phys. Rev. Lett.* **72,** 3262–3265 (1994).

119. Sinjukow, P. & Nolting, W. Exact mapping of periodic Anderson model to Kondo lattice model. *Phys. Rev. B* **65,** 212303 (2002).

120. Coleman, P. New approach to the mixed-valence problem. *Phys. Rev. B* **29,** 3035–3044 (1984).

121. Sabitova, A., Temirov, R. & Tautz, F. S. Lateral scattering potential of the PTCDA/Ag(111) interface state. *Phys. Rev. B* **98,** 205429 (2018).

122. Nazin, G. V., Qiu, X. H. & Ho, W. Charging and Interaction of Individual Impurities in a Monolayer Organic Crystal. *Phys. Rev. Lett.* **95,** 166103 (16 2005).

123. Lu, J. *et al.* Frustrated supercritical collapse in tunable charge arrays on graphene. *Nature Communications* **10,** 477 (2019).

124. Edmonds, M. T. *et al.* Spatial charge inhomogeneity and defect states in topological Dirac semimetal thin films of Na_3Bi. *Science Advances* **3,** eaao6661 (2017).

125. Wong, D. *et al.* Cascade of electronic transitions in magic-angle twisted bilayer graphene. *Nature* **582,** 198–202 (2020).

126. Zhao, H. *et al.* Cascade of correlated electron states in the kagome superconductor CsV3Sb5. *Nature* **599,** 216–221 (2021).

127. Fan, F.-R. F. *et al.* Charge Transport through Self-Assembled Monolayers of Compounds of Interest in Molecular Electronics. *Journal of the American Chemical Society* **124,** 5550–5560 (2002).

128. Pham, V. D. *et al.* Selective control of molecule charge state on graphene using tip-induced electric field and nitrogen doping. *npj 2D Materials and Applications* **3,** 5 (2019).

129. Gonzalez-Lakunza, N. *et al.* Formation of Dispersive Hybrid Bands at an Organic-Metal Interface. *Phys. Rev. Lett.* **100,** 156805 (2008).

130. Guisinger, N. P., Yoder, N. L. & Hersam, M. C. Probing charge transport at the single-molecule level on silicon by using cryogenic ultra-high vacuum scanning tunneling microscopy. *Proceedings of the National Academy of Sciences* **102,** 8838–8843 (2005).

131. Collins, J. L. *et al.* Electric-field-tuned topological phase transition in ultrathin Na_3Bi. *Nature* **564,** 390–394 (2018).

132. Peierls, R. Zur Theorie des Diamagnetismus von Leitungselektronen. *Zeitschrift für Physik* **80,** 763–791 (1933).

133. Hofstadter, D. R. Energy levels and wave functions of Bloch electrons in rational and irrational magnetic fields. *Phys. Rev. B* **14,** 2239–2249 (1976).

134. Haldane, F. D. M. Model for a Quantum Hall Effect without Landau Levels: Condensed-Matter Realization of the "Parity Anomaly". *Phys. Rev. Lett.* **61,** 2015–2018 (1988).

135. Wang, Y., Arabi, S., Kern, K. & Ternes, M. Symmetry mediated tunable molecular magnetism on a 2D material. *Communications Physics* **4,** 103 (2021).

136. Cao, Y. *et al.* Unconventional superconductivity in magic-angle graphene superlattices. *Nature* **556,** 43–50 (2018).

137. Dzialoshinskii, I. Thermodynamic theory of weak ferromagnetism in antiferromagnetic substances. *Sov. Phys. JETP* **5,** 1259–1272 (1957).

138. Moriya, T. Anisotropic superexchange interaction and weak ferromagnetism. *Phys. Rev.* **120,** 91 (1960).

139. Xi, X. *et al.* Ising pairing in superconducting $NbSe_2$ atomic layers. *Nat. Phys.* **12,** 139–143 (2016).

140. Bawden, L. *et al.* Spin–valley locking in the normal state of a transition-metal dichalcogenide superconductor. *Nature Communications* **7,** 11711 (2016).

141. Kezilebieke, S., Dvorak, M., Ojanen, T. & Liljeroth, P. Coupled Yu-Shiba-Rusinov states in molecular dimers on $NbSe_2$. *Nano Lett.* **18,** 2311–2315 (2018).

142. Mugarza, A. *et al.* Spin coupling and relaxation inside molecule–metal contacts. *Nature Communications* **2,** 490 (2011).

143. Mugarza, A. *et al.* Electronic and magnetic properties of molecule-metal interfaces: Transition-metal phthalocyanines adsorbed on Ag(100). *Phys. Rev. B* **85,** 155437 (2012).

144. Hu, Z., Li, B., Zhao, A., Yang, J. & Hou, J. Electronic and magnetic properties of metal phthalocyanines on Au (111) surface: A first-principles study. *The Journal of Physical Chemistry C* **112,** 13650–13655 (2008).

145. Ribeiro-Soares, J. *et al.* Group theory analysis of phonons in two-dimensional transition metal dichalcogenides. *Phys. Rev. B* **90,** 115–438 (2014).

146. Wagner, C. *et al.* Scanning quantum dot microscopy. *Phys. Rev. Lett.* **115,** 026101 (2015).

147. Yu, L. Bound state in superconductors with paramagnetic impurities. *Acta Phys. Sin.* **21,** 75–91 (1965).

148. Shiba, H. Classical spins in superconductors. *Prog. Theor. Exp. Phys.* **40,** 435–451 (1968).

149. Rusinov, A. Theory of gapless superconductivity in alloys containing paramagnetic impurities. *JETP Lett.* **29,** 1101–1106 (1969).

150. Heinrich, B. W., Pascual, J. I. & Franke, K. J. Single magnetic adsorbates on s-wave superconductors. *Prog. Surf. Sci.* **93,** 1–19 (2018).

151. Salkola, M., Balatsky, A. & Schrieffer, J. Spectral properties of quasiparticle excitations induced by magnetic moments in superconductors. *Phys. Rev. B* **55,** 12648 (1997).

152. Franke, K., Schulze, G. & Pascual, J. Competition of superconducting phenomena and Kondo screening at the nanoscale. *Science* **332,** 940–944 (2011).

153. Zhang, Y.-h. *et al.* Temperature and magnetic field dependence of a Kondo system in the weak coupling regime. *Nature Communications* **4,** 2110 (2013).

154. Filippone, M., Moca, C., Weichselbaum, A., von Delft, J. & Mora, C. At which magnetic field, exactly, does the Kondo resonance begin to split? A Fermi liquid description of the low-energy properties of the Anderson model. *Phys. Rev. B* **98,** 075404 (2018).

155. Anderson, P. W. Localized Magnetic States and Fermi-Surface Anomalies in Tunneling. *Phys. Rev. Lett.* **17,** 95–97 (1966).

156. Appelbaum, J. "$s-d$" Exchange Model of Zero-Bias Tunneling Anomalies. *Phys. Rev. Lett.* **17,** 91–95 (1966).

157. Dynes, R., Narayanamurti, V & Garno, J. P. Direct measurement of quasiparticle-lifetime broadening in a strong-coupled superconductor. *Phys. Rev. Lett.* **41,** 1509 (1978).

158. Šmakov, J., Martin, I. & Balatsky, A. V. Theory of scanning tunneling microscopy measurement of single spin decoherence in a superconductor. *Phys. Rev. Lett.* **88,** 037003 (2002).

159. Ruby, M. *et al.* Tunneling processes into localized subgap states in superconductors. *Phys. Rev. Lett.* **115,** 087001 (2015).

160. Ingold, G.-L., Grabert, H. & Eberhardt, U. Cooper-pair current through ultrasmall Josephson junctions. *Phys. Rev. B* **50,** 395 (1994).

161. Ternes, M. Probing magnetic excitations and correlations in single and coupled spin systems with scanning tunneling spectroscopy. *Prog. Surf. Sci.* **92,** 83–115 (2017).

162. Gupta, J., Lutz, C., Heinrich, A. & Eigler, D. Strongly coverage-dependent excitations of adsorbed molecular hydrogen. *Phys. Rev. B* **71,** 115416 (2005).

163. Rossnagel, K *et al.* Fermi surface of 2H-$NbSe_2$ and its implications on the charge-density-wave mechanism. *Phys. Rev. B* **64,** 235119 (2001).

164. Straub, T. *et al.* Charge-Density-Wave Mechanism in 2H-$NbSe_2$: Photoemission Results. *Phys. Rev. Lett.* **82,** 4504 (1999).

165. Chen, C. J. *Introduction to Scanning Tunneling Microscopy: Second Edition* (Oxford University Press, Oxford, 2007).

166. Lyo, I.-W. & Avouris, P. Negative Differential Resistance on the Atomic Scale: Implications for Atomic Scale Devices. *Science* **245,** 1369–1371 (1989).

167. Klein, J., Léger, A., Belin, M., Défourneau, D. & Sangster, M. J. L. Inelastic-Electron-Tunneling Spectroscopy of Metal-Insulator-Metal Junctions. *Phys. Rev. B* **7,** 2336–2348 (1973).